IEEE P802.15
Wireless Personal Area Networks

Project	IEEE P802.15 Working Group for Wireless Personal Area Networks (WPANs)	
Title	**Narrowband Channel Characterization for Body Area Networks**	
Date Submitted	Tuesday 8th July, 2008	
Source	Dino Miniutti, Leif Hanlen, David Smith, Andrew Zhang, Daniel Lewis, David Rodda, Ben Gilbert NICTA 7 London Circuit, Canberra ACT 2600, Australia	Voice: +61-2-6267-6256 Fax: +61-2-6267-6220 Email: dino.miniutti@nicta.com.au
Re:	15-08-0033-02-0006-draft-of-channel-model-for-body-area-network	
Abstract	This document presents the results of narrowband on-body wireless channel measurements around the 900 and 2400 MHz ISM bands. The focus is on characterizing the effects of movement on the BAN channel.	
Purpose	This document is intended to aid in the formation of a channel model for the IEEE 802.15.6 BAN standard.	
Notice	This document has been prepared to assist the IEEE P802.15. It is offered as a basis for discussion and is not binding on the contributing individual(s) or organization(s). The material in this document is subject to change in form and content after further study. The contributor(s) reserve(s) the right to add, amend or withdraw material contained herein.	
Release	The contributor acknowledges and accepts that this contribution becomes the property of IEEE and may be made publicly available by P802.15.	

Contents

1 Introduction

With computers, sensors and devices getting smaller, there now exist many electronic devices that can be worn on, or attached to, the human body. These wearable devices have a wide-ranging number of uses; including defense, medical and sporting applications. As the number of devices that people wear increases, the potential for an interconnected network of these devices (that is greater than the sum of its parts) becomes more likely. There are many challenges involved with building such a network, but one that is particularly useful is the elimination of wires to improve comfort and mobility of the human user. It is thus important to understand the on-body wireless channel as such understanding can maximize capacity and minimize power consumption of these body area networks.

The purpose of this paper is to promote such understanding by presenting the results of a number of on-body channel studies that can be used to aid in the design of body area network systems and channel models. It is hoped that this paper will provide assistance in the design of a channel model for The Institute of Electrical and Electronic Engineers (IEEE) 802.15.6 Body Area Network (BAN) standard [1]. In particular, the authors wish to use it to stress the dramatic effect that movement of the human body has on on-body wireless networks.

The investigation presented here involve the measurement of on-body narrowband wireless channels centered in regions around the 900 and 2400 MHz Industrial Scientific and Medical (ISM) bands. All measurements were performed on a human test subject in an indoor office environment with wearable antennas placed at different points on his body.

The study of this type of on-body wireless system (in an indoor environment) is challenging as there are many possible propagation paths between the antennas, including the often identified diffracted path around the human body, e.g. [2]. Each of these paths can experience fading due to the movement of the human body, as well as from multipath around the body and the surrounding environment. Of these effects, as described here, the fading effects due to movement are identified to be the most significant. This is partly due to the fact that movement affects the coupling of the transmitting and receiving antennas by affecting their relative geometry (alignment and displacement), but also because movement can significantly change the environment between the antennas by introducing obstacles between them.

A further challenge is that the body changes the near and far-field electromagnetic radiation characteristics of the body-worn antennas [3–7]. This coupled with the variable geometry and placement of the antennas makes it very difficult to separate the effects of the propagation path from the response of the antennas. To separate these effects would require the characterization of the radiation fields close to the antenna[1], through and in close proximity to the body, which is outside the intended scope of this work. Rather in this study, more practically, the antennas are considered to be a part of the channel as they are used in a standard indoor environment.

There have been other similar studies that have measured on-body narrowband wireless channels [8, 9][2] but they differ in a number of important ways. The innovation in this study is the analysis of the effects of continuous movement of the human body on the wireless channel, as an important addition to prior studies of human standing still or having a change in stance. Thus in this dynamic characterization of movement, measurements were taken while the test subject was walking and running on the spot, for a variety of transmit and receive antenna positions on the subject's

[1] Commonly done with an anechoic chamber

[2] Also, more generally studies on measurement, simulation, modeling and characterization of on-body wideband or narrowband wireless channels [2, 10–13]

body. Additional measurements were made with the subject standing still to serve as a reference. For each type of movement, post-measurement analysis was done to characterize the movement-induced variability in link gain, or path loss. The distribution of the normalized received power found by path loss measurements was statistically described using a probability density compared to a number of common statistical distributions to find the best match for all scenarios. Further analysis was also performed to estimate the coherence time, and hence characterize stability in a dynamic environment, of the on-body channel.

A more detailed description of the experimental method follows in the next section. Section 3 describes the analytical results found from measurements taken, including: - description of the channel's power spectral density; a characterization of path loss in all measurement positions; a statistical description of received power ; and channel coherence time analysis. The final section provides some concluding remarks. There is an appendix (after references) which gives a comprehensive catalog of analytical results described in Section 3.

2 Experimental Method

Wireless on-body channel measurements were made using two commercial wearable antennas strapped with VELCRO® tape to the body of a 181.5 cm / 78 kg male test subject in an office environment.

Channel measurements were performed by transmitting test signals centered in regions around the 900 and 2400 MHz ISM bands. The test signals were separately transmitted over one antenna while the subject was asked to perform three different actions: 1) standing still; 2) walking on the spot; and 3) running on the spot. The signal received at the other antenna was down-converted, sampled for approximately 10 seconds, and saved to disk. Analysis of the measurements was later done offline.

For each set of the three movement scenarios, the transmitting and receiving antennas were strapped to different locations on the test subject's body. Figure 1 illustrates the possible locations of the antennas on the test subject. Table 1 lists the combinations of transmit and receive antenna locations used, with separate channel measurements made for each combination. Table 2 lists the approximate antenna separations (in cm) for each element in Table 1. For reasons of symmetry, the left wrist and left ankle to chest measurements were not recorded.

Note that the purpose of these measurements is to support the synthesis of a channel model for the the IEEE 802.15.6 BAN standard [1]. As such, appropriate choices were made when choosing the bit rate, modulation scheme and pulse shaping filters. The combination used provided a relatively flat (1 dB attenuation in the sidelobes) signal spectrum over a 10 MHz bandwidth. A wireless system with 1 bit/s/Hz modulation efficiency could provide the 10 Mbps required by the 802.15.6 technical requirements document [15] within this bandwidth. More efficient systems could use less bandwidth, but the largest bandwidth was chosen to maximise frequency coverage and channel resolution in the time domain. The relatively flat spectrum also facilitated in the power spectral analysis performed in Section 3.1.

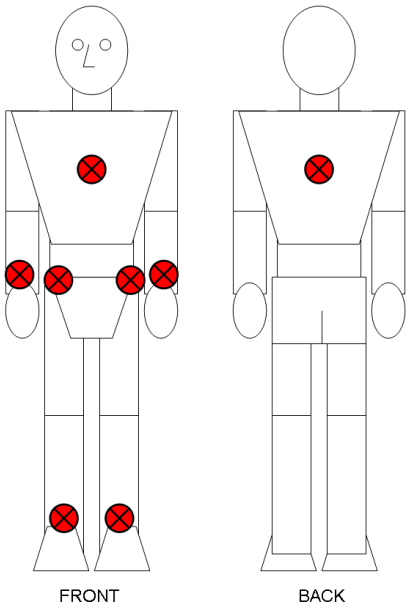

Figure 1: Possible antenna locations on test subject.

Table 1: Matrix of transmit and receive antenna locations. The symbol × in the matrix denotes that the corresponding channel measurement was conducted.

Receiver location	Transmitter location					
	Chest	Right wrist	Left wrist	Right ankle	Left ankle	Back
Right hip	×	×	×	×	×	×
Chest		×		×		×

Table 2: Matrix of the distance (cm) between transmit and receive antennas while the test subject is standing still.

Receiver location	Transmitter location					
	Chest	Right wrist	Left wrist	Right ankle	Left ankle	Back
Right hip	38	11	30	90	93	45
Chest		36		115		25 (50)

Note: The distances represent an approximate measure of the line-of-sight (LOS) path. In the case of back to chest measurement, the length of a direct path through the body is shown and the length of a path along the surface of the chest in the horizontal plane is shown in parentheses.

2.1 Detailed Experiment Description

Figure 2 illustrates the key features of the environment, including the location of the test subject. The block diagram in Figure 3 represents the arrangement of systems that was used to perform the measurements. Section 2.2 details the hardware that was used.

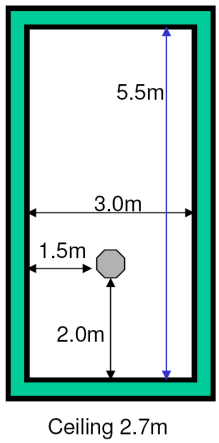

Figure 2: Experimental environment. The position of the test subject is indicated by the gray hexagon.

Before any measurements were performed, suitable center frequencies in regions around the 900 and 2400 MHz ISM bands were chosen. 820 MHz[3] and 2360 MHz were experimentally identified as suitable frequencies according to the criterion of: 1) low measured levels of interference from other devices; and 2) being sufficiently close to the operating frequencies of the antennas. For the purposes of this study, it is believed that these frequencies are adequately proximate to the ISM

[3]This is even closer to 868 MHz ISM band, with potential identified for medical BAN in [16]

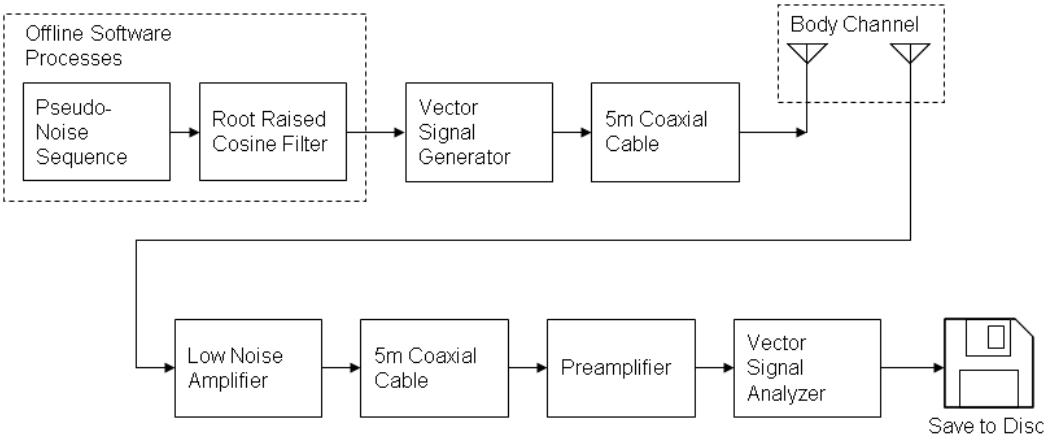

Figure 3: Block diagram of experimental setup.

bands of interest to characterize the behavior of radio signals within those bands.

The transmitter was configured to continuously transmit a 63 bit pseudo-noise (PN) binary phase shift keyed (BPSK) sequence at a bitrate of 12.5 Mbps. This sequence was filtered by a root-raised-cosine filter with a roll-off factor of 0.5, resulting in a 10 MHz 1 dB passband and a negligible amount of ripple. An identical filter was used in the receiver. Figure 4 and Figure 5 show the magnitude of the filter's frequency response. The sequence was then upsampled, by a factor of eight, to 100 MHz, to match the sampling rate of the vector signal generator. The power at the output of the vector signal generator was set to -10 dBm.

The receiver sampled the received signal at 50 MHz and was set to capture eight cycles of the transmitted PN sequence. The duration of a capture is approximately 40 μs. Due to limitations in the receiver hardware, each capture of the eight PN sequences was separated by 2.5 ms, during which time the captured data was saved to disk. The total observation period, including the 2.5 ms gaps, was 10 seconds. A timeline of the data acquisition cycle at the receiver is shown in Figure 6.

The gain of the amplifiers and cables were measured before the measurements were performed. During analysis the gain of the channel was obtained by removing the gain of the amplifiers and cables.

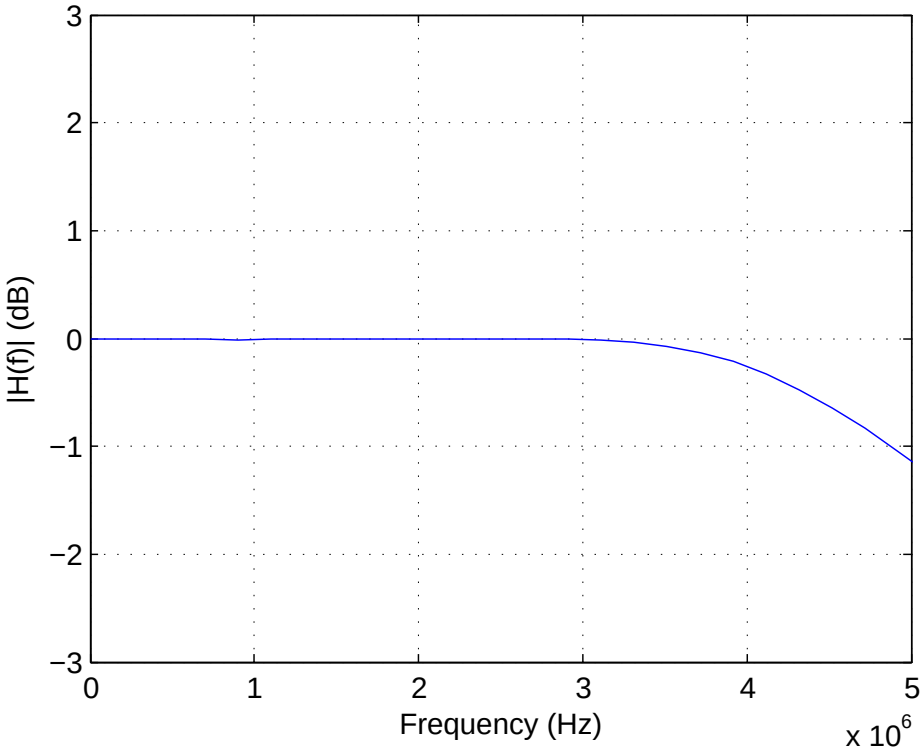

Figure 4: Passband of the root-raised-cosine-filter.

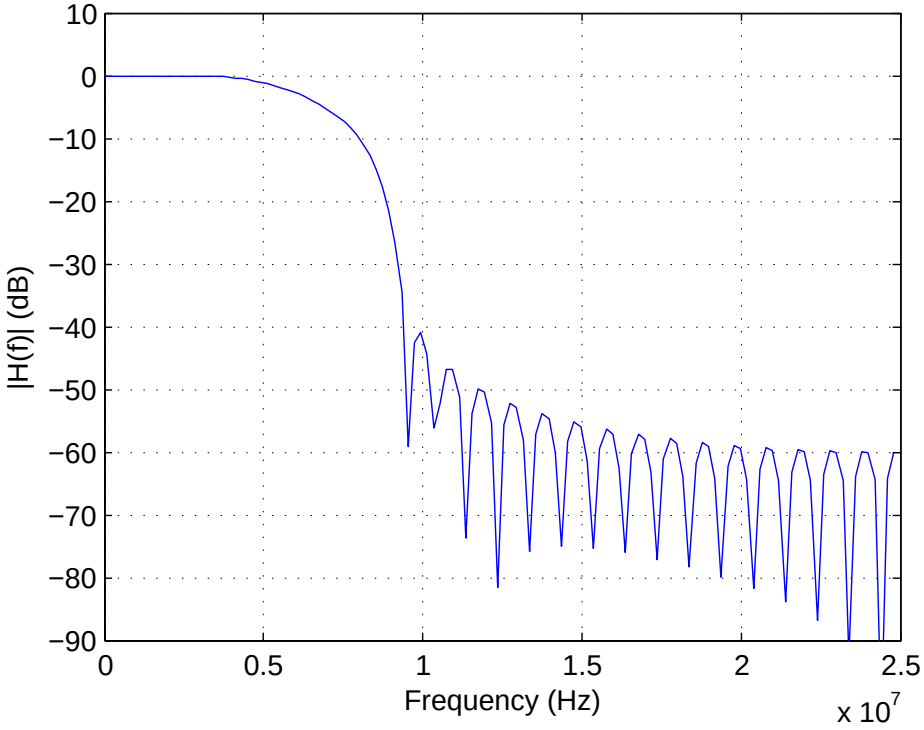

Figure 5: Response of the root-raised-cosine-filter.

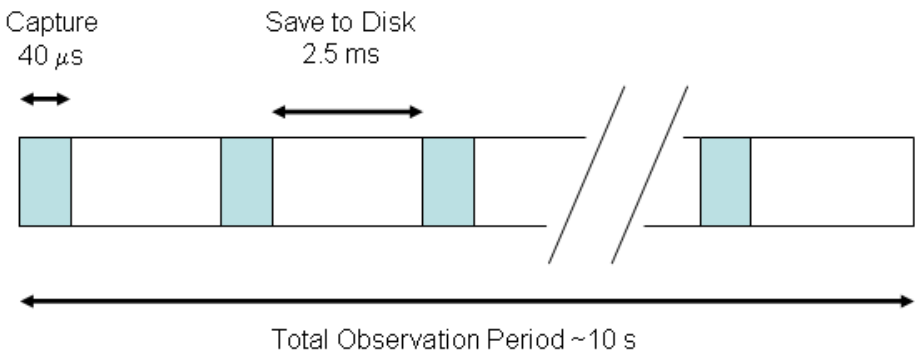

Figure 6: A timeline of the data acquisition cycle at the receiver.

2.2 List of equipment

This section lists the hardware that was used to perform the experiments.

- **Vector Signal Generator**: National Instruments PXIe-5672 RF Vector Signal Generator. This is comprised of a National Instruments PXI-5610 RF Upconverter and a National Instruments PXIe-5442 Arbitrary Waveform Generator.
- **Antennas used at 820 MHz** : Octane Wireless BW-800-900 wearable flexible antennas. Dimensions: $4.5 \times 7 \times 0.8$ cm. These antennas are approximately omnidirectional. The radiation pattern is shown in Figure 7.
- **Antennas used at 2.36 GHz Antennas**: Octane Wireless BW-2400-2500 wearable flexible antennas. Dimensions: $6 \times 5 \times 0.8$ cm. These antennas are approximately omnidirectional. The radiation pattern is shown in Figure 8.
- **Vector Signal Analyzer**: National Instruments PXI-5661 RF Vector Signal Analyzer. This is comprised of a National Instruments PXI-5600 Downconverter and a National Instruments PXI-5142 Digitizer.
- **Low Noise Amplifier used at 2.36 GHz**: Mini-Circuits ZQL-2700MLNW.
- **Low Noise Amplifier used at 820 MHz**: Mini-Circuits ZEL-0812LN.
- **Preamplifier**: National Instruments PXI-5690 Preamplifier.
- **National Instruments Controller**: The vector signal generator, vector signal analyzer and the preamplifier were all housed in a National Instruments PXIe-1065 Chassis and controlled by a National Instruments PXIe-8106 Host Controller.

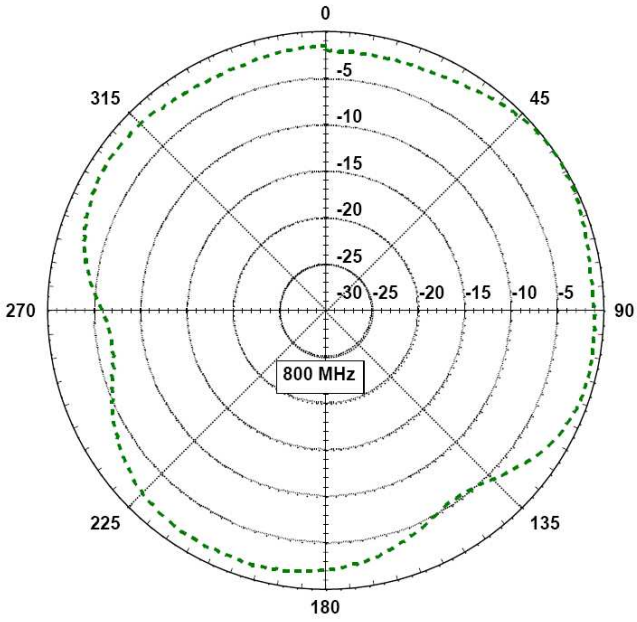

Figure 7: Radiation pattern (at 800 MHz) of antenna used at 820 MHz . Obtained from manufacturer's datasheet [17] (We assume pattern shown depicts H-plane co-polarization).

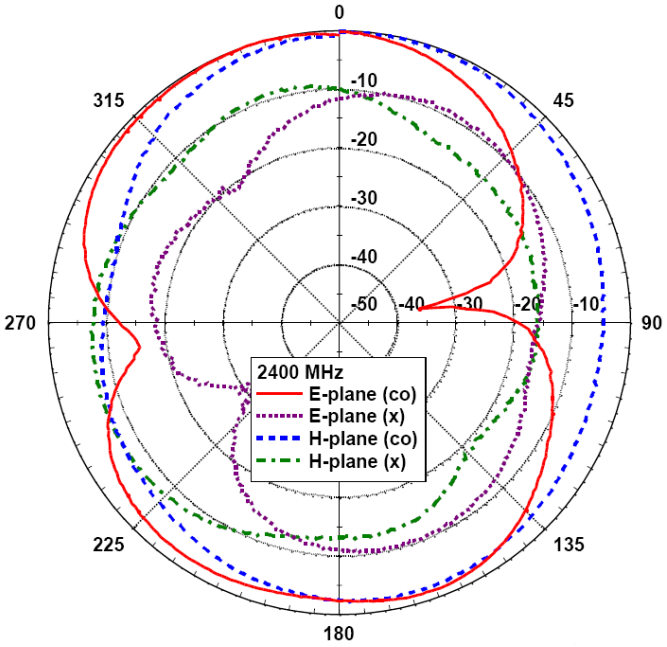

Figure 8: Radiation pattern (at 2.4 GHz) of antenna used at 2.36 GHz. Obtained from manufacturer's datasheet [18]

3 Results of Channel Measurement Analysis

This section presents the results of analysis performed on the channel measurements detailed in the previous section. A number of representative measurements and results which highlight important features are presented and discussed here. A comprehensive catalog of the results has been placed in the Appendix at the end of this document for the convenience of those who do not want to print out the large number of figures contained therein.

3.1 Channel Power Spectral Density

This section presents a qualitative discussion of the channel response through the examination of the channel's power spectral density (PSD). This analysis was performed with the intent of providing the reader with a high-level understanding of the on-body wireless channel through illustration, rather than analysis. In particular, it observes the relationship between channel fading and the activity performed by the test subject through power spectral density surface plots of the channel gain with respect to frequency and time.

3.1.1 PSD Calculation

The following technique was used to produce surface plots of the channel gain:

The samples within a single 40 μs capture were separated into eight vectors $\{v_1, v_2, \ldots, v_8\}$, each representing the duration of a single PN sequence. These vectors were then averaged to reduce the effects of noise in subsequent operations. The average received PN sequence vector $\bar{v}$ was calculated by

$$\bar{v}[n] = \frac{1}{8} \sum_{i=1}^{8} v_i[n]. \tag{1}$$

Given the relatively short duration of a single capture, it is assumed that the channel is static during the period of each capture. Therefore, performing an averaging operation over the eight sets of PN sequences would not destroy information.

The power spectral density for each capture was obtained by correlating $\bar{v}$ for each capture with a replica of the transmitted PN sequence and then applying a fast Fourier transform. The resultant PSD represents the power spectral density of a system that includes the channel and two root-raised-cosine filters. The root-raised-cosine filters have a relatively flat passband within 5 MHz of DC, with a 1 dB roll-off near the edge (see Section 2.1). Hence, their effect on the power spectral density is small within $\pm$5 MHz of the carrier frequency, allowing us to disregard their effect (for this section's qualitative analysis) within that region and consider the PSD to be that of the channel alone.

3.1.2 Observations

Power spectral density plots for all of the channel measurements can be found in Section A.1. This section provides observations on a number of the more interesting results.

- The dominant factor affecting fading in the channel appears to be the movement of the test subject. This is to be expected as movement causes the separation and orientation of the antennas to change. It can also significantly alter the environment between the antennas by introducing obstacles between them. These fading scenarios are expected to result in

frequency non-selective fading (or flat fading), which the PSD plots clearly show as the dominant type of fade. In most measurements frequency-selective fading can not be resolved from the flat-fading.

- Figure 9 represents the most obvious example of a frequency-selective fade in the collected data. It illustrates a measurement taken between antennas placed on the right ankle and chest of the test subject while he attempts to remain still. The large variations of the PSD in time are due to small involuntary movements in the test subject, while the frequency-selective variations are due to multipath. It is clear that the flat-fading effects due to movement (even when the movement is small) is still greater than the effects of frequency-selective fading from multipath (even when the fading is the largest identified).

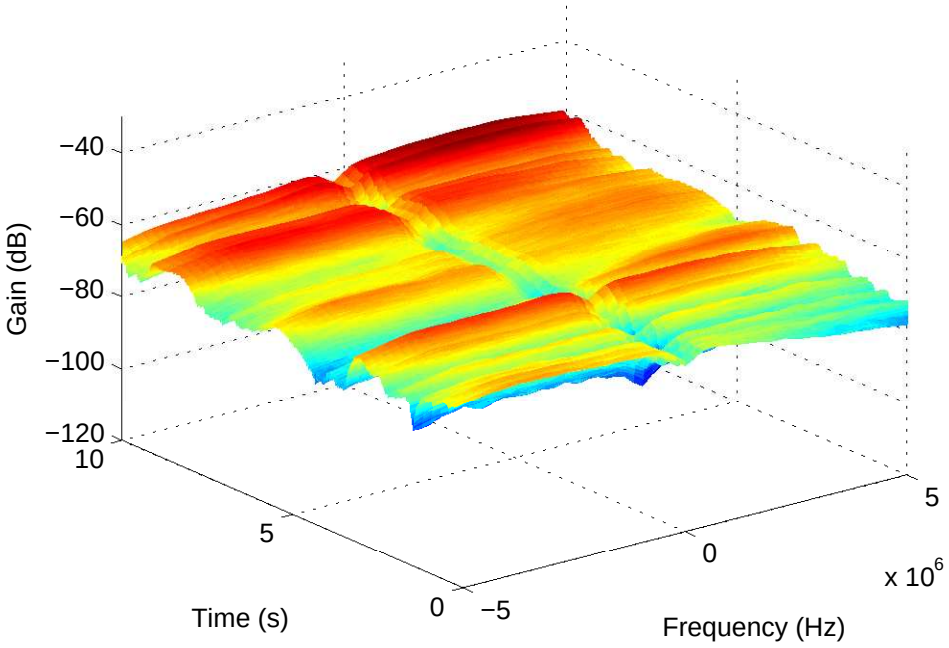

Figure 9: Right ankle to chest, standing, 2.36 GHz

- The variation of the channel PSD is generally consistent with the movement of the test subject; the PSD for measurements where the subject is standing still are generally flatter than those for when the subject is moving[4]. Compare Figures 10 and 11 for an example. Similarly, running caused more variation in the PSD than walking.

[4]Note that some flat fading is still seen in the standing measurements due to small movements made by the subject.

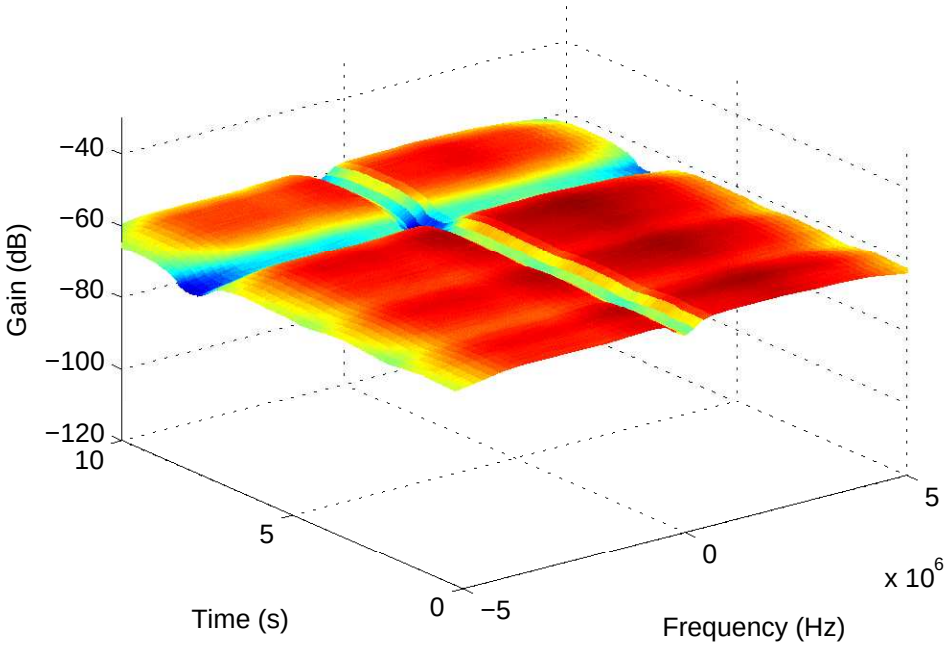

Figure 10: Back to right hip, standing, 820 MHz

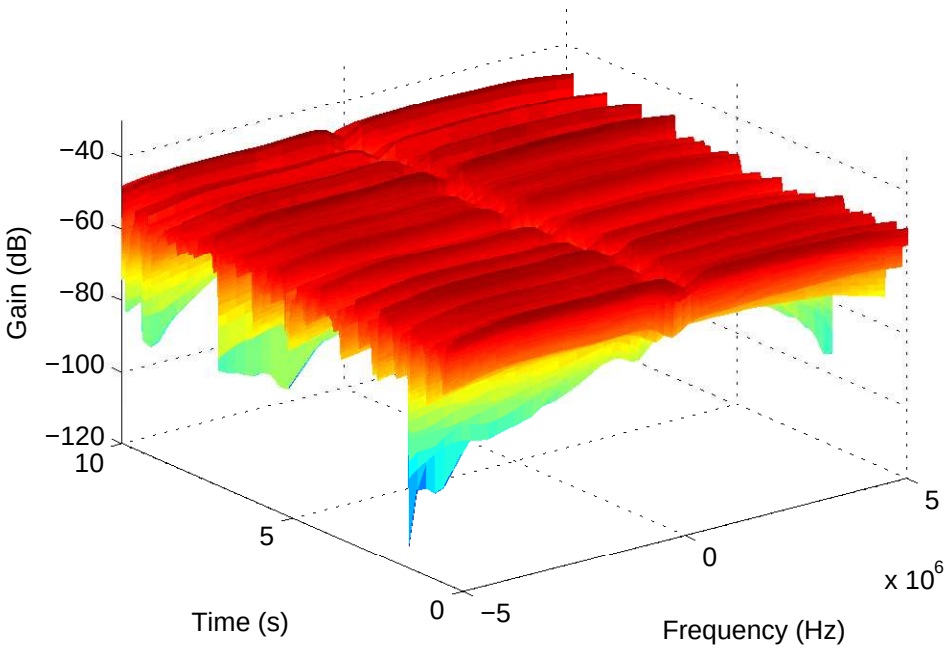

Figure 11: Chest to right hip, walking, 820 MHz

- In cases where the channel attenuation is large, such as in Figure 12, the power of the received signal can fall below the noise floor of the receiver. In such cases, the signal is not discernible from noise. Figure 13 is another example of this, however it differs in that this particular

channel measurement exhibits frequency-selective fading that only pushes part of the received signal below the noise floor.

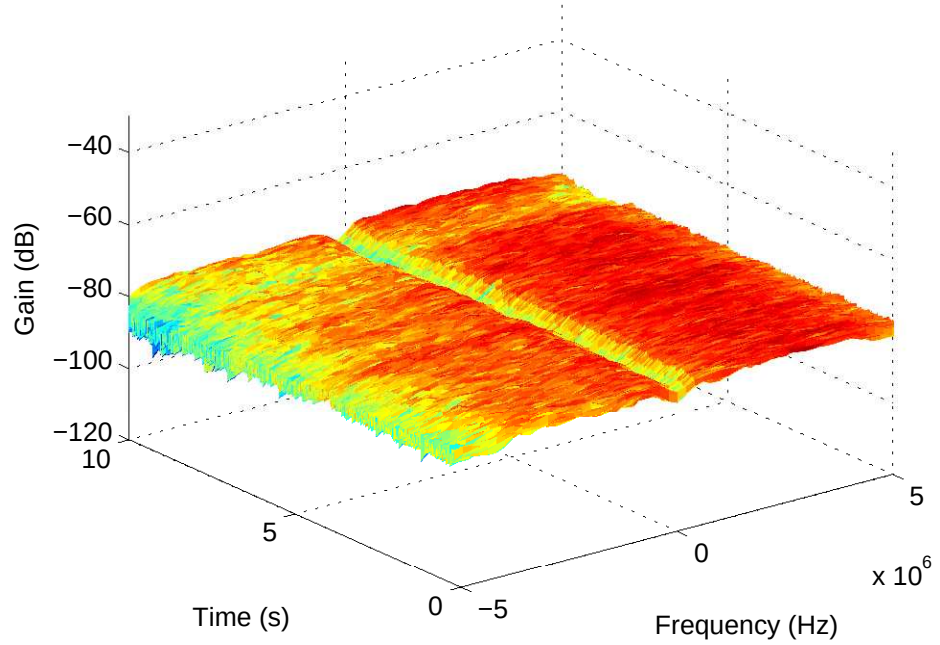

Figure 12: Left wrist to right hip, standing, 2.36 GHz

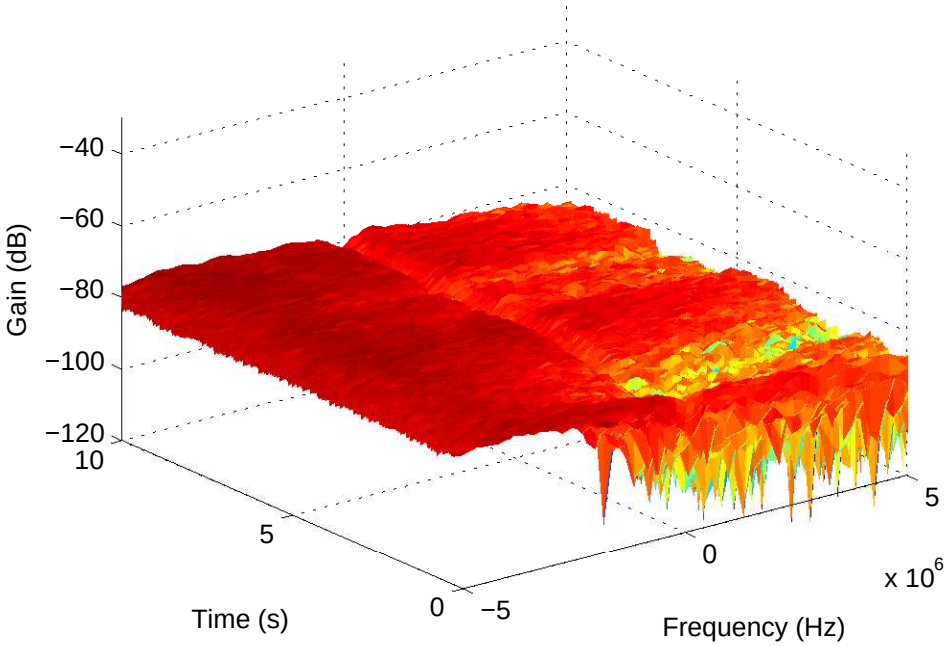

Figure 13: Back to right hip, standing, 2.36 GHz

- A distinct null can be observed at the carrier frequency in all of the PSD plots. This is an artifact of the PN sequence used. The transmitted PN sequence has a relatively small DC value compared to the rest of its spectrum and the correlation retains that null at DC.
- There is no observable difference between the shape of the plots at 820 MHz and 2.36 GHz.
- It is clear that the generally flat fading for the moving human body is neither static or quasi-static. However considering the time span of PSD analysis the fading channel, even with movement, is slow, flat fading (as opposed to fast fading).

3.2 Path Loss Characterization

This section presents results for channel path loss performance analysis found by measuring the received signal power for each respective combination of transmit and receive antenna position and test subject action.

3.2.1 Path Loss Calculation

Each channel measurement is of approximately 10 s in duration and consists of multiple 40 μs blocks that are separated in time by 2.5 ms. The RMS power of the received baseband signal (i.e., after down-conversion and sampling, no pulse-shaping) was calculated for each 40 μs block. Path loss is then calculated as the difference between transmitted power and received power. As the received signal amplitude is measured after the amplifiers, these effects must be removed from the path loss. The channel path loss $PL(t)$ at a given time t is given by

$$PL(t) = P_{tx} - P_{rx}(t) + G_{amplifiers} - L_{cable}, \tag{2}$$

where P_{tx} is transmitted power, $P_{rx}(t)$ is the RMS received power at time t, $G_{amplifiers}$ is amplifier gain, and L_{cable} is cable loss. The amplifier gains and cable losses were measured at 820 MHz and 2.36 GHz, with the appropriate result removed from the path loss.

Note that, due to finite receiver sensitivity, the path loss must be less than 78 dB at 820 MHz and 76 dB at 2.36 GHz to distinguish the transmitted signal from noise. The noise floor of the receiver is calculated by taking a measurement with the transmitting antenna replaced by a 50 Ω load. The measurement then taken at the receiver represented thermal noise and cross-talk between transmitter and receiver which, for the purpose of this study, are consolidated into a single noise figure. The maximum observable path loss then follows from (2).

3.2.2 Observations

The average path loss for each action and antenna placement is shown in Table 3a for 820 MHz and Table 3b for 2.36 GHz. The peak-to-trough path loss variation for each action and antenna placement is shown in Table 4a for 820 MHz and Table 4b for 2.36 GHz. The variation is calculated as the difference between maximum and minimum (peak-to-trough) path loss for each measurement.

Sections A.2.1 and A.2.2 illustrate path loss over time, with figures for each antenna placement and action at 820 MHz and 2.36 GHz. The measured noise floor is shown as a horizontal dashed black line. From these results, the following is observed:

- Path loss around the human body is greater than it would be with a similar antenna separation in free space, even when a line of sight path exists.
- Path loss is generally greater at 2.36 GHz than at 820 MHz.
- The variation in path loss is consistent with the movement of the test subject; as the level of movement increases (standing < walking < running), so does the level of variation. For example, the maximum path loss variation observed in the 2.36 GHz measurements for a standing subject was 7.1 dB, while it was 46.8 dB with a running subject. The relative path loss variation between the types of movement is generally consistent in both frequency bands.

- The relationship between path loss variation and the level of movement holds even when the transmit and receive antenna are stationary with respect to each other. See the back to chest measurements in Figures 14 and 15 for an example.
- Even when the test subject tries to stand still, there can still be large variations in the path loss caused by small involuntary movements of the body. This is particularly evident in Figure 15, where path loss varies throughout the entire measurement, and in Figure 16, which shows an involuntary movement at 5.5 s.
- This observed variation in path loss is particularly large when transmitter or receiver are moved such that the line of sight path is obstructed. For example, the right wrist to right hip measurement in Figure 17.
- The path loss variation is repetitive and consistent with the speed of movement of the test subject. This is particularly evident in situations where the line of sight path is obstructed by the movement, such as in Figure 17.

Table 3: Average path loss (dB)

(a) 820 MHz

Action	Receiver at Right Hip; Transmitter at:						Receiver at chest; Transmitter at:		
	Chest	Right Wrist	Left Wrist	Right Ankle	Left Ankle	Back	Back	Right Wrist	Right Ankle
Standing	57.4	50.2	59.8	54.3	68.7	61.8	66.3	54.5	54.3
Walking	52.9	38.4	63.6	48.1	55.5	57.1	63.8	51.3	56.9
Running	44.1	37.2	60.2	48.9	54.2	62.3	66.3	49.4	54.1

(b) 2.36 GHz

Action	Receiver at Right Hip; Transmitter at:						Receiver at chest; Transmitter at:		
	Chest	Right Wrist	Left Wrist	Right Ankle	Left Ankle	Back	Back	Right Wrist	Right Ankle
Standing	65.3	44.5	74.7	60.9	70.7	75.3	73.0	70.5	66.3
Walking	59.1	47.3	59.8	53.9	58.5	67.4	72.0	64.9	62.4
Running	55.9	36.3	52.5	55.0	59.0	68.5	71.7	57.4	63.3

Table 4: Peak-to-trough path loss variation (dB)

(a) 820 MHz

Action	Receiver at Right Hip; Transmitter at:						Receiver at chest; Transmitter at:		
	Chest	Right Wrist	Left Wrist	Right Ankle	Left Ankle	Back	Back	Right Wrist	Right Ankle
Standing	1.6	0.7	2.2	5.1	1.8	5.1	3.0	2.2	0.7
Walking	30.0	35.1	24.4	24.4	26.5	13.5	23.7	34.0	17.2
Running	38.0	45.6	28.0	32.8	27.9	23.8	30.9	27.8	32.5

(b) 2.36 GHz

Action	Receiver at Right Hip; Transmitter at:						Receiver at chest; Transmitter at:		
	Chest	Right Wrist	Left Wrist	Right Ankle	Left Ankle	Back	Back	Right Wrist	Right Ankle
Standing	3.3	2.0	1.8	2.4	7.1	1.4	4.2	1.3	11.3
Walking	20.0	39.6	24.5	22.5	21.1	14.1	8.6	21.2	20.4
Running	30.3	46.8	33.7	28.4	24.1	16.3	9.3	29.4	19.5

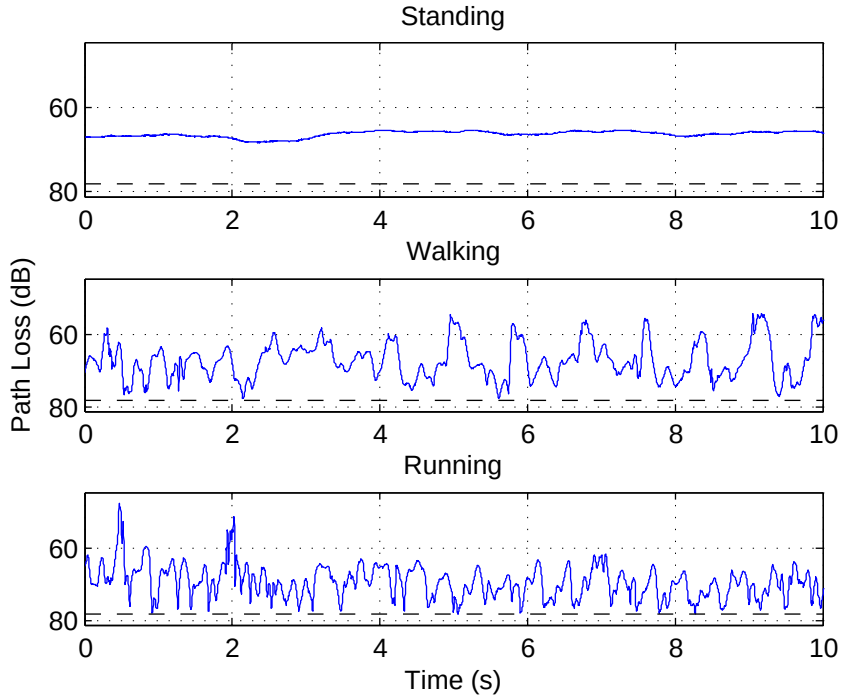

Figure 14: Path Loss measurements over time: Back to Chest, 820 MHz

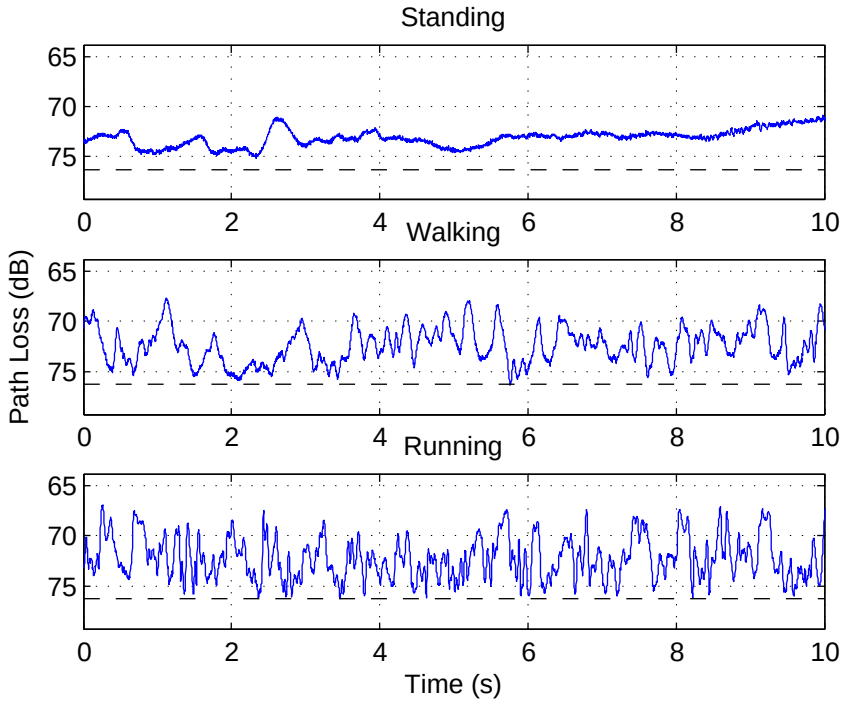

Figure 15: Path Loss measurements over time: Back to Chest, 2.36 GHz

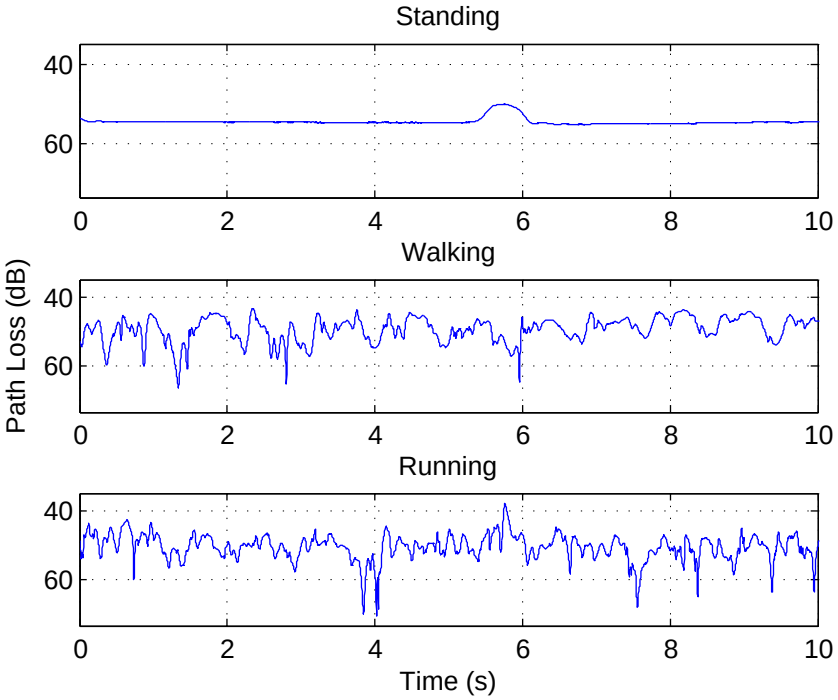

Figure 16: Path Loss measurements over time: Right Ankle to Right Hip, 820 MHz

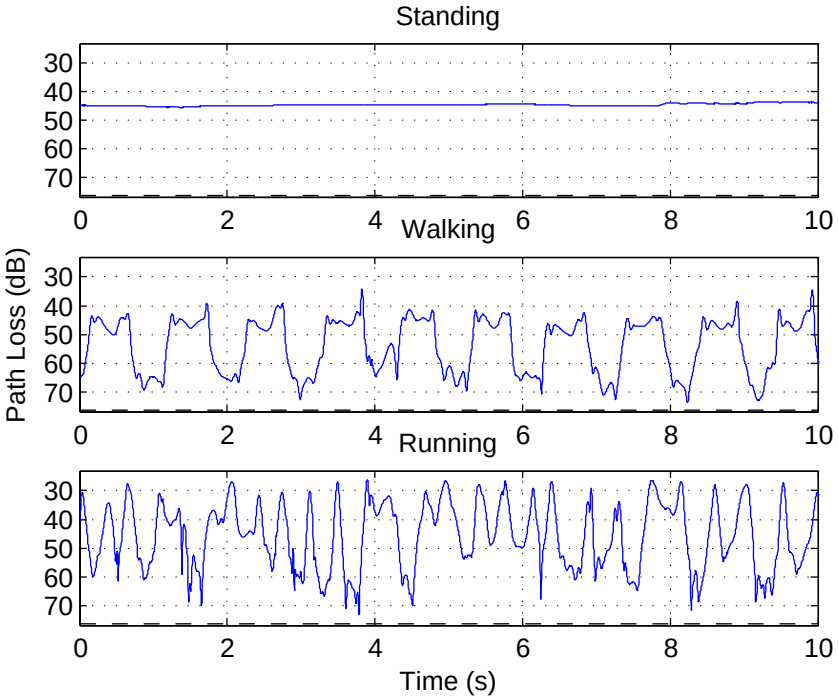

Figure 17: Path loss over time: Right Wrist to Right Hip, 2.36 GHz.

3.3 Statistical Description of Received Power

This section presents a statistical analysis of the received signal power around the subject's body, used to describe path loss in the previous section 3.2. Three statistical distributions were fit to each set of a data for any given scenario, the Gamma distribution, the Lognormal distribution and the Normal distribution[5].

The measured received power across one set of measurements for a given scenario was normalized according to the maximum received power for that set of measures. Thus, due to normalization, distributions are fitted to data that can only take values between 0 and 1, and we effectively ignore those parts of fitted distribution that takes on values outside this range.

The probability density functions of these distributions are defined as follows:

- Gamma probability density function (PDF)

$$y = f(x|a,b) = \frac{1}{b^a \Gamma(a)} x^{a-1} e^{\frac{x}{b}} \tag{3}$$

  where $\Gamma(\cdot)$ is the Gamma function.

- Normal PDF

$$y = f(x|\mu,\sigma) = \frac{1}{\sigma\sqrt{2\pi}} e^{\frac{-(x-\mu)^2}{2\sigma^2}} \tag{4}$$

- Lognormal PDF

$$y = f(x|\mu,\sigma) = \frac{1}{x\sigma\sqrt{2\pi}} e^{\frac{-(\ln(x)-\mu)^2}{2\sigma^2}} \tag{5}$$

  where $\ln(\cdot)$ represents the natural logarithm.

Thus, for each scenario we match a best fit from the three distributions and choose the best of these "best fits" as the distribution that best matches the measured data set for normalized receive power. These best distributions, for each scenario at the two operating frequencies of 820 MHz and 2.36 GHz, are listed in Table 5.

3.3.1 Observations

It is clear from Table 5 that there is no distribution that is consistently the best match for all scenarios. However, for cases when the subject is in motion, there is only one case, that of transmitting from chest to hip when the best matching distribution is Normal; the majority are either Gamma or Lognormal. However when standing, the best matching distribution is most often the Normal distribution.

We note that for the distribution fits compiled in Table 5, the best fits are least accurate in the cases where the subject is standing still. This is illustrated in the following figures (once again figures for all scenarios are placed in the appendix). The first six PDFs relate to measurements at 2.36 GHz, the remaining six PDFs are for the same scenarios as the first six PDFs but for measurements at 820 MHz. In each figure, the three PDFs for the "best-fits" of the three distributions are overlayed over the empirical PDF. The bin size for the histogram used to describe the PDF from the measured data is chosen according to the "Freedman-Diaconis" rule (see appendix) [19].

Inspection of the following figures (and also those in the appendix) illustrate the choice of best matching distributions given in Table 5, they also show the following:

[5]These three distributions, amongst various others tested, are both common distributions, and consistently the best fitting to the variety of those tested.

Table 5: Scenarios and the distribution that gives the best of the "best fits" to those scenarios at 820 MHz and 2.36 GHz

Tx Antenna	Rx Antenna	Action	Distribution	
			820 MHz	2.36 GHz
Chest	Right Hip	Standing	Normal	Normal
Chest	Right Hip	Walking	Normal	Normal
Chest	Right Hip	Running	Gamma	Lognormal
Right Wrist	Right Hip	Standing	Normal	Normal
Right Wrist	Right Hip	Walking	Lognormal	Gamma
Right Wrist	Right Hip	Running	Lognormal	Lognormal
Left Wrist	Right Hip	Standing	Normal	Normal
Left Wrist	Right Hip	Walking	Lognormal	Lognormal
Left Wrist	Right Hip	Running	Lognormal	Gamma
Right Ankle	Right Hip	Standing	Lognormal	Normal
Right Ankle	Right Hip	Walking	Gamma	Gamma
Right Ankle	Right Hip	Running	Gamma	Gamma
Left Ankle	Right Hip	Standing	Lognormal	Normal
Left Ankle	Right Hip	Walking	Gamma	Gamma
Left Ankle	Right Hip	Running	Gamma	Gamma
Back	Right Hip	Standing	Normal	Normal
Back	Right Hip	Walking	Lognormal	Lognormal
Back	Right Hip	Running	Lognormal	Lognormal
Back	Chest	Standing	Normal	Normal
Back	Chest	Walking	Lognormal	Lognormal
Back	Chest	Running	Gamma	Lognormal
Right Wrist	Chest	Standing	Normal	Normal
Right Wrist	Chest	Walking	Lognormal	Lognormal
Right Wrist	Chest	Running	Lognormal	Gamma
Right Ankle	Chest	Standing	Lognormal	Lognormal
Right Ankle	Chest	Walking	Lognormal	Lognormal
Right ankle	Chest	Running	Lognormal	Lognormal

- For the case of transmitting from back to chest while the subject is running or walking, a far greater majority of measured normalized received power is near minimum at 820 MHz than at 2.36 GHz. See Figures 18, 19, 24 and 25.
- For the case of transmitting from right wrist to right hip the results for running show great similarity with Lognormal distribution providing the best fit. See Figures 21 and 27.
- As described in Table 5, a slightly better fit of the Gamma distribution for right wrist to right hip with subject walking can be observed at 2.36 GHz (Figure 22), as opposed to the same case at 820 MHz (Figure 28) where the Lognormal distribution is the better fit.
- As already mentioned the cases for subject standing still, the best fits are the least accurate. However, as can be observed from Figures 20, 26, 23, 29, the Normal distribution is the best fit in all cases, although this is still a rather inaccurate fit[6].
- Furthermore, generally it is demonstrated in all figures that the Normal distribution is a very poor fit to the received power data when the subject is in motion.

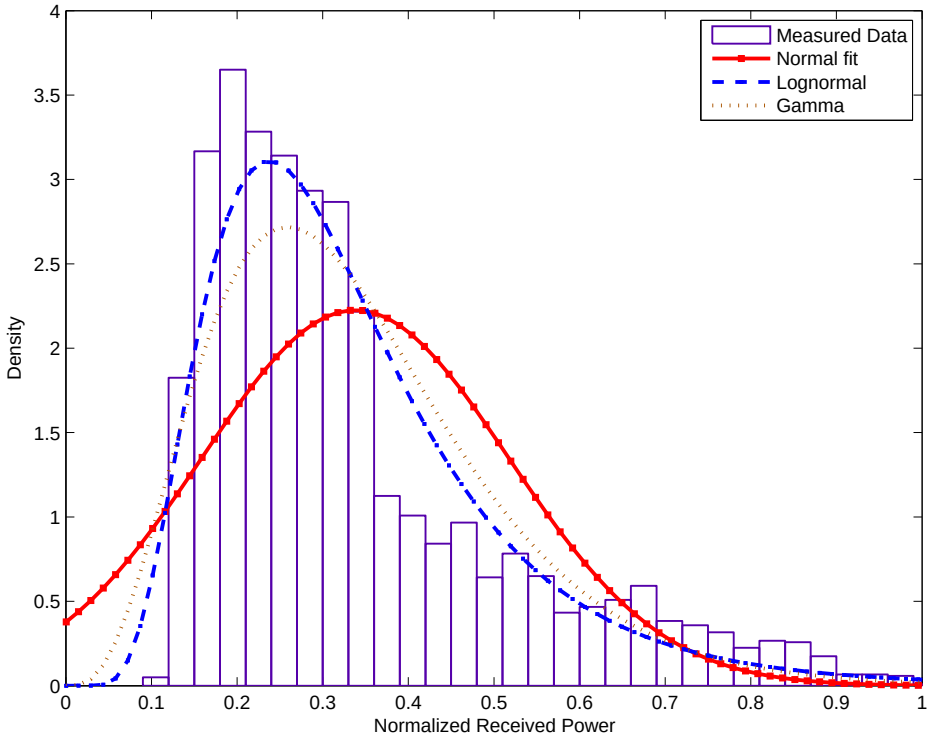

Figure 18: PDF Back to Chest, Running at 2.36 GHz

[6]Some other probability distributions, apart from the three mentioned here, were used to try to match subject standing, but all gave poor fits, generally worse than the Normal fit.

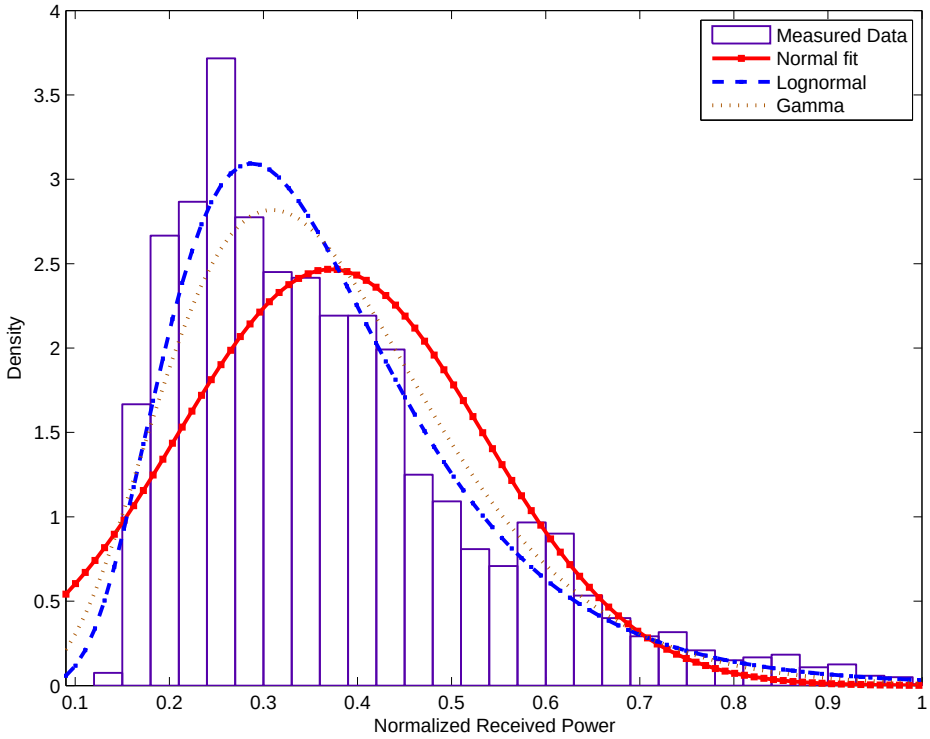

Figure 19: PDF Back to Chest, Walking at 2.36 GHz

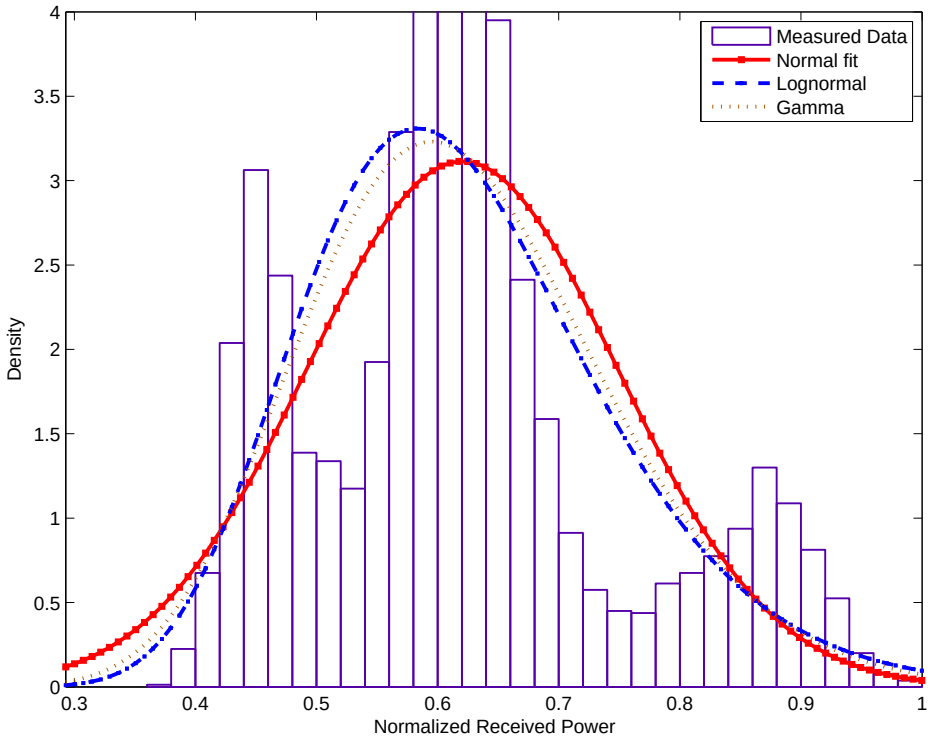

Figure 20: PDF Back to Chest, Standing at 2.36 GHz

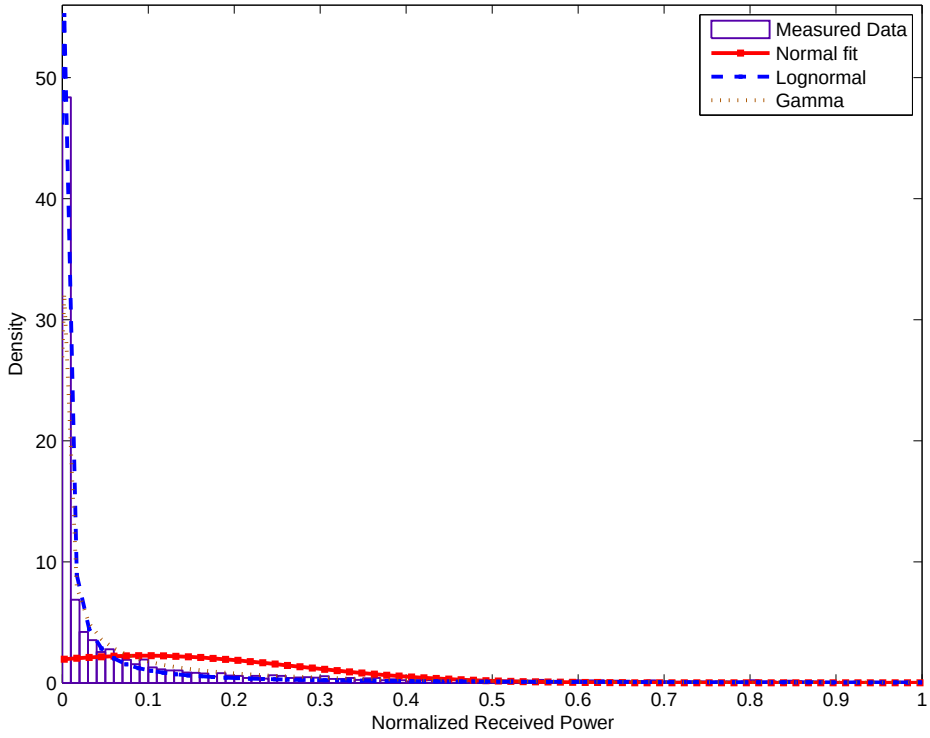

Figure 21: PDF Right wrist to right hip, running at 2.36 GHz

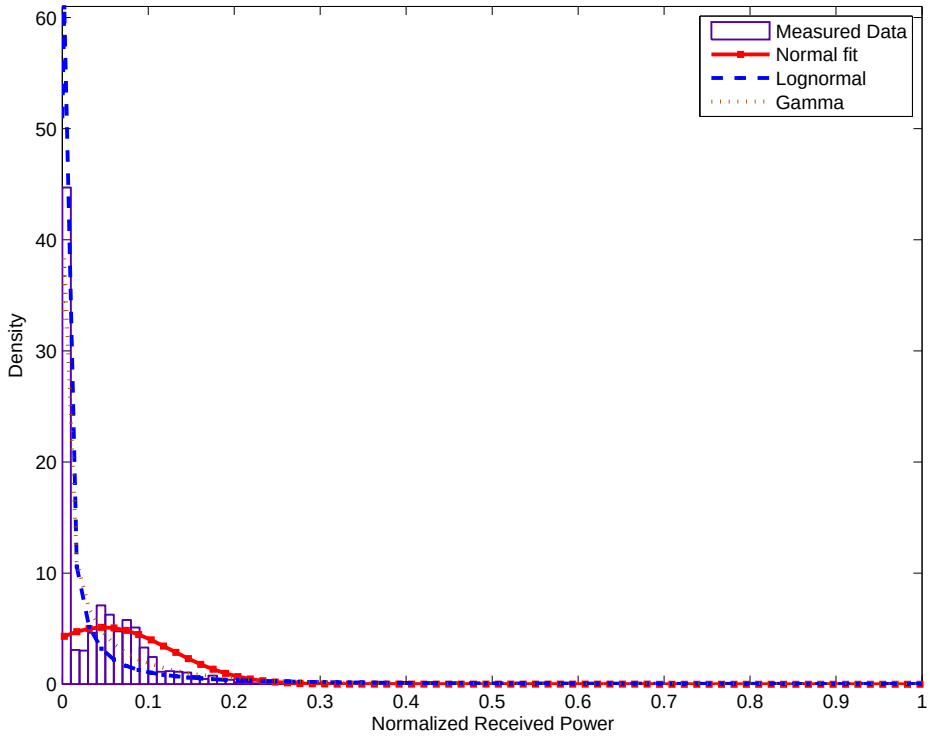

Figure 22: PDF Right wrist to right hip, walking at 2.36 GHz

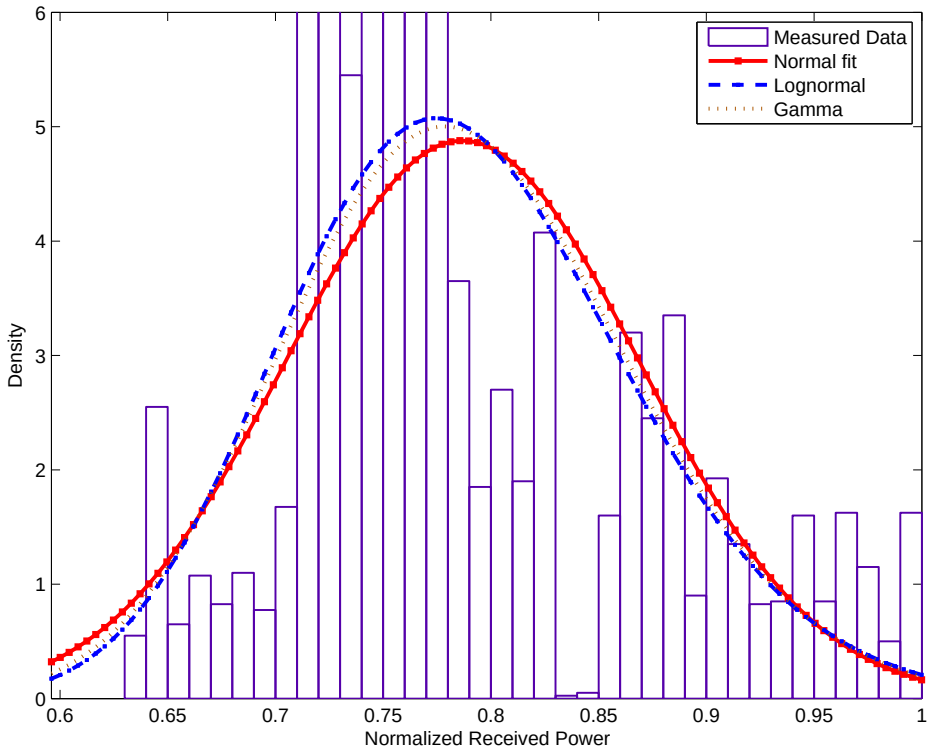

Figure 23: Right wrist to right hip, standing at 2.36 GHz

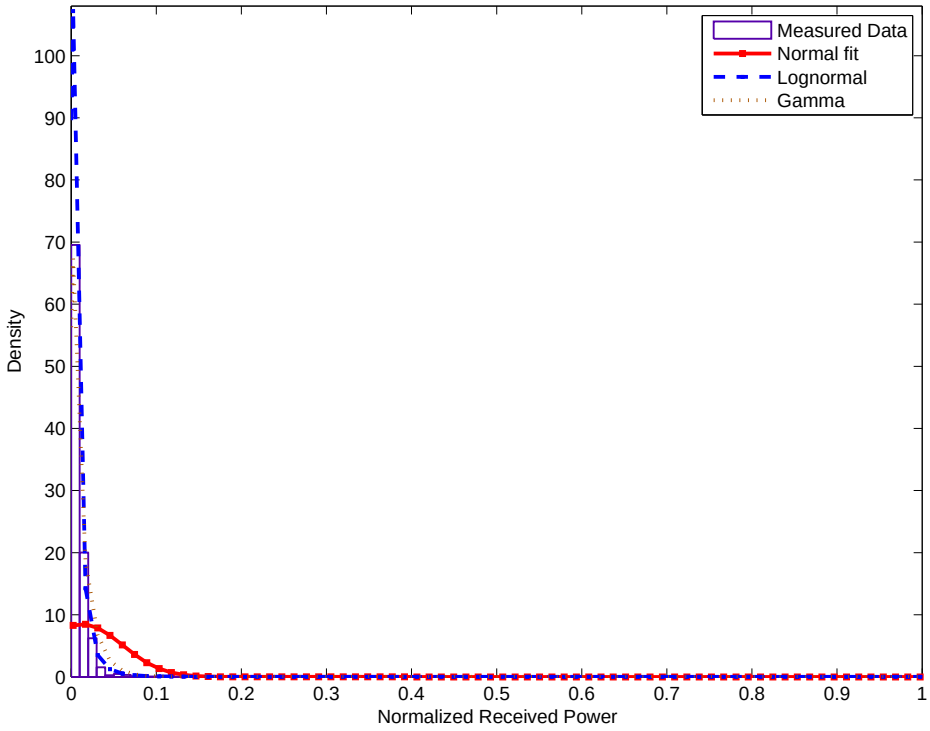

Figure 24: PDF Back to Chest, Running at 820 MHz

In Tables 6 and 7, we present best fit parameters for all scenarios with respect to the three chosen probability distributions, a and b for the Gamma distribution, and μ and σ for both the Lognormal and the Normal distributions. The variation in parameters for a given distribution for the same scenarios in comparison between Tables 6 and 7 is not consistent and is scenario dependent. Thus we can observe that there is no general rule (based on normalized receive power) about differences in best fitting distribution parameters between 820 MHz and 2.36 GHz.

Table 6: Distribution Parameters for Gamma, Normal and Lognormal "best fits" to Normalized Received Power at 2.36 GHz for all scenarios

Tx Antenna	Rx Antenna	Action	Gamma		Normal		Lognormal	
			a	b	μ	σ	μ	σ
Chest	Right Hip	Standing	29.338	0.023	0.680	0.128	-0.403	0.184
Chest	Right Hip	Walking	1.844	0.156	0.287	0.197	-1.544	0.850
Chest	Right Hip	Running	0.837	0.053	0.044	0.095	-3.817	1.116
Right Wrist	Right Hip	Standing	96.517	0.0082	0.787	0.082	-0.245	0.101
Right Wrist	Right Hip	Walking	0.430	0.112	0.048	0.078	-4.549	2.195
Right Wrist	Right Hip	Running	0.308	0.309	0.095	0.178	-4.584	2.617
Left Wrist	Right Hip	Standing	218.895	0.0038	0.834	0.055	-0.184	0.068
Left Wrist	Right Hip	Walking	0.563	0.279	0.157	0.215	-2.962	1.597
Left Wrist	Right Hip	Running	0.432	0.212	0.091	0.127	-3.898	2.148
Right Ankle	Right Hip	Standing	50.618	0.015	0.737	0.104	-0.316	0.141
Right Ankle	Right Hip	Running	1.123	0.125	0.140	0.141	-2.473	1.111
Right Ankle	Right Hip	Walking	2.154	0.136	0.294	0.191	-1.475	0.783
Left Ankle	Right Hip	Standing	11.860	0.032	0.380	0.117	-1.011	0.287
Left Ankle	Right Hip	Walking	1.678	0.167	0.281	0.212	-1.596	0.886
Left Ankle	Right Hip	Running	1.326	0.152	0.202	0.178	-2.021	0.992
Back	Right Hip	Standing	257.26	0.0033	0.852	0.053	-0.163	0.063
Back	Right Hip	Walking	2.258	0.100	0.226	0.164	-1.727	0.689
Back	Right Hip	Running	1.751	0.085	0.149	0.131	-2.213	0.778
Back	Chest	Standing	24.367	0.025	0.620	0.128	-0.498	0.202
Back	Chest	Walking	5.933	0.063	0.372	0.162	-1.077	0.412
Back	Chest	Running	4.274	0.079	0.338	0.179	-1.206	0.482
Right Wrist	Chest	Standing	272.434	0.0032	0.869	0.053	-0.143	0.061
Right Wrist	Chest	Walking	0.832	0.131	0.109	0.147	-2.925	1.198
Right Wrist	Chest	Running	0.519	0.177	0.092	0.146	-3.606	1.721
Right Ankle	Chest	Standing	3.903	0.081	0.315	0.180	-1.289	0.503
Right Ankle	Chest	Walking	1.245	0.155	0.193	0.181	-2.095	1.023
Right Ankle	Chest	Running	1.706	0.090	0.153	0.135	-2.199	0.817

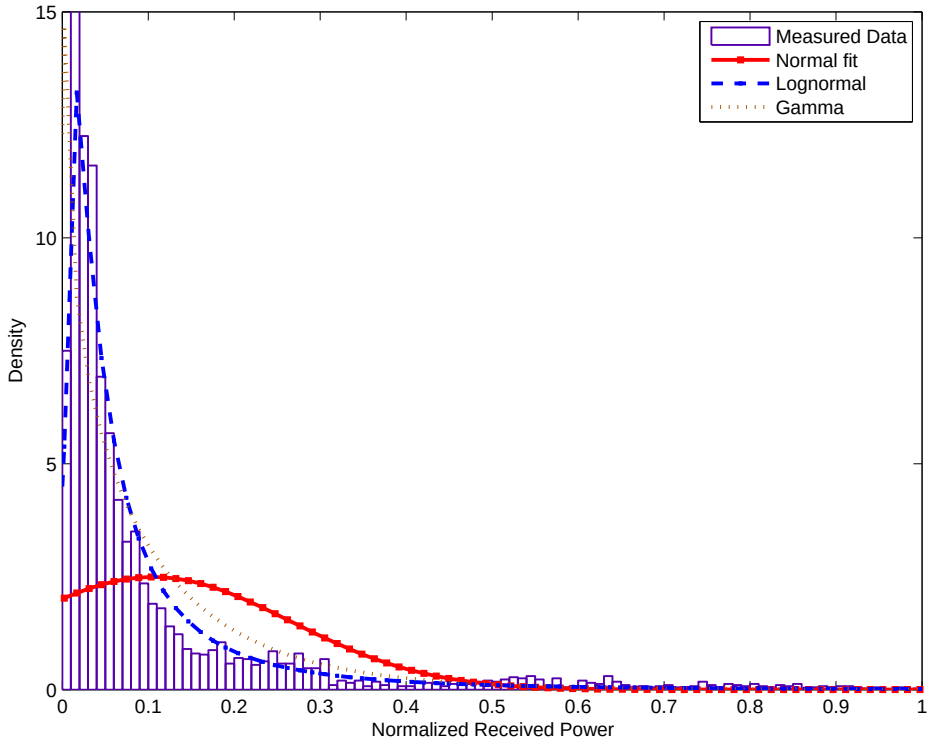

Figure 25: PDF Back to Chest, Walking at 820 MHz

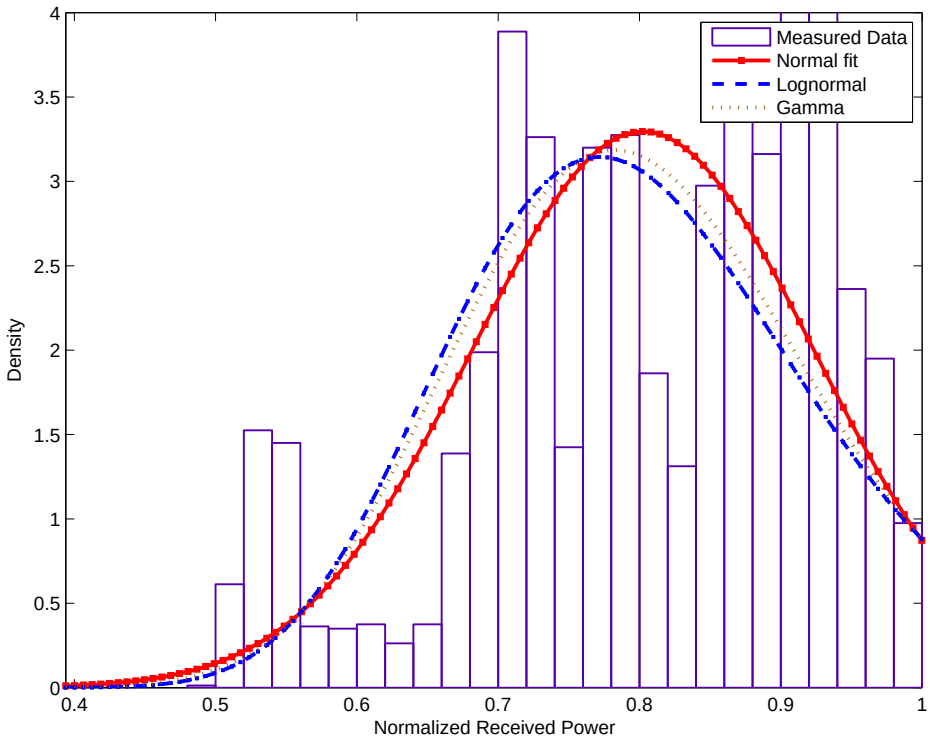

Figure 26: PDF Back to Chest, Standing at 820 MHz

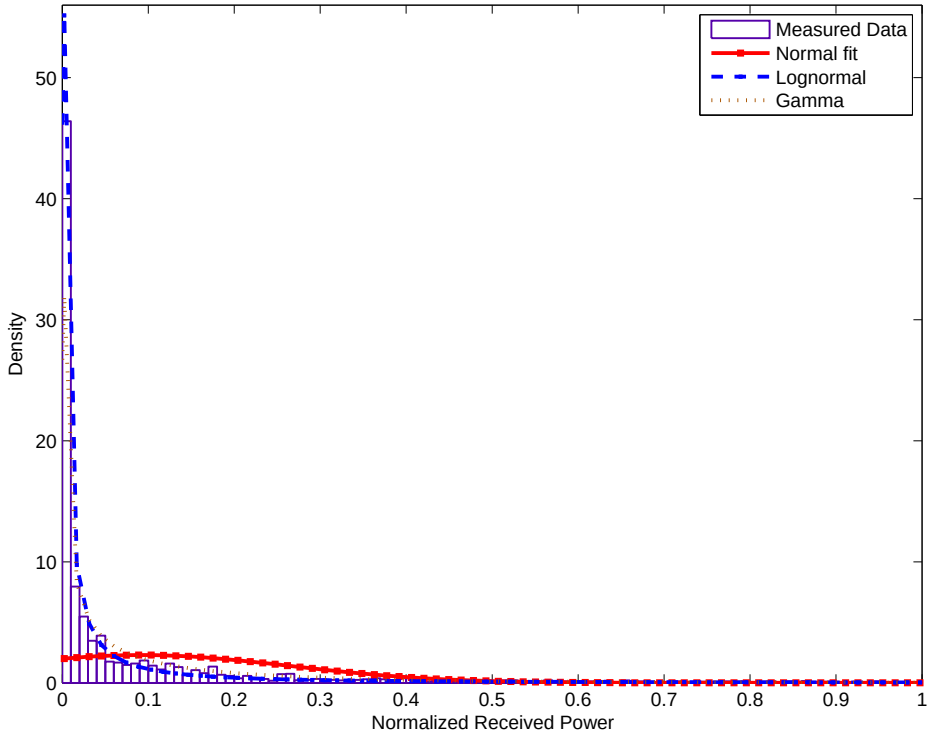

Figure 27: PDF Right wrist to right hip, running at 820 MHz

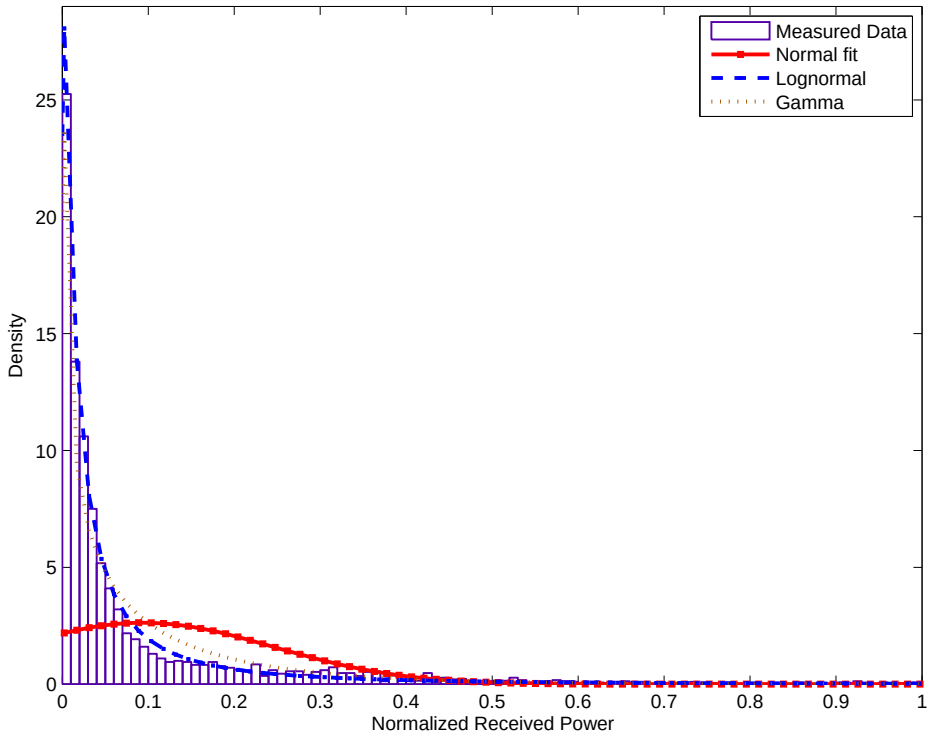

Figure 28: PDF Right wrist to right hip, walking at 820 MHz

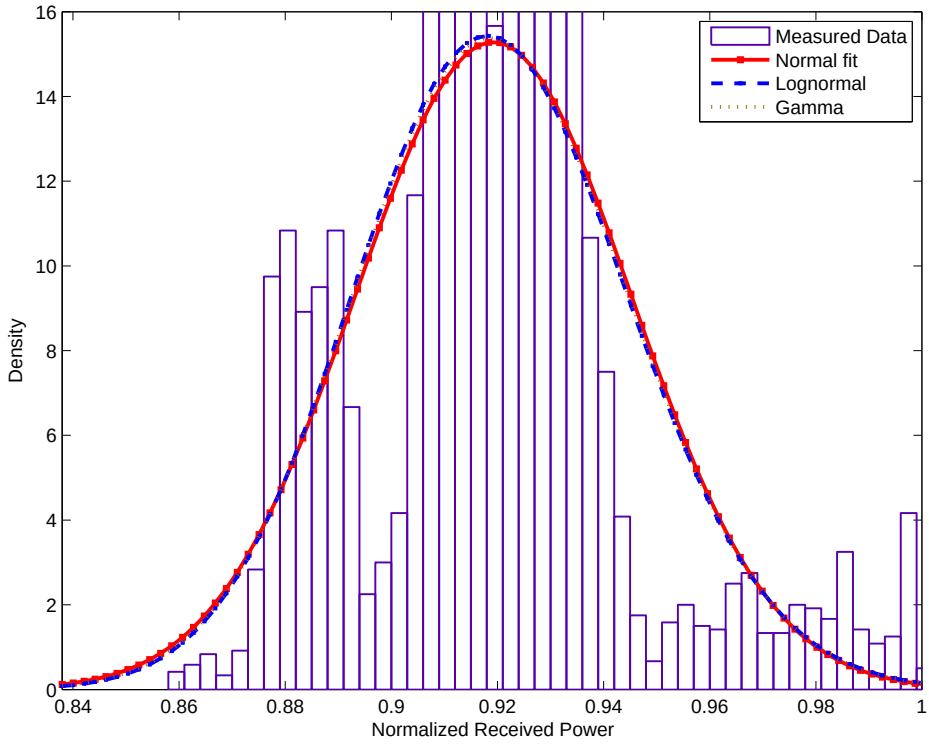

Figure 29: Right wrist to right hip, standing at 820 MHz

Table 7: Distribution Parameters for Gamma, Normal and Lognormal "best fits" to Normalized Received Power at 820 MHz for all scenarios

Tx Antenna	Rx Antenna	Action	Gamma		Normal		Lognormal	
			a	b	μ	σ	μ	σ
Chest	Right Hip	Standing	144.41	0.0058	0.844	0.070	-0.173	0.083
Chest	Right Hip	Walking	1.630	0.130	0.211	0.157	-1.891	0.950
Chest	Right Hip	Running	0.631	0.069	0.043	0.093	-4.111	1.418
Right Wrist	Right Hip	Standing	1255.9	0.00073	0.919	0.026	-0.085	0.028
Right Wrist	Right Hip	Walking	0.569	0.165	0.094	0.152	-3.458	1.586
Right Wrist	Right Hip	Running	0.337	0.273	0.092	0.174	-4.390	2.422
Left Wrist	Right Hip	Standing	95.696	0.0071	0.682	0.075	-0.389	0.099
Left Wrist	Right Hip	Walking	0.790	0.139	0.110	0.156	-2.963	1.240
Left Wrist	Right Hip	Running	1.059	0.084	0.089	0.102	-2.964	1.117
Right Ankle	Right Hip	Standing	19.058	0.019	0.372	0.113	-1.017	0.201
Right Ankle	Right Hip	Walking	1.966	0.125	0.246	0.163	-1.679	0.835
Right Ankle	Right Hip	Running	1.494	0.052	0.078	0.085	-2.916	0.912
Left Ankle	Right Hip	Standing	31.825	0.013	0.398	0.088	-0.937	0.162
Left Ankle	Right Hip	Walking	1.670	0.167	0.278	0.189	-1.607	0.942
Left Ankle	Right Hip	Running	1.410	0.144	0.203	0.168	-1.989	0.997
Back	Right Hip	Standing	15.382	0.052	0.806	0.173	-0.249	0.281
Back	Right Hip	Walking	2.548	0.095	0.241	0.168	-1.630	0.635
Back	Right Hip	Running	1.020	0.124	0.127	0.141	-2.629	1.112
Back	Chest	Standing	40.187	0.020	0.802	0.121	-0.233	0.162
Back	Chest	Walking	0.786	0.134	0.106	0.160	-3.005	1.189
Back	Chest	Running	0.788	0.016	0.013	0.047	-5.098	1.026
Right Wrist	Chest	Standing	100.04	0.0076	0.759	0.077	-0.281	0.100
Right Wrist	Chest	Walking	0.654	0.128	0.083	0.129	-3.417	1.466
Right Wrist	Chest	Running	1.394	0.077	0.107	0.120	-2.633	0.881
Right Ankle	Chest	Standing	673.98	0.0012	0.816	0.032	-0.204	0.038
Right Ankle	Chest	Walking	706.02	0.00089	0.628	0.024	-0.465	0.037
Right Ankle	Chest	Running	219.68	0.0035	0.769	0.053	-0.266	0.067

3.4 Channel Time-Coherence

Channel time coherence analysis is used to determine the time period during which the channel can be treated as being stable. In general, for coherence analysis of two sequences, a correlation function is applied to the sequences, and a normalized correlation factor is obtained to describe the coherence between the two sequences. However, for channel time coherence analysis, conventional correlation analysis can not characterize the variation of the channel within a time period well. This is because the correlation method detects only linear dependencies between two sequences, rather than the variability of the two sequences. So instead of using correlation analysis, we define the following **channel variation factor**, ρ, which is the ratio between the standard deviation (square root of variance) and the root-mean-square power of a sequence $\mathbf{s} = \{s_0, s_1, \ldots, s_{M-1}\}$

$$\rho = \sqrt{\frac{\text{var}(\mathbf{s})}{\frac{1}{M}\sum_{m=0}^{M-1}|s_m|^2}}, \tag{6}$$

where var($\mathbf{s}$) denotes the variance of a vector $\mathbf{s}$.

The variance of a sequence characterizes the variation of the sequence well. By normalizing the standard deviation by the root-mean-square power, the channel variation factor becomes independent of the signal power and is consistent over the whole observation period. Furthermore, it is clear that $0 \leq \rho \leq 1$.

In our application of this channel variation factor we note the following:

As previously described in Section 2 there are gaps of approximately 2.5 ms between subsets of measurements within a complete measurement set that spans 10 s. The discontinuity between measurement subsets introduces random phase shifts to every measured channel response. To account for this, only the magnitude of the channel response is considered in the following analysis. Note that the magnitude of channel response generally describe the variability of channel quite well as the channel rarely only varies in phase.

Secondly, from the measured channel response, we observe that signals from different propagation paths are mostly overlapped and unresolvable, and they cause extended symbol period and waveform distortion. Hence, the received signal is upsampled at the output of the pulse shaping filter before being correlated with a copy of the transmitted PN sequence. Thus for the mth channel response, we have a vector of L samples, denoted as $\mathbf{h}_m = \{h_m(0), h_m(1), \ldots, h_m(L-1)\}$, with $L = 11$ used in the analysis here. These samples include the peak point and five points on either side of the peak. Channel responses at different times over the complete measurement span are aligned with respect to the peak of all channel responses. For a period of $\tau = MT_f$ (from kT_f to $(k+M-1)T_f$), where T_f is the interval between two adjoint measured channel responses, the overall channel variation factor is computed as follows: 1) Compute the constituent channel variation factor for the ℓth sample $h_m(\ell)$, $\ell = 0, 1, \cdots, L-1$, in the M channel responses according to (6) to obtain $\rho(\ell)$; 2) Compute the mean over all L samples. Mathematically, this is written as

$$\rho(\ell) = \sqrt{\frac{\text{var}\big(\{|h_k(\ell)|, |h_{k+1}(\ell)|, \cdots, |h_{k+M-1}(\ell)|\}\big)}{\frac{1}{M}\sum_{m=k}^{M+k-1}|h_m(\ell)|^2}}; \tag{7}$$

and

$$\rho = \frac{1}{L}\sum_{\ell=0}^{L-1}\rho(\ell). \tag{8}$$

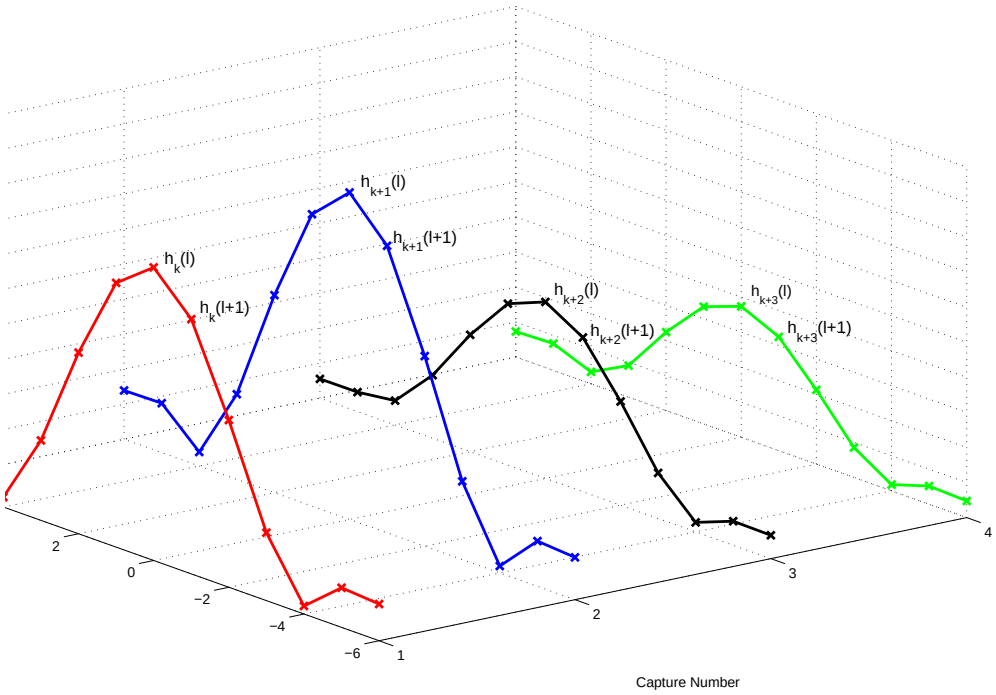

Figure 30: Illustration of some measured impulse responses over time span, $\tau = 4T_f$, (measured along the *Capture Number* axis) used in the calculation of the channel variation factor.

Illustrative example:
In Figure 30 we show four typical measured impulse responses (time span of $4T_f$) in a 3-D graph. The overall channel variation factor ρ over a time span of $\tau = MT_f$ is computed in the following steps:

1. Align the impulse responses according to the peak so that the peaks have the same index ℓ in all impulse responses;
2. Compute the constituent channel variation factor, $\rho(\ell)$, for the ℓth sample $h_m(\ell)$, $\ell = \{0, 1, \ldots, L-1\}$, in the M channel responses according to (7) to get $\rho(\ell)$;
3. Compute the mean over all L samples as in (8) to obtain ρ.

The channel variation factor ρ is a good indicator of the channel stability. For example, $\rho = 0.1$ is roughly equivalent to a channel variation within a range of 10% during the measurement period.

The analysis described above was conducted with spanning periods τ of 5 ms, 10 ms and 25 ms for all the subject's activities and Tx/Receiver positions, over a full measurement period of 10 s. Some figures showing the values of ρ over time are presented here for $\tau = 10$ ms (Figure 31 and Figure 32) when transmitting from the chest to right hip. In the appendix these two figures are repeated, with other figures depicting time spans of 5 ms, 10 ms and 25 ms, for the chest to right hip and left wrist to right hip measurement scenarios. From Figure 31 and Figure 32 there is clearly greater stability while walking than while running, and the subject's motion clearly affects channel variation, and thus, coherence time.

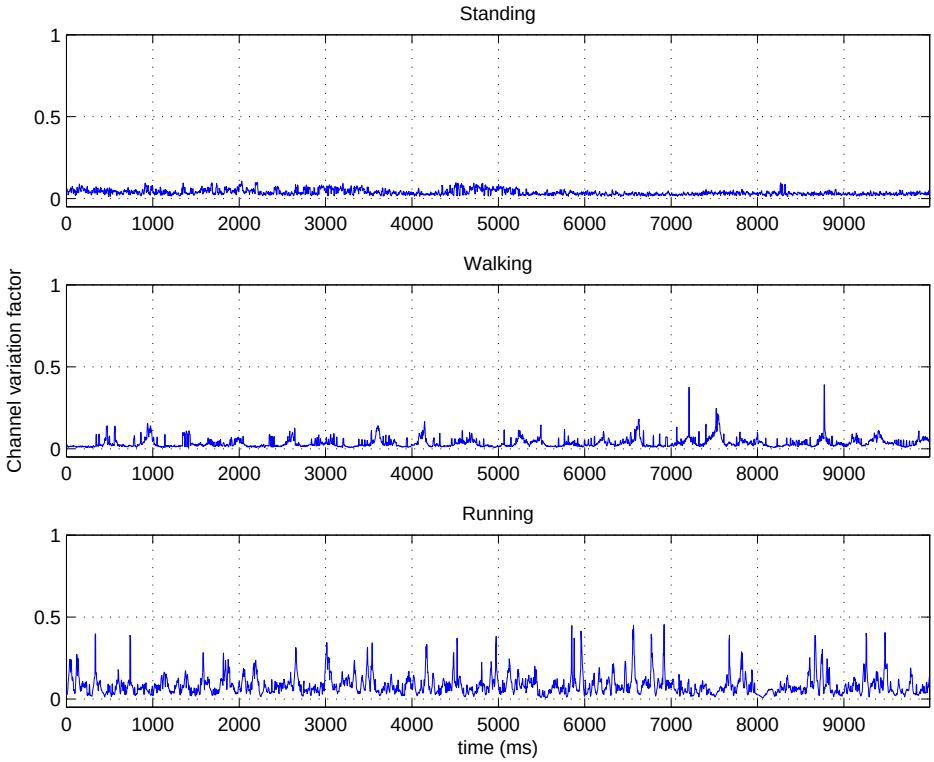

Figure 31: Channel variation factor for a time varying period of 10ms, Chest to right hip standing, walking and running - 2.36 GHz

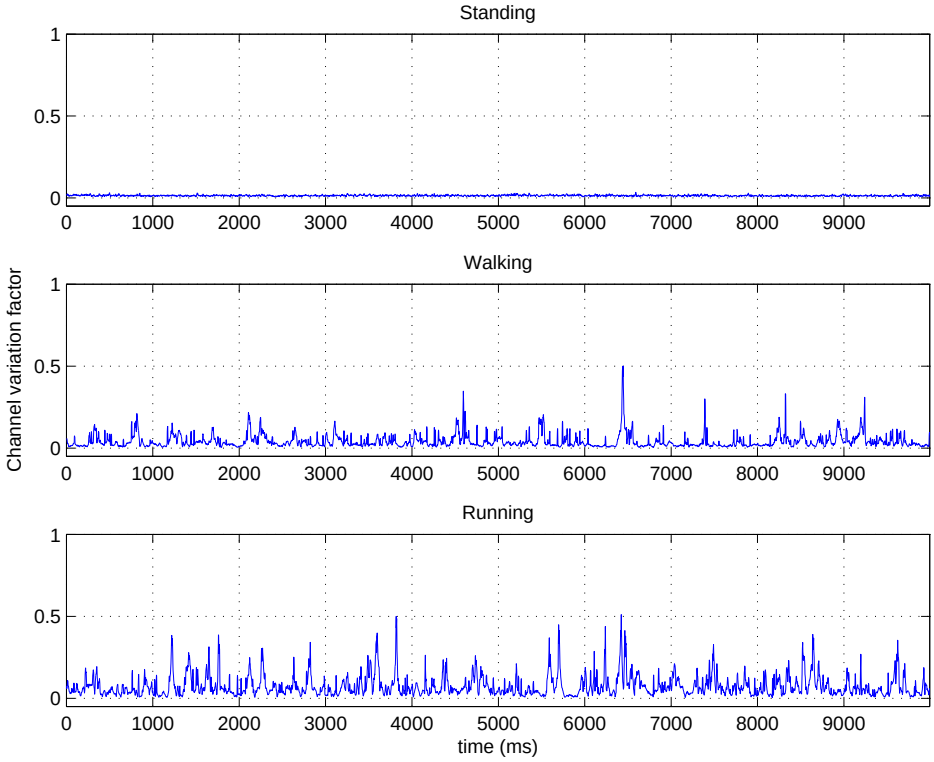

Figure 32: Channel variation factor for a time varying period of 10ms, Chest to right hip standing, walking and running - 820 MHz

To better characterize the channel stability, statistical analysis over the channel variation factors was performed on all measurements. We computed empirical cumulative distribution functions (CDFs) from the measured data for the factors for all scenarios, some of the results are shown in the following figures, Figures 33, 34, 35, 36, 37, 38. In these figures we depict scenarios for transmitting from chest to right hip and transmitting from left wrist to right hip. Note in this section we combine in one figure CDF results for 820 MHz and 2.36 GHz. Figures for all scenarios are shown in the appendix.

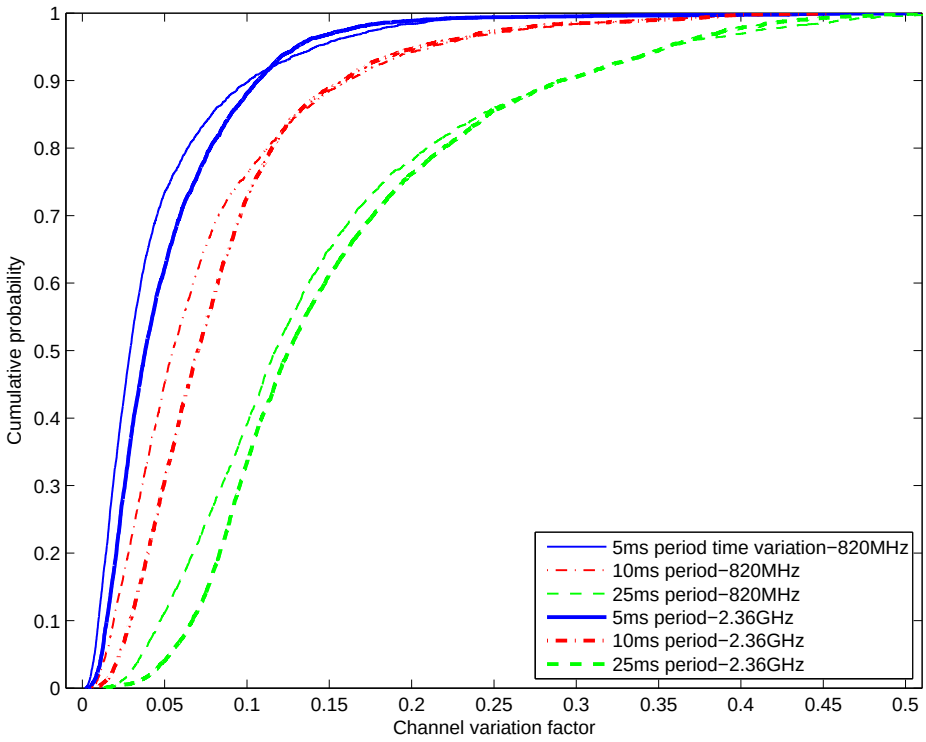

Figure 33: Cumulative probability of channel variation factor, Chest to right hip running

Note in these figures the sharper rise in cumulative probability for channel variation factors closer to zero is evident while the subject is standing, Figures 35 and 38. The slowest increase in cumulative probability with an increase in correlation factor is observed for the case of running, Figures 33 and 36. Figures showing cumulative probability curves for 820 MHz to the right of those for 2.36 GHz (i.e. suggesting less stability) as shown from the two subject walking scenarios in Figures 34 and 37 are less common, i.e. it is more often common across all scenarios for the 2.36 GHz curves to be to the right of those for 820 MHz, suggesting less stability as shown for respective scenarios in Figures 33 and 38 which are running and standing cases. Thus from all figures depicting CDFs, represented here and in the appendix, we make the following important observations:

- In all figures depicting CDFs it is indicated that the slower the rise in cumulative probability is with respect to increase in channel variation for the larger the time-varying period, indicating less stability, over $\tau = 25$ ms than $\tau = 10$ ms, and less stability over $\tau = 10$ ms than $\tau = 5$ ms. This is the expected result.
- We note that the variation in stability for different τ is greater with increasing movement of the subject.

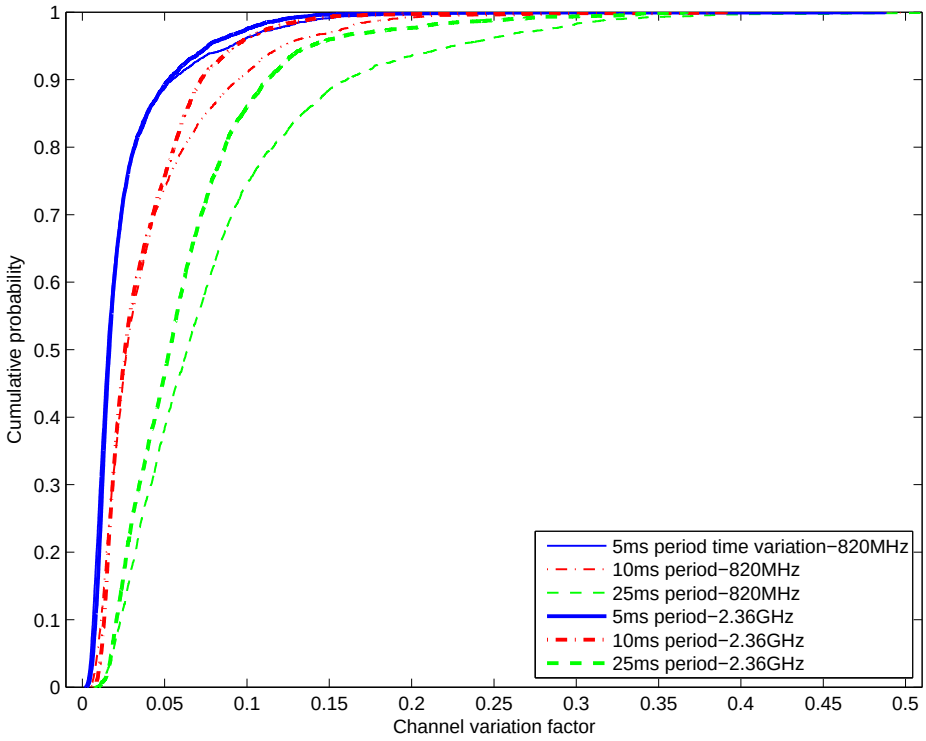

Figure 34: Cumulative probability of channel variation factor, Chest to right hip walking

- Channels are generally stable within a $5-10$ ms period, often with a probability larger than 90% with $\rho < 0.15$;
- The channel is very stable for most scenarios when the test subject is standing at both 820 MHz and 2.36 GHz.
- There is greater variability in channel coherence for running than for walking, as is expected. Thus time-varying results are consistent with the physical movement of subject.
- There is greater coherence stability (with larger probability for a small variation factor) at 820 MHz than 2.36 GHz. This is a general trend illustrated for the majority of scenarios by a comparison of curves within the same figures depicting cumulative probability (see appendix) for the same scenario at 820 MHz and 2.36 GHz.

Based on these empirical CDFs as a way of describing the stability of the channel, we compute the probability, for a given scenario and time period, that the variation factor is less than 0.1, or 10%. These probabilities for all scenarios are given in Table 8.

From Table 8 it is clear that in most cases, as the time span of interest increases, the channel is less likely to remain stable within that time span (shown by a decrease in probability in most cases). It also demonstrates increased channel variation, i.e. decreased coherence, with an increase in movement of the subject (with probabilities decreasing). We also note that the generally greater probabilities at 820 MHz than 2.36 GHz, for the same measurement positions, demonstrate a greater stability at the lower frequency, which can be attributed to the longer wavelength. Finally, we note that some small probabilities, for example, the one for left wrist to right hip, should not lead to the conclusion of low stability of the channel by itself. It is because the cumulative probability

Table 8: Probabilities, based on cumulative distribution functions, that the channel variation factor, for coherence is < 0.1 (or 10%) for time varying periods of 5ms, 10ms and 25ms respectively for all scenarios

Tx Antenna	Rx Antenna	Action	Probability channel variation factor < 0.1					
			Periods at 2.36 GHz			Periods at 820 MHz		
			5 ms	10 ms	25 ms	5 ms	10 ms	25 ms
Chest	Right Hip	Standing	0.986	1.000	1.000	1.000	1.000	1.000
Chest	Right Hip	Walking	0.975	0.961	0.860	0.963	0.910	0.748
Chest	Right Hip	Running	0.881	0.727	0.334	0.897	0.763	0.391
Right Wrist	Right Hip	Standing	1.000	1.000	1.000	1.000	1.000	1.000
Right Wrist	Right Hip	Walking	0.947	0.849	0.532	0.952	0.851	0.400
Right Wrist	Right Hip	Running	0.919	0.715	0.333	0.871	0.704	0.352
Left Wrist	Right Hip	Standing	0.533	0.288	0.090	1.000	1.000	1.000
Left Wrist	Right Hip	Walking	0.834	0.656	0.364	0.840	0.651	0.307
Left Wrist	Right Hip	Running	0.842	0.631	0.287	0.862	0.677	0.315
Right Ankle	Right Hip	Standing	0.989	0.991	0.994	1.000	1.000	1.000
Right Ankle	Right Hip	Walking	0.974	0.959	0.805	0.980	0.943	0.769
Right Ankle	Right Hip	Running	0.869	0.680	0.264	0.948	0.863	0.586
Left Ankle	Right Hip	Standing	0.996	1.000	1.000	1.000	1.000	1.000
Left Ankle	Right Hip	Walking	0.954	0.888	0.593	0.938	0.863	0.617
Left Ankle	Right Hip	Running	0.876	0.677	0.265	0.932	0.829	0.476
Back	Right Hip	Standing	0.722	0.592	0.504	1.000	1.000	1.000
Back	Right Hip	Walking	0.940	0.874	0.559	0.969	0.950	0.901
Back	Right Hip	Running	0.777	0.513	0.177	0.894	0.777	0.456
Back	Chest	Standing	0.952	0.957	0.961	0.997	1.000	1.000
Back	Chest	Walking	0.852	0.765	0.480	0.904	0.803	0.506
Back	Chest	Running	0.766	0.536	0.175	0.786	0.601	0.272
Right Wrist	Chest	Standing	0.938	0.980	1.000	1.000	1.000	1.000
Right Wrist	Chest	Walking	0.779	0.573	0.250	0.864	0.706	0.363
Right Wrist	Chest	Running	0.722	0.470	0.143	0.940	0.839	0.569
Right Ankle	Chest	Standing	0.997	1.000	1.000	0.995	0.994	0.991
Right Ankle	Chest	Walking	0.965	0.928	0.749	0.967	0.953	0.895
Right Ankle	Chest	Running	0.854	0.651	0.212	0.890	0.745	0.386

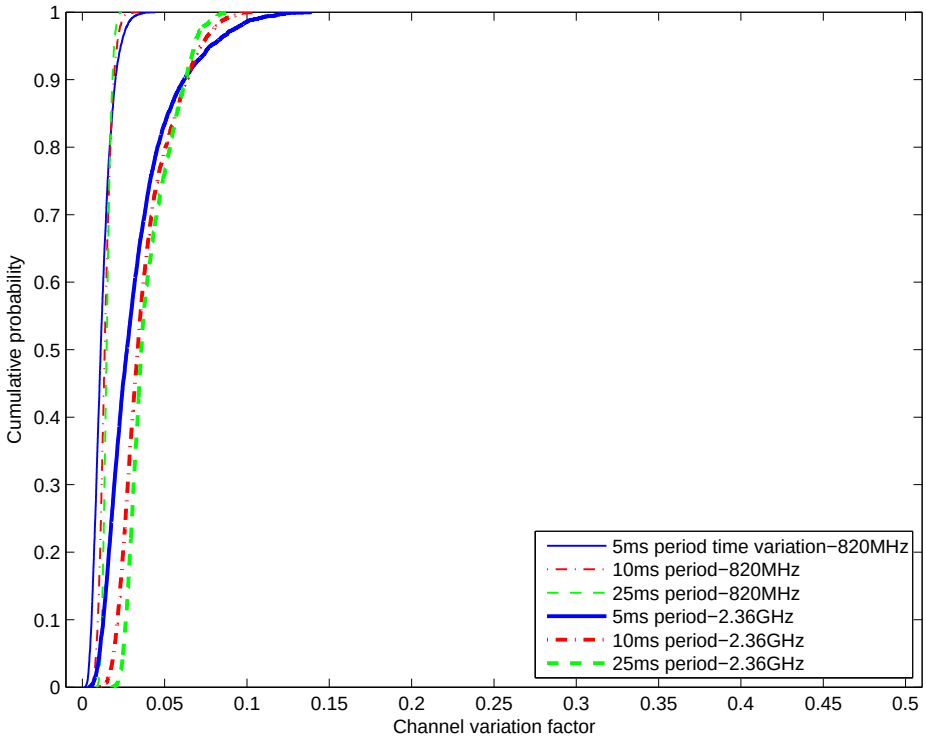

Figure 35: Cumulative probability of channel variation factor, Chest to right hip standing

increases very rapidly at a slightly larger channel variation factor just above 0.1. A thorough channel variation analysis is thus better referred to the cumulative probability curves. *However, the probabilities in Table 8 clearly indicate that the greater the motion of the subject, the less stable the channel, thus subject movement is an important consideration in channel coherence.*

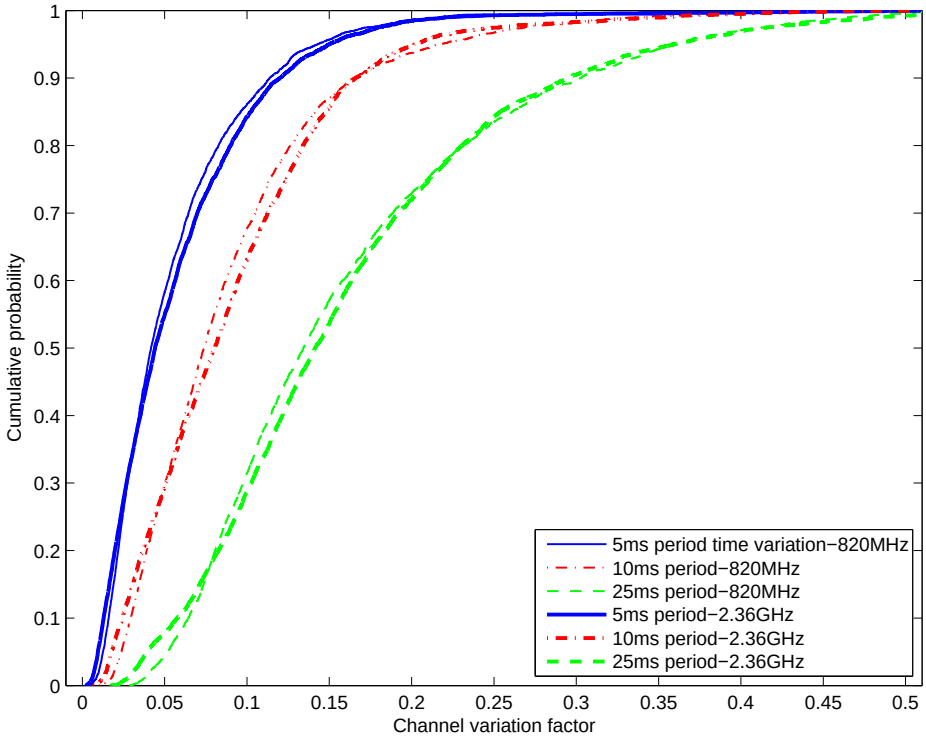

Figure 36: Cumulative probability of channel variation factor, left wrist to right hip running

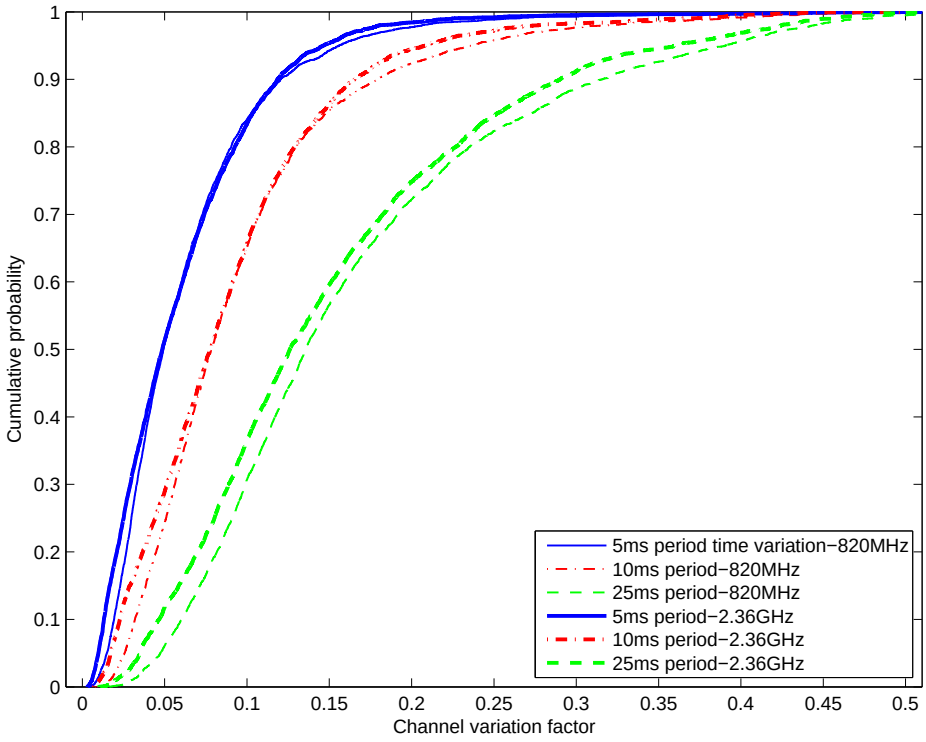

Figure 37: Cumulative probability of channel variation factor, left wrist to right hip walking

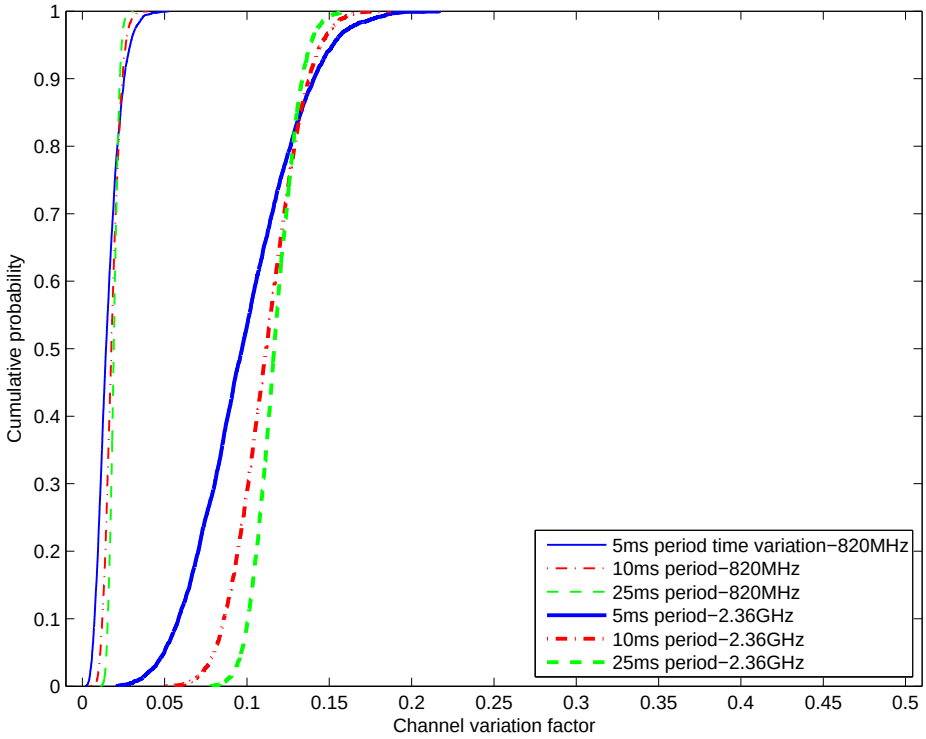

Figure 38: Cumulative probability of channel variation factor, left wrist to right hip standing

4 Concluding Remarks

Of the fading scenarios likely for an on-body wireless network in an indoor environment, we have shown that movement of the human body is the dominant fading effect. Even in the largest identified case of frequency-selective fading, the fading due to movement of a subject that was ostensibly standing still was still the dominant effect. Moreover, the fading effects due to movement were consistent with the level of movement from the test subject; with more movement generating a larger variation in the fading. *In summary, the predominant fading effect in the body area channel measurements made is slow and flat fading, although in some cases frequency-selective effects were observed.*

It is clear that path loss around the human body is far greater than it would be with a similar antenna separation in free space, even when a direct line of sight path exists. There is greater path loss at 2.36 GHz than at 820 MHz, but the difference is not as significant as might be expected. The more significant variation in path loss at these two frequencies is when there is no line-of-sight path during the measurement period.

Typically either the Lognormal or the Gamma distributions are the best match to data sets of normalized received power for body area communications while the subject is in motion, for any transmitter and receiver location. However, when the subject is stationary, there is no probability distribution that fits the data set well, but in most cases the Normal distribution is the best fit (even if not a good fit).

Generally, from time varying coherence analysis, it can be observed that the channel is generally quite stable, and more so at 820 MHz than 2.36 GHz. However, as previously mentioned, the motion of the subject has considerable impact on the stability of the channel, particularly as the period of interest increases. The generally greater stability at lower frequency has been attributed to the longer wavelength. From coherence analysis it could be concluded that carrier frequency and subject movement need to be carefully considered in body area wireless system design.

References

[1] K. Yazdandoost and K. Sayrafian, "Channel Model for Body Area Network (BAN)," 15-08-0033-02-0006-draft-of-channel-model-for-body-area-network.

[2] T. Zasowski, G. Meyer, F. Althaus, and A. Wittneben, "Propagation effects in uwb body area networks," in *Ultra-Wideband, 2005. ICU 2005. 2005 IEEE International Conference on*, September 2005, pp. 16–21.

[3] H.-R. Chuang and W.-T. Chen, "Computer simulation of the human-body effects on a circular-loop-wire antenna for radio-pager communications at 152, 280, and 400 mhz," *Vehicular Technology, IEEE Transactions on*, vol. 46, no. 3, pp. 544–559, Aug 1997.

[4] S. Obayashi and J. Zander, "A body-shadowing model for indoor radio communication environments," *Antennas and Propagation, IEEE Transactions on*, vol. 46, no. 6, pp. 920–927, Jun 1998.

[5] W.-T. Chen and H.-R. Chuang, "Numerical computation of human interaction with arbitrarily oriented superquadric loop antennas in personal communications," *Antennas and Propagation, IEEE Transactions on*, vol. 46, no. 6, pp. 821–828, June 1998.

[6] P.-S. Hall and Y. Hao, *Antennas and Propagation for Body Centric Wireless Networks.* Artech House, 2006.

[7] Y. Rahmat-Samii, K. W. Kim, M. Jensen, K. Fujimoto, and O. Edvardsson, "Antennas and humans in personal communications," in *Mobile Antenna Systems Handbook*, K. Fujimoto and J. James, Eds. Artech House, 2001, ch. 7.

[8] P. Hall, Y. Hao, Y. Nechayev, A. Alomalny, C. Constantinou, C. Parini, M. Kamarudin, T. Salim, D. Hee, R. Dubrovka, A. Owadally, W. Song, A. Serra, P. Nepa, M. Gallo, and M. Bozzetti, "Antennas and propagation for on-body communication systems," *Antennas and Propagation Magazine, IEEE*, vol. 49, no. 3, pp. 41–58, June 2007.

[9] G. Roqueta, A. Fort, C. Craeye, and C. Oestges, "Analytical propagation models for body area networks," in *Antennas and Propagation for Body-Centric Wireless Communications, 2007 IET Seminar on*, April 2007, pp. 90–96.

[10] D. Neirynck., C. Williams, A. Nix, and M. Beach, "Wideband channel characterisation for body and personal area networks," in *2nd International Workshop on Wearable and Implantable Body Sensor Networks*, April 2004.

[11] K. Yazdandoost, H. Sawada, S.-T. Choi, J. Takada, and R. Kohno, "Channel Characterization for BAN Communications," 15-07-0641-00-0ban-channel-characterization-ban-communications.

[12] D. Neirynck, "Channel measurements and PHY development for wearable devices," 15-07-0547-00-0ban-channel-measurements-and-phy-development-wearable-devices.

[13] G. Dolmans, "Applications, Channels, and Radio Architectures," 15-08-0163-00-0006-applications-channels-architectures.

[14] D. Miniutti, L. Hanlen, D. Smith, A. Zhang, D. Lewis, D. Rodda, and B. Gilbert, "Dynamic narrowband channel measurements around 2.4 GHz for body area networks," 15-08-0354-01-0006-dynamic-narrowband-channel-measurements-around-2-4-ghz-for-body-area-networks.

[15] B. Zhen, M. Patel, S. Lee, and E. Won, "Body Area Network (BAN) Technical Requirements," 15-08-0037-01-0006-ieee-802-15-6-technical-requirements-document-v-4-0.

[16] W. Scanlon, G. Conway, and S. Cotton, "Antennas, propagation considerations for robust wireless communications in medical body area networks," in *Antennas and Propagation for Body-Centric Wireless Communications, 2007 IET Seminar on*, April 2007, p. 37.

[17] *800 MHz Voice Communications Wearable Antenna*, Octane Wireless, Glen Burnie, USA.

[18] *WLAN Wearable Antenna; PRR Wearable Antenna*, Octane Wireless, Glen Burnie, USA.

[19] D. Freedman and P. Diaconis, "On the histogram as a density estimator:L_2 theory," *Probability Theory and Related Fields*, vol. 57, no. 4, pp. 453–476, December 1981.

A Appendix

This appendix catalogs the entire set of results obtained from the measurements that were performed. It is located at the end of the document to accommodate those who wish to print this section separately, or not at all.

The following sections have a one-to-one correspondence to their respective counterparts in Section 3. See Section 3 for an explanation of the figures presented here.

A.1 Channel Power Spectral Density

A.1.1 820 MHz Measurements

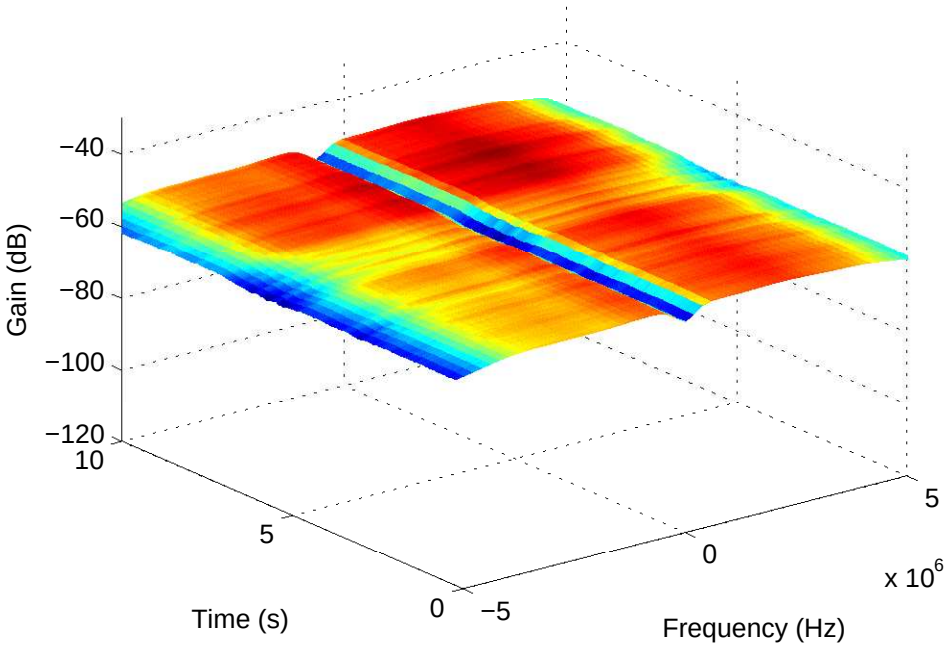

Figure 39: Chest to right hip, standing, 820 MHz

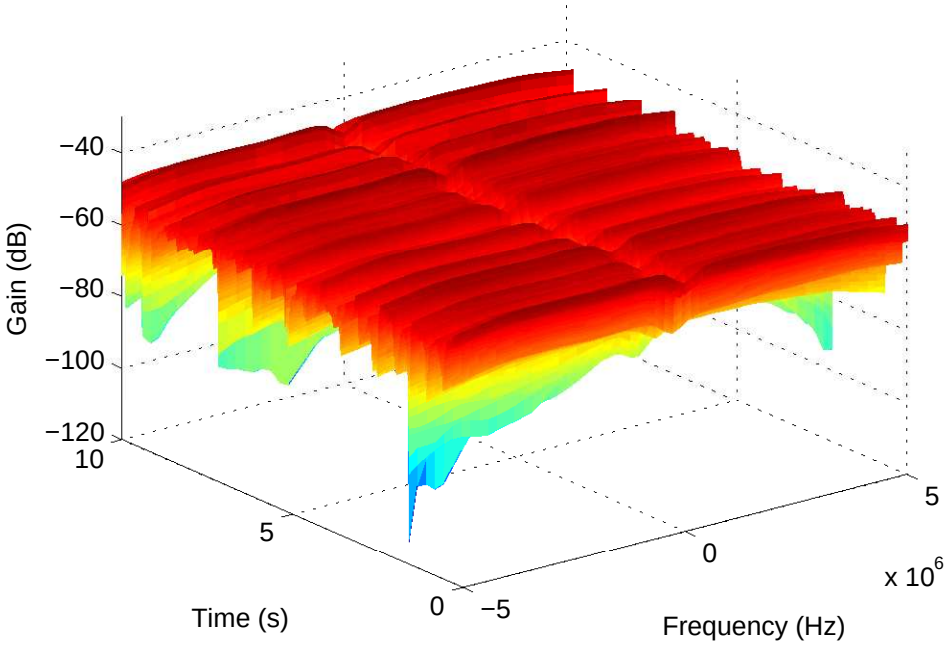

Figure 40: Chest to right hip, walking, 820 MHz

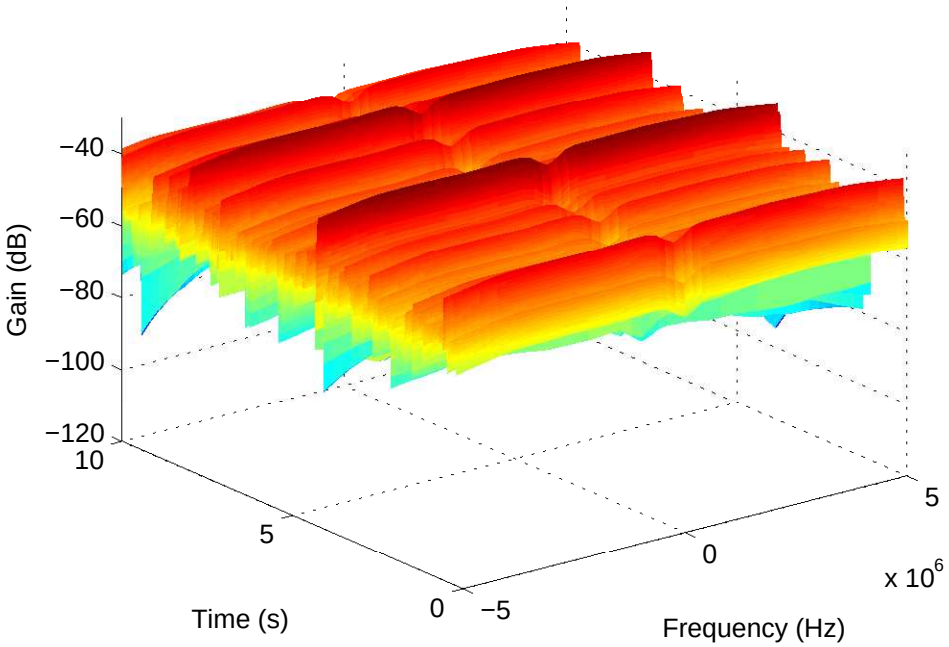

Figure 41: Chest to right hip, running, 820 MHz

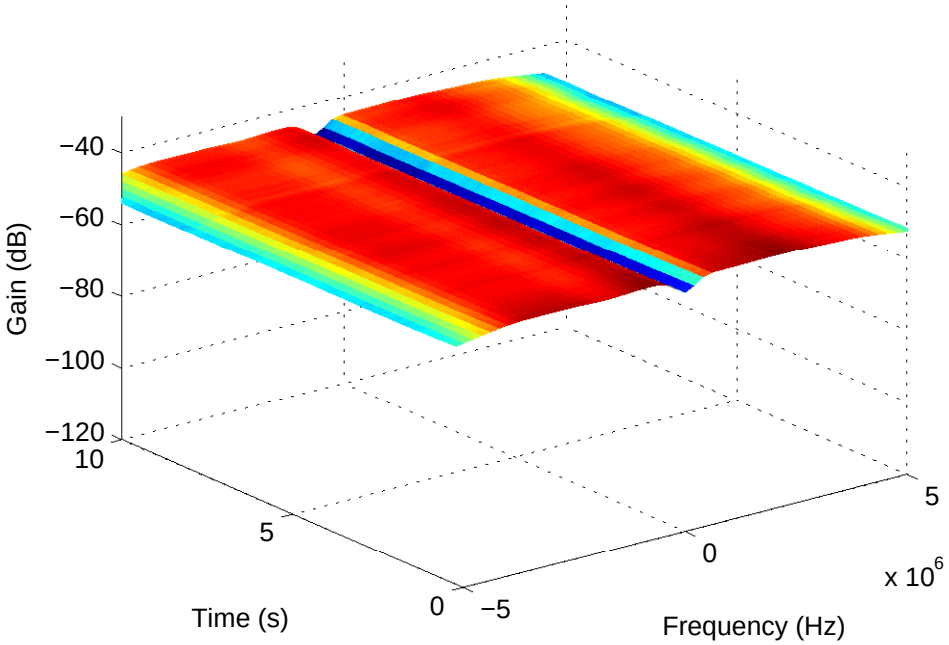

Figure 42: Right wrist to right hip, standing, 820 MHz

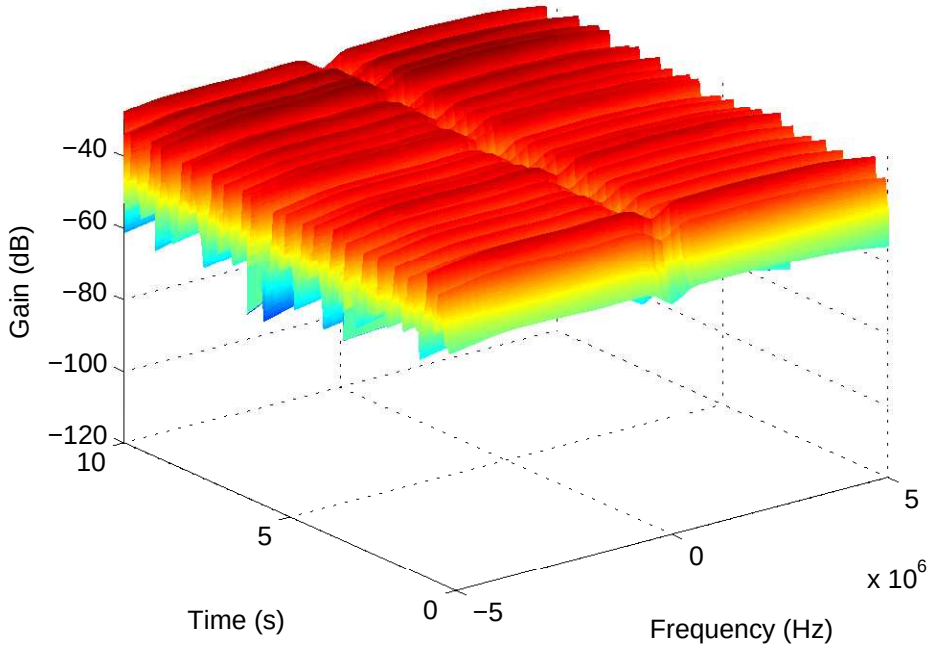

Figure 43: Right wrist to right hip, walking, 820 MHz

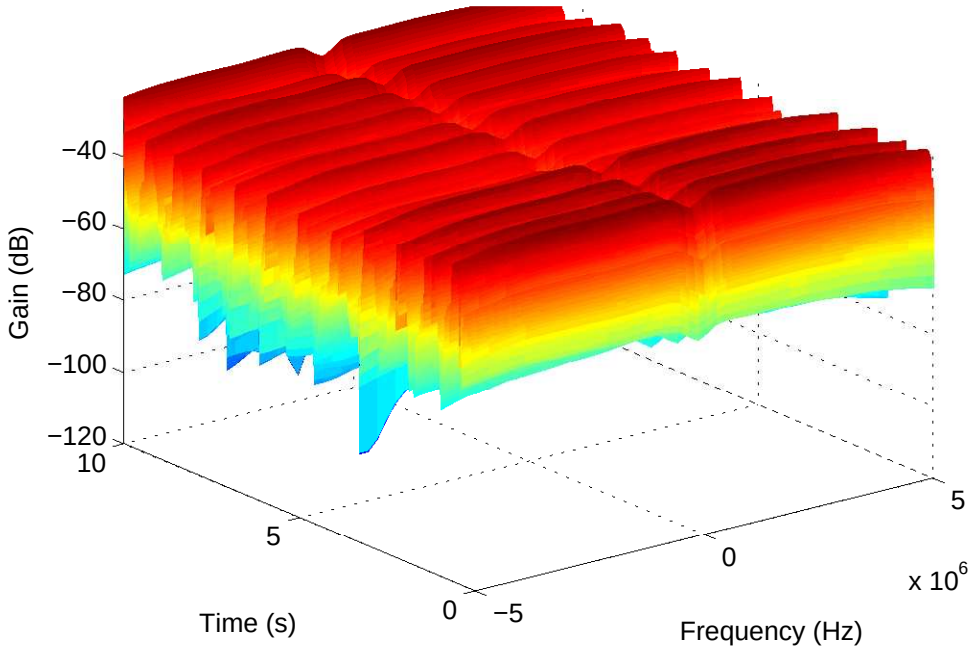

Figure 44: Right wrist to right hip, running, 820 MHz

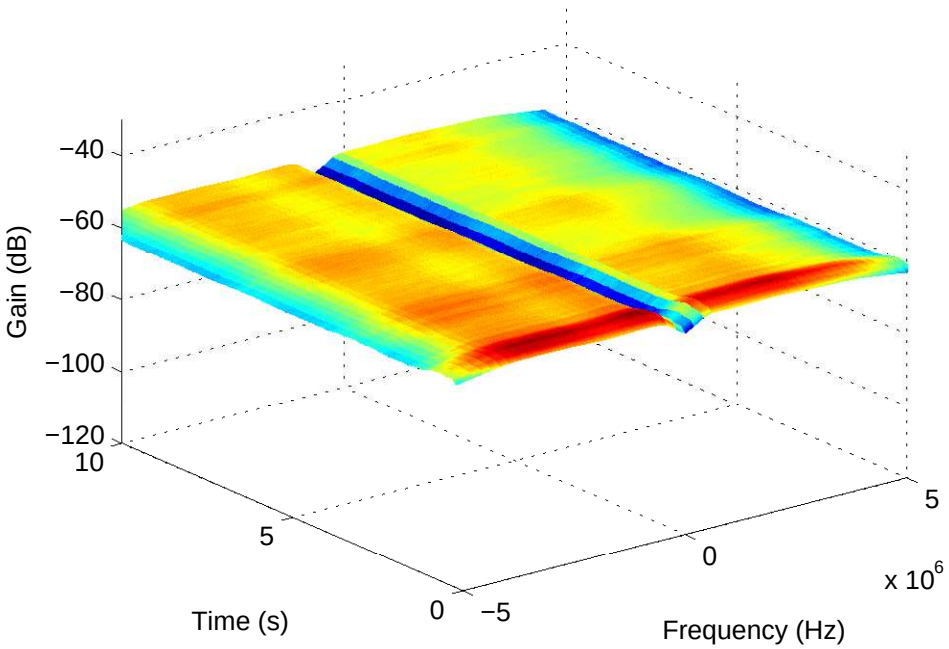

Figure 45: Left wrist to right hip, standing, 820 MHz

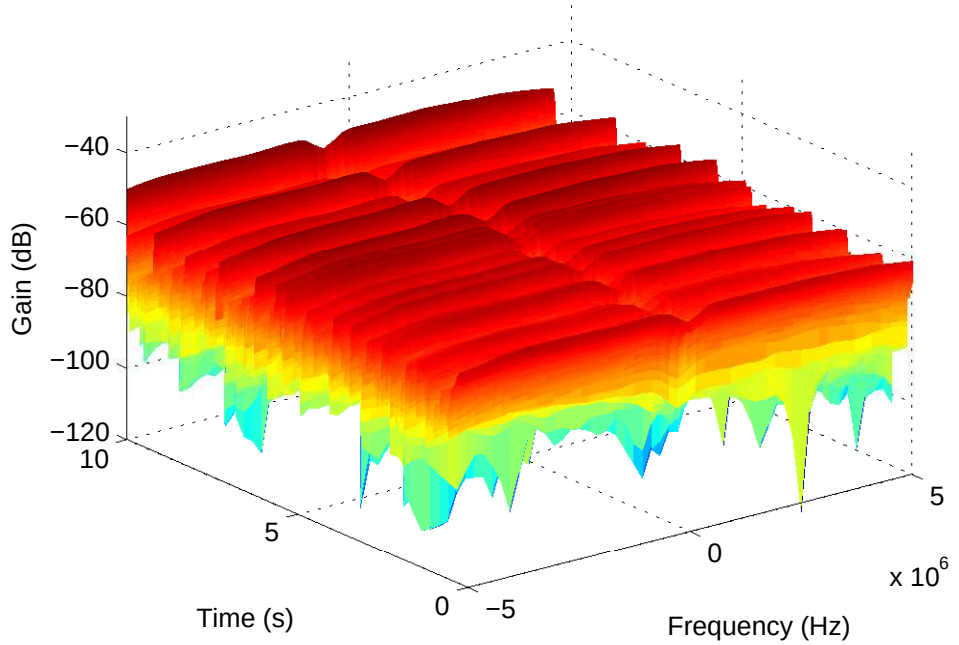

Figure 46: Left wrist to right hip, walking, 820 MHz

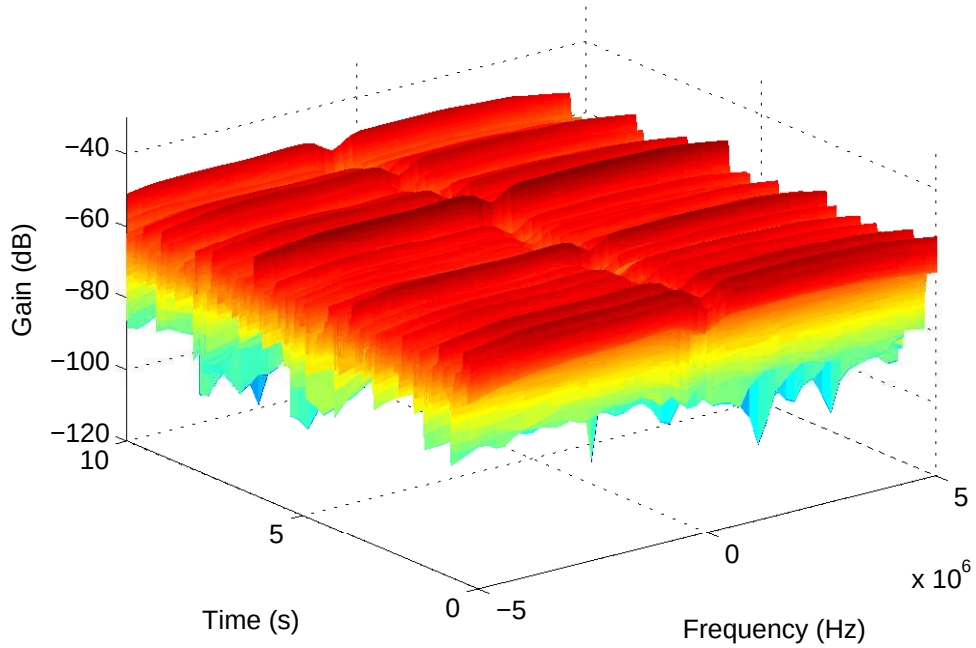

Figure 47: Left wrist to right hip, running, 820 MHz

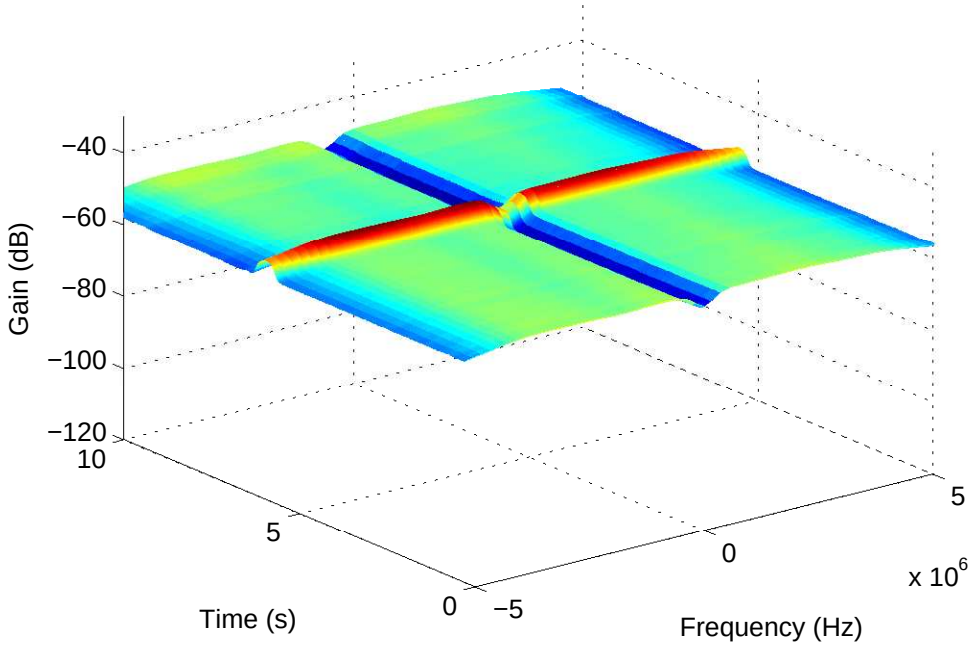

Figure 48: Right ankle to right hip, standing, 820 MHz

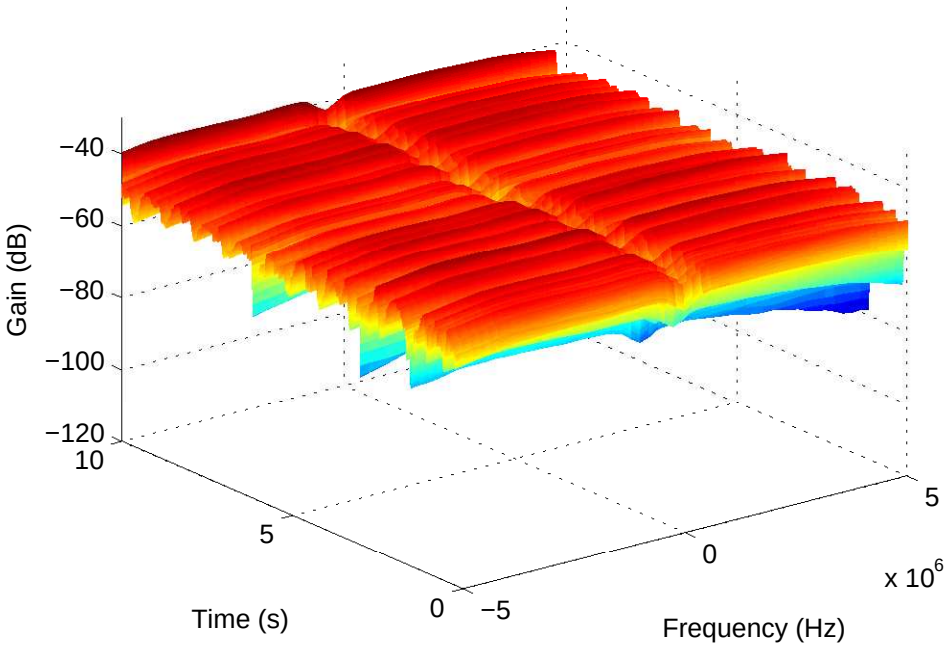

Figure 49: Right ankle to right hip, walking, 820 MHz

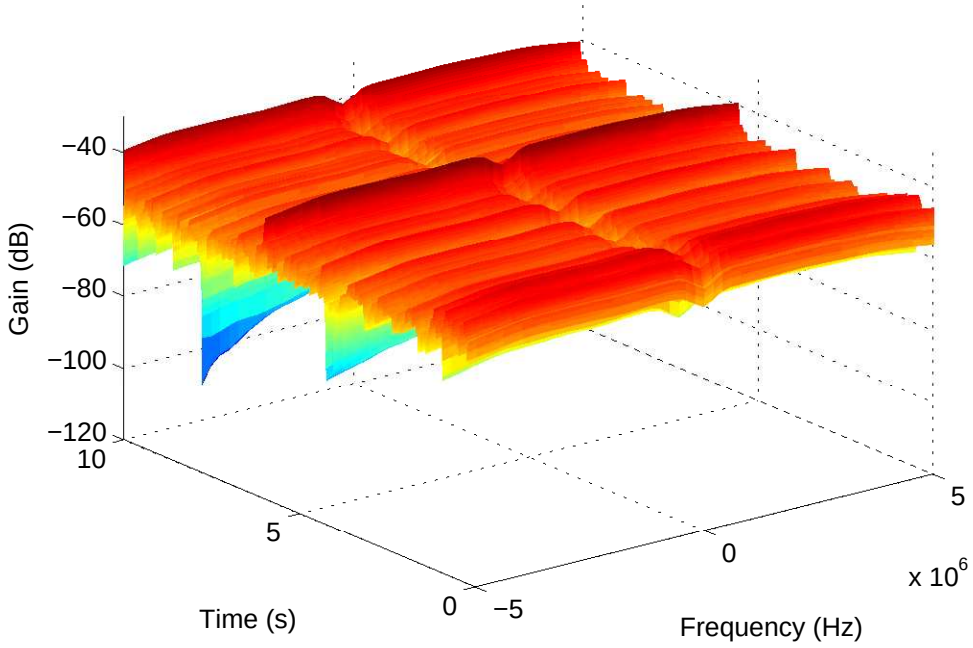

Figure 50: Right ankle to right hip, running, 820 MHz

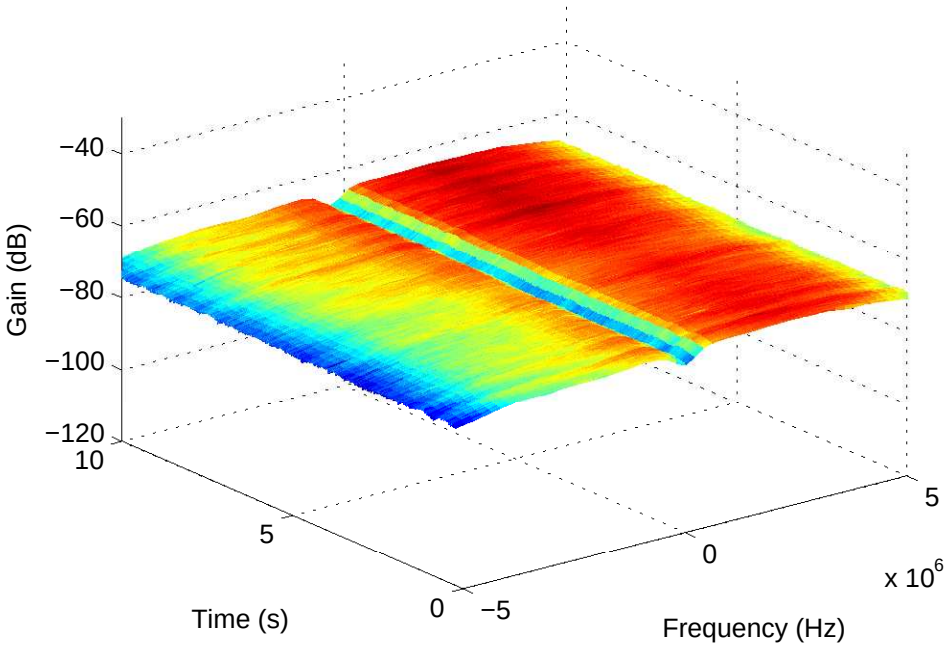

Figure 51: Left ankle to right hip, standing, 820 MHz

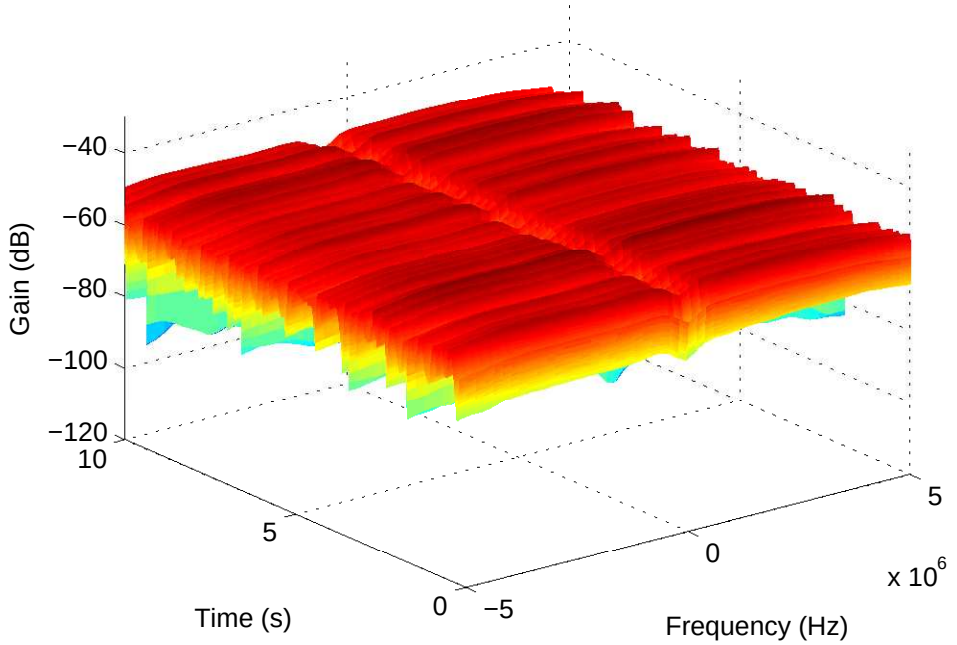

Figure 52: Left ankle to right hip, walking, 820 MHz

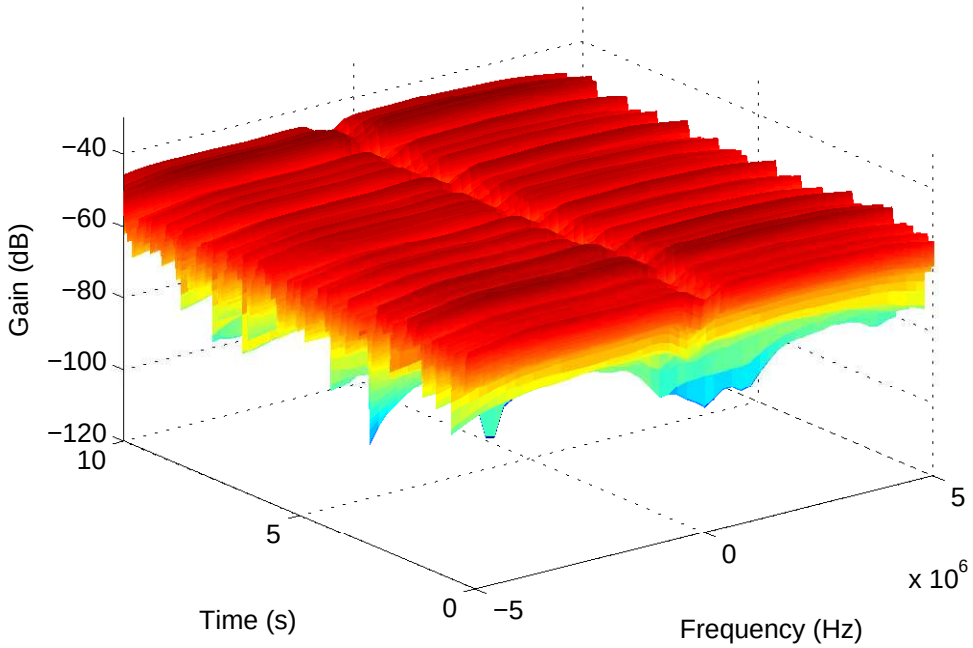

Figure 53: Left ankle to right hip, running, 820 MHz

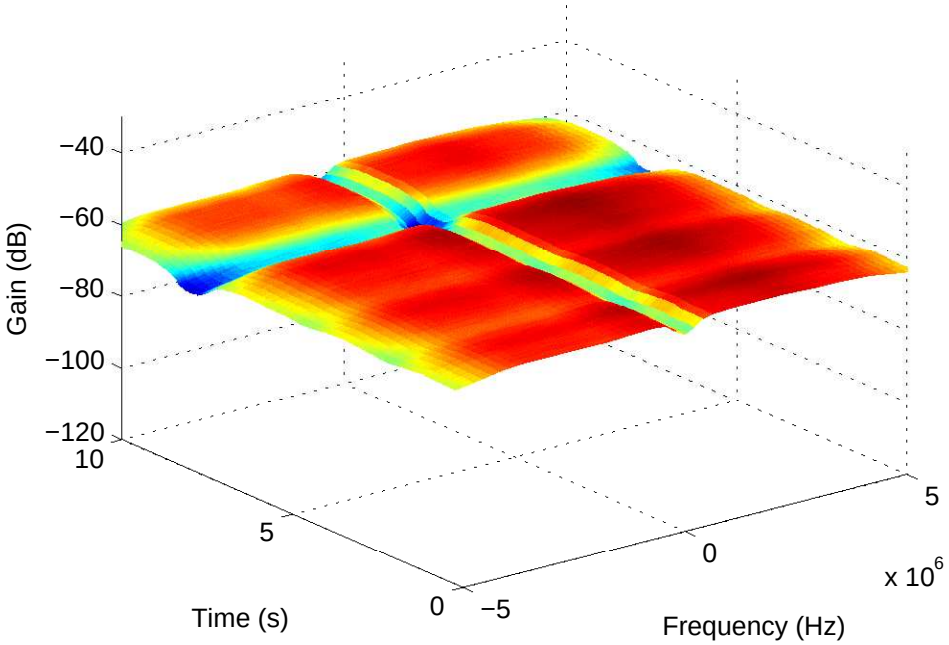

Figure 54: Back to right hip, standing, 820 MHz

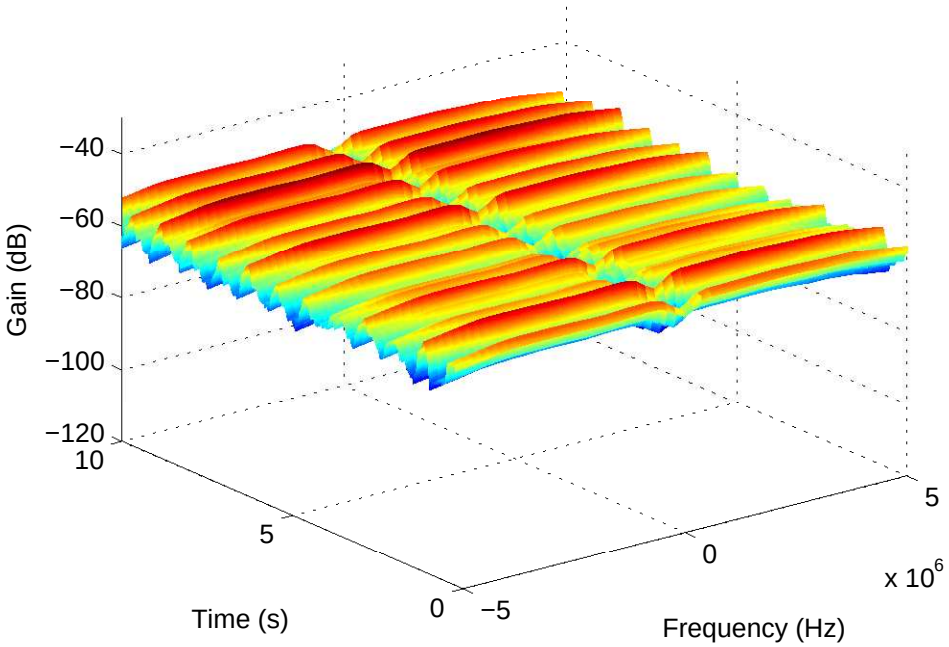

Figure 55: Back to right hip, walking, 820 MHz

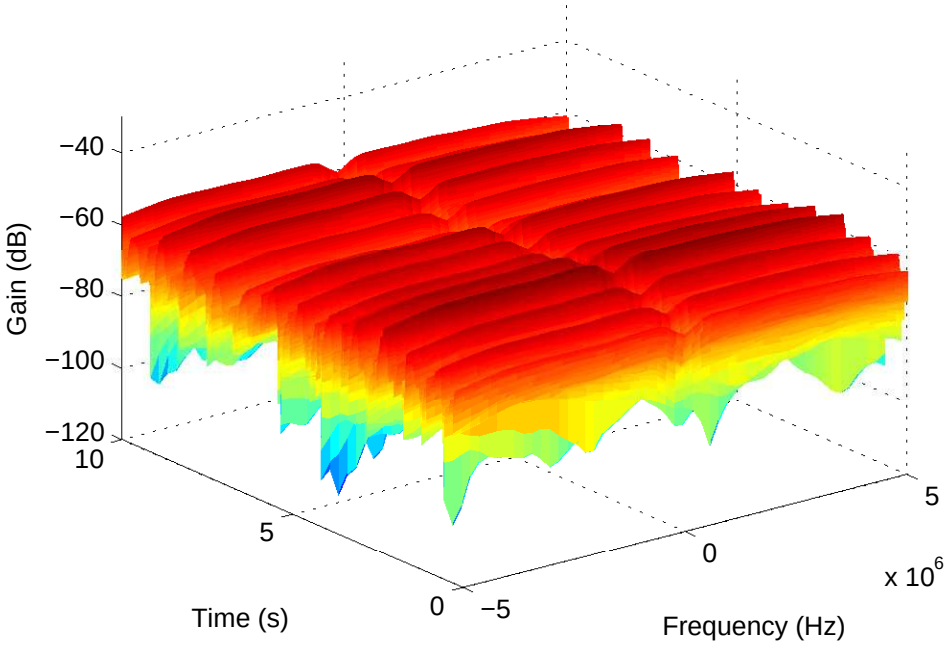

Figure 56: Back to right hip, running, 820 MHz

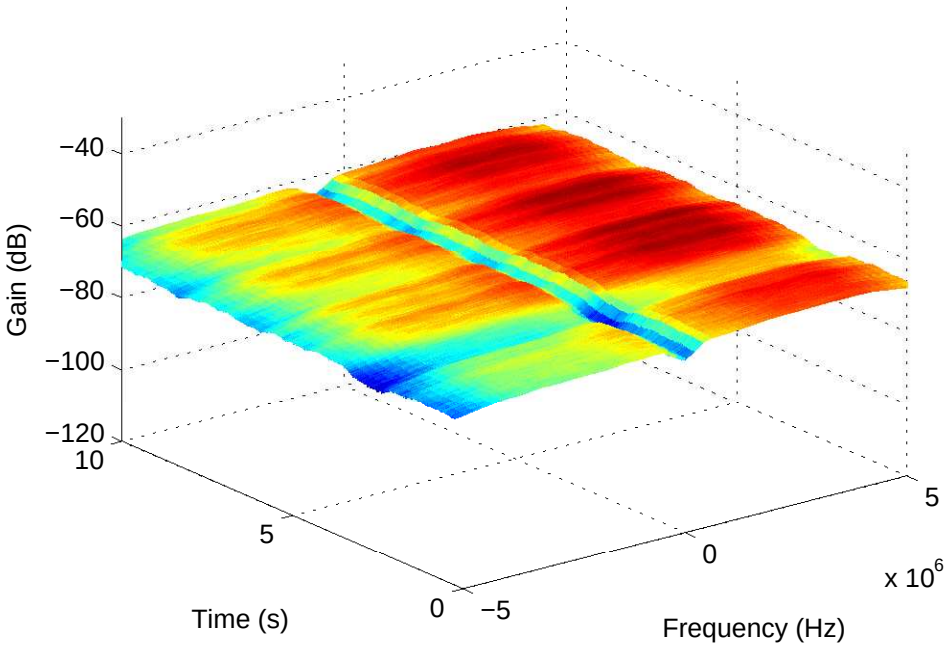

Figure 57: Back to chest, standing, 820 MHz

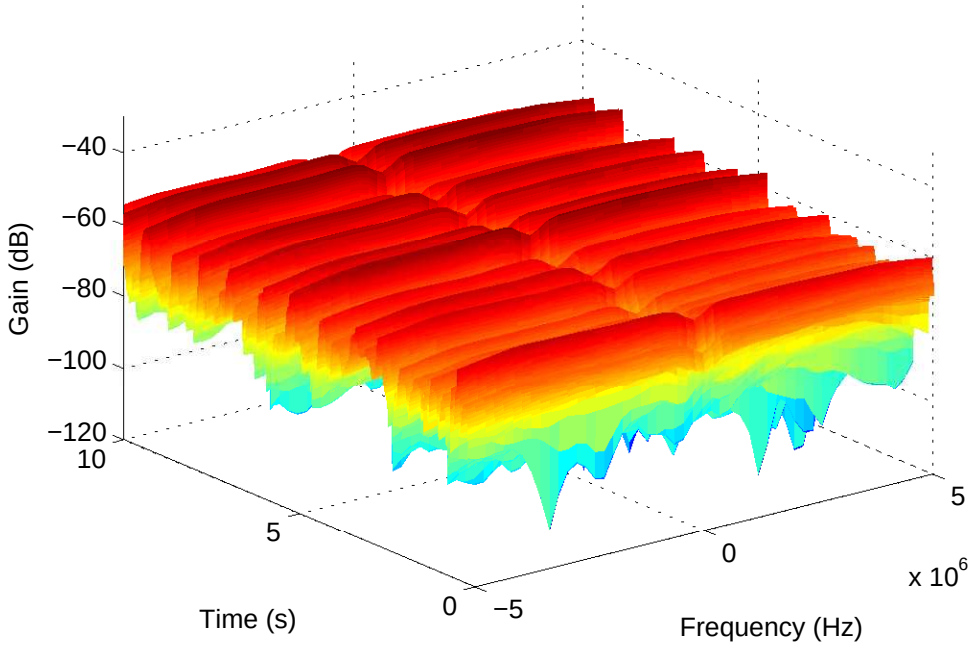

Figure 58: Back to chest, walking, 820 MHz

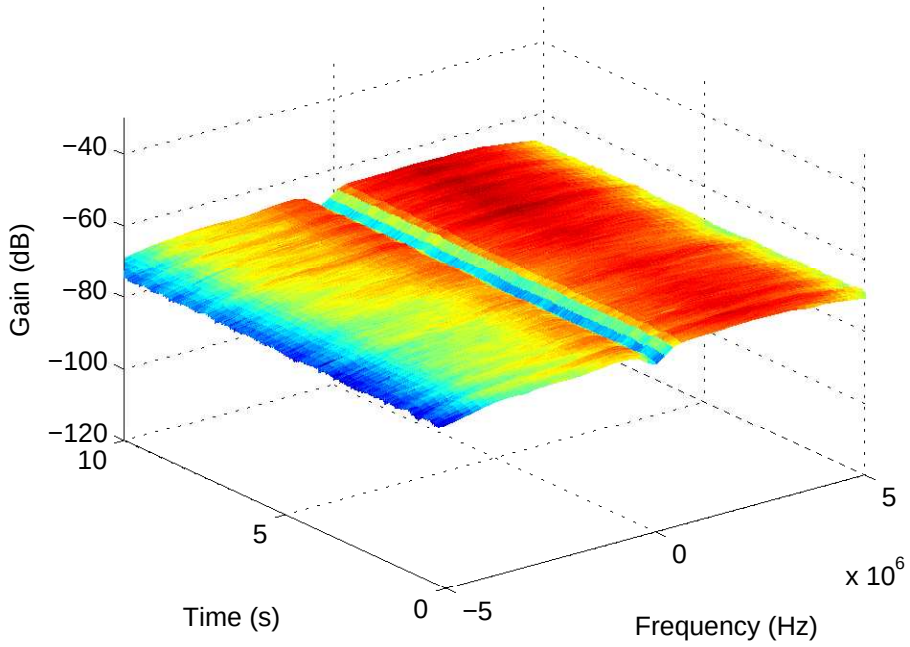

Figure 59: Back to chest, running, 820 MHz

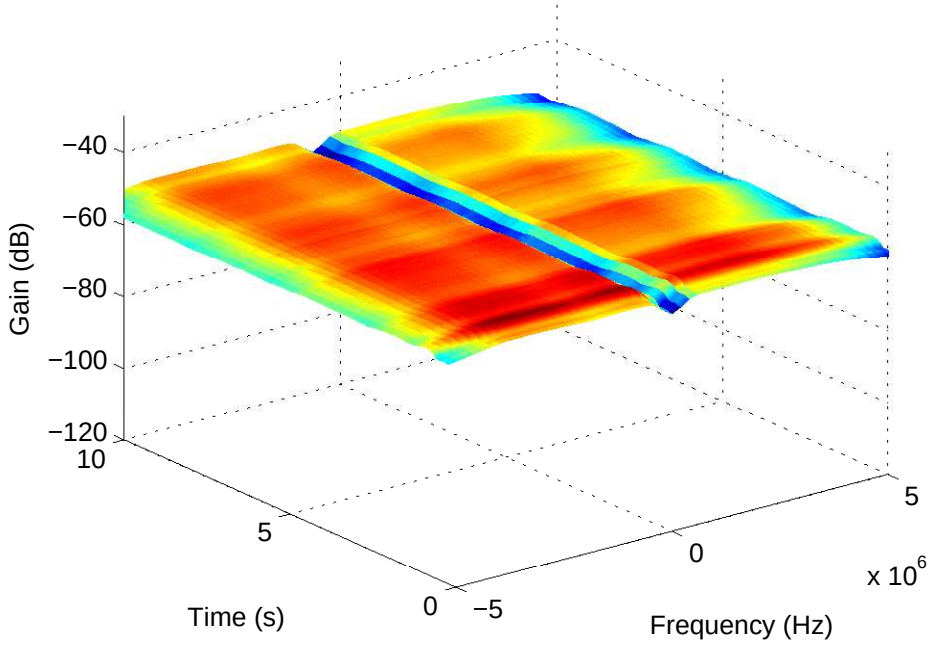

Figure 60: Right wrist to chest, standing, 820 MHz

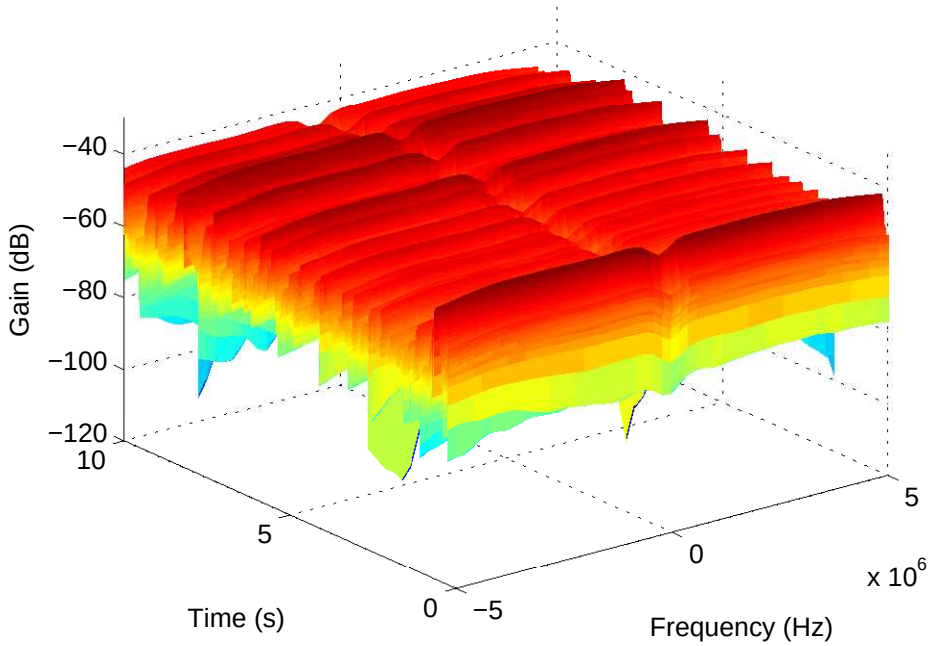

Figure 61: Right wrist to chest, walking, 820 MHz

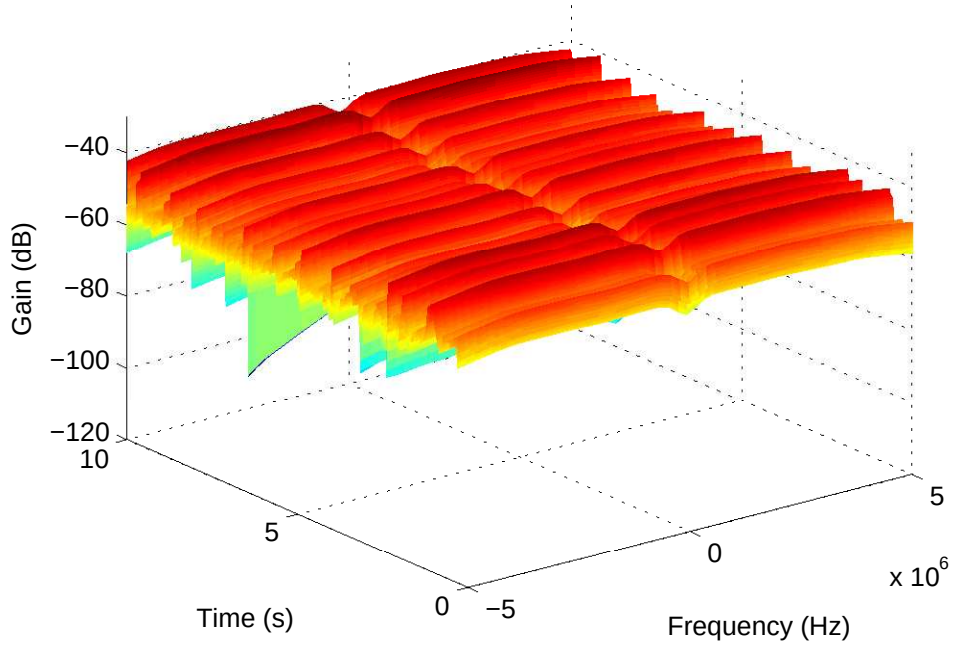

Figure 62: Right wrist to chest, running, 820 MHz

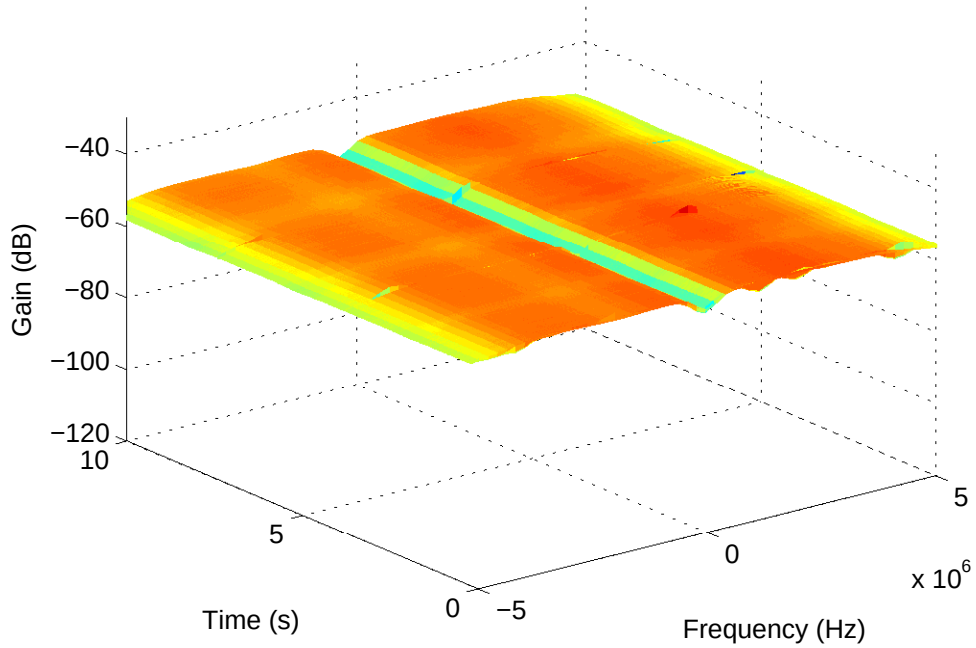

Figure 63: Right ankle to chest, standing, 820 MHz

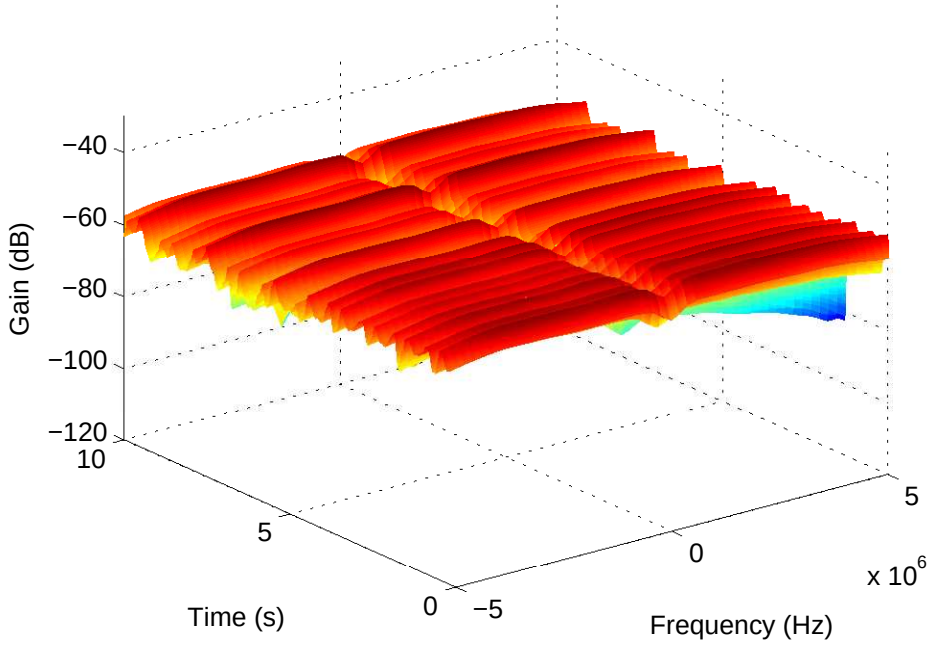

Figure 64: Right ankle to chest, walking, 820 MHz

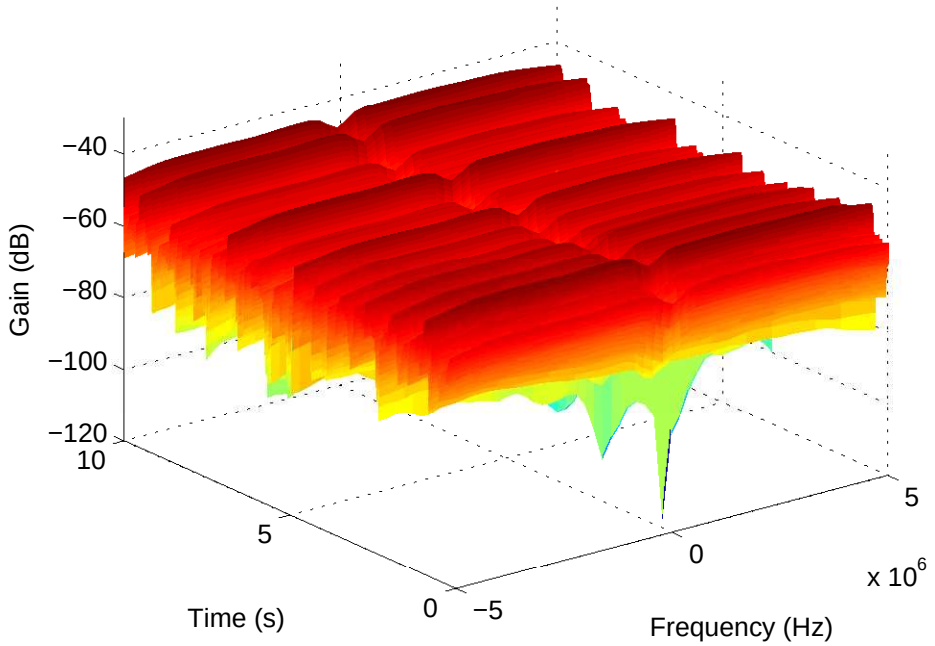

Figure 65: Right ankle to chest, running, 820 MHz

A.1.2 2.36 GHz Measurements

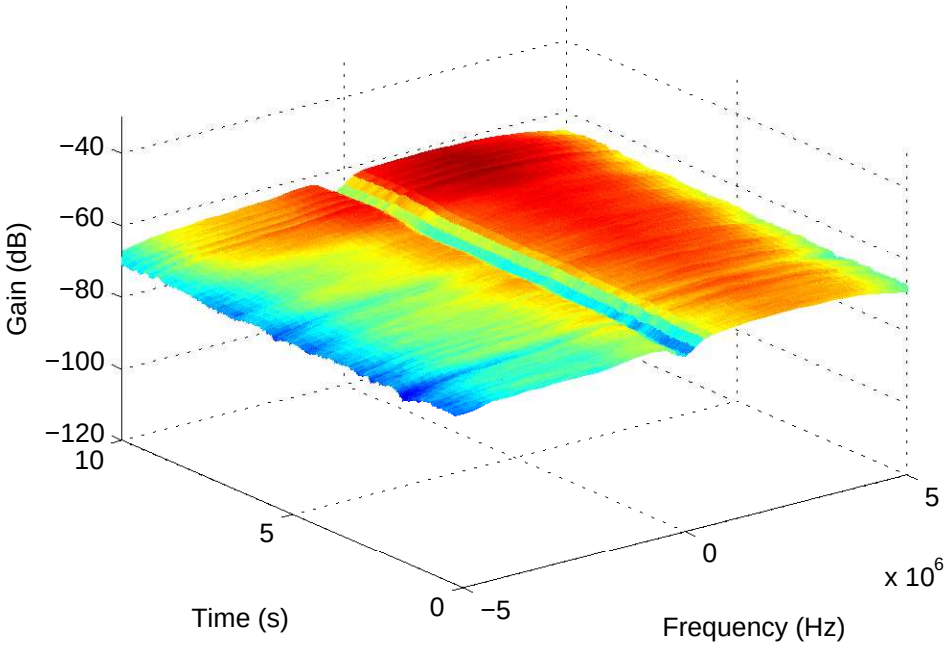

Figure 66: Chest to right hip, standing, 2.36 GHz

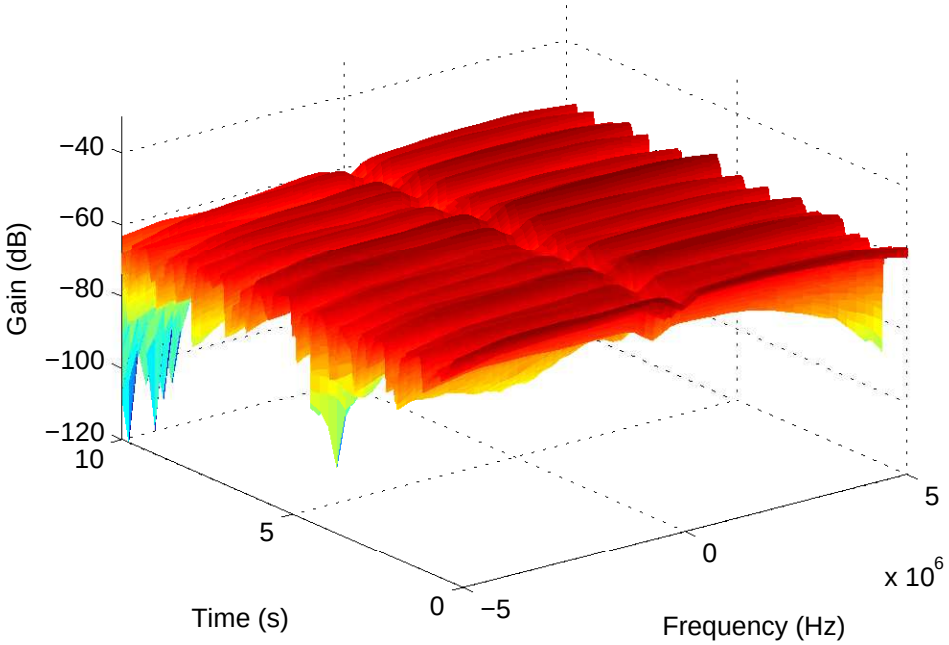

Figure 67: Chest to right hip, walking, 2.36 GHz

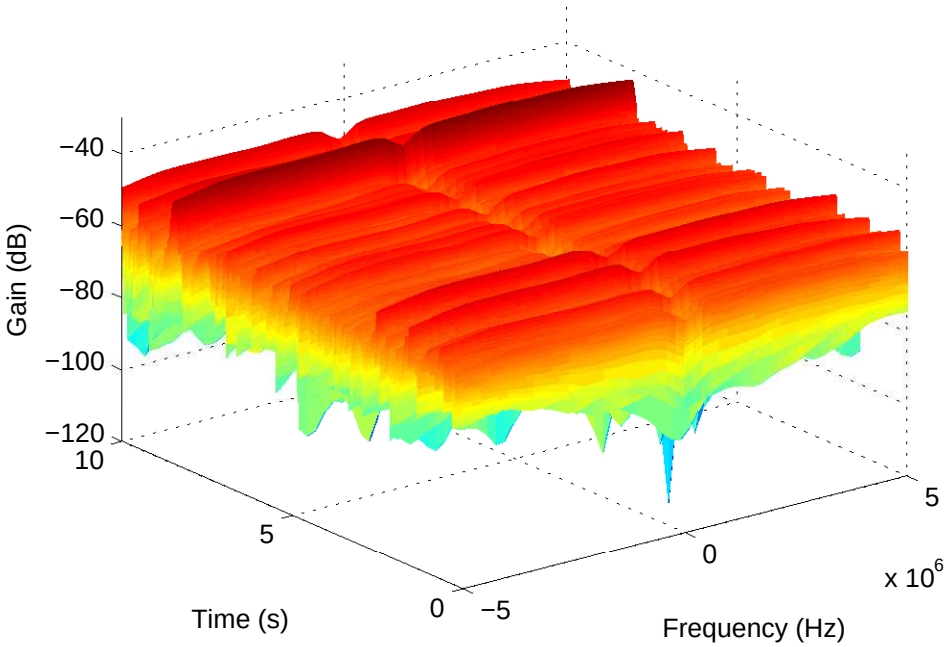

Figure 68: Chest to right hip, running, 2.36 GHz

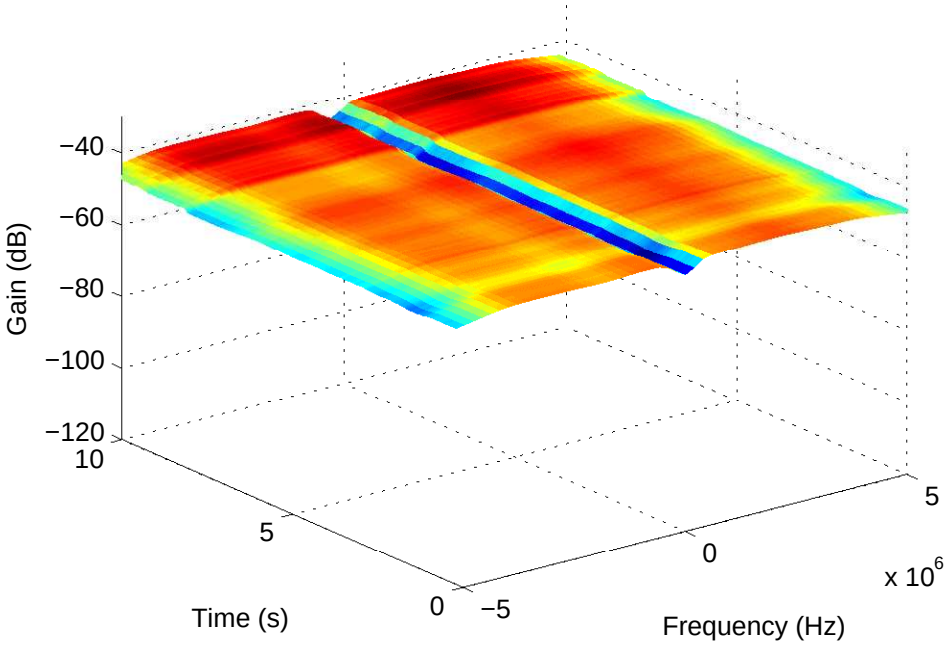

Figure 69: Right wrist to right hip, standing, 2.36 GHz

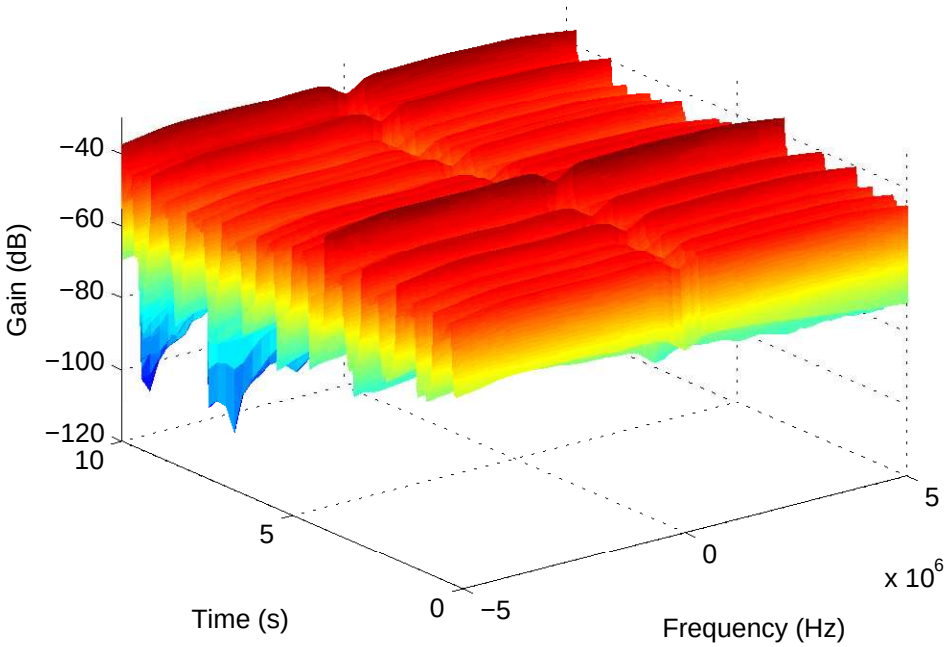

Figure 70: Right wrist to right hip, walking, 2.36 GHz

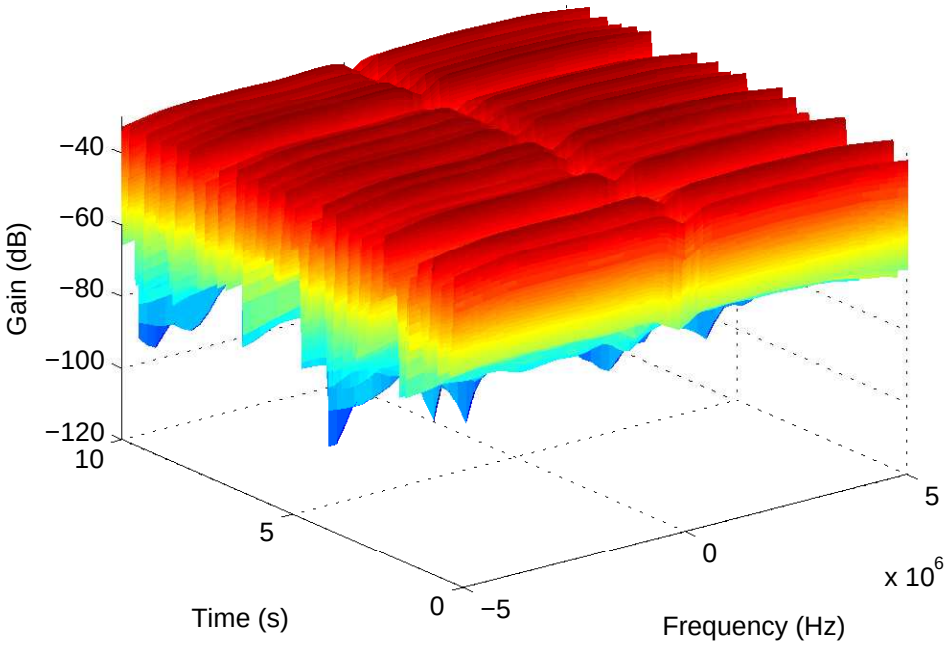

Figure 71: Right wrist to right hip, running, 2.36 GHz

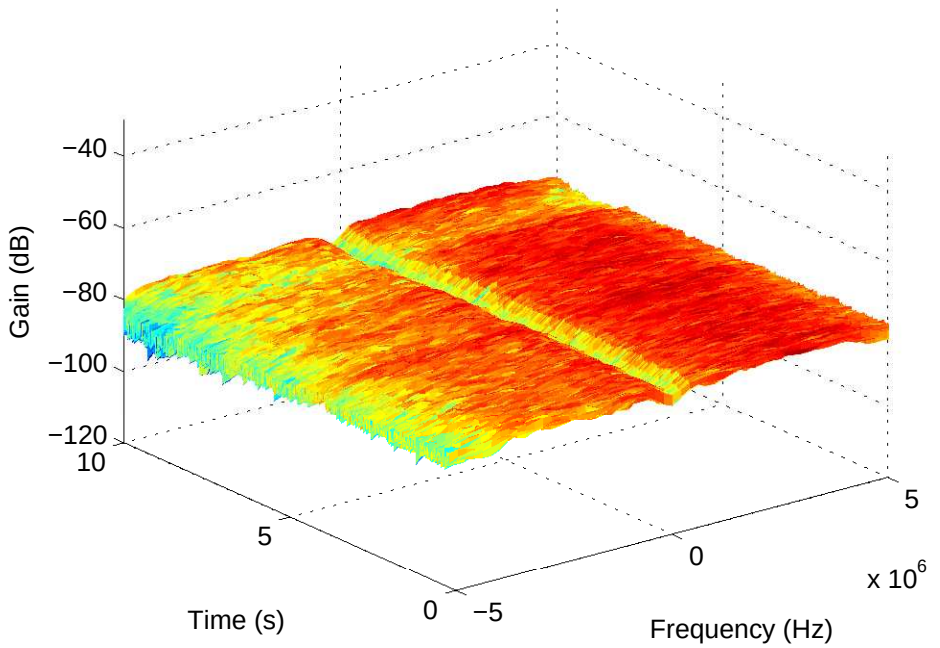

Figure 72: Left wrist to right hip, standing, 2.36 GHz

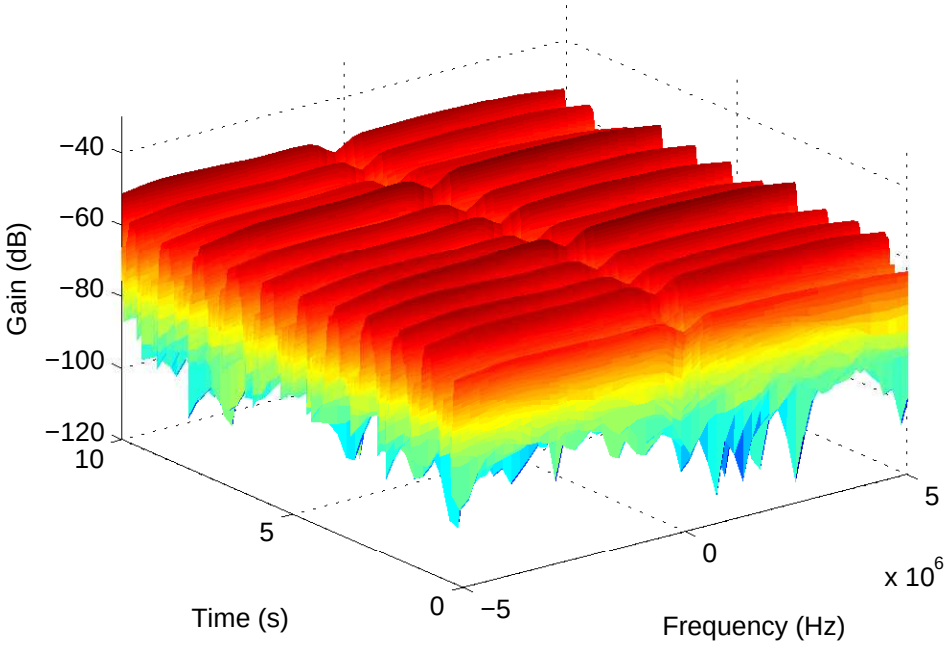

Figure 73: Left wrist to right hip, walking, 2.36 GHz

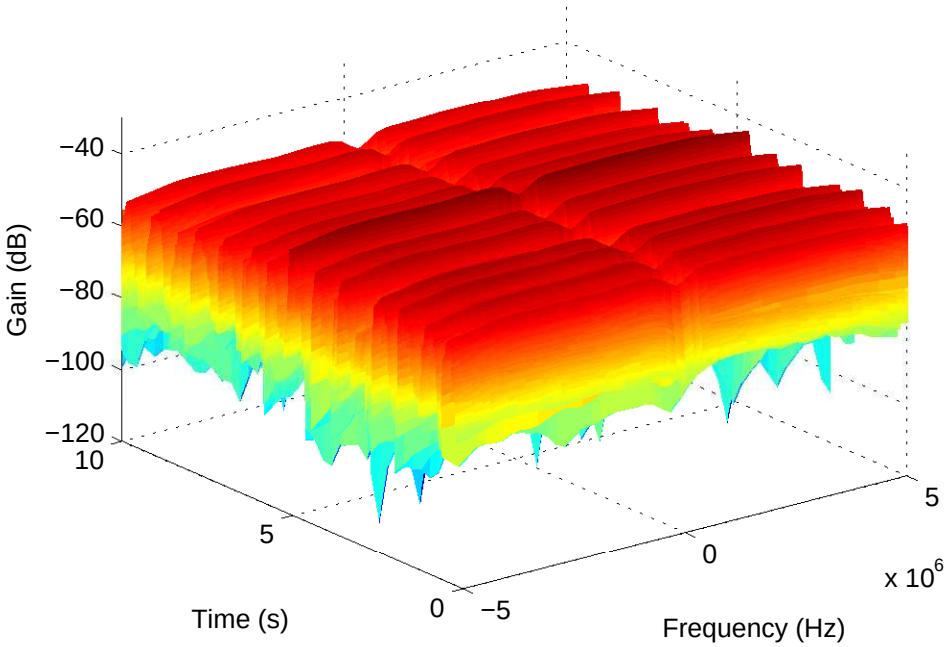

Figure 74: Left wrist to right hip, running, 2.36 GHz

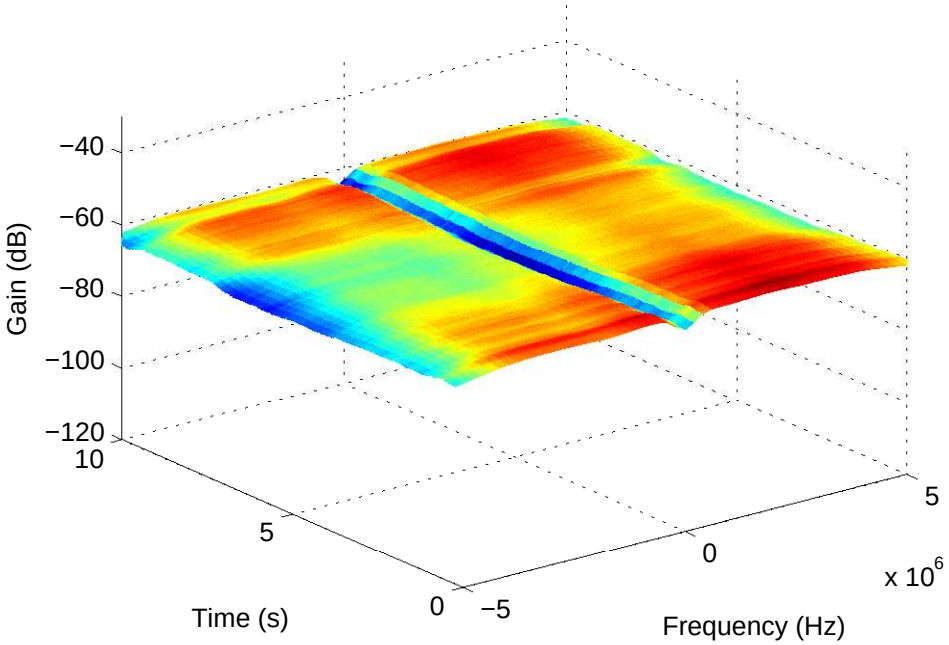

Figure 75: Right ankle to right hip, standing, 2.36 GHz

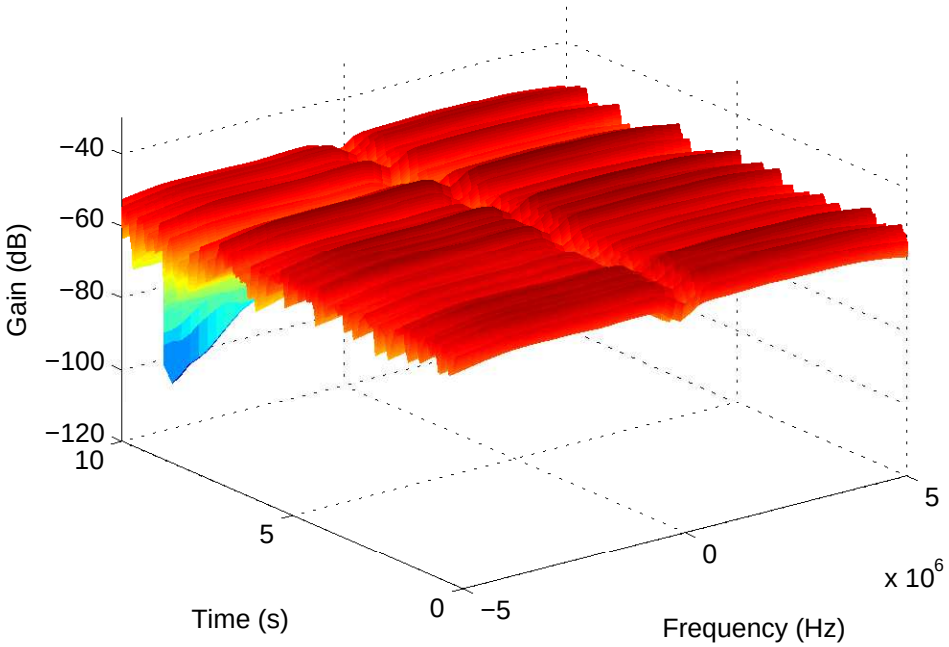

Figure 76: Right ankle to right hip, walking, 2.36 GHz

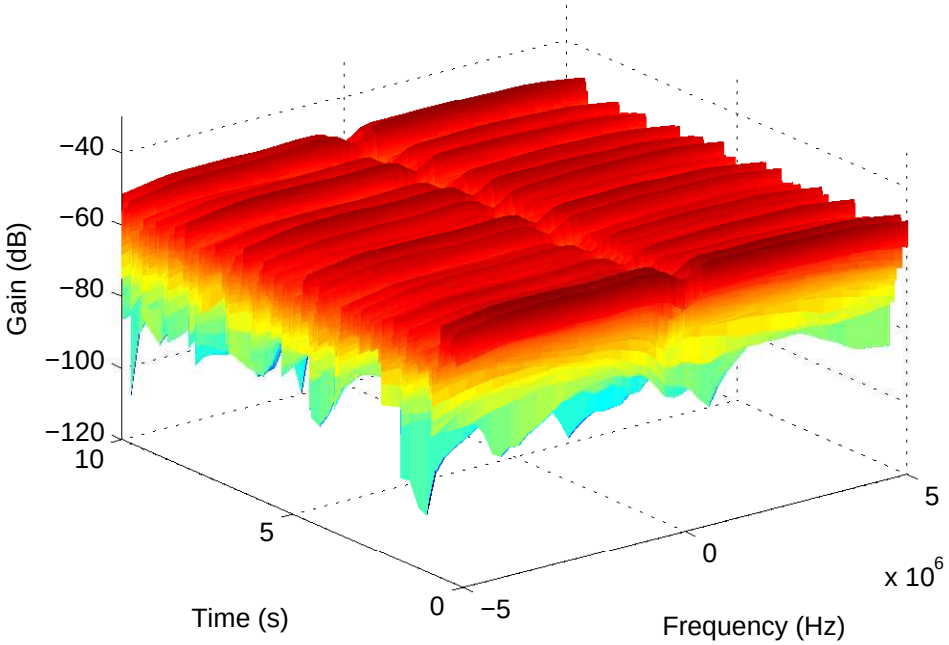

Figure 77: Right ankle to right hip, running, 2.36 GHz

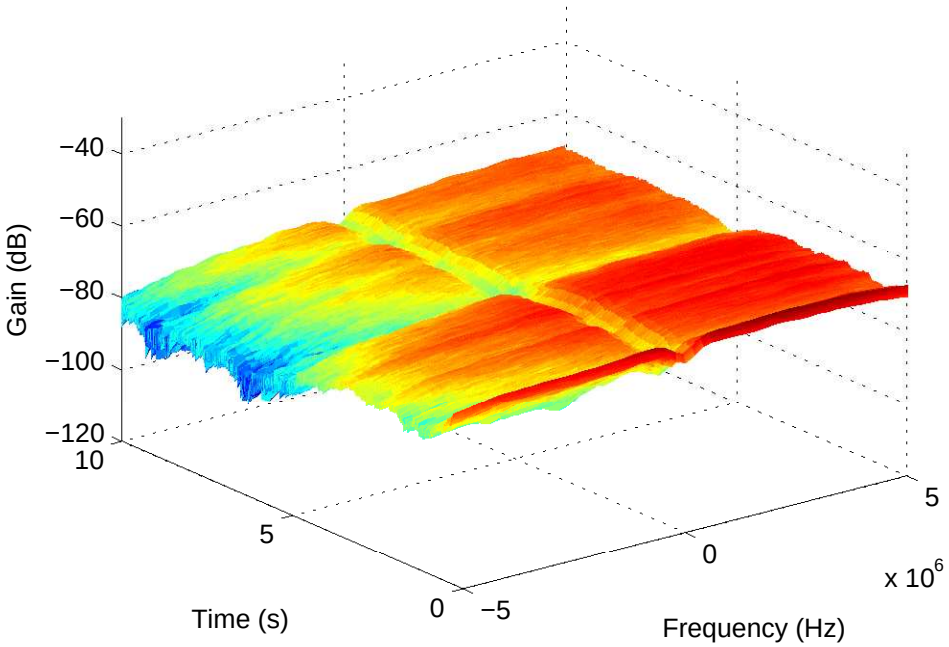

Figure 78: Left ankle to right hip, standing, 2.36 GHz

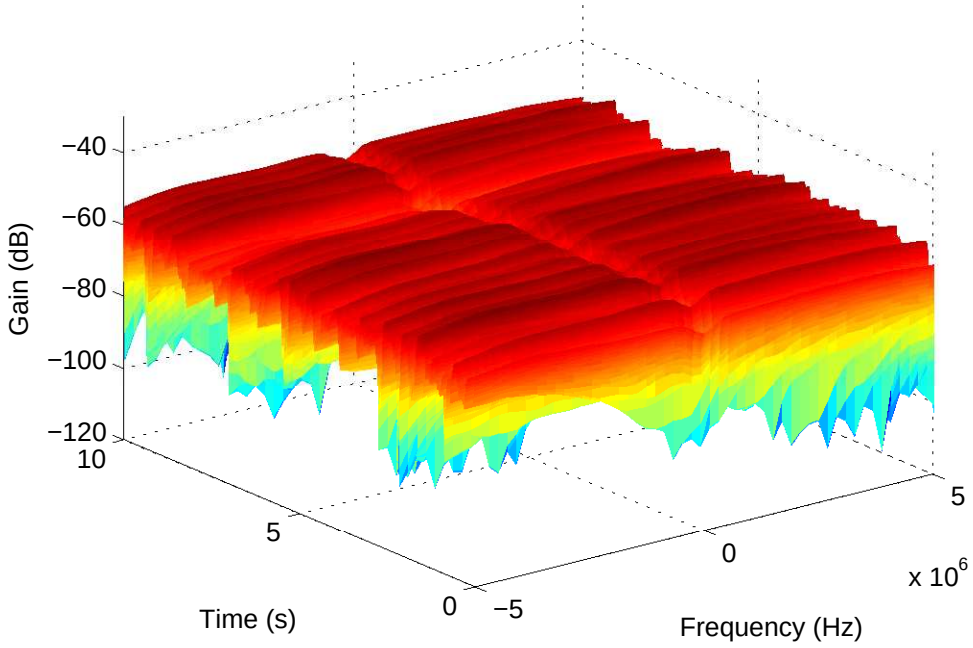

Figure 79: Left ankle to right hip, walking, 2.36 GHz

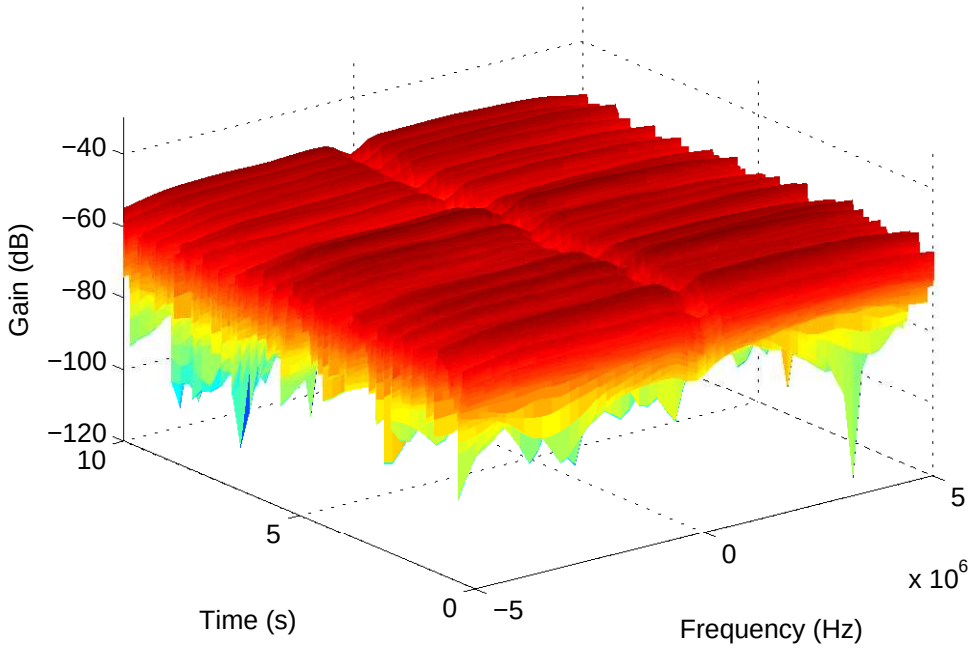

Figure 80: Left ankle to right hip, running, 2.36 GHz

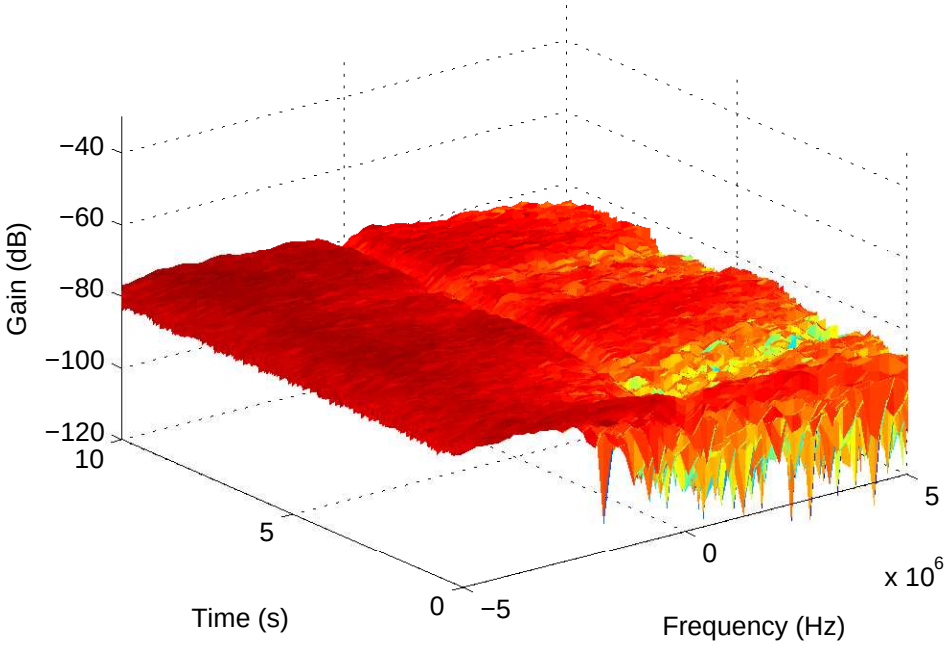

Figure 81: Back to right hip, standing, 2.36 GHz

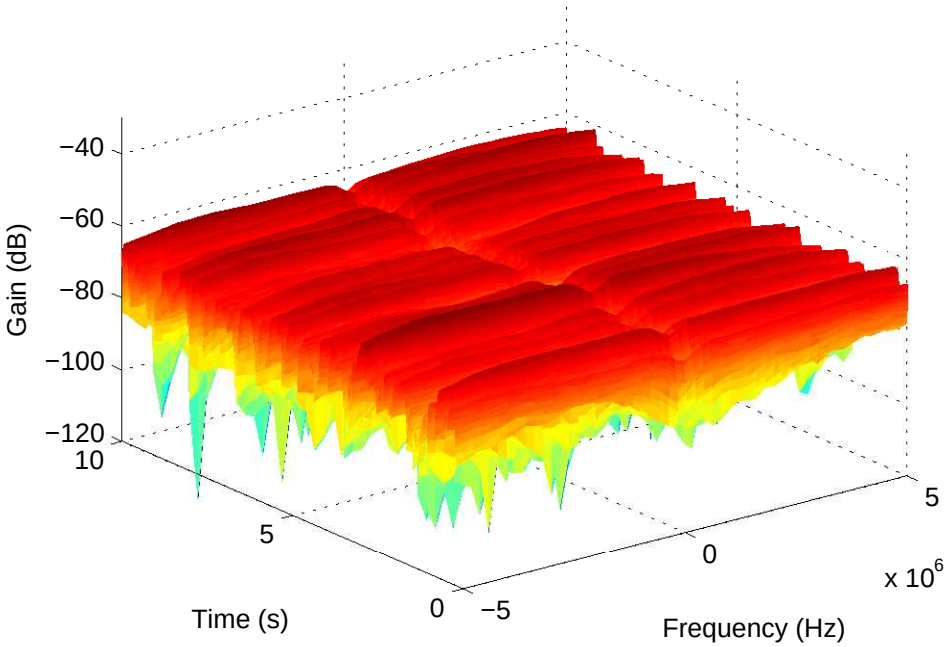

Figure 82: Back to right hip, walking, 2.36 GHz

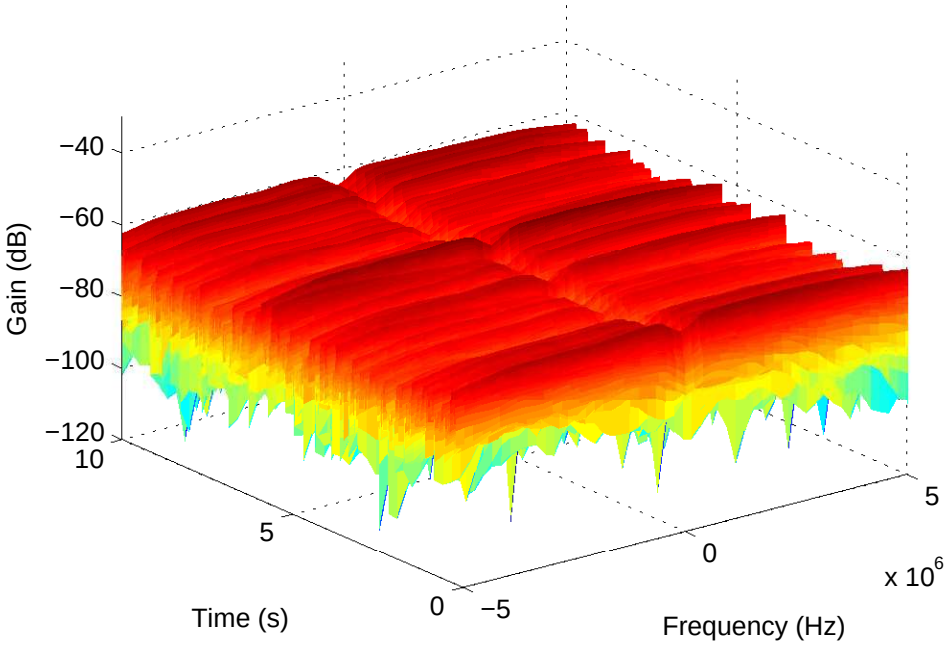

Figure 83: Back to right hip, running, 2.36 GHz

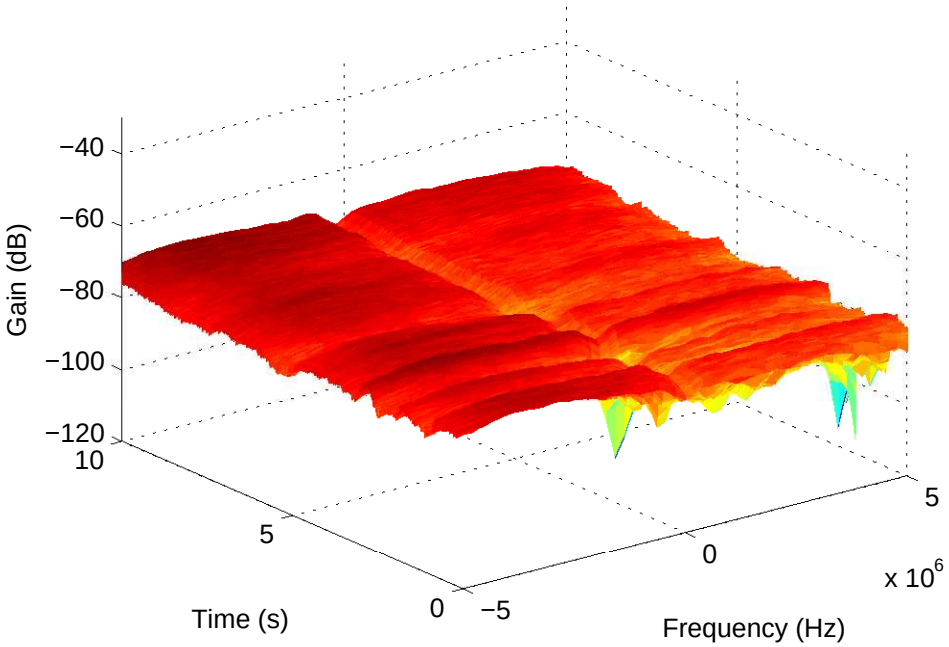

Figure 84: Back to chest, standing, 2.36 GHz

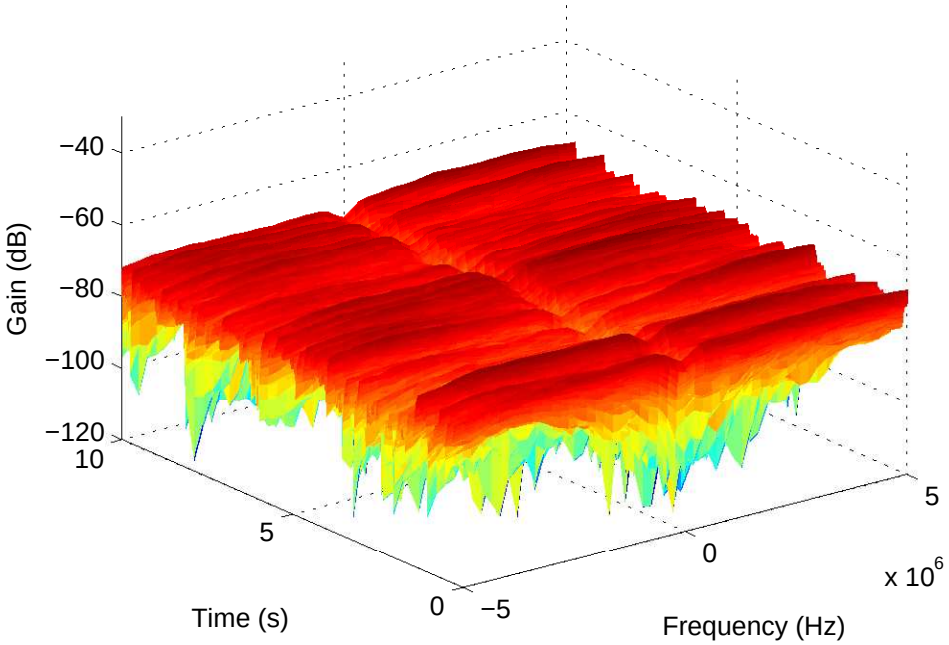

Figure 85: Back to chest, walking, 2.36 GHz

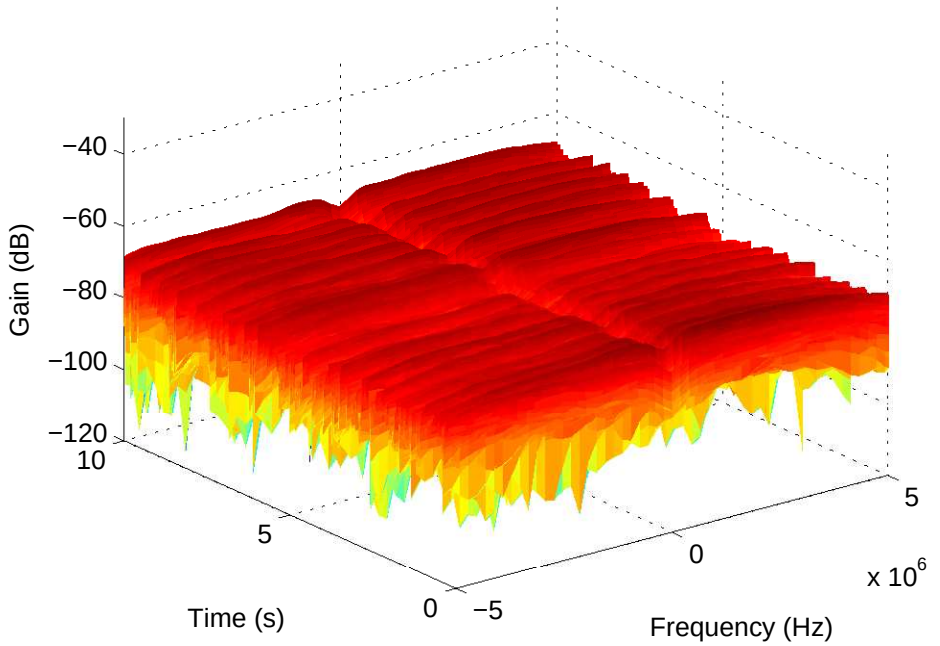

Figure 86: Back to chest, running, 2.36 GHz

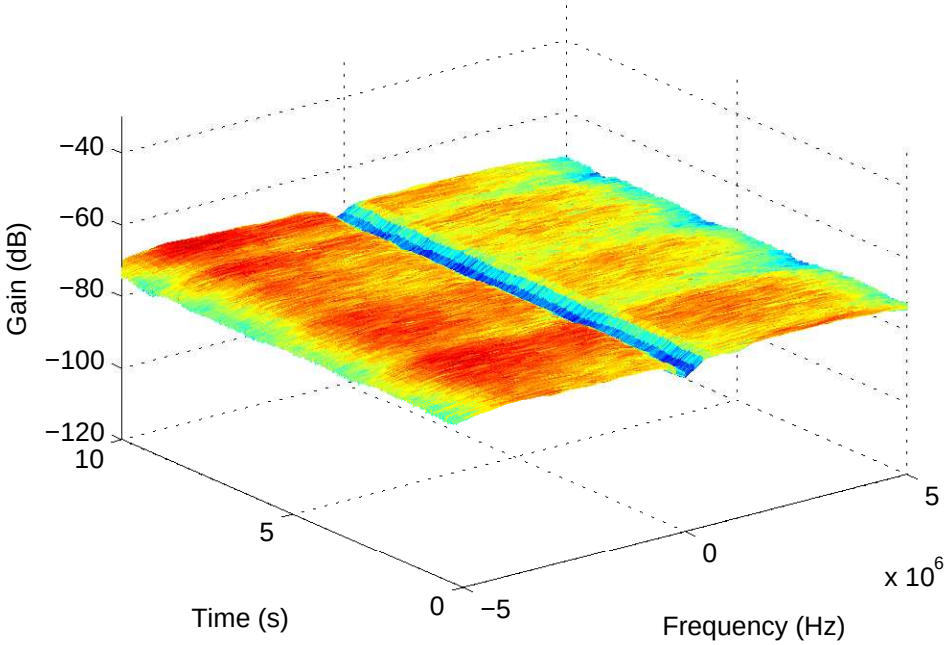

Figure 87: Right wrist to chest, standing, 2.36 GHz

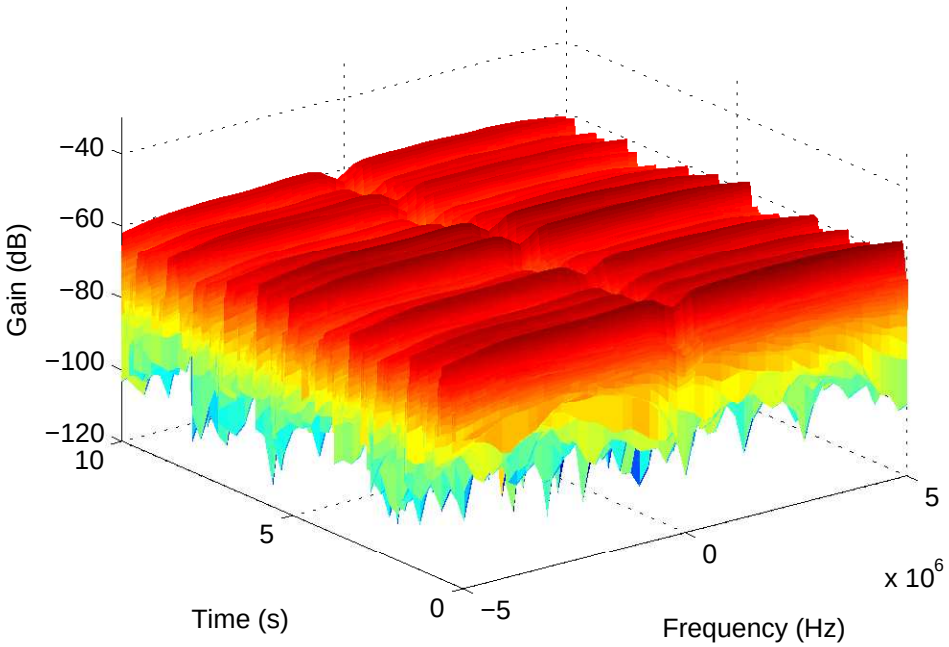

Figure 88: Right wrist to chest, walking, 2.36 GHz

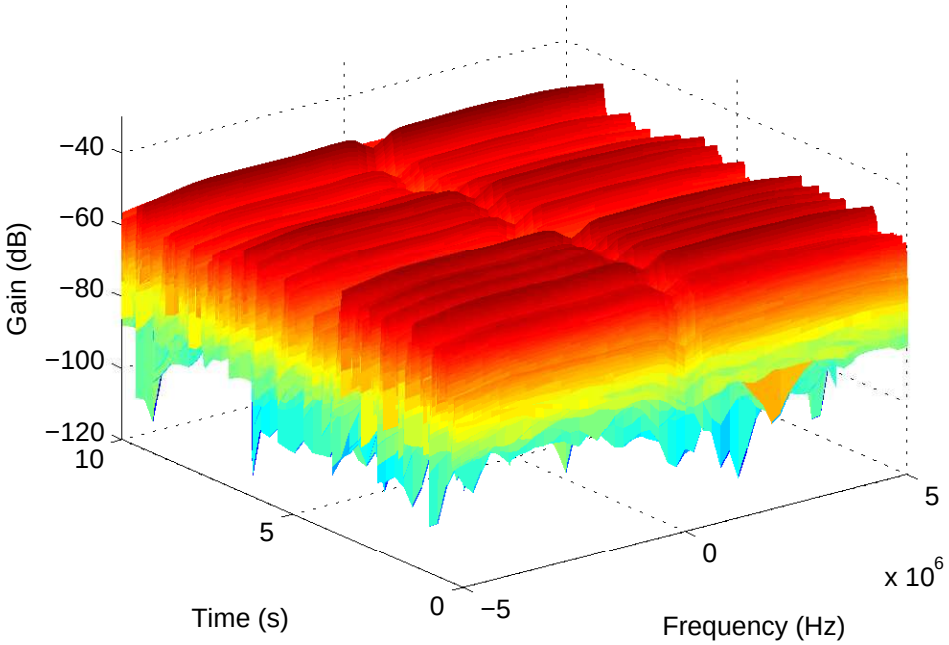

Figure 89: Right wrist to chest, running, 2.36 GHz

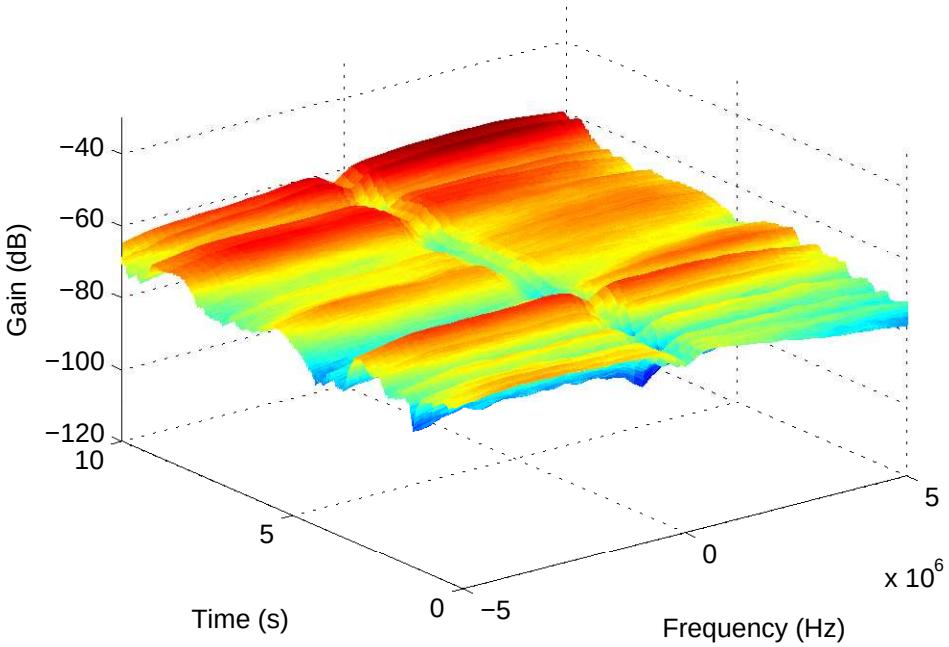

Figure 90: Right ankle to chest, standing, 2.36 GHz

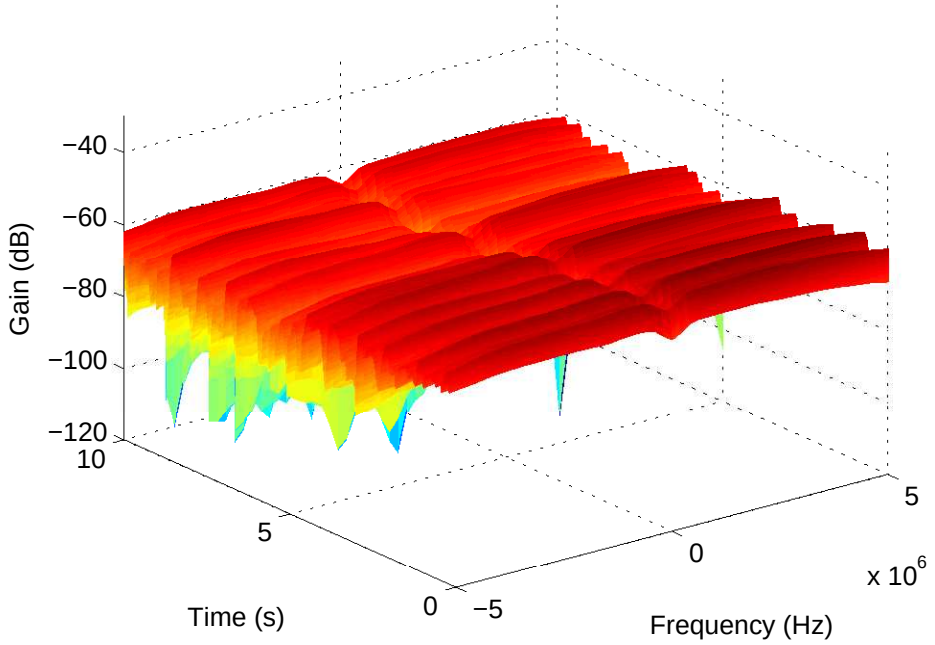

Figure 91: Right ankle to chest, walking, 2.36 GHz

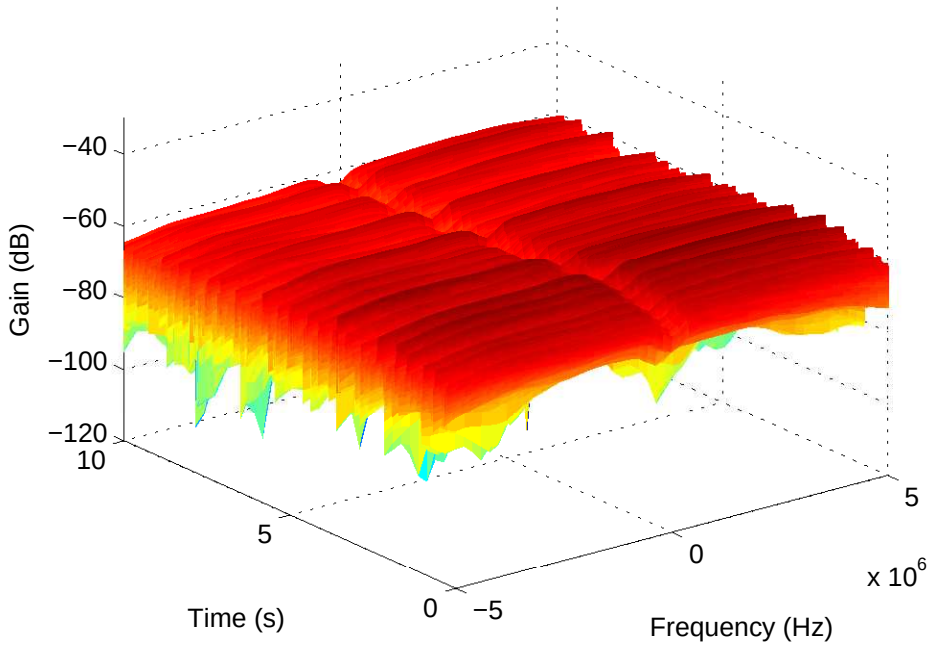

Figure 92: Right ankle to chest, running, 2.36 GHz

A.2 Path Loss Characterization

A.2.1 820 MHz measurements

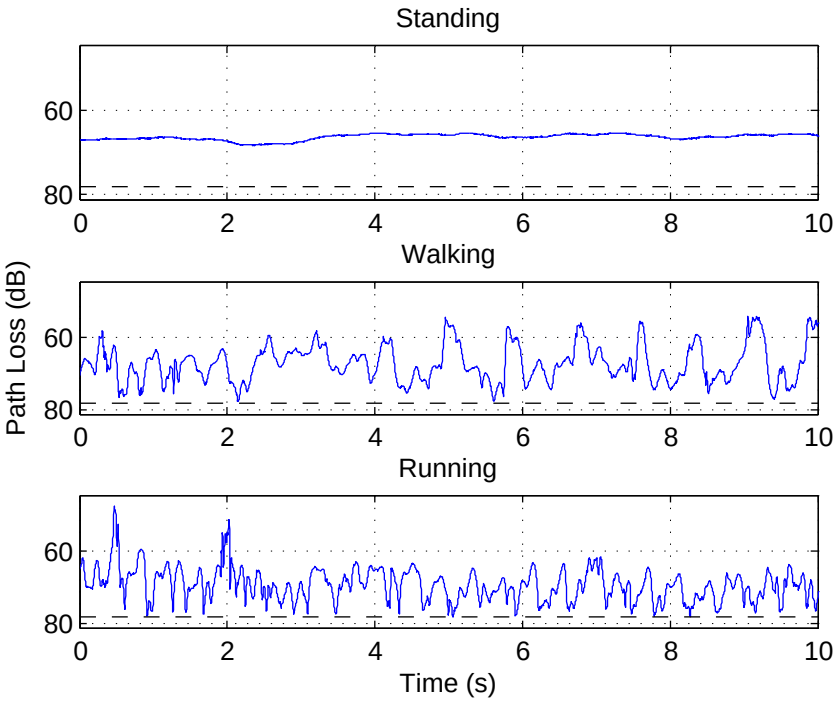

Figure 93: Path Loss measurements over time: Back to Chest, 820 MHz

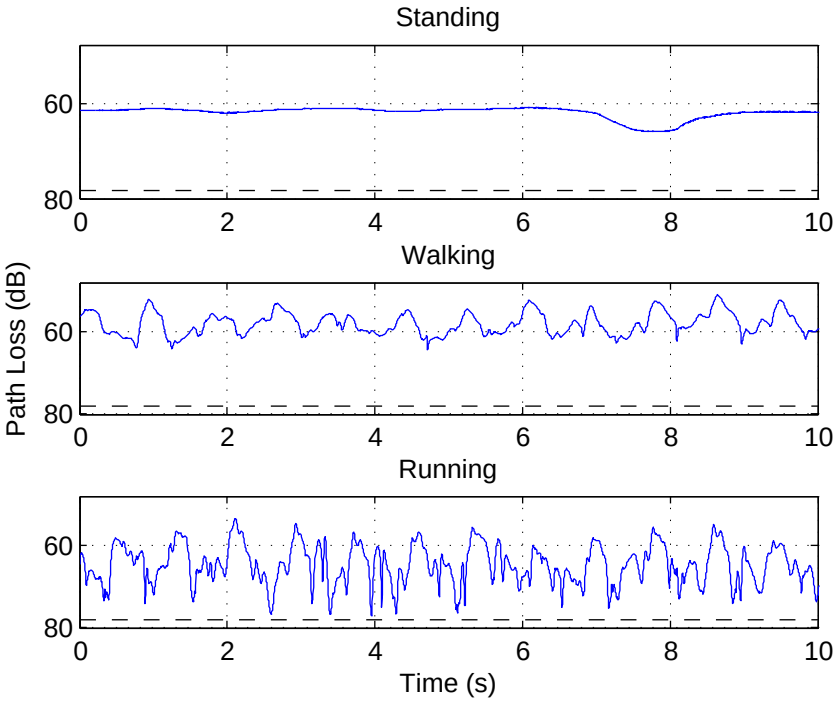

Figure 94: Path Loss measurements over time: Back to Right Hip, 820 MHz

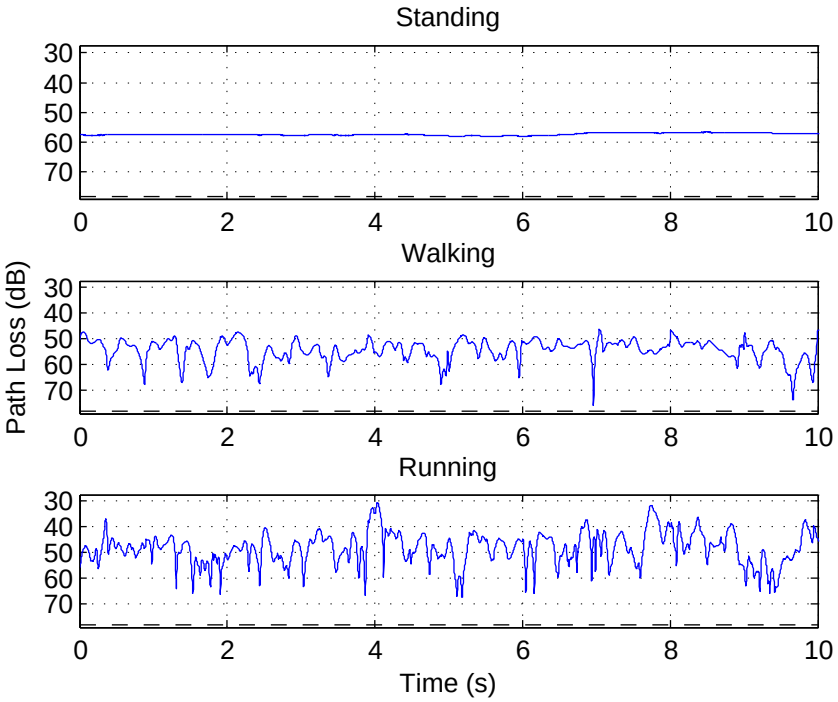

Figure 95: Path Loss measurements over time: Chest to Right Hip, 820 MHz

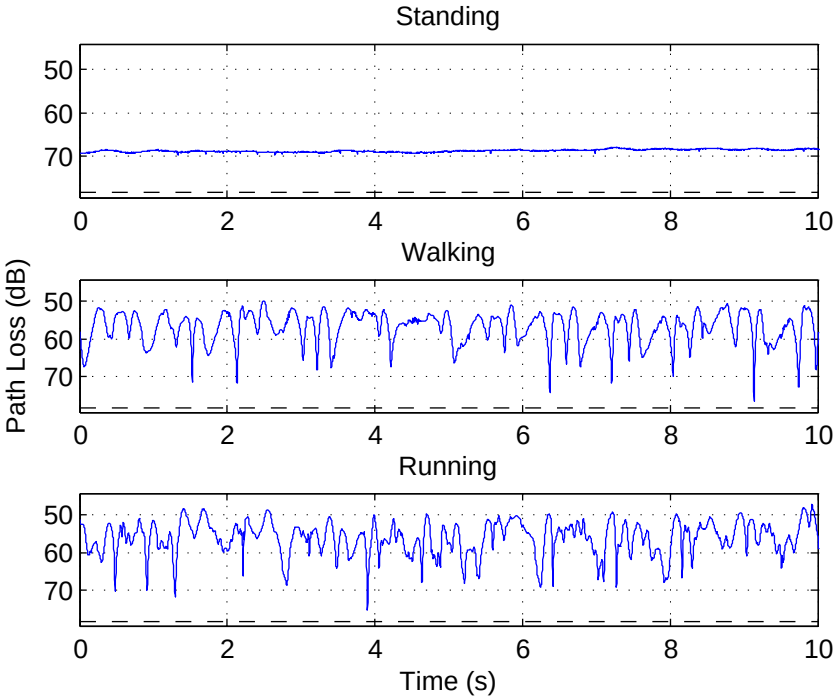

Figure 96: Path Loss measurements over time: Left Ankle to Right Hip, 820 MHz

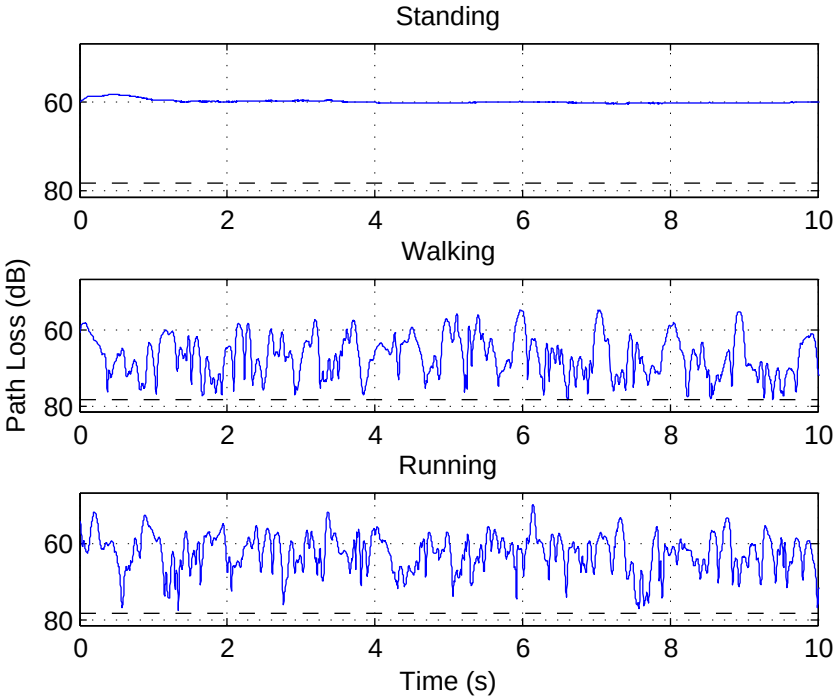

Figure 97: Path Loss measurements over time: Left Wrist to Right Hip, 820 MHz

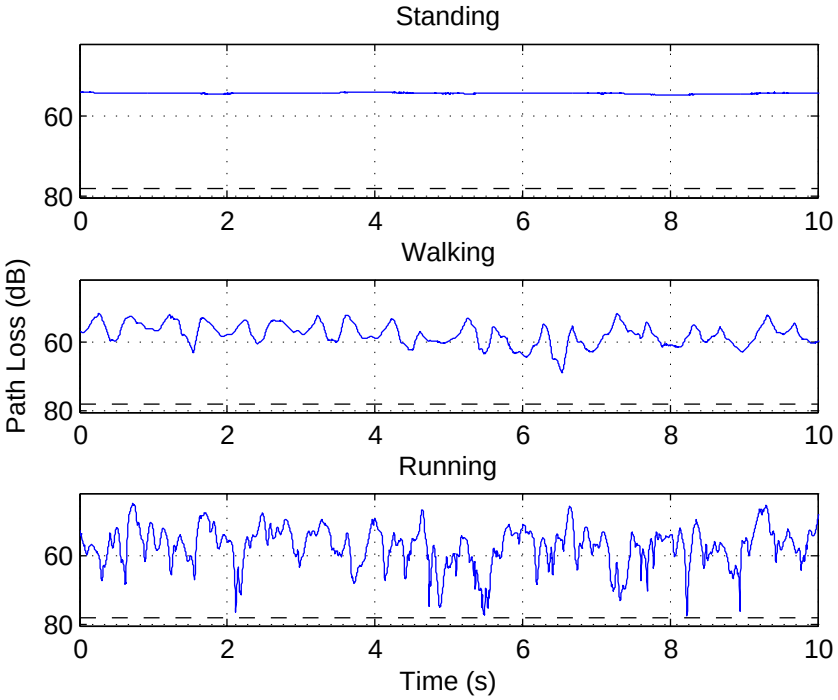

Figure 98: Path Loss measurements over time: Right Ankle to Chest, 820 MHz

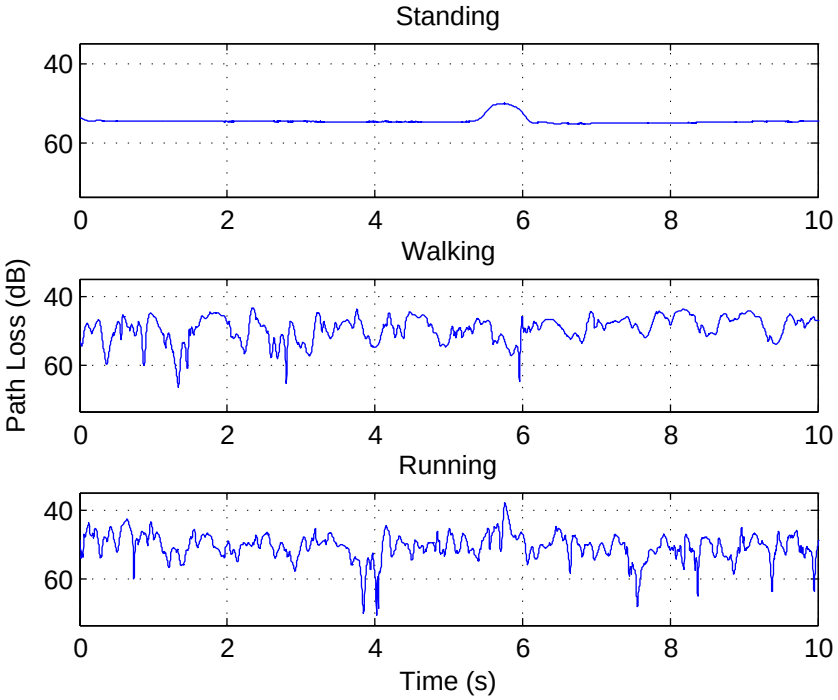

Figure 99: Path Loss measurements over time: Right Ankle to Right Hip, 820 MHz

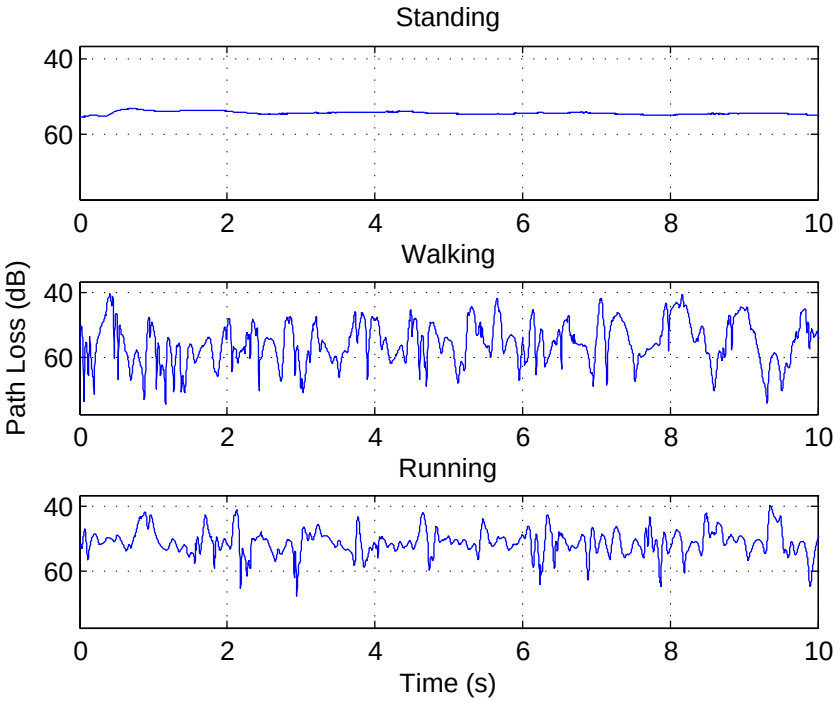

Figure 100: Path Loss measurements over time: Right Wrist to Chest, 820 MHz

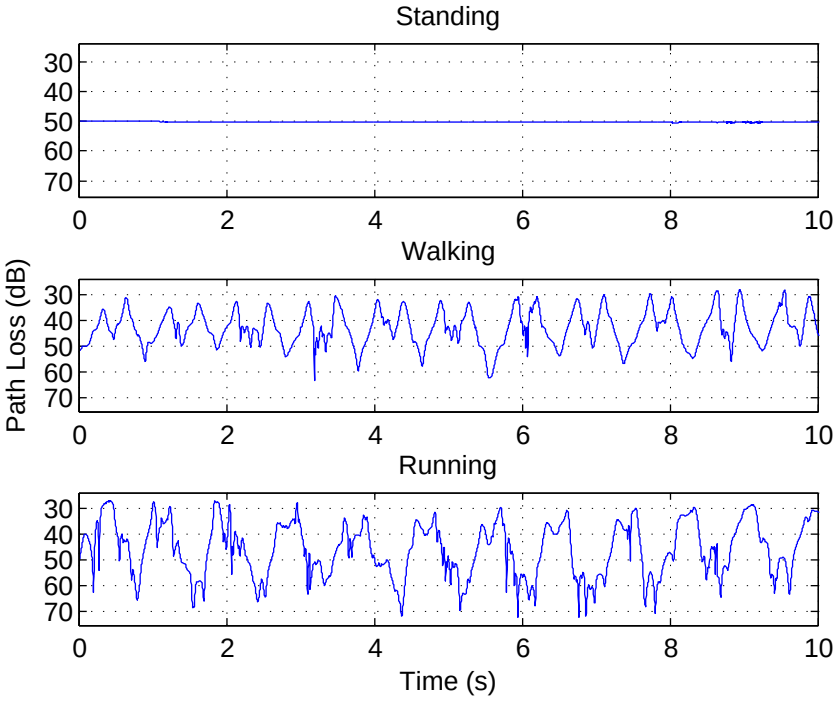

Figure 101: Path Loss measurements over time: Right Wrist to Right Hip, 820 MHz

A.2.2 2.36 GHz measurements

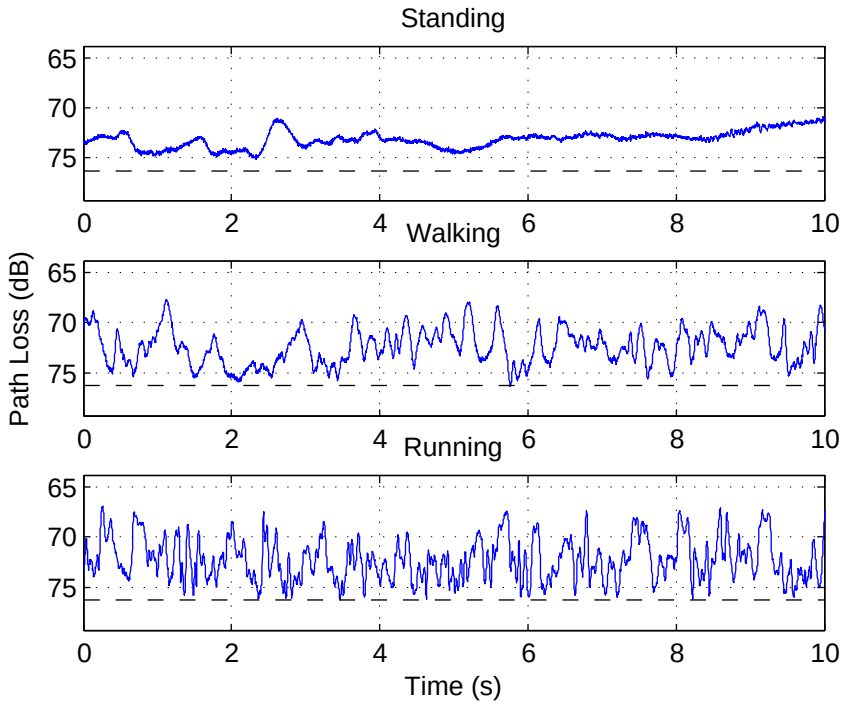

Figure 102: Path Loss measurements over time: Back to Chest, 2.36 GHz

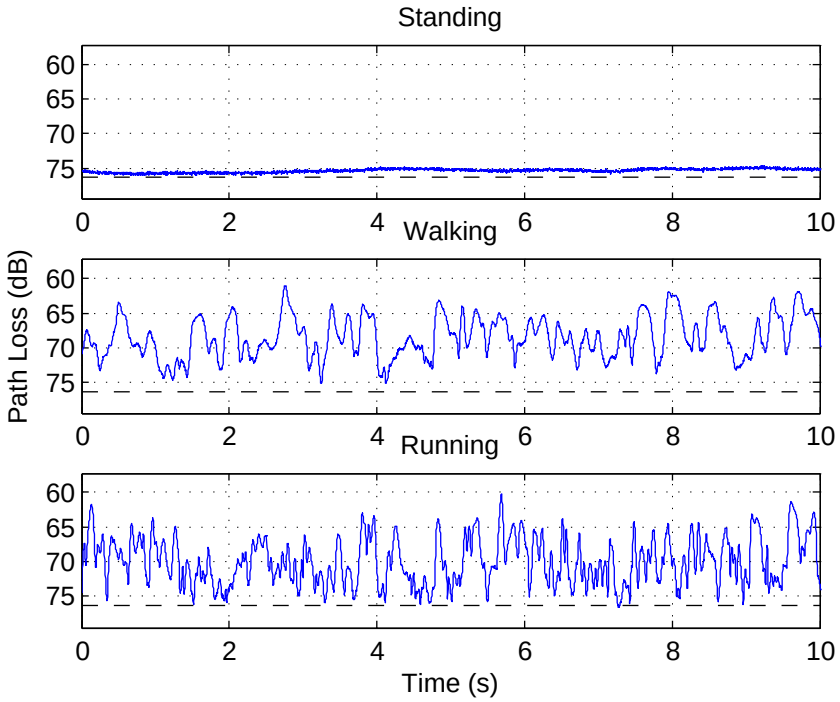

Figure 103: Path loss over time: Back to Right Hip, 2.36 GHz

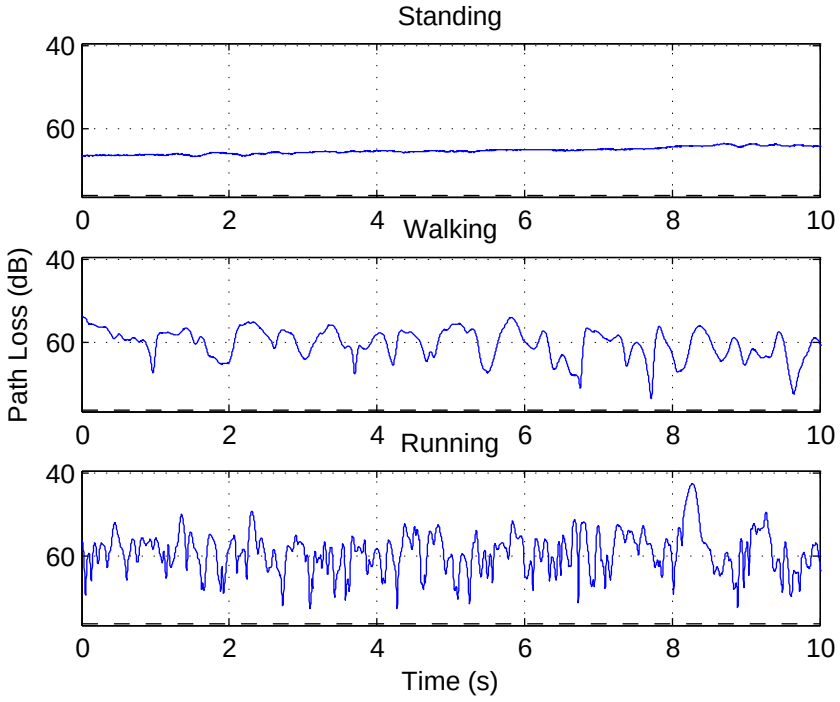

Figure 104: Path loss over time: Chest to Right Hip, 2.36 GHz

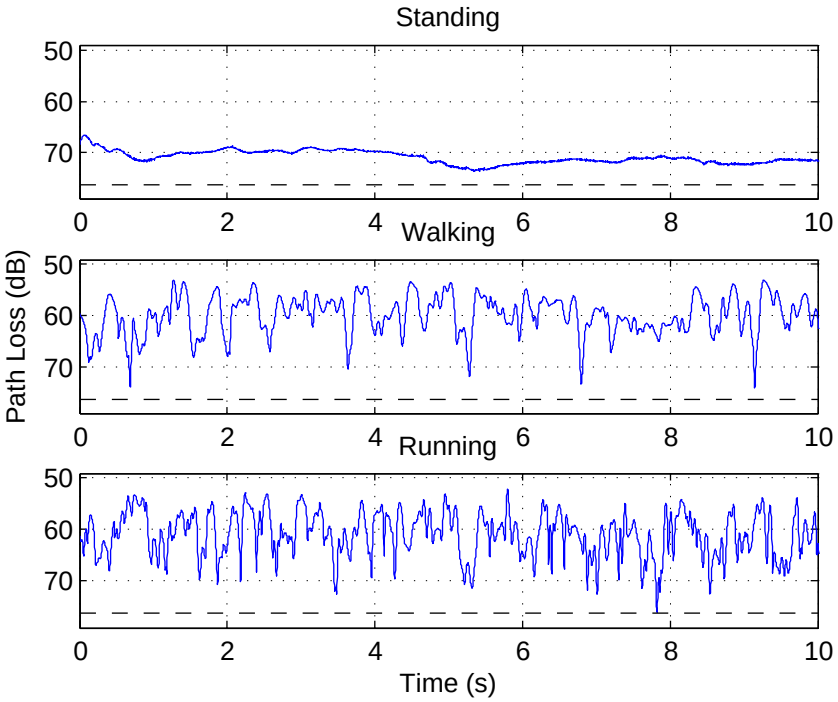

Figure 105: Path loss over time: Left Ankle to Right Hip, 2.36 GHz

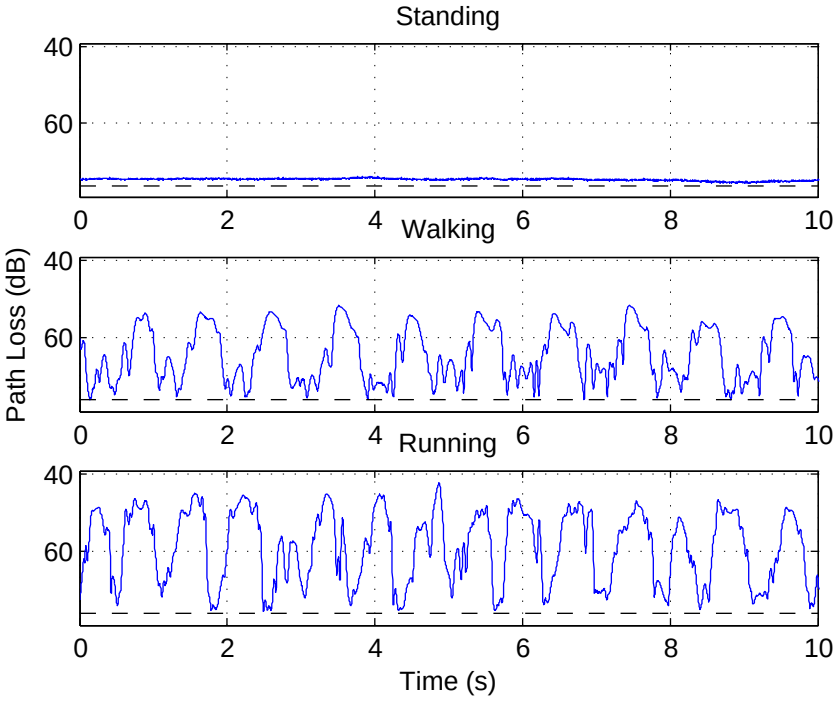

Figure 106: Path loss over time: Left Wrist to Right Hip, 2.36 GHz

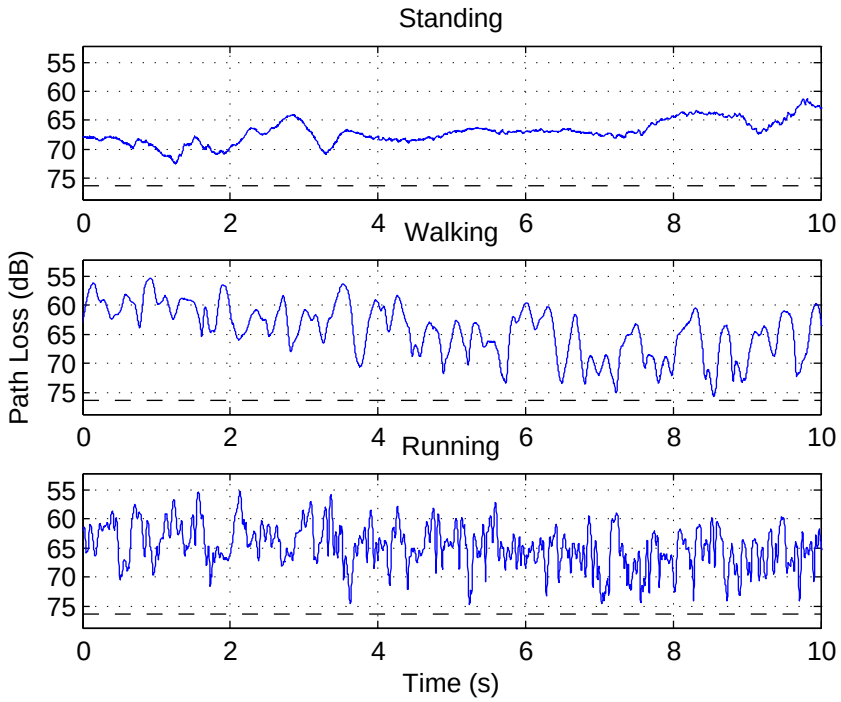

Figure 107: Path loss over time: Right Ankle to Chest, 2.36 GHz

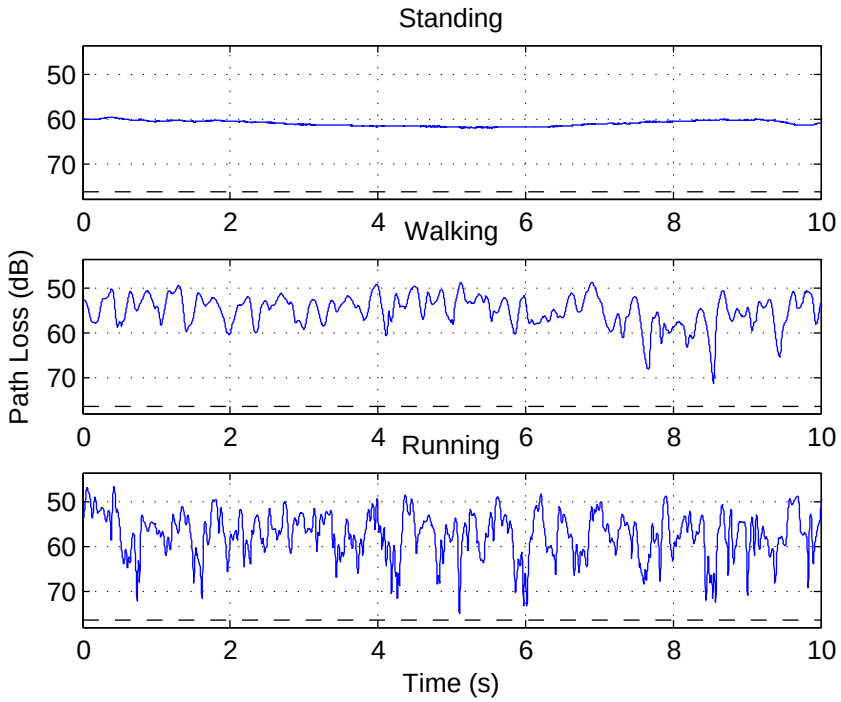

Figure 108: Path loss over time: Right Ankle to Right Hip, 2.36 GHz

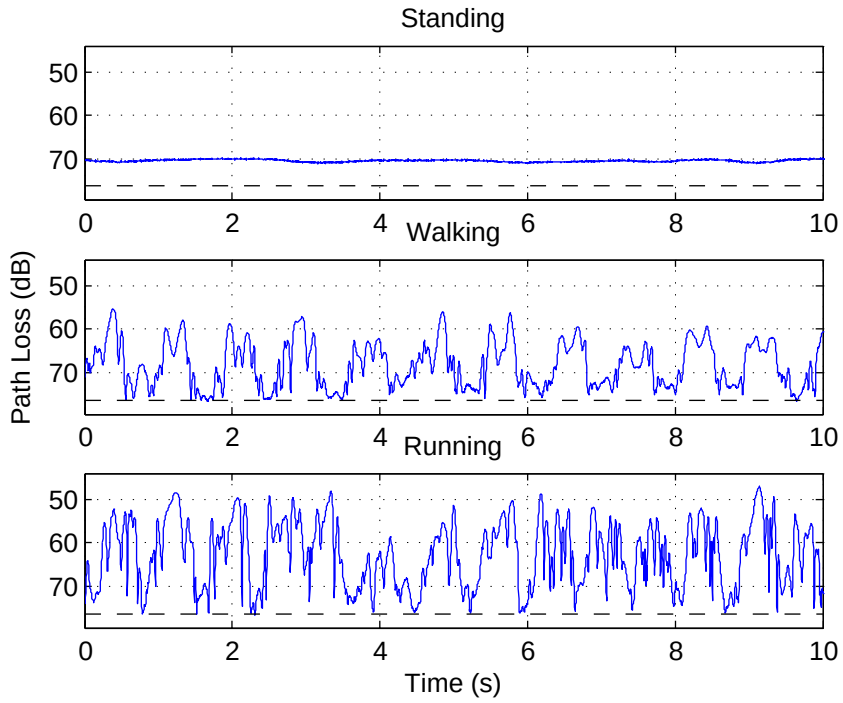

Figure 109: Path loss over time: Right Wrist to Chest, 2.36 GHz

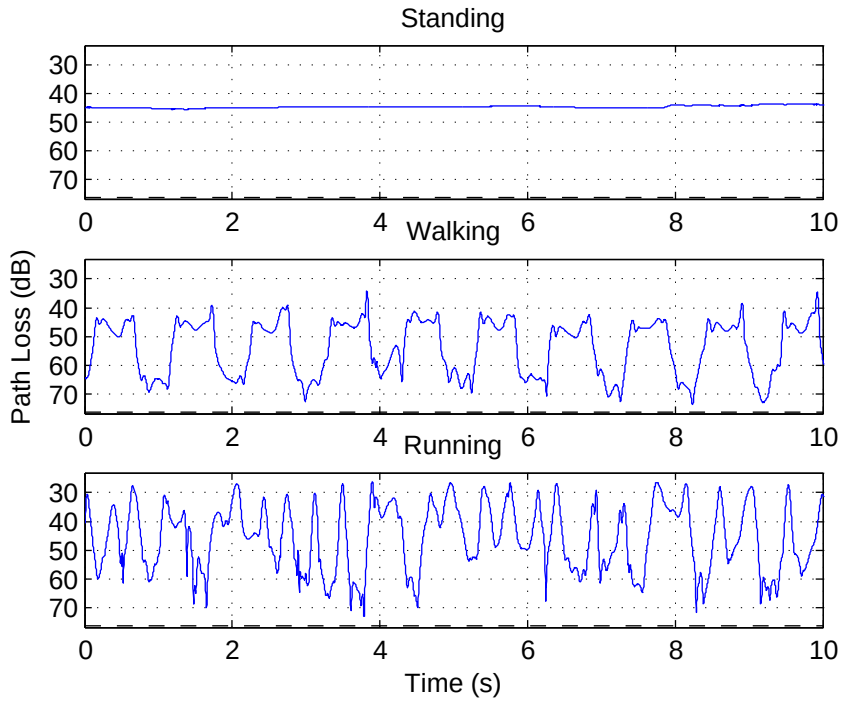

Figure 110: Path loss over time: Right Wrist to Right Hip, 2.36 GHz

A.3 Statistical Description of Received Power

The "Freedman-Diaconis" rule used to select the bin size, B_s, for the histogram that describes the empirical PDF from the measured data is defined as

$$B_s = 2I_r(x)n^{-1/3} \tag{9}$$

where I_r is the inter-quartile range of the data sample x (in this case measured normalized received power) and n is the sample size of x.

A.3.1 PDFs at 2.36 GHz

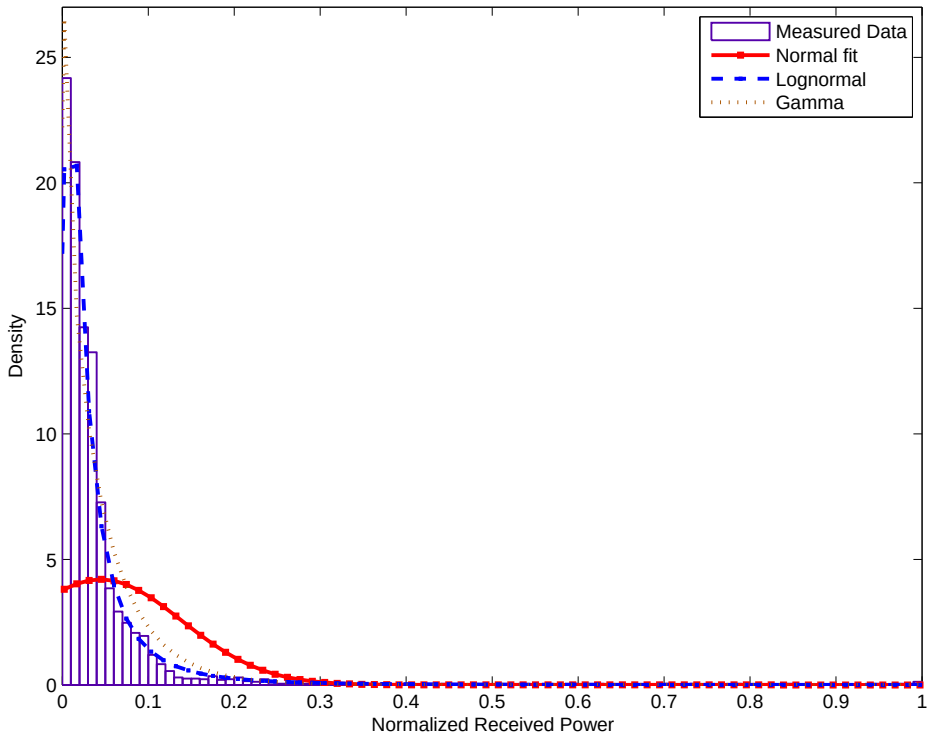

Figure 111: PDF Chest to right hip, running at 2.36 GHz

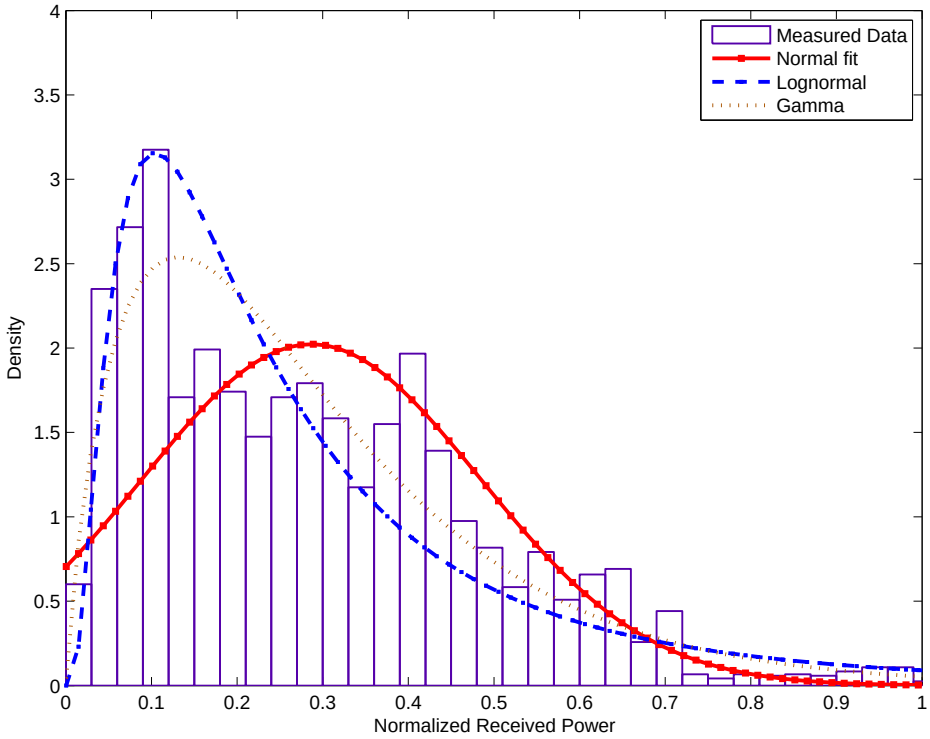

Figure 112: PDF Chest to right hip, walking at 2.36 GHz

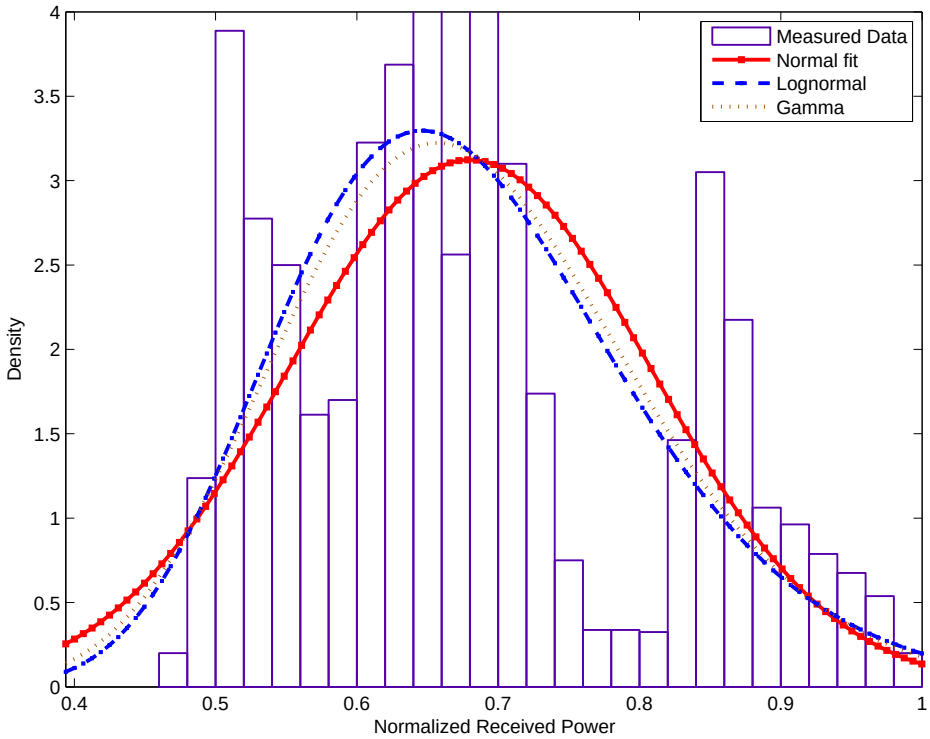

Figure 113: PDF Chest to right hip, standing at 2.36 GHz

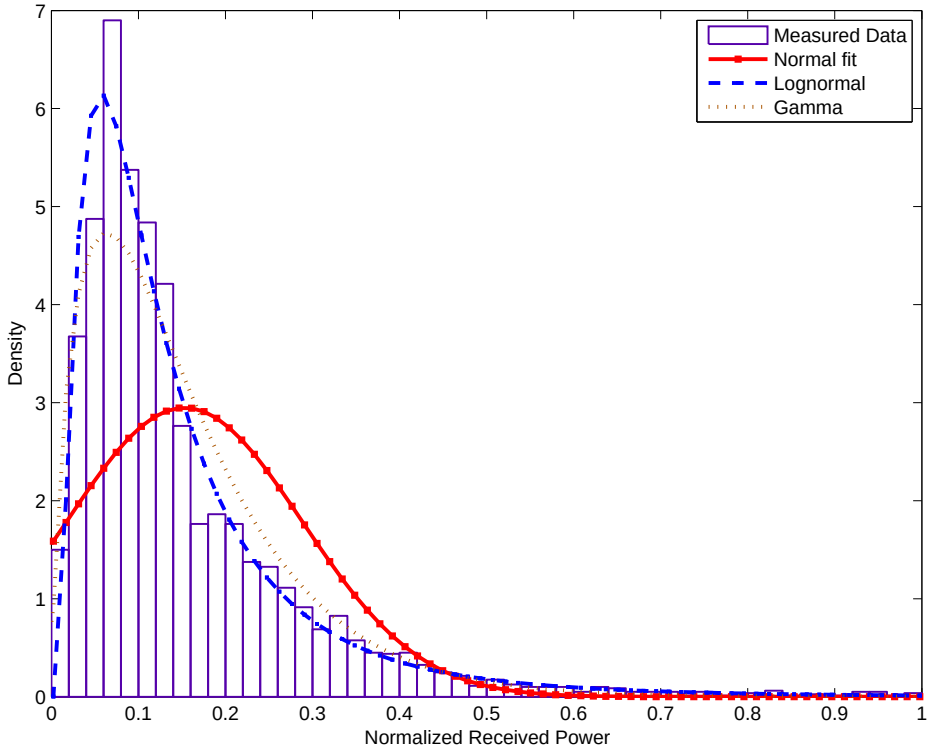

Figure 114: PDF Right ankle to chest, running at 2.36 GHz

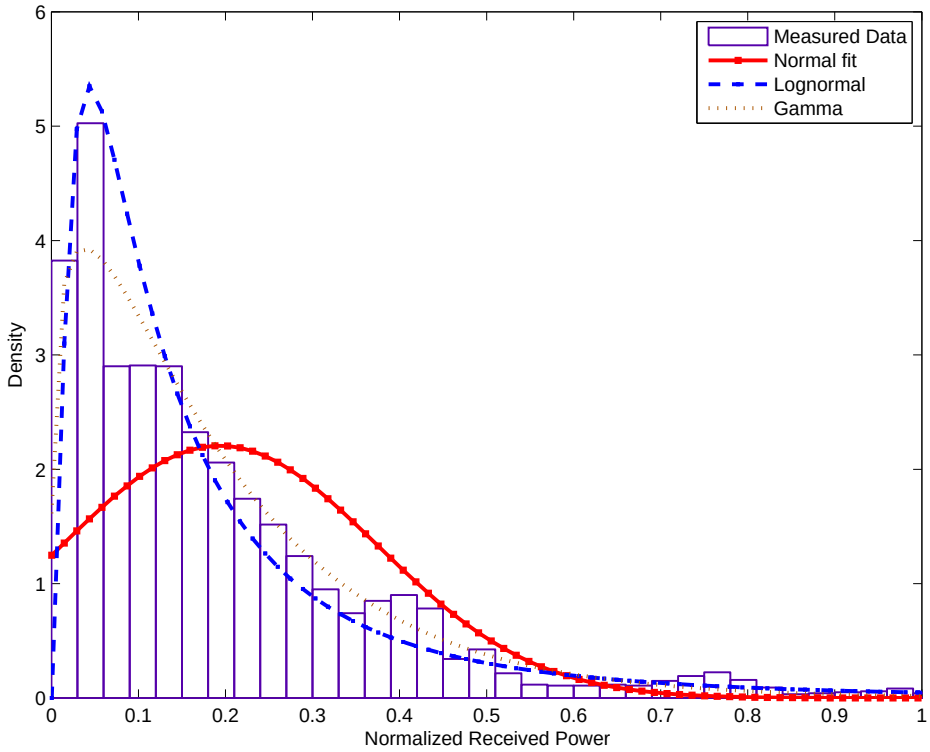

Figure 115: PDF Right ankle to chest, walking at 2.36 GHz

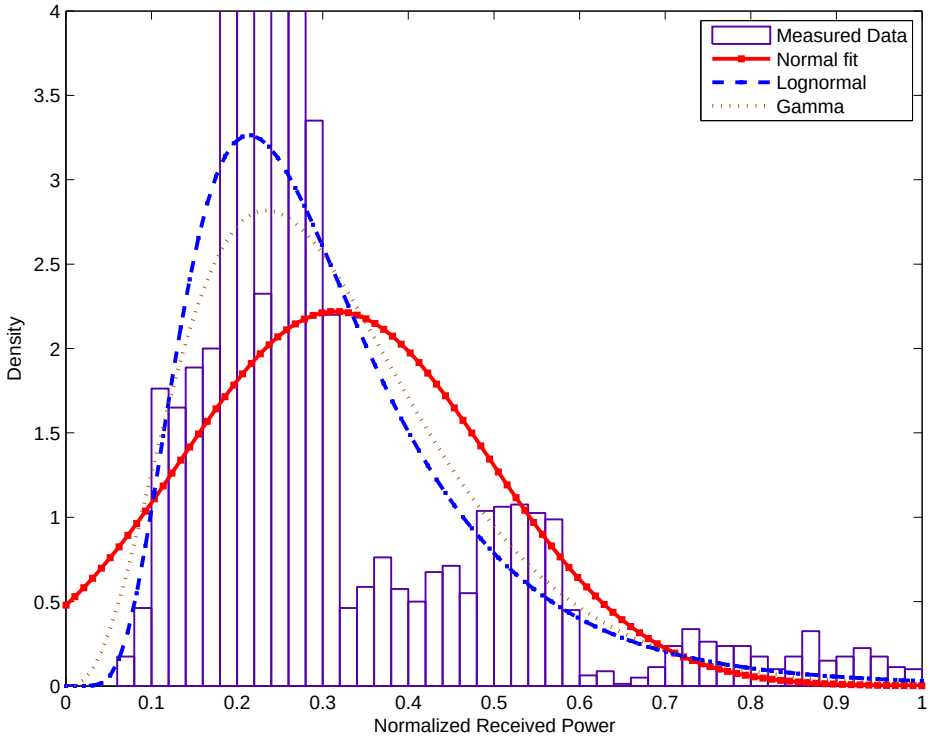

Figure 116: Right ankle to chest, standing at 2.36 GHz

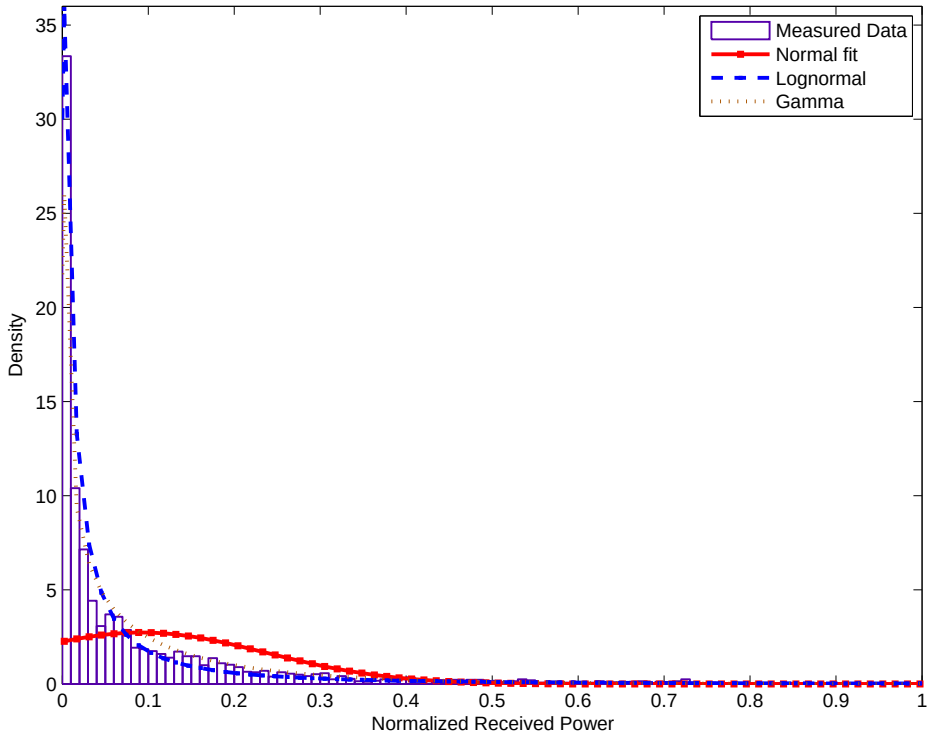

Figure 117: PDF Right wrist to chest, running at 2.36 GHz

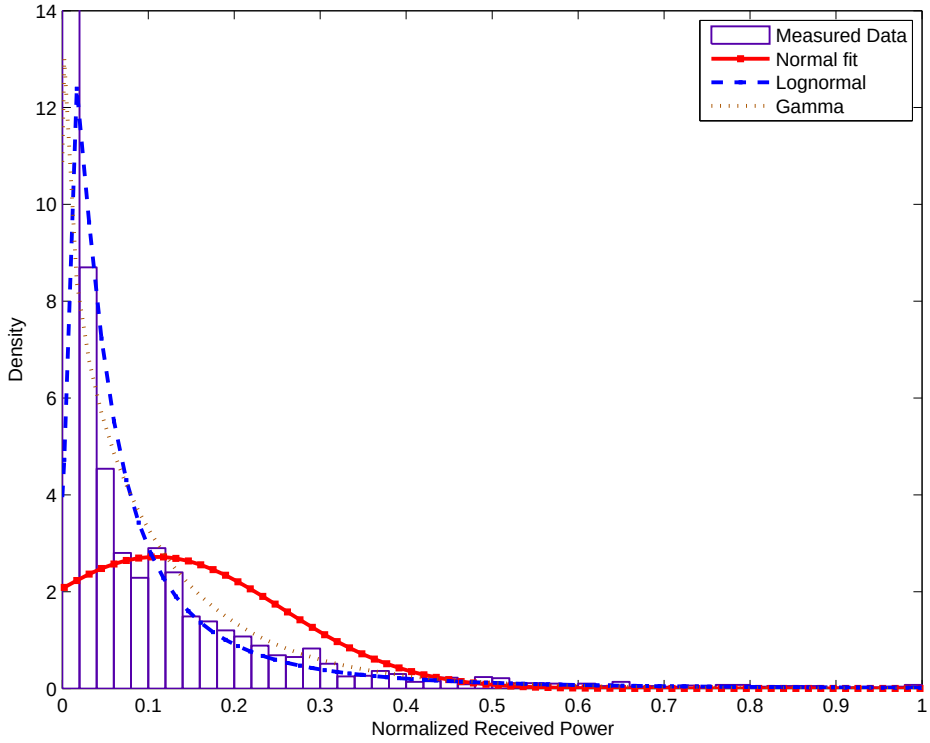

Figure 118: PDF Right wrist to chest, walking at 2.36 GHz

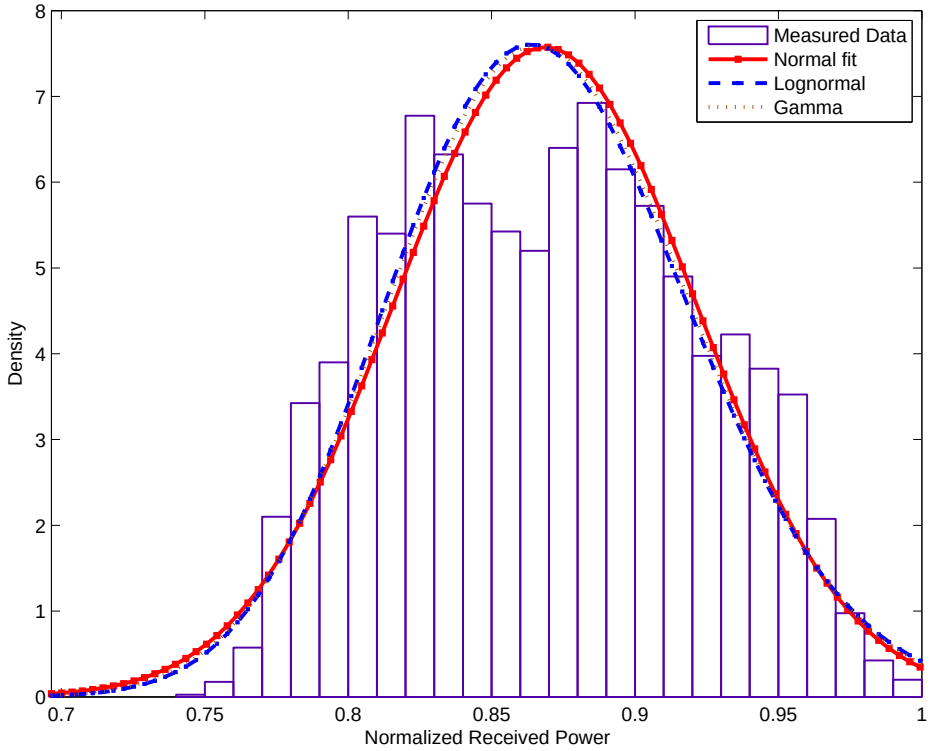

Figure 119: Right wrist to chest, standing at 2.36 GHz

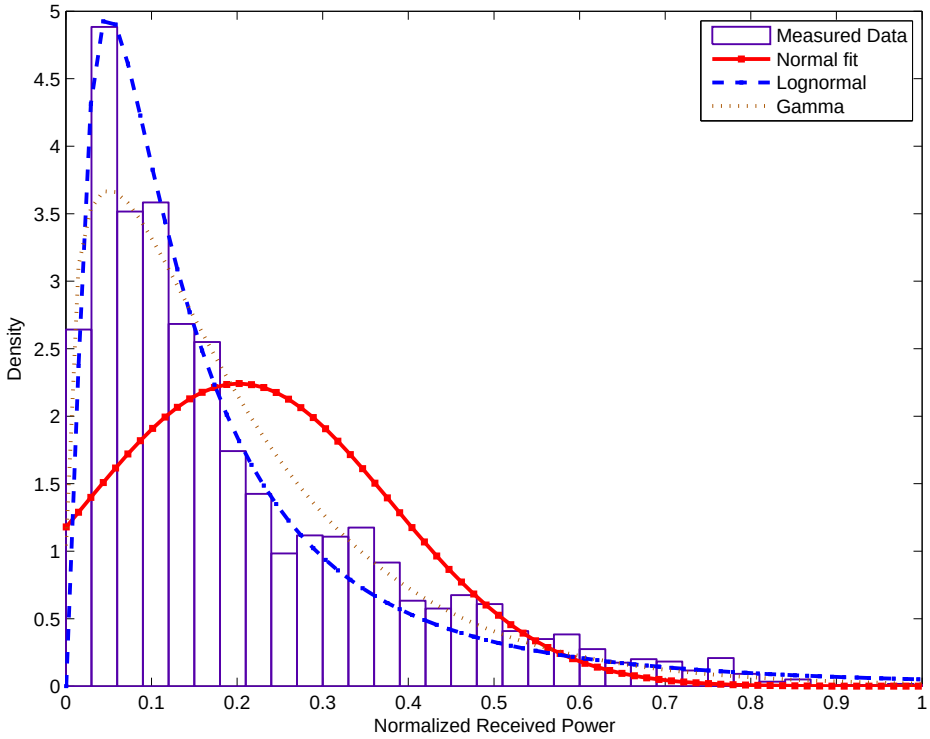

Figure 120: PDF Left ankle to right hip, running at 2.36 GHz

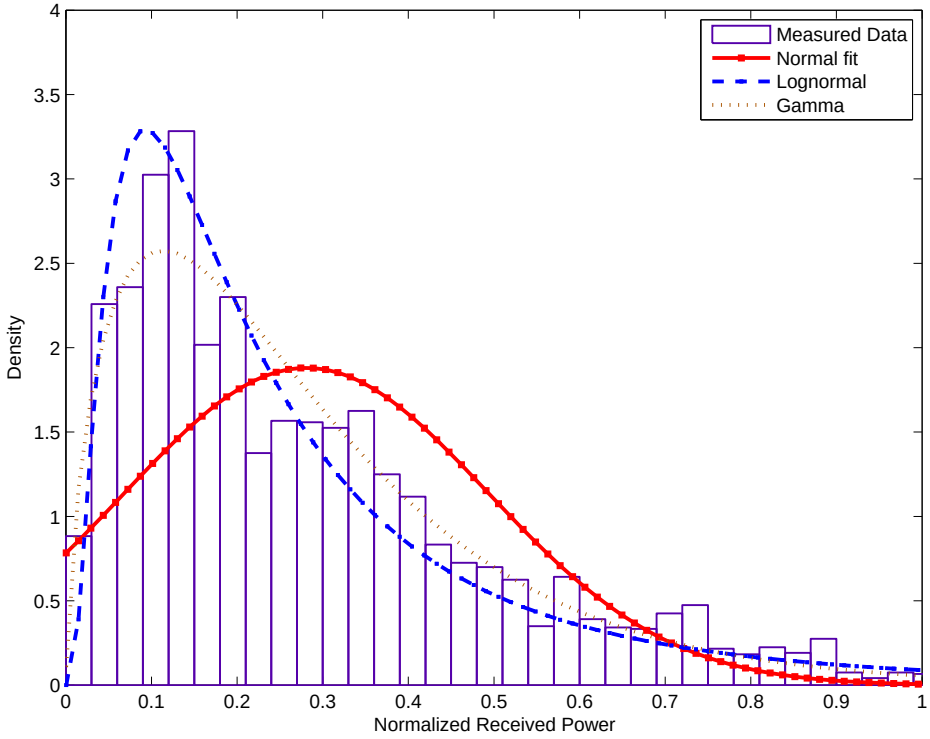

Figure 121: PDF Left ankle to right hip, walking at 2.36 GHz

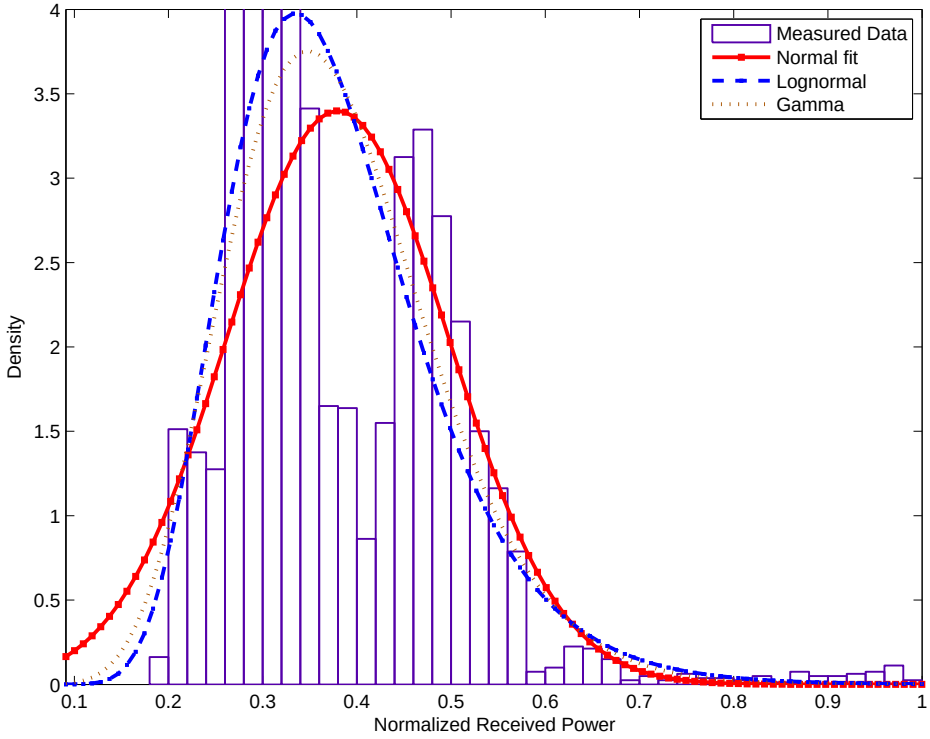

Figure 122: PDF Left ankle to right hip, standing at 2.36 GHz

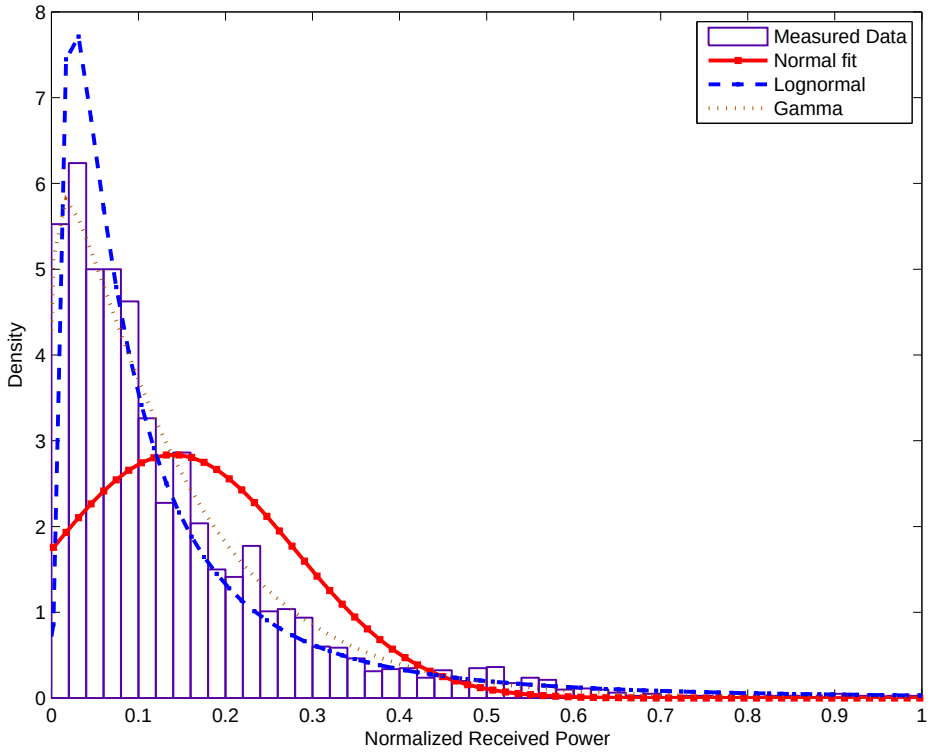

Figure 123: PDF Right ankle to right hip, running at 2.36 GHz

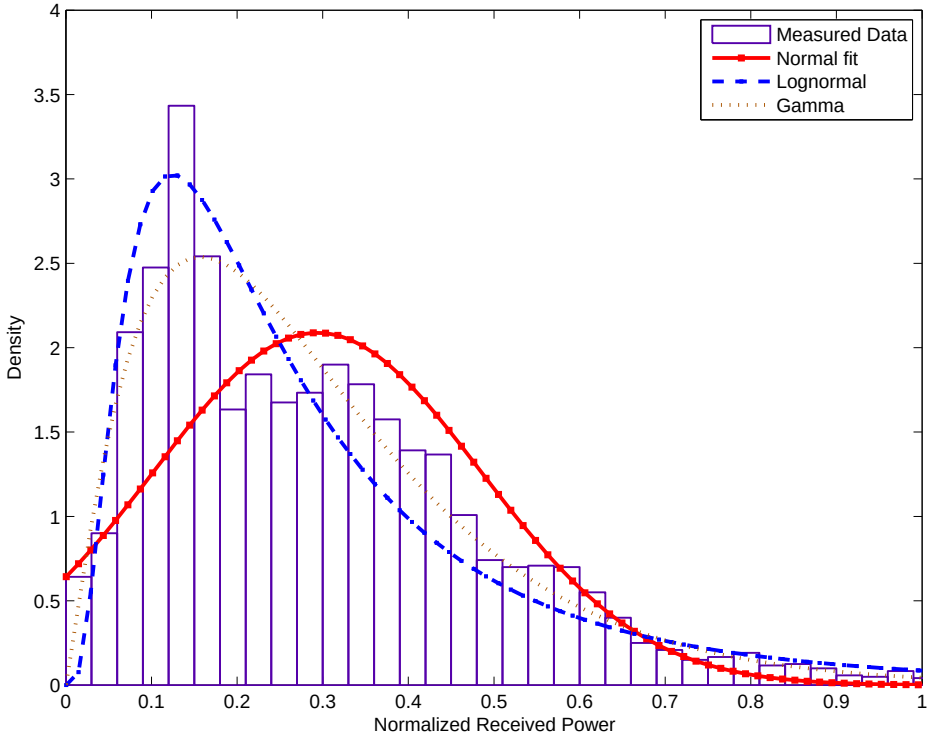

Figure 124: PDF Right ankle to right hip, walking at 2.36 GHz

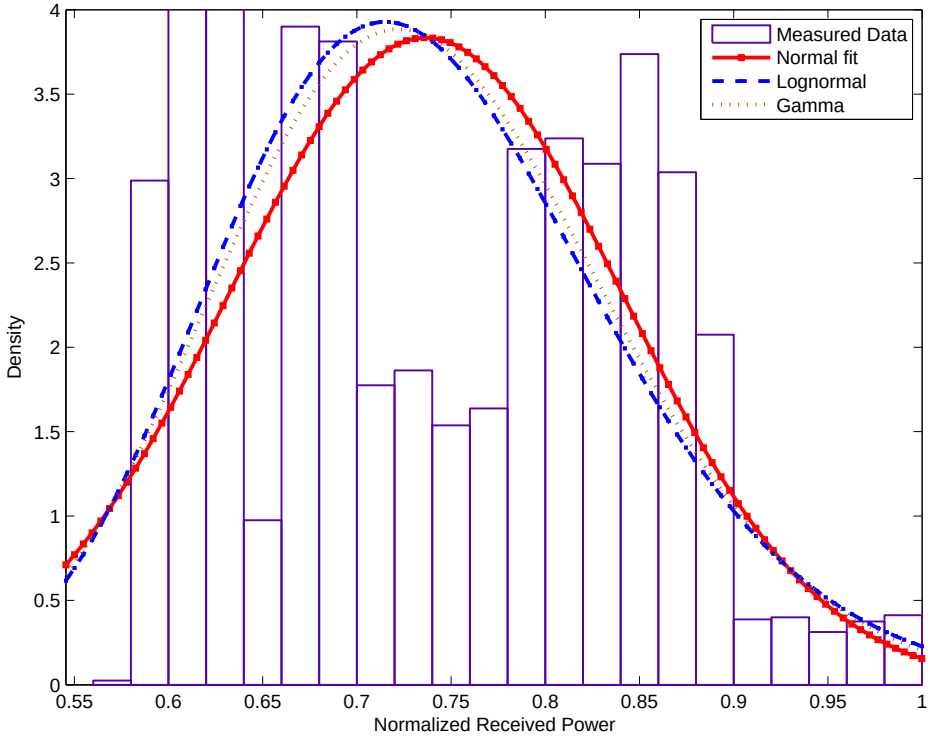

Figure 125: PDF Right ankle to right hip, standing at 2.36 GHz

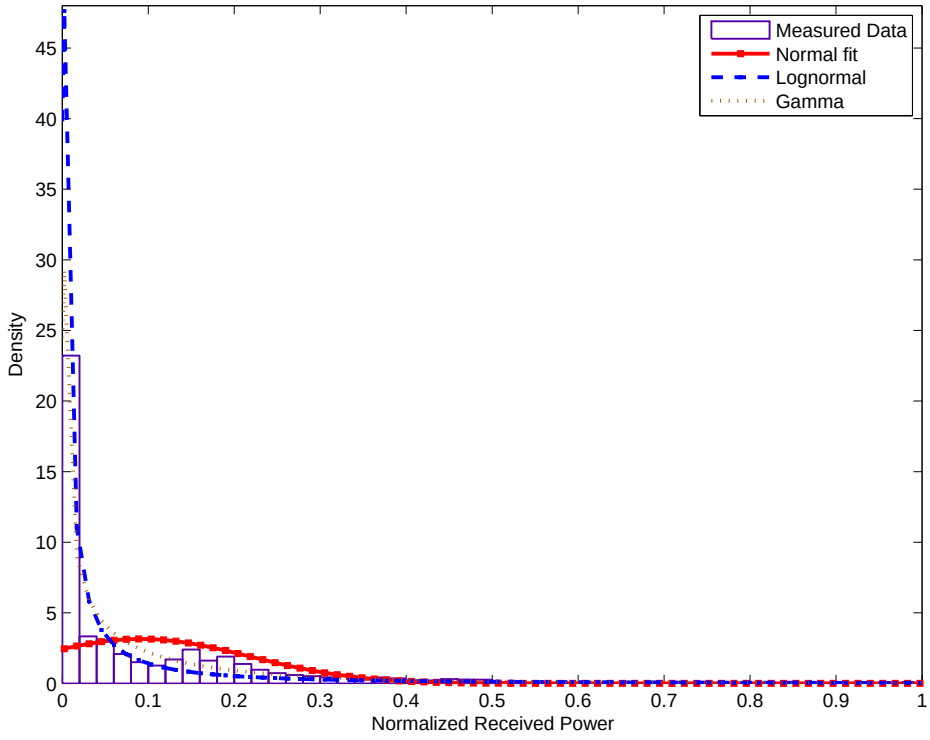

Figure 126: PDF Left wrist to right hip, running at 2.36 GHz

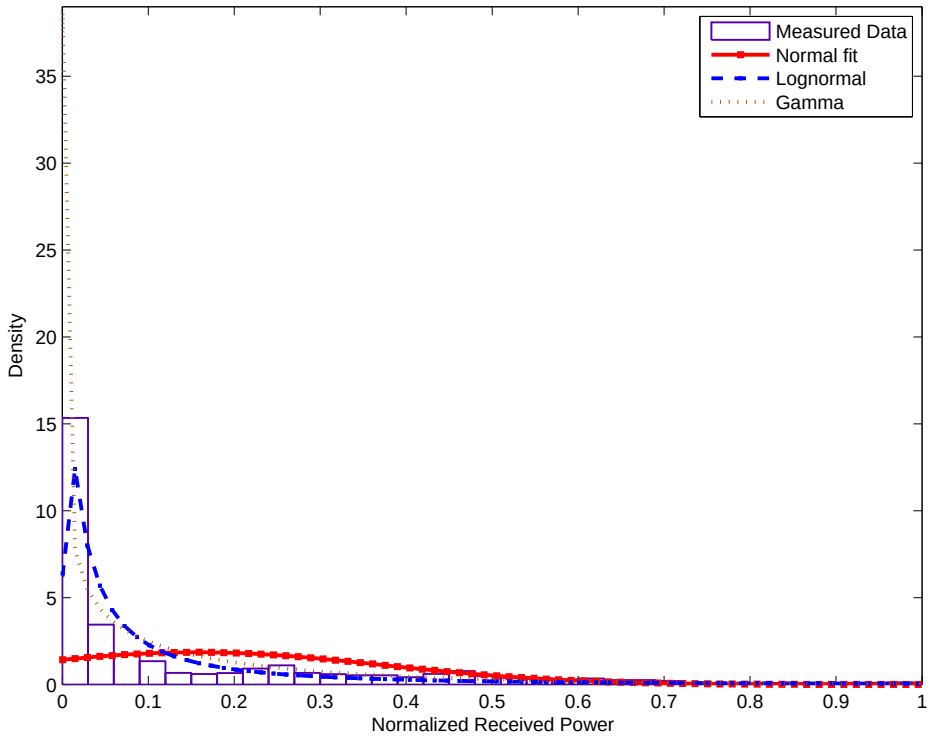

Figure 127: PDF Left wrist to right hip, walking at 2.36 GHz

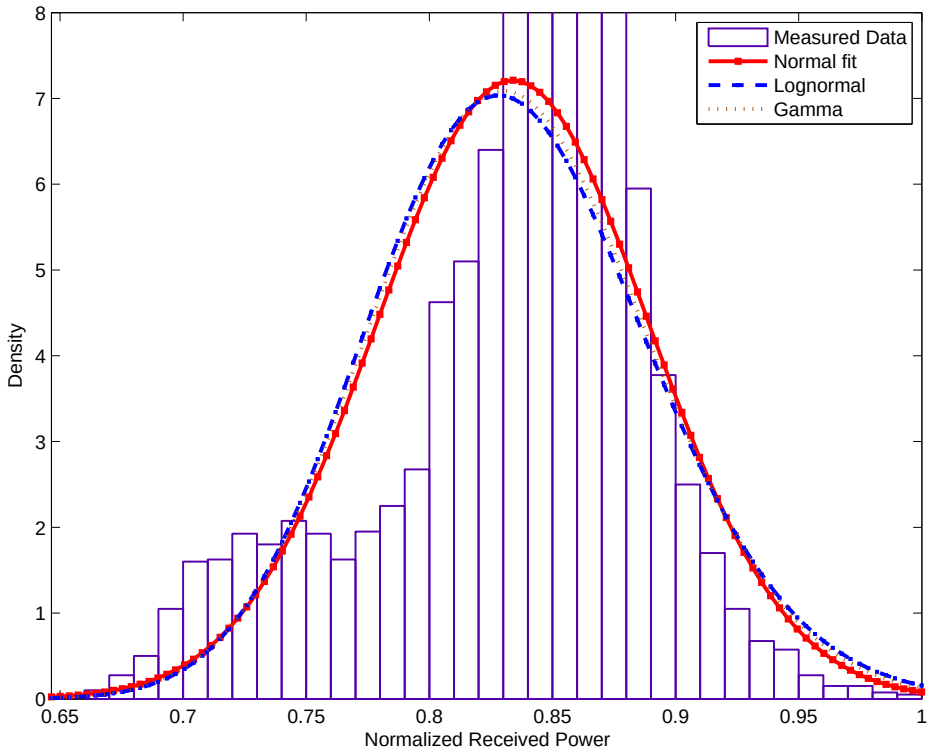

Figure 128: PDF Left wrist to right hip, standing at 2.36 GHz

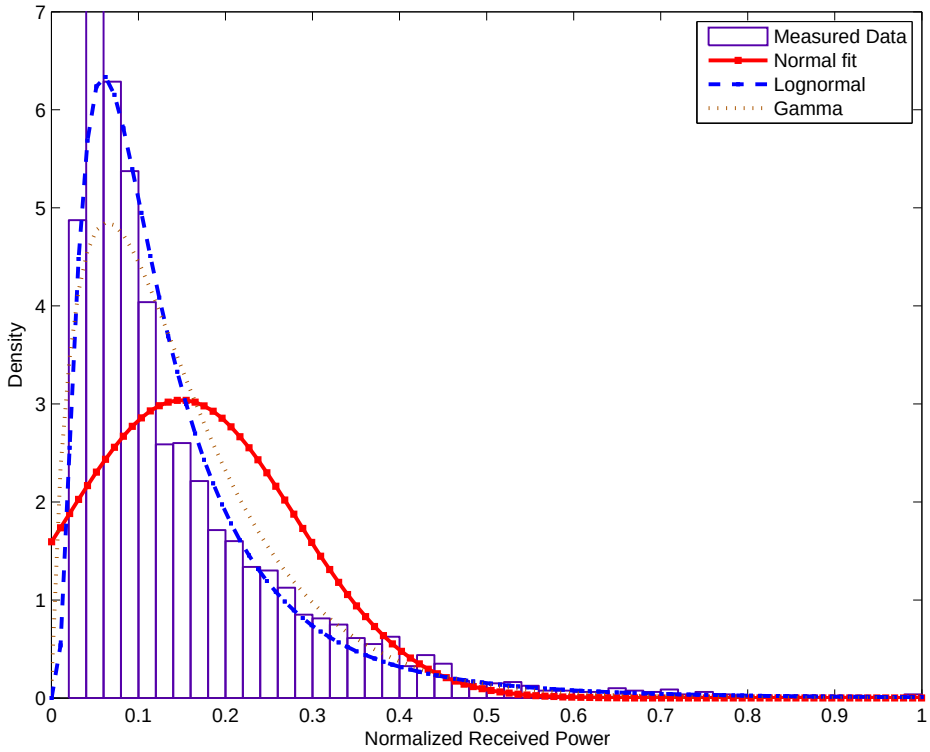

Figure 129: PDF Back to Right hip, Running at 2.36 GHz

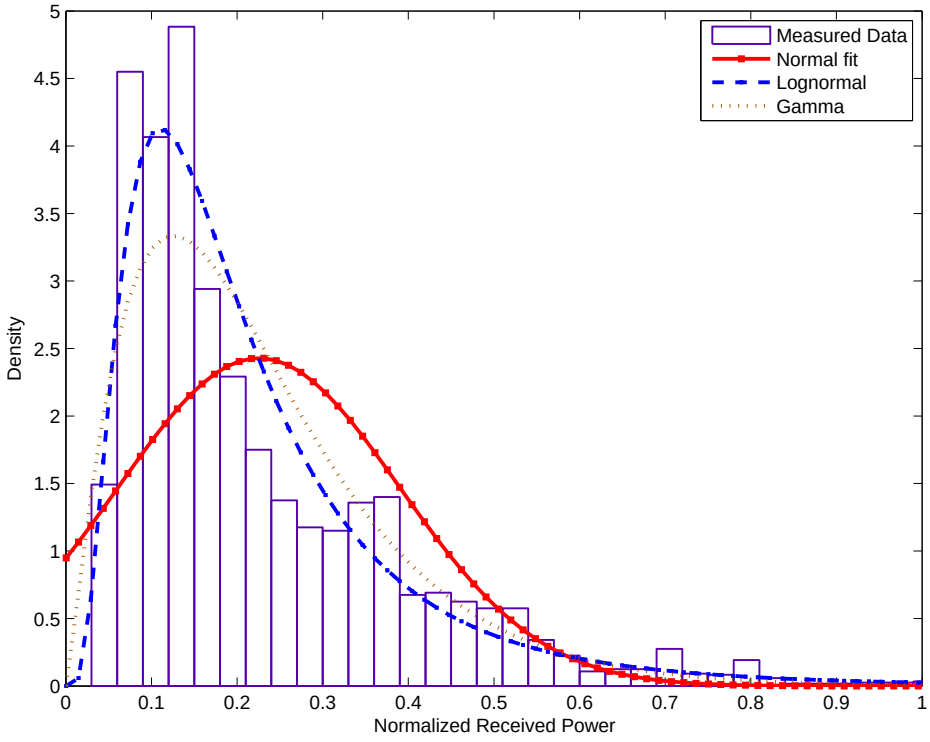

Figure 130: PDF Back to Right hip, Walking at 2.36 GHz

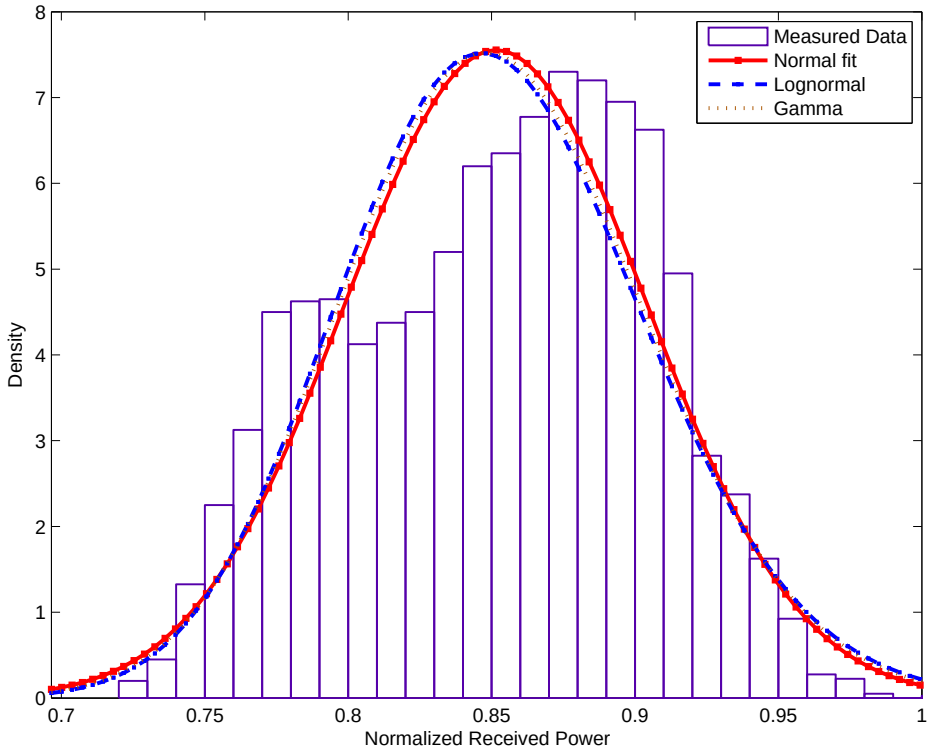

Figure 131: PDF Back to Right hip, Standing at 2.36 GHz

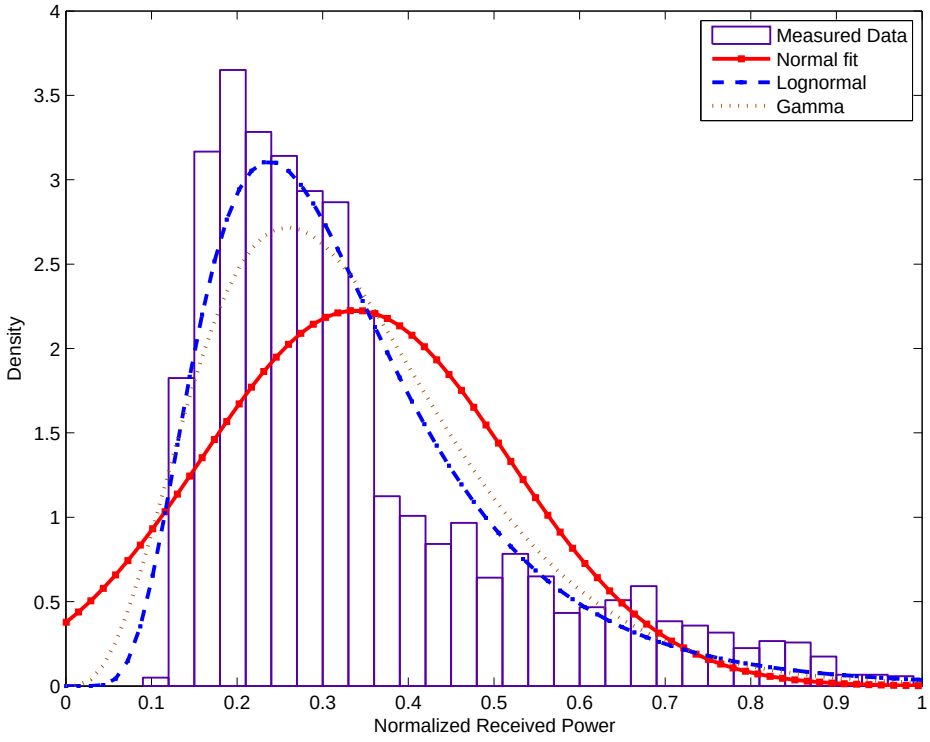

Figure 132: PDF Back to Chest, Running at 2.36 GHz

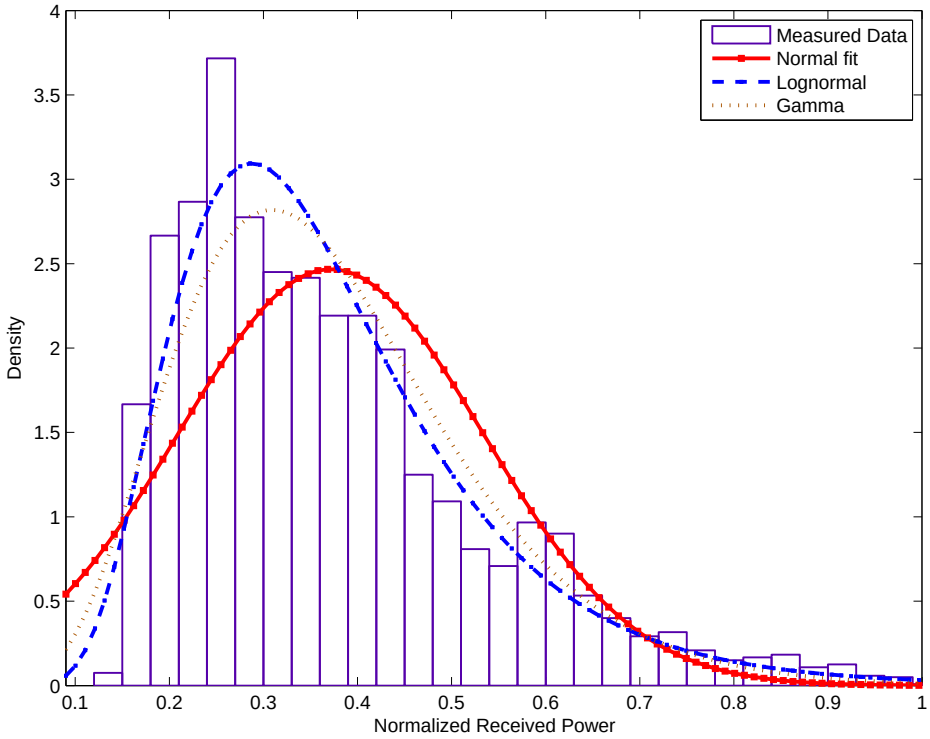

Figure 133: PDF Back to Chest, Walking at 2.36 GHz

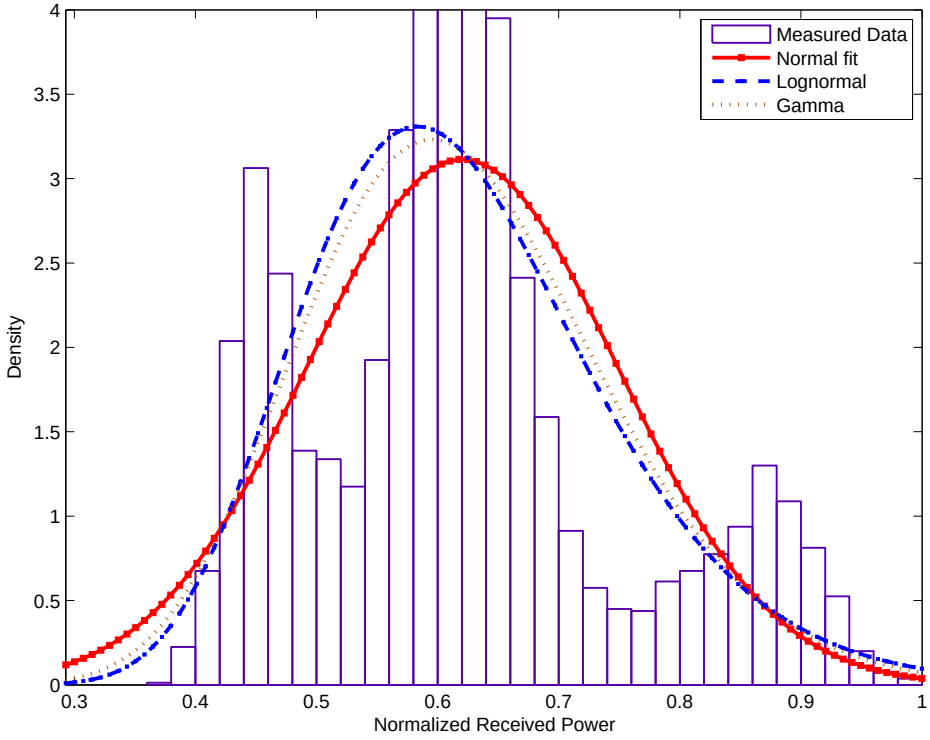

Figure 134: PDF Back to Chest, Standing at 2.36 GHz

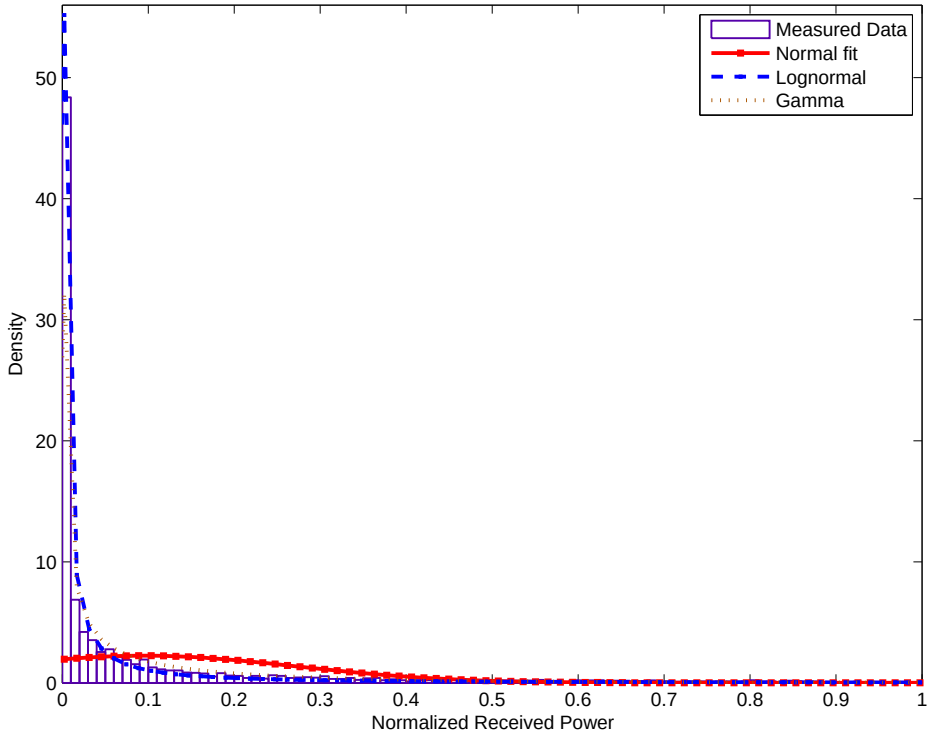

Figure 135: PDF Right wrist to right hip, running at 2.36 GHz

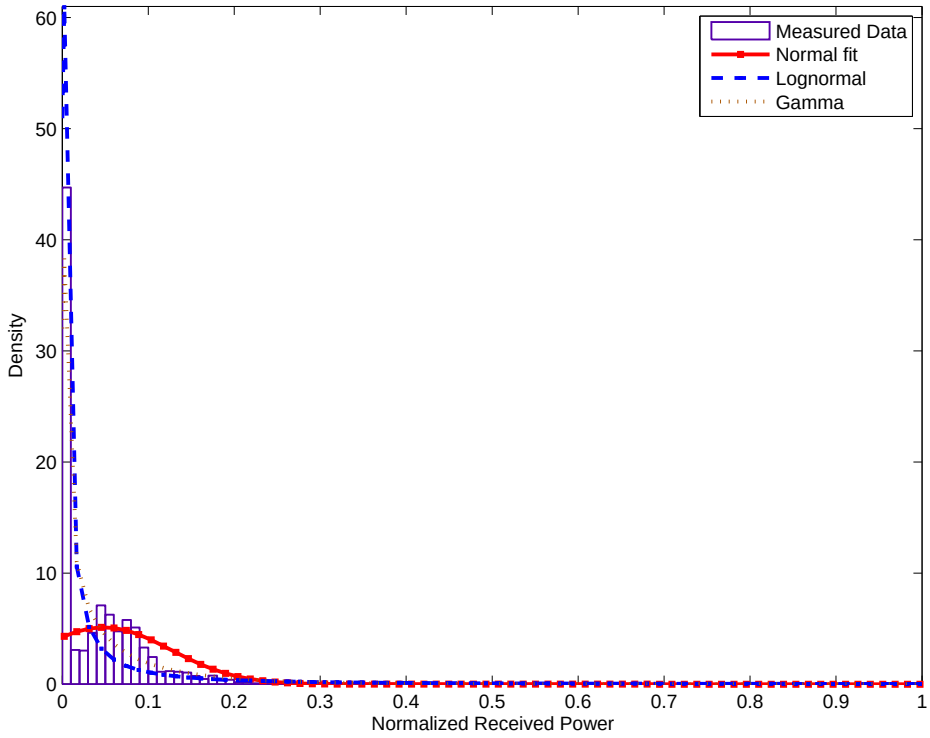

Figure 136: PDF Right wrist to right hip, walking at 2.36 GHz

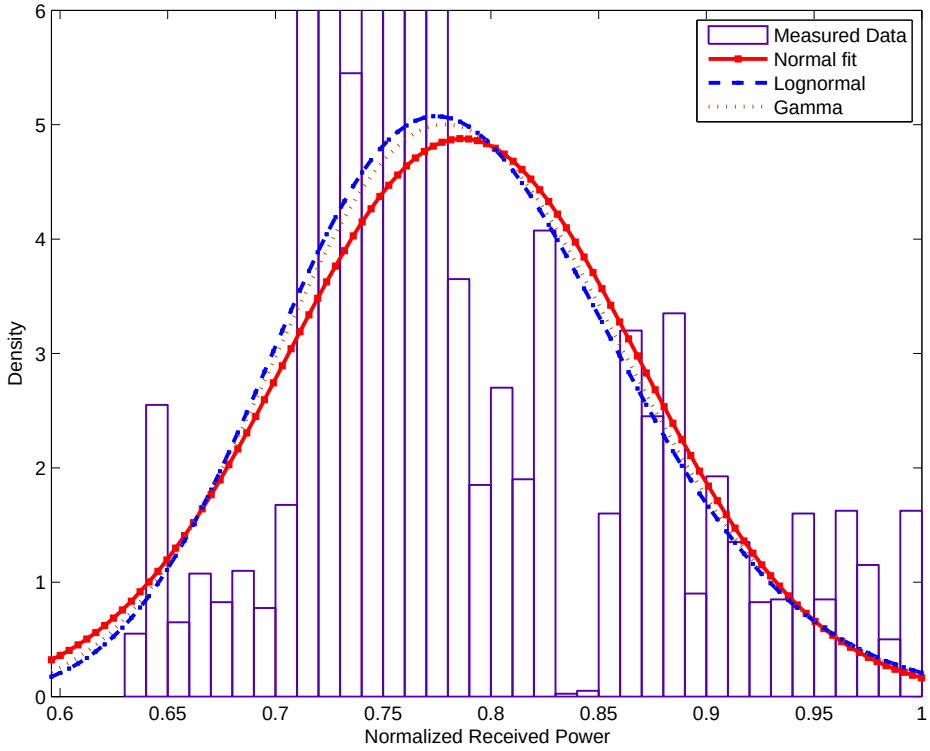

Figure 137: PDF Right wrist to right hip, standing at 2.36 GHz

A.3.2 PDFs at 820 MHz

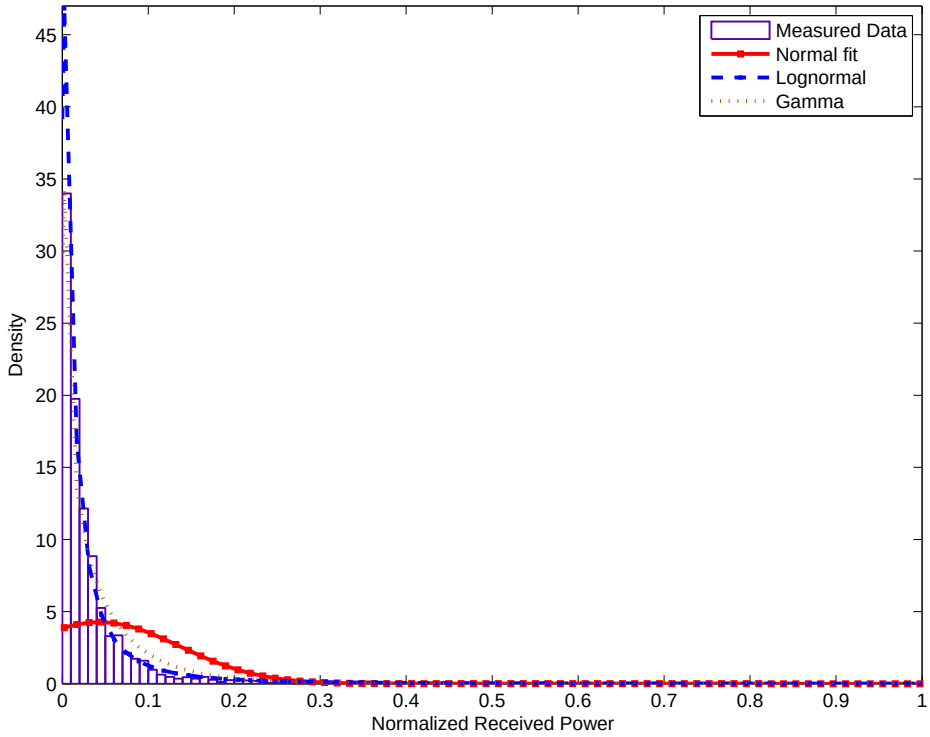

Figure 138: PDF Chest to right hip, running at 820 MHz

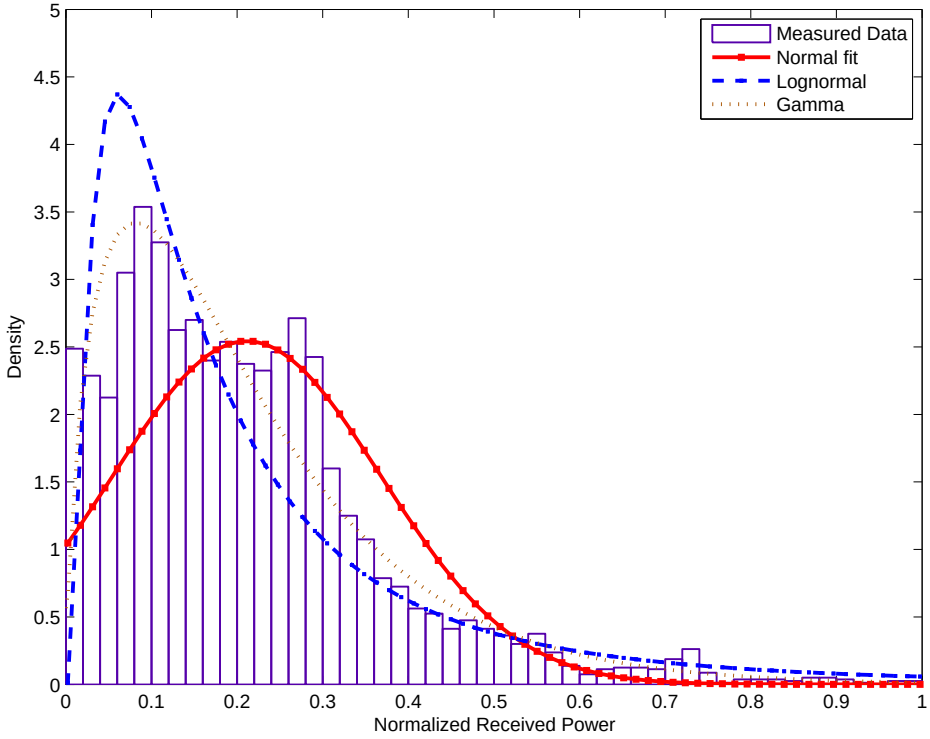

Figure 139: PDF Chest to right hip, walking at 820 MHz

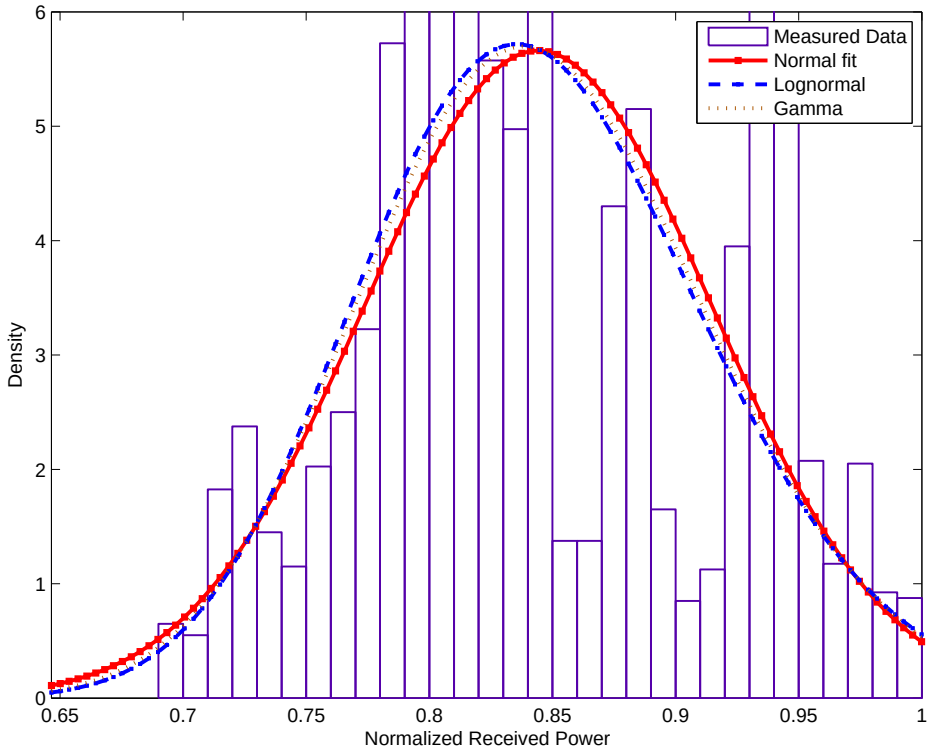

Figure 140: PDF Chest to right hip, standing at 820 MHz

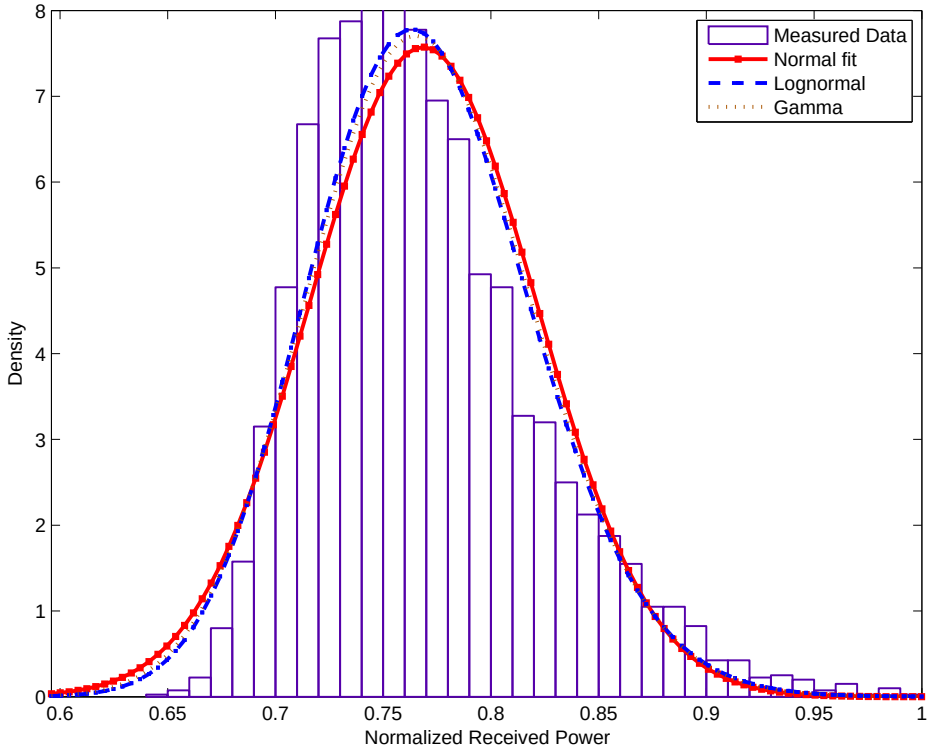

Figure 141: PDF Right ankle to chest, running at 820 MHz

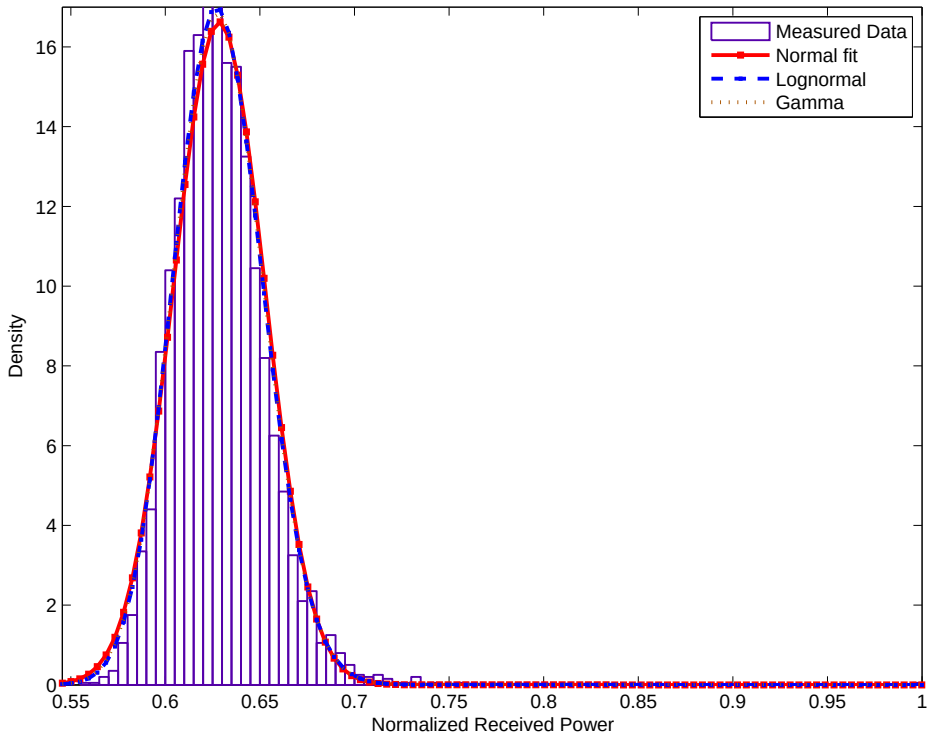

Figure 142: PDF Right ankle to chest, walking at 820 MHz

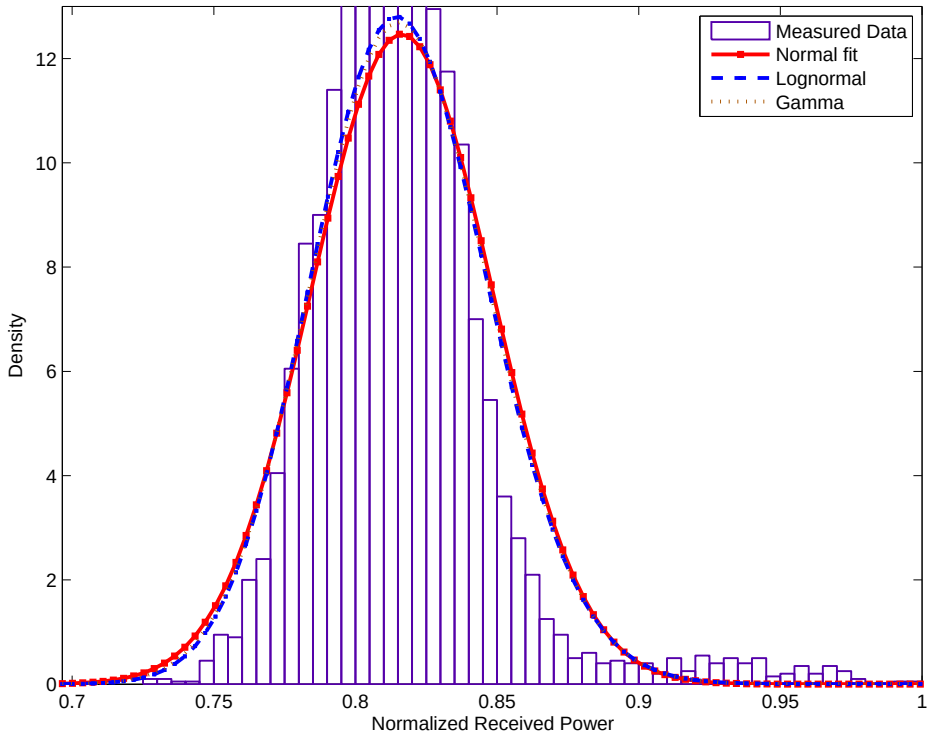

Figure 143: Right ankle to chest, standing at 820 MHz

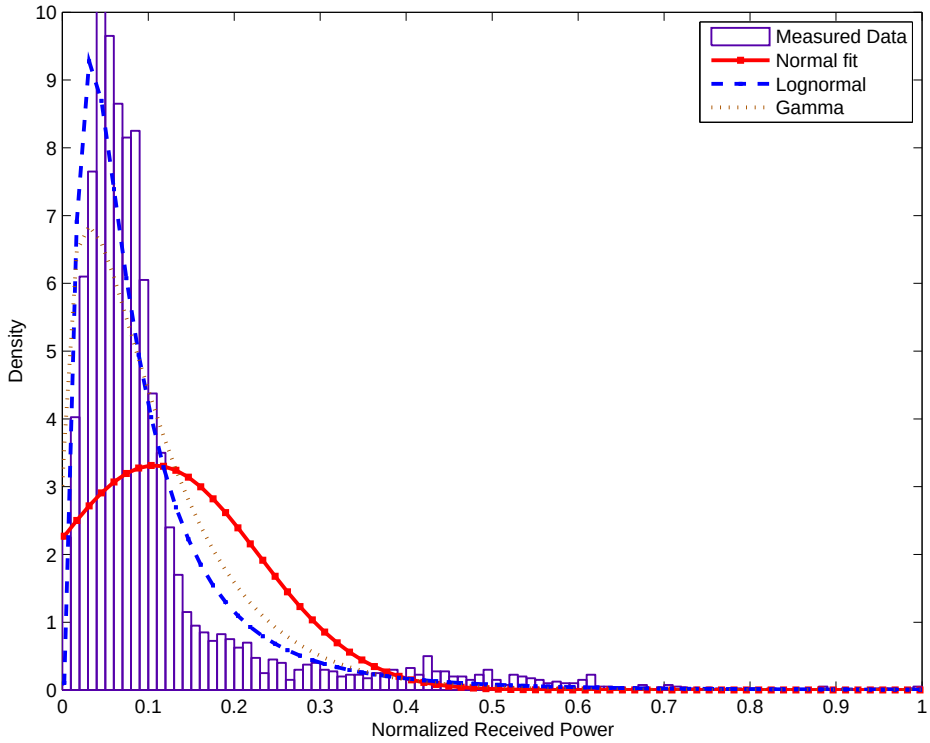

Figure 144: PDF Right wrist to chest, running at 820 MHz

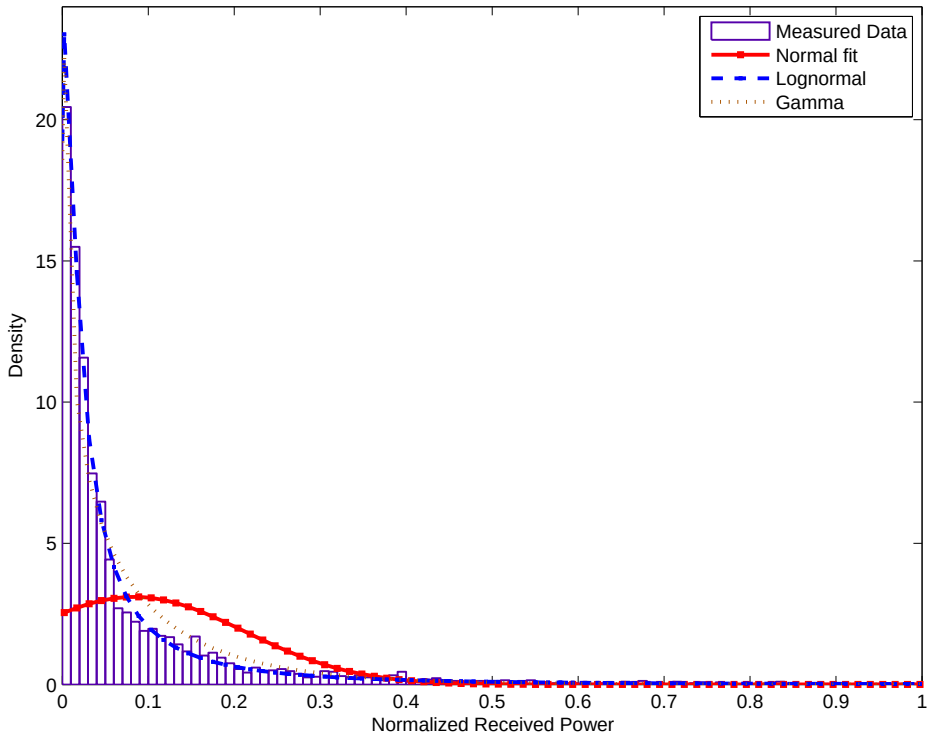

Figure 145: PDF Right wrist to chest, walking at 820 MHz

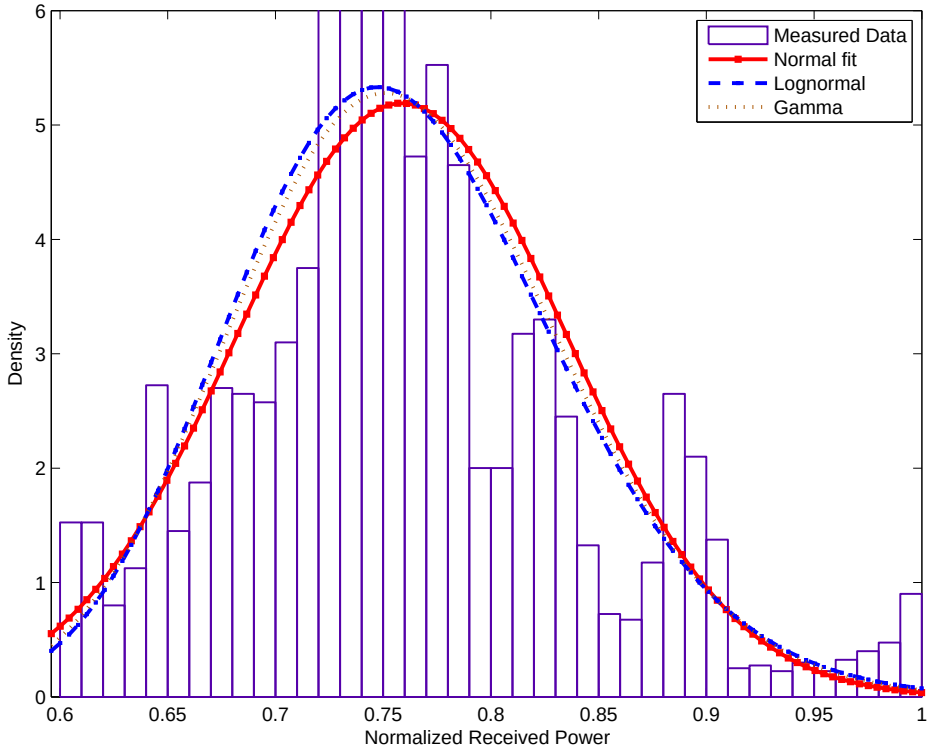

Figure 146: PDF Right wrist to chest, standing at 820 MHz

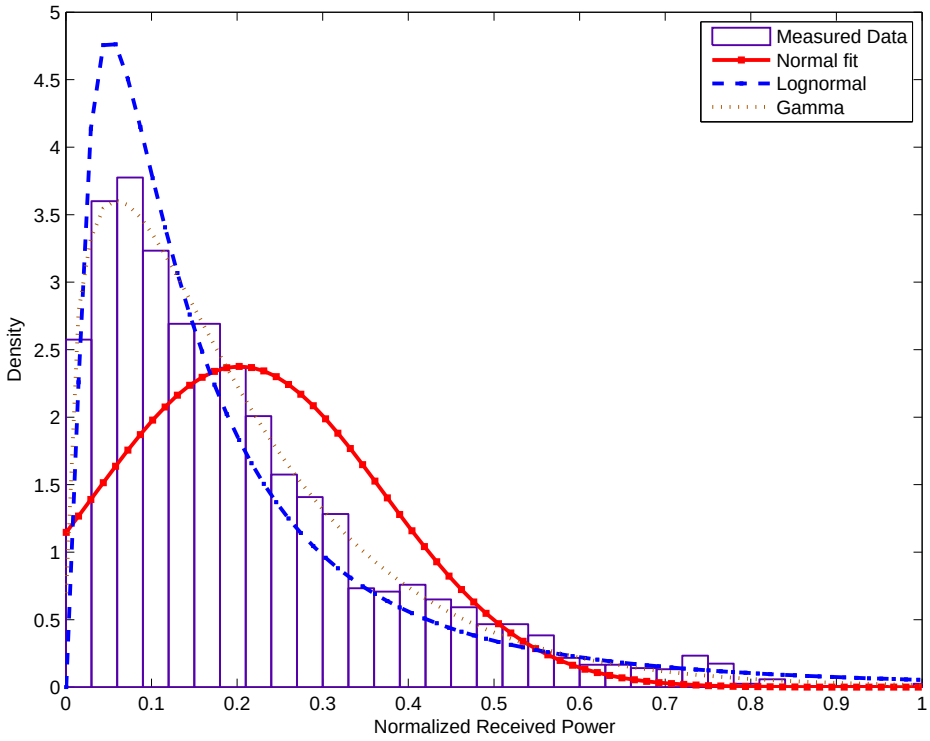

Figure 147: PDF Left ankle to right hip, running at 820 MHz

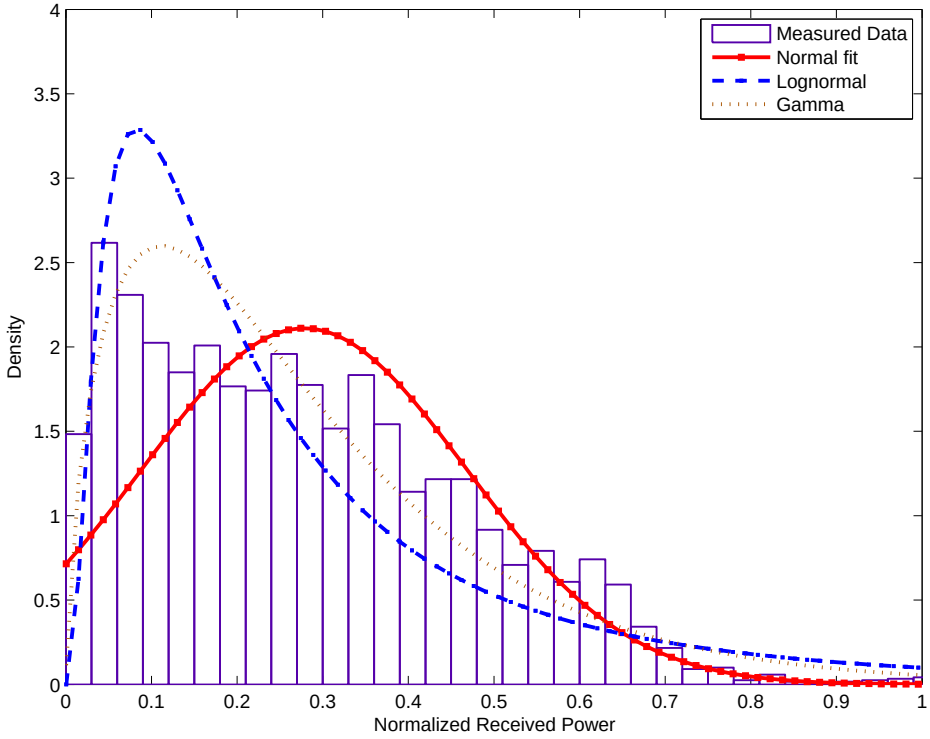

Figure 148: PDF Left ankle to right hip, walking at 820 MHz

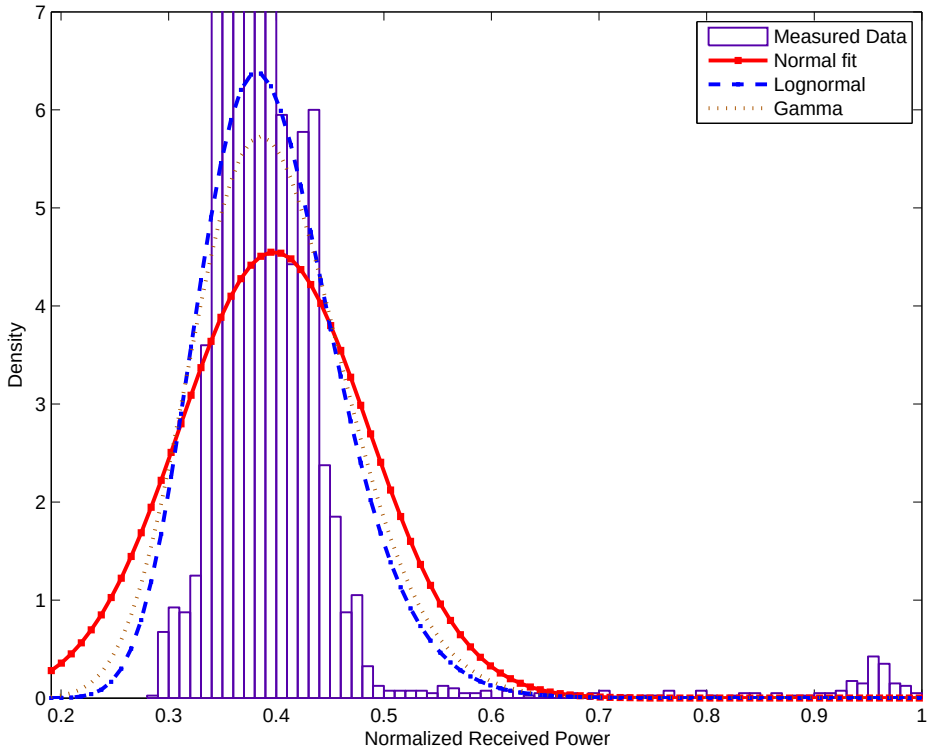

Figure 149: PDF Left ankle to right hip, standing at 820 MHz

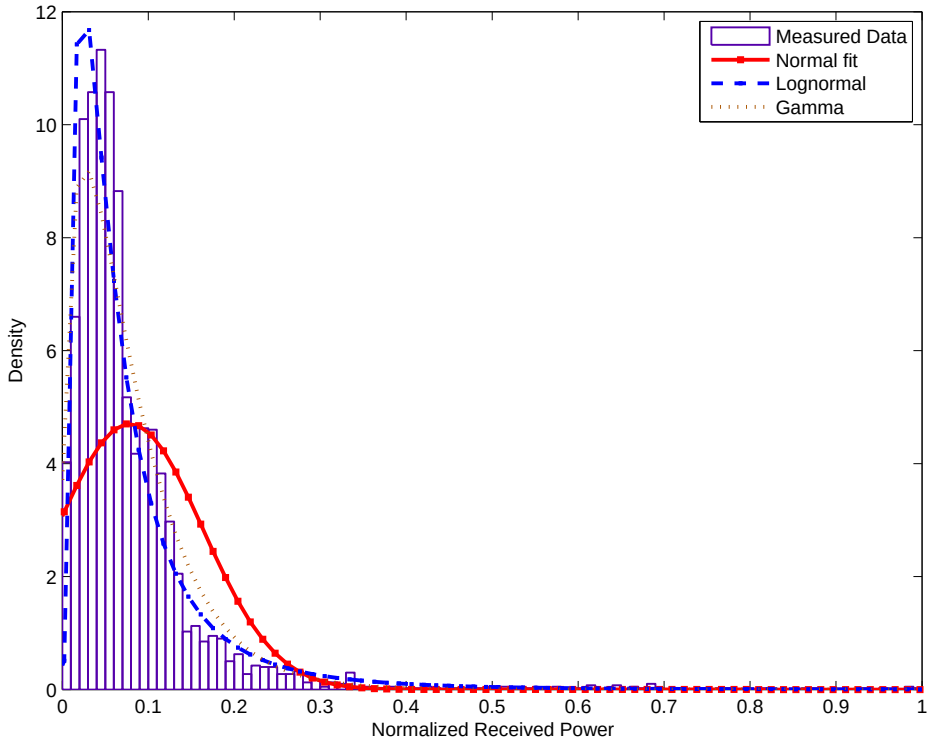

Figure 150: PDF Right ankle to right hip, running at 820 MHz

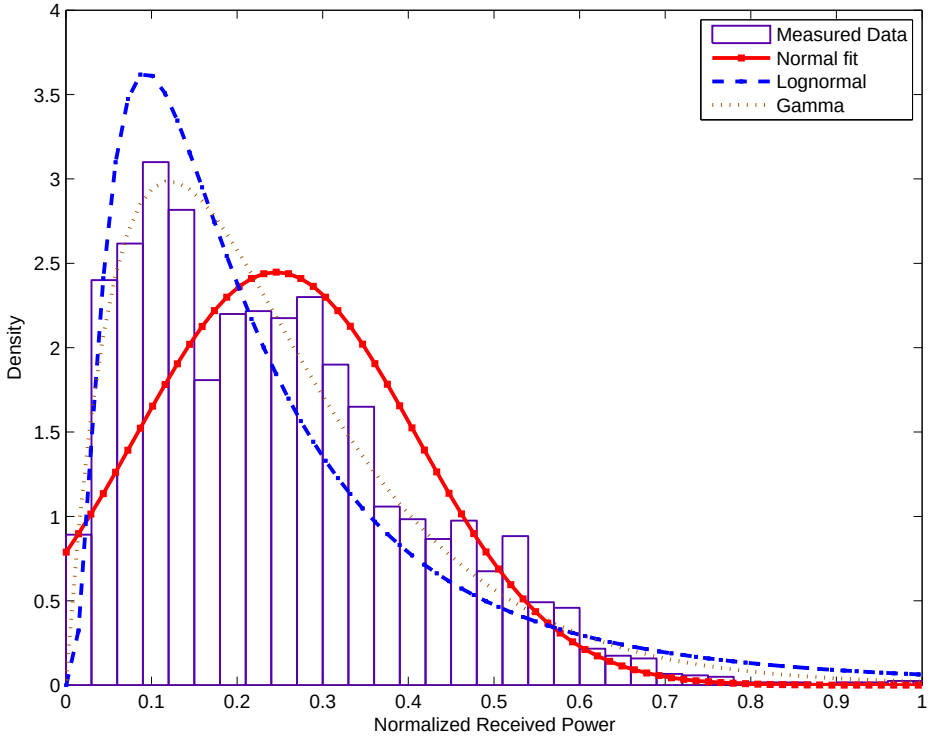

Figure 151: PDF Right ankle to right hip, walking at 820 MHz

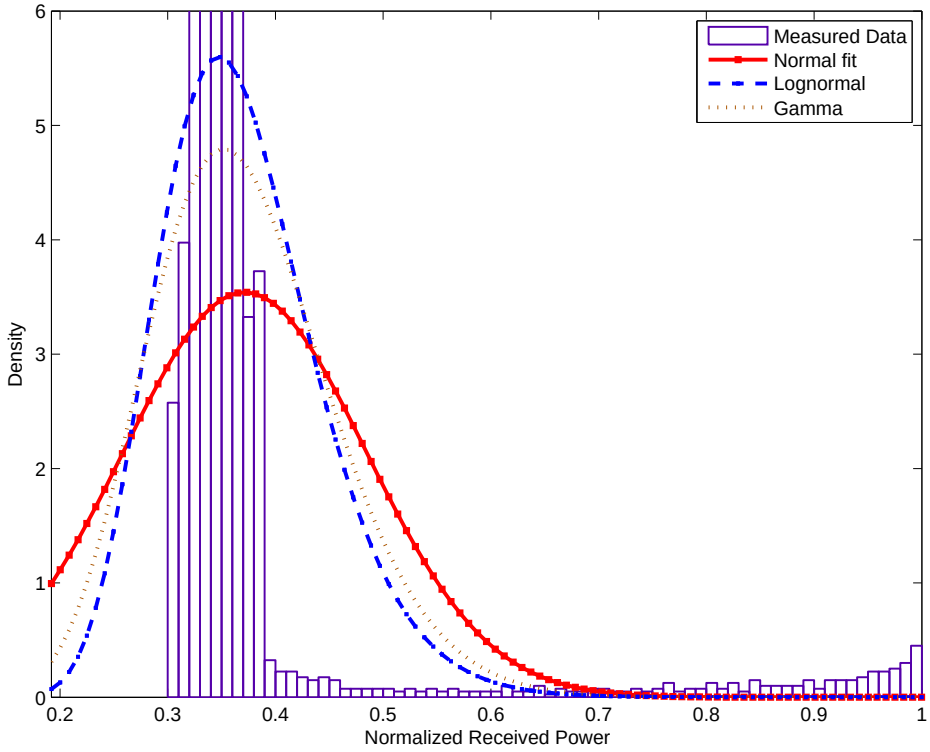

Figure 152: PDF Right ankle to right hip, standing at 820 MHz

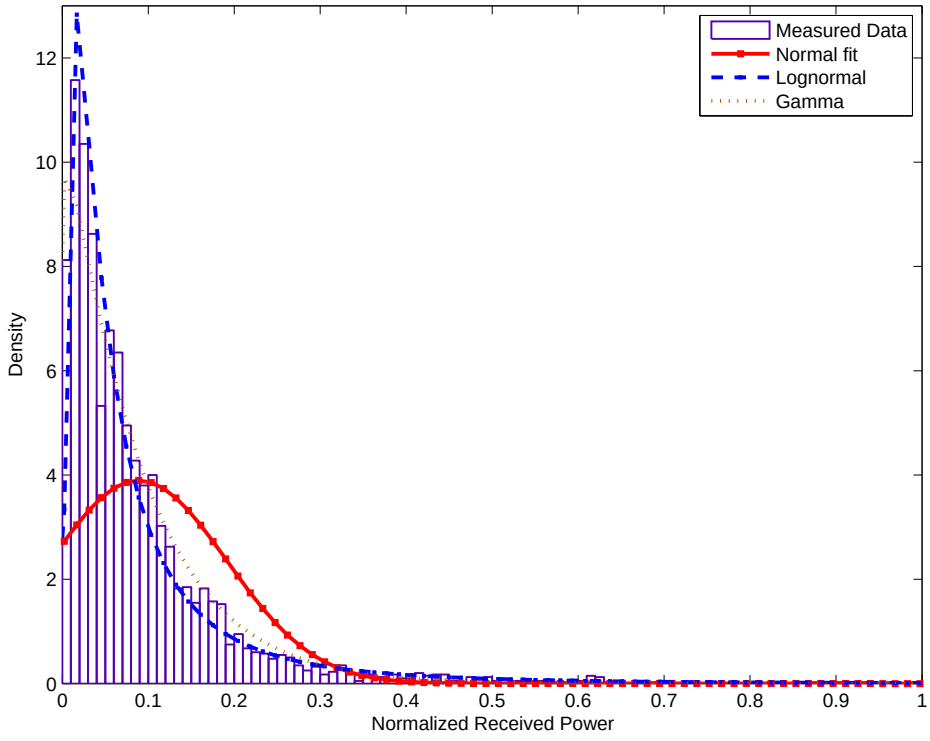

Figure 153: PDF Left wrist to right hip, running at 820 MHz

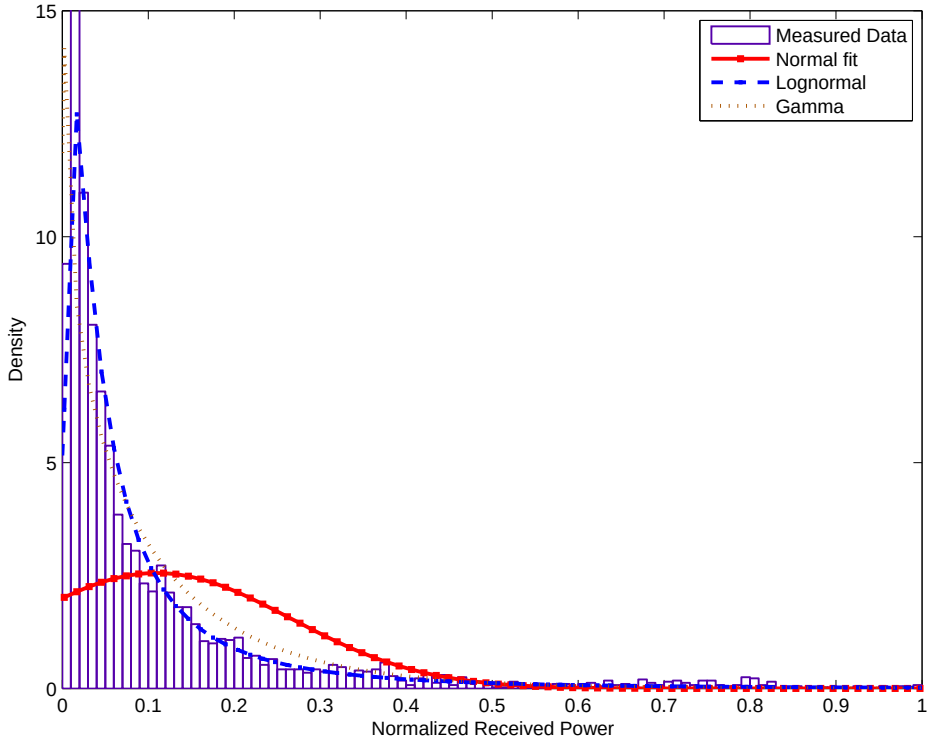

Figure 154: PDF Left wrist to right hip, walking at 820 MHz

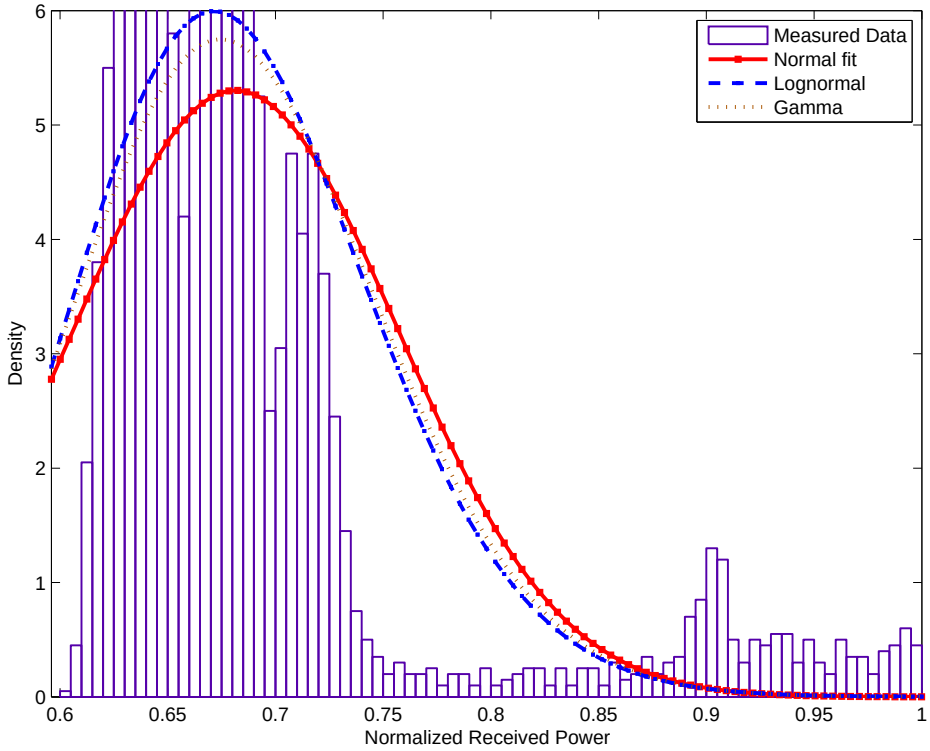

Figure 155: PDF Left wrist to right hip, standing at 820 MHz

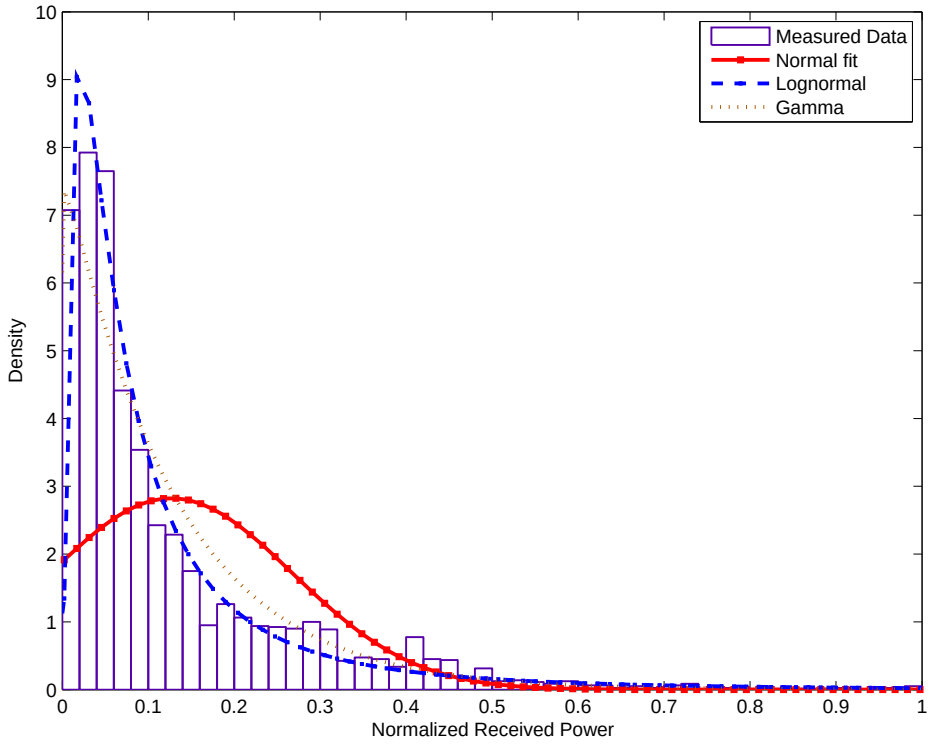

Figure 156: PDF Back to Chest, Running at 820 MHz

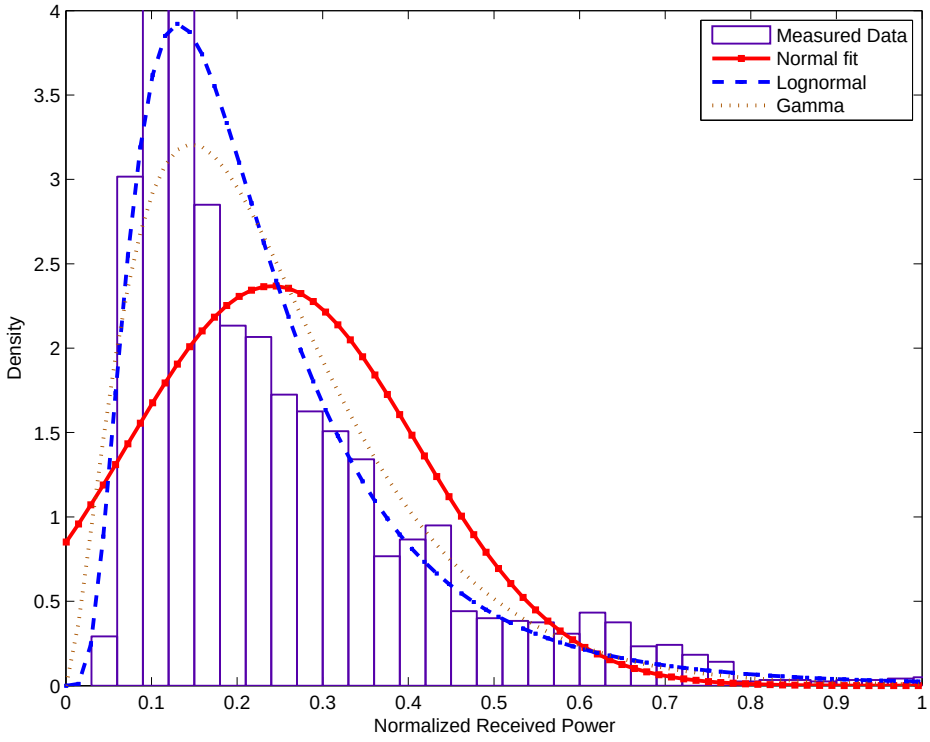

Figure 157: PDF Back to Chest, Walking at 820 MHz

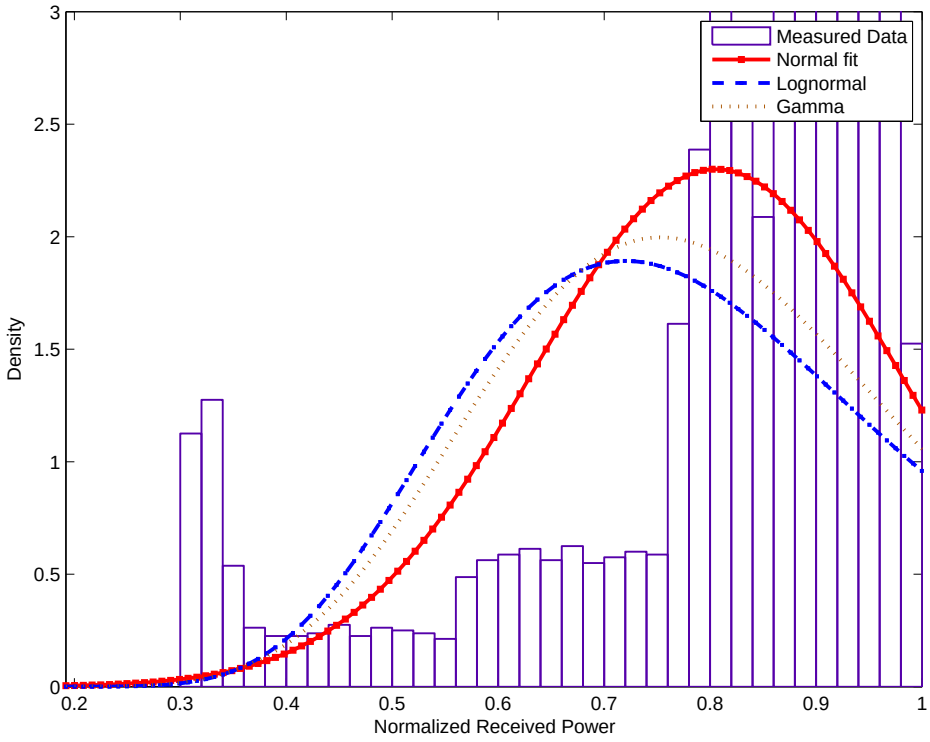

Figure 158: PDF Back to Chest, Standing at 820 MHz

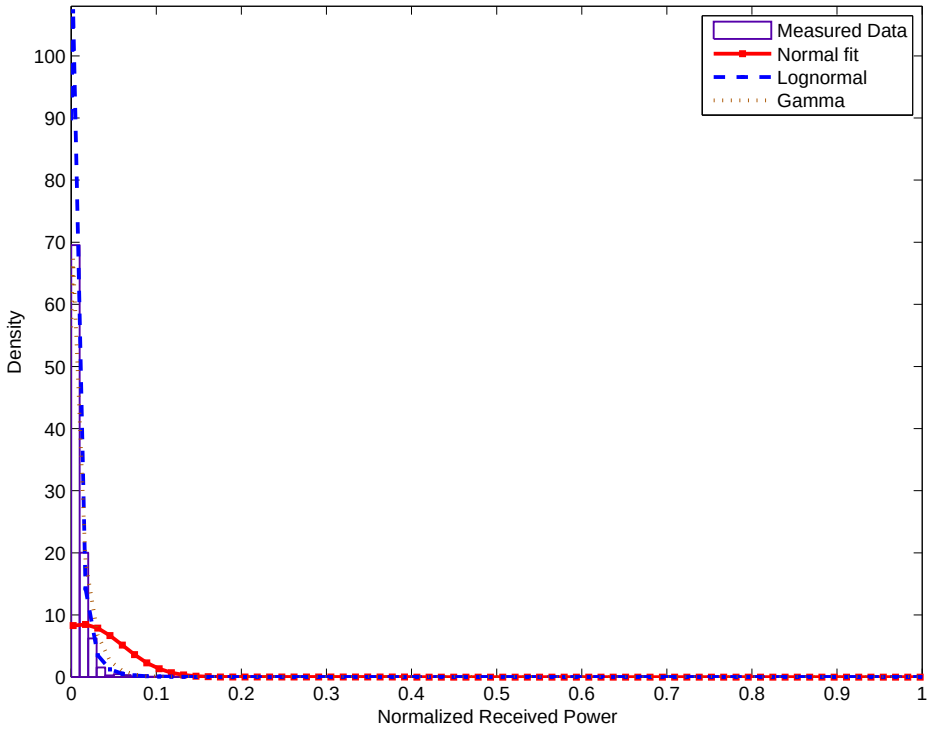

Figure 159: PDF Back to Chest, Running at 820 MHz

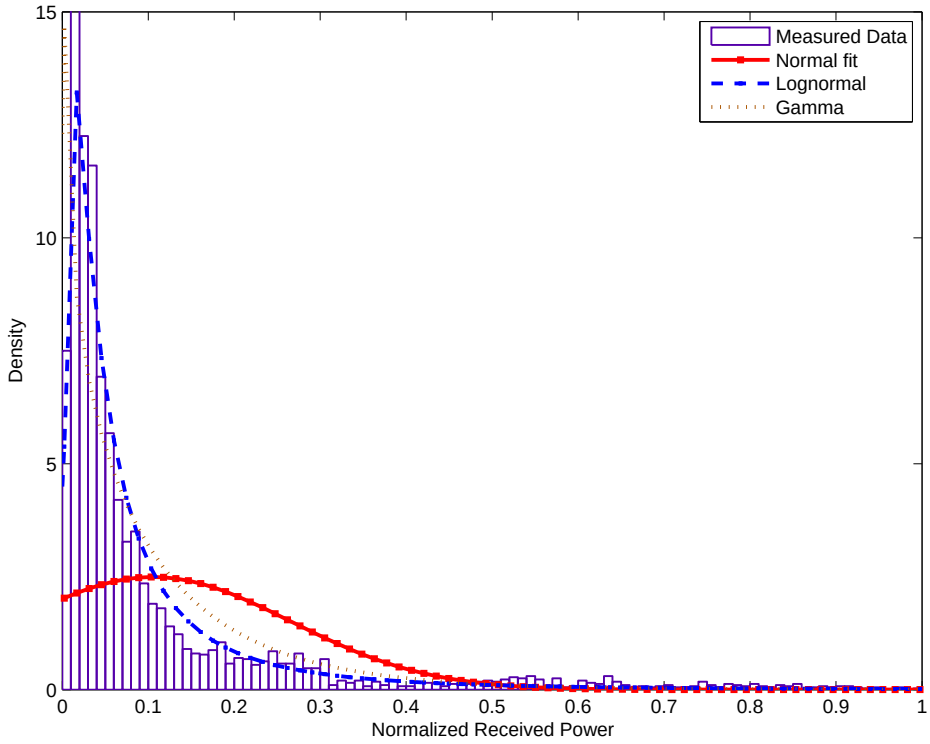

Figure 160: PDF Back to Chest, Walking at 820 MHz

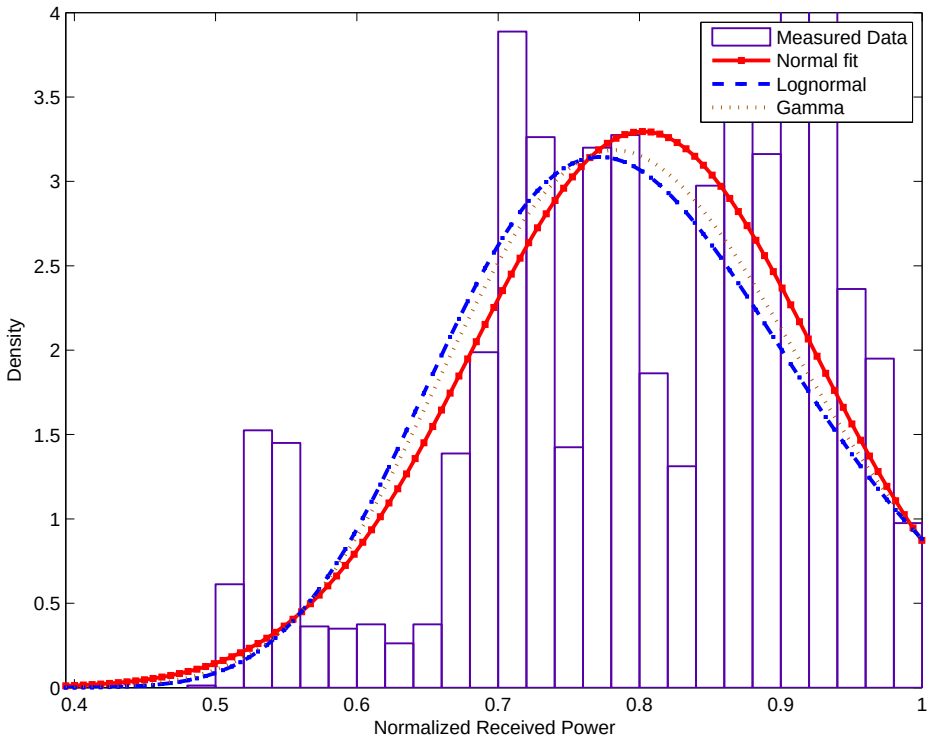

Figure 161: PDF Back to Chest, Standing at 820 MHz

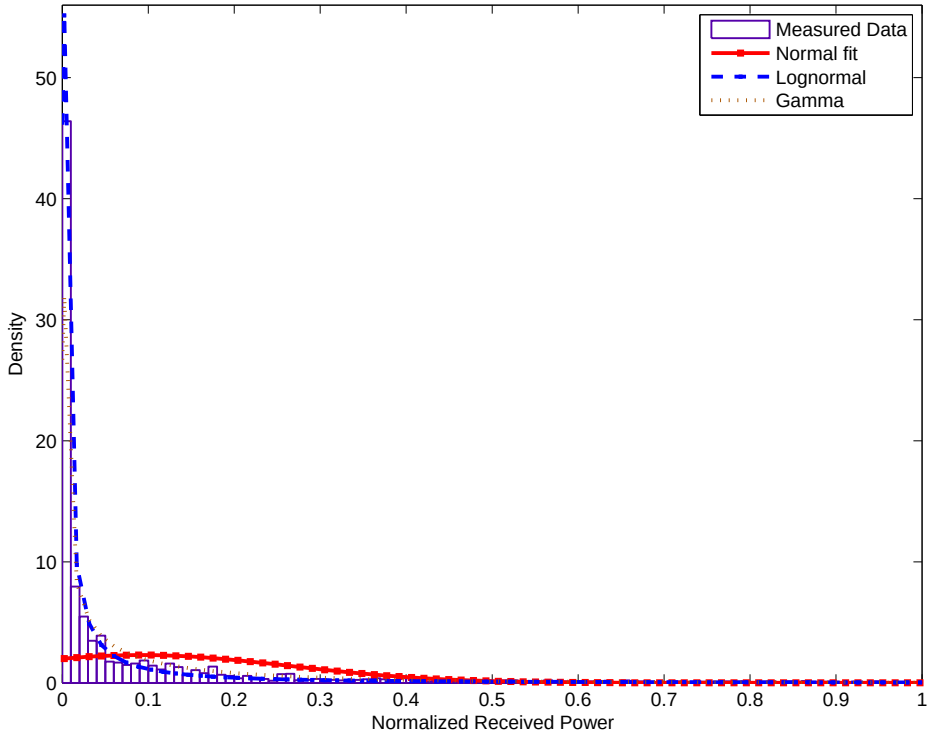

Figure 162: PDF Right wrist to right hip, running at 820 MHz

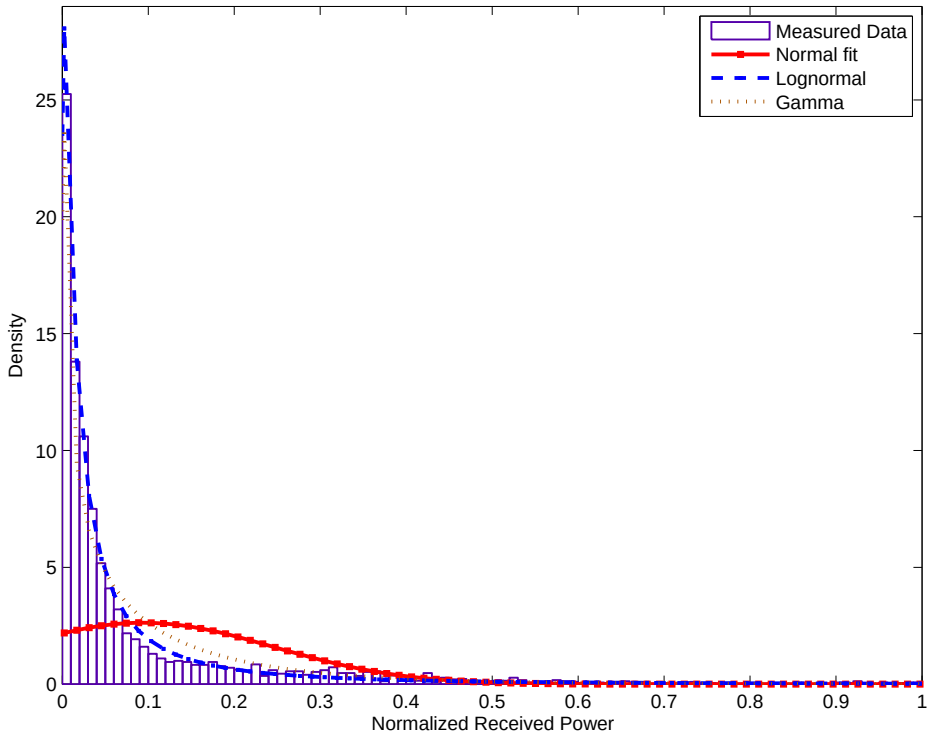

Figure 163: PDF Right wrist to right hip, walking at 820 MHz

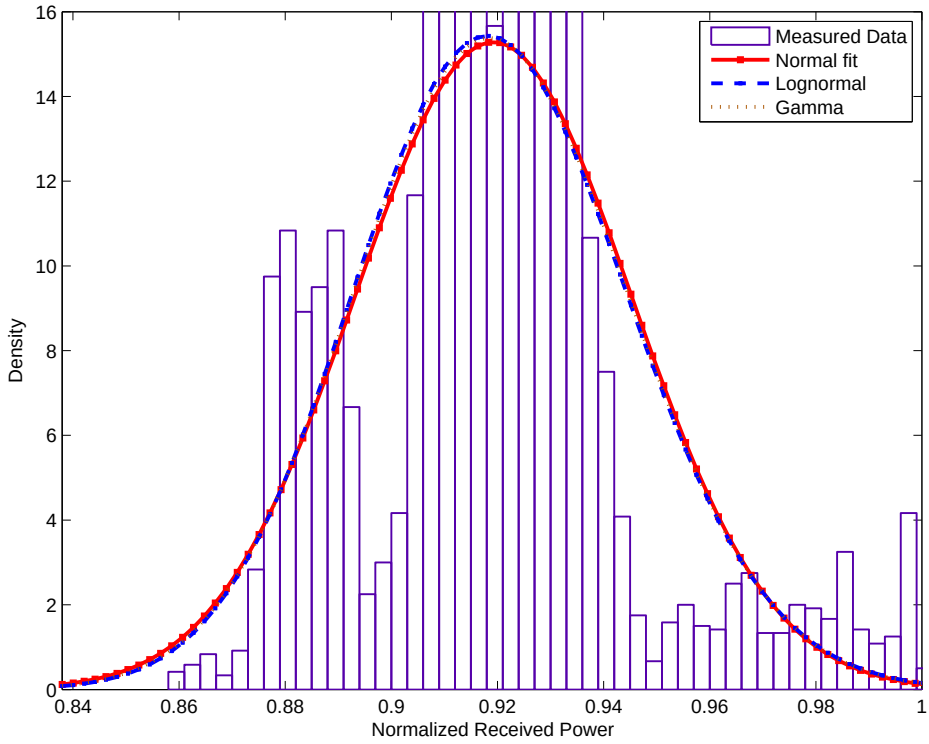

Figure 164: PDF Right wrist to right hip, standing at 820 MHz

A.4 Channel Time-Coherence

A.4.1 820 MHz Measurements

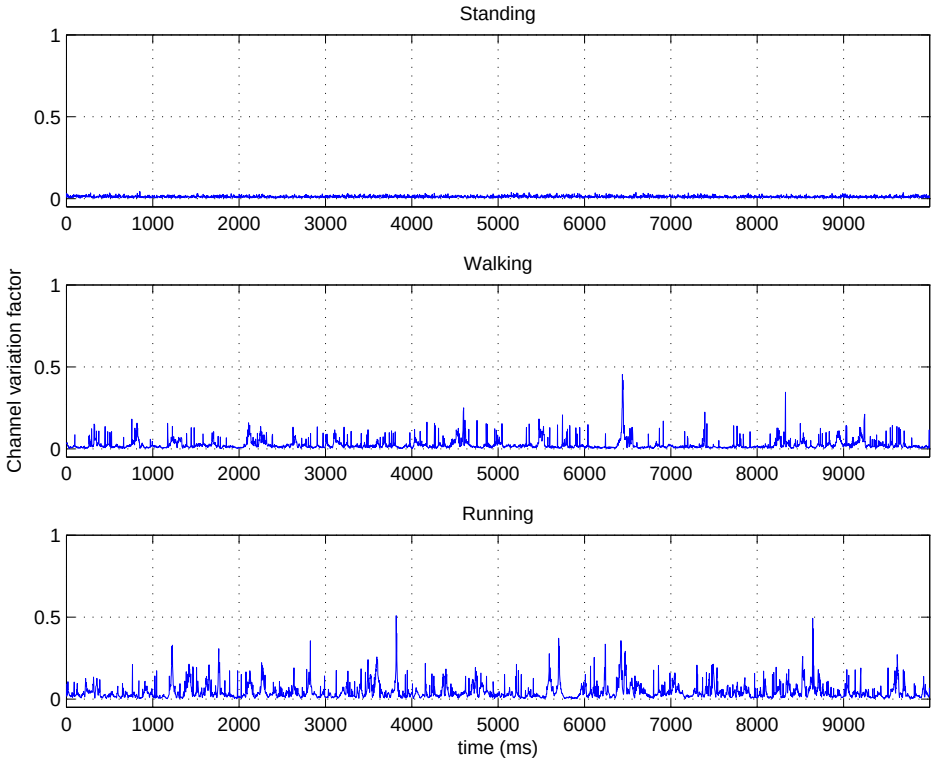

Figure 165: Channel variation factor for a time varying period of 5ms, Chest to right hip standing, walking and running - 820 MHz

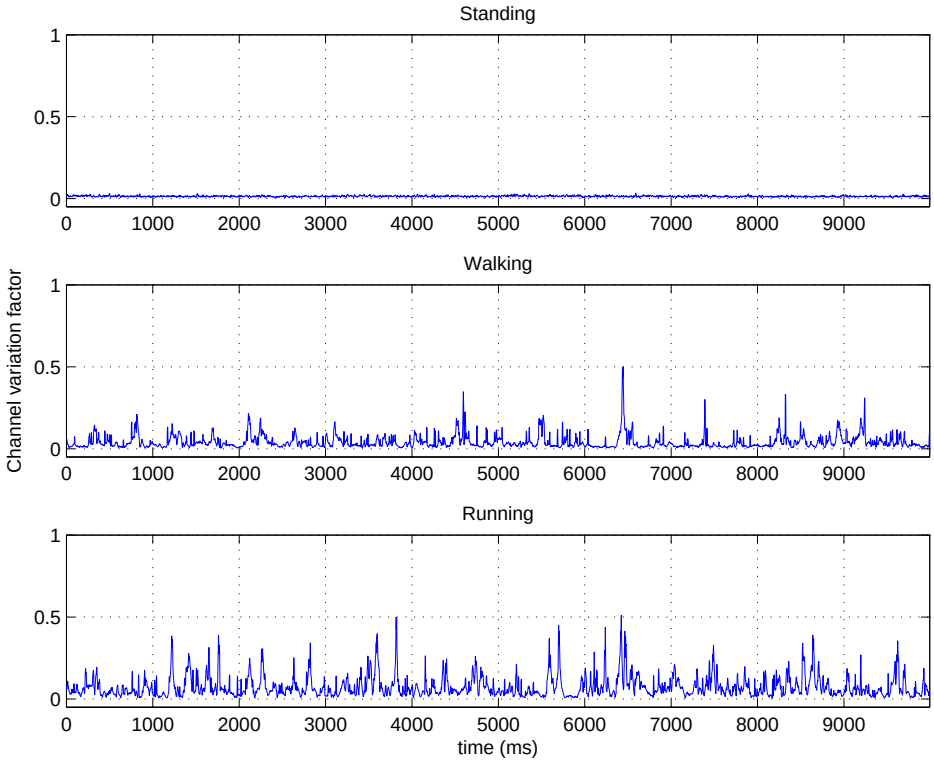

Figure 166: Channel variation factor for a time varying period of 10ms, Chest to right hip standing, walking and running - 820 MHz

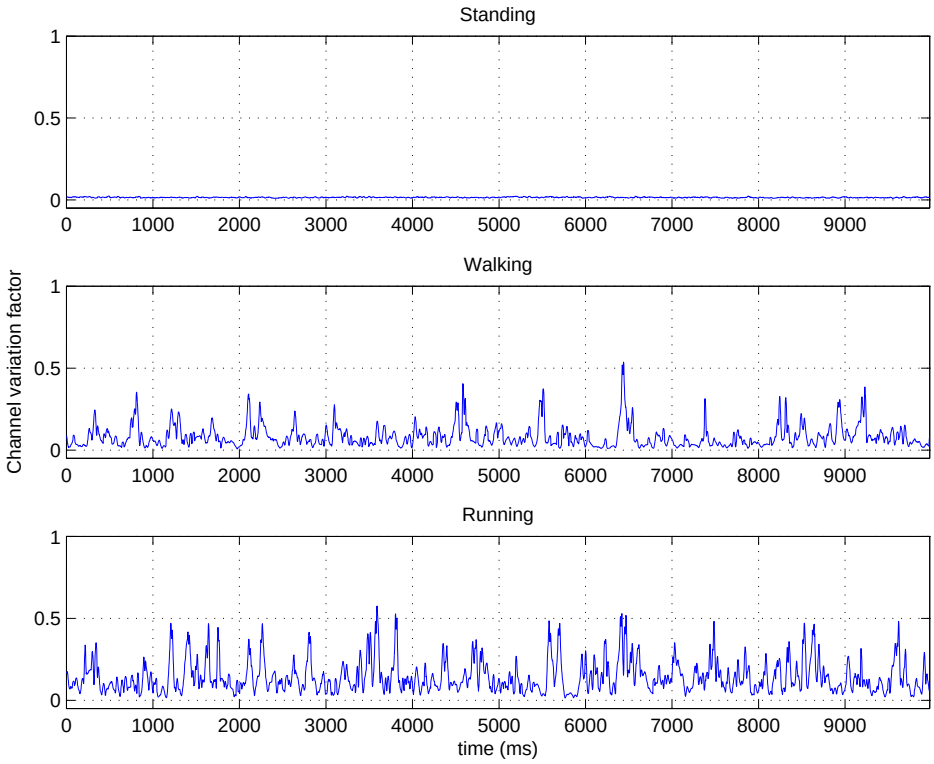

Figure 167: Channel variation factor for a time varying period of 25ms, Chest to right hip standing, walking and running - 820 MHz

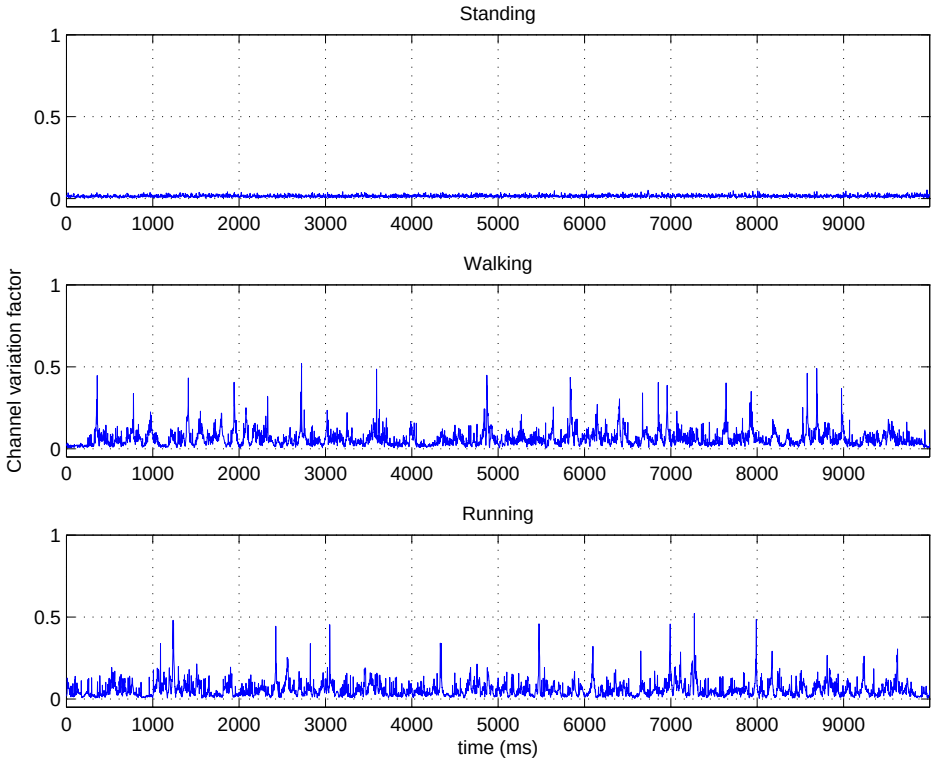

Figure 168: Channel variation factor for a time varying period of 5ms, Left wrist to right hip standing, walking and running - 820 MHz

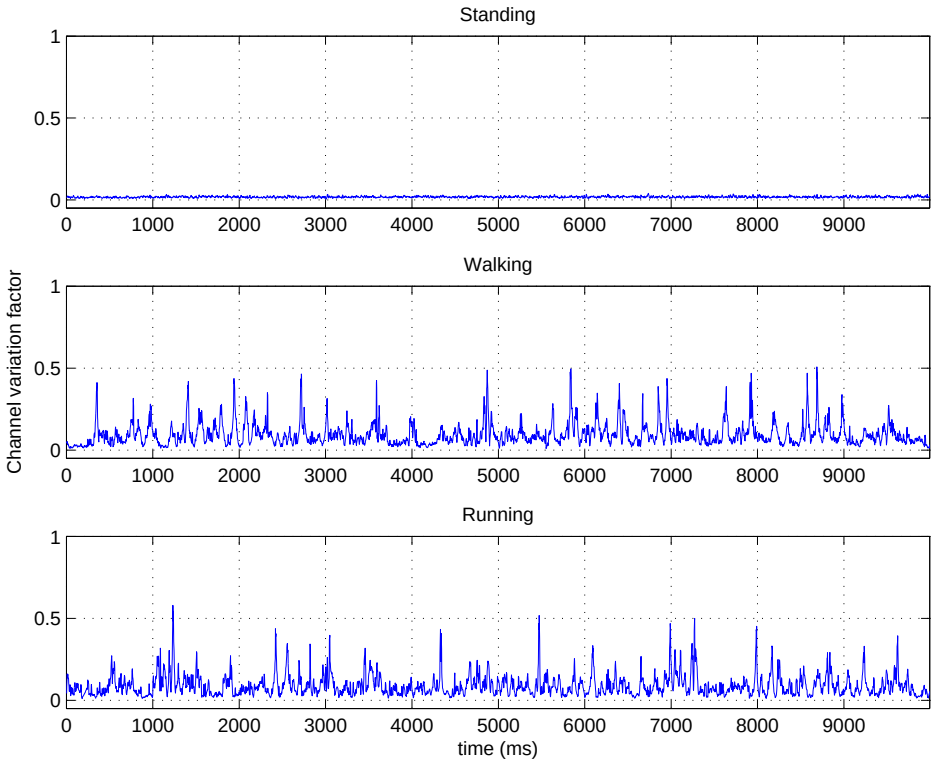

Figure 169: Channel variation factor for a time varying period of 10ms, Left wrist to right hip standing, walking and running - 820 MHz

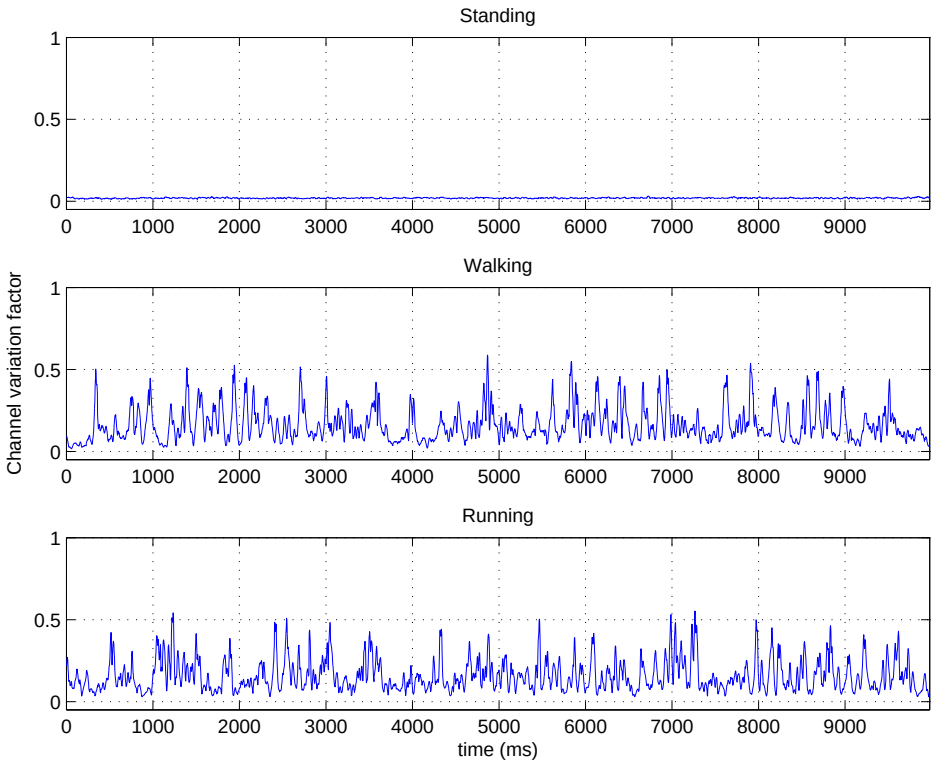

Figure 170: Channel variation factor for a time varying period of 25ms, Left wrist to right hip standing, walking and running - 820 MHz

A.4.2 2.36 GHz Measurements

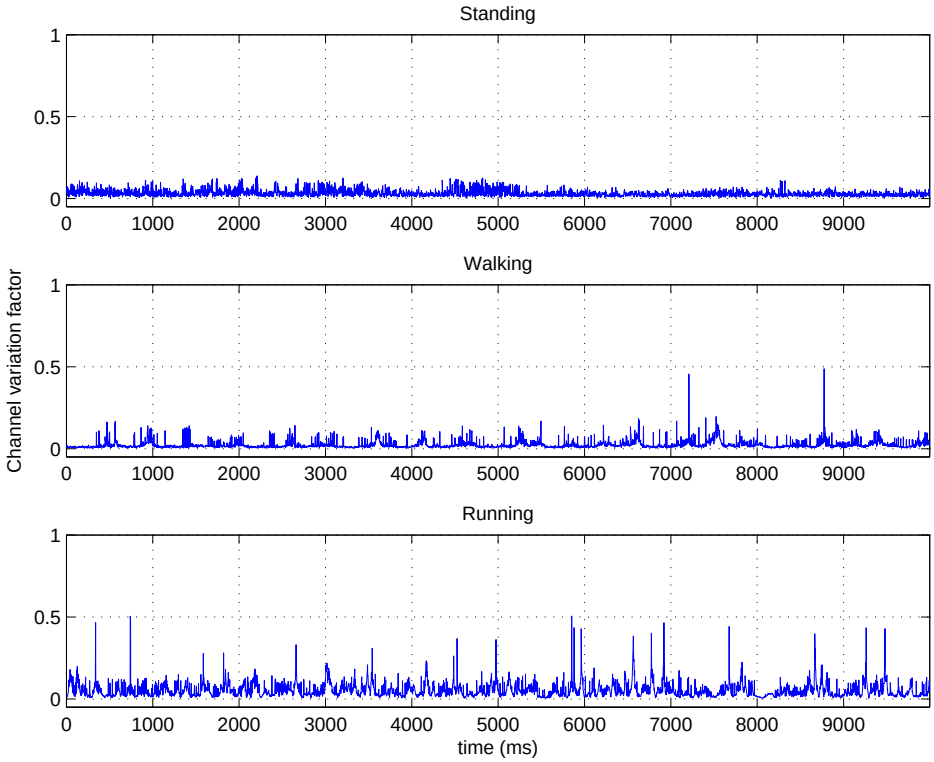

Figure 171: Channel variation factor for a time varying period of 5ms, Chest to right hip standing, walking and running - 2.36 GHz

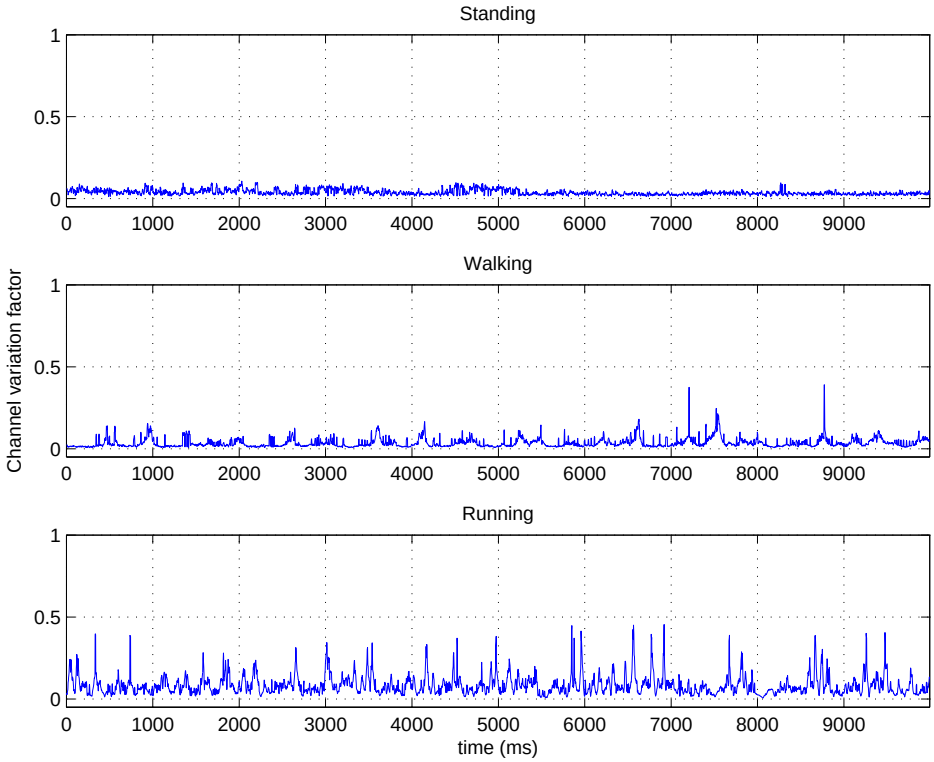

Figure 172: Channel variation factor for a time varying period of 10ms, Chest to right hip standing, walking and running - 2.36 GHz

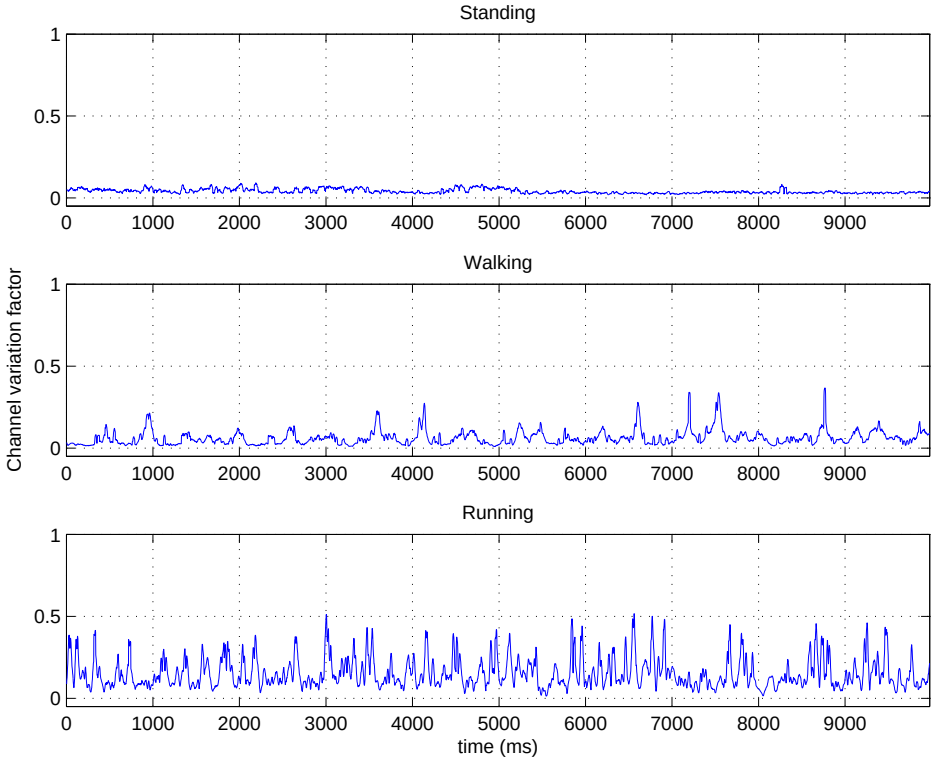

Figure 173: Channel variation factor for a time varying period of 25ms, Chest to right hip standing, walking and running - 2.36 GHz

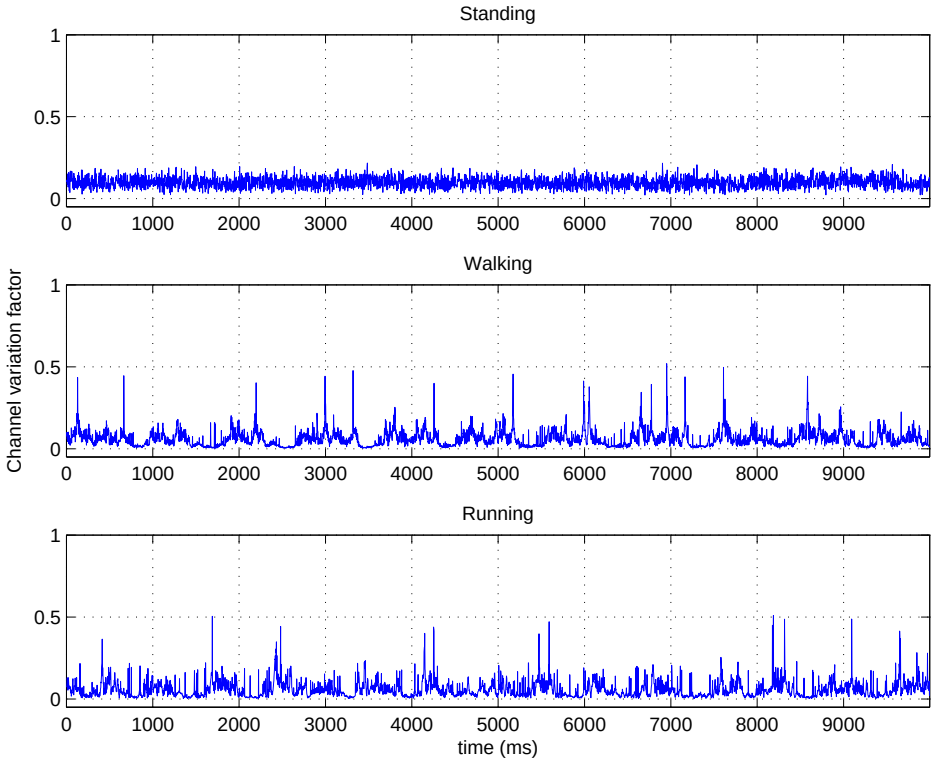

Figure 174: Channel variation factor for a time varying period of 5ms, Left wrist to right hip standing, walking and running - 2.36 GHz

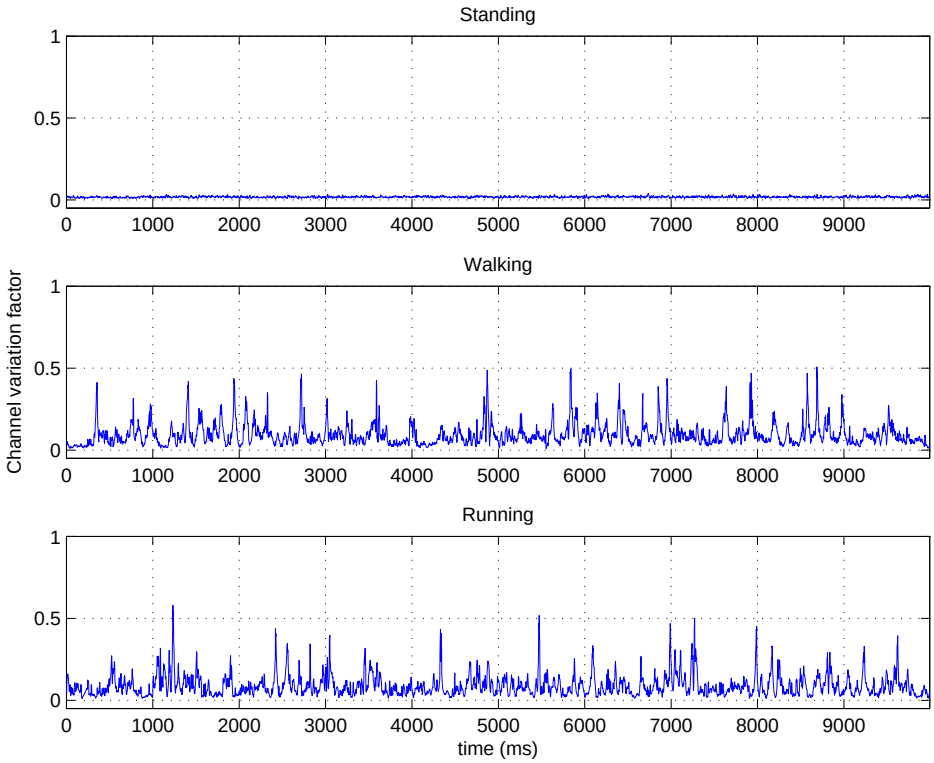

Figure 175: Channel variation factor for a time varying period of 10ms, Left wrist to right hip standing, walking and running - 2.36 GHz

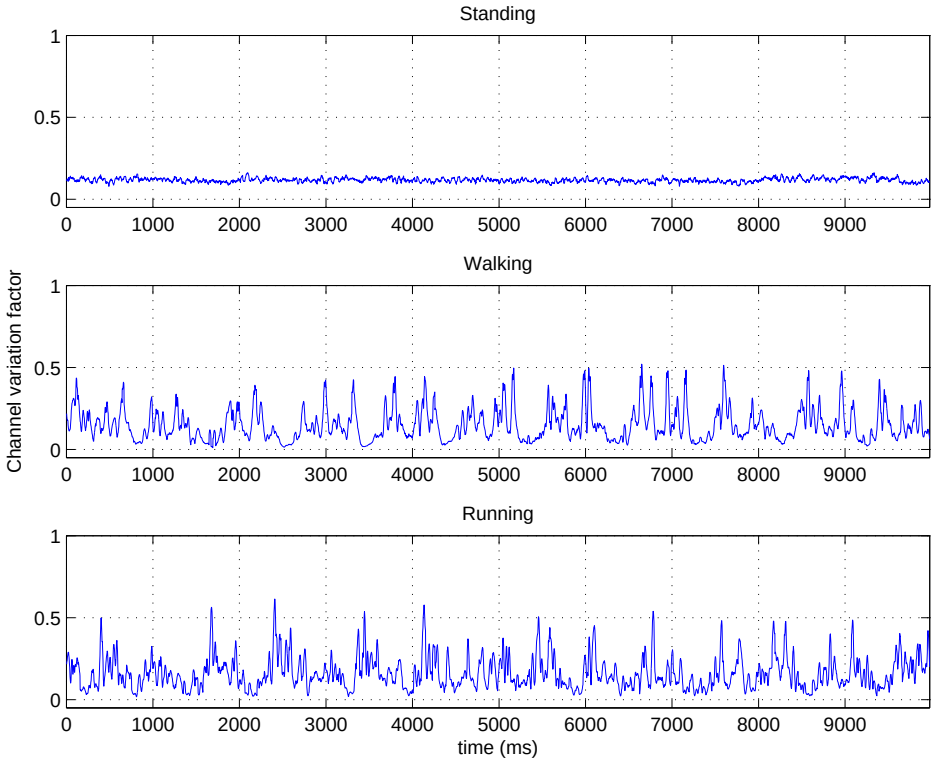

Figure 176: Channel variation factor for a time varying period of 25ms, Left wrist to right hip standing, walking and running - 2.36 GHz

A.4.3 Channel Variation CDF for 820 MHz and 2.36 GHz

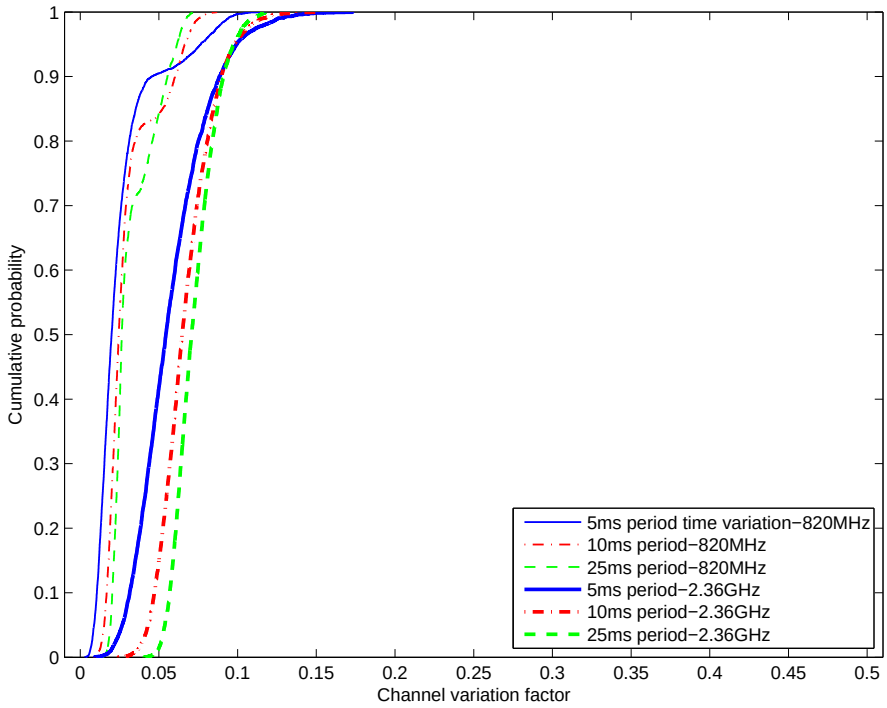

Figure 177: CDF of channel variation factor, back to chest standing, at 820 MHz and 2.36 GHz

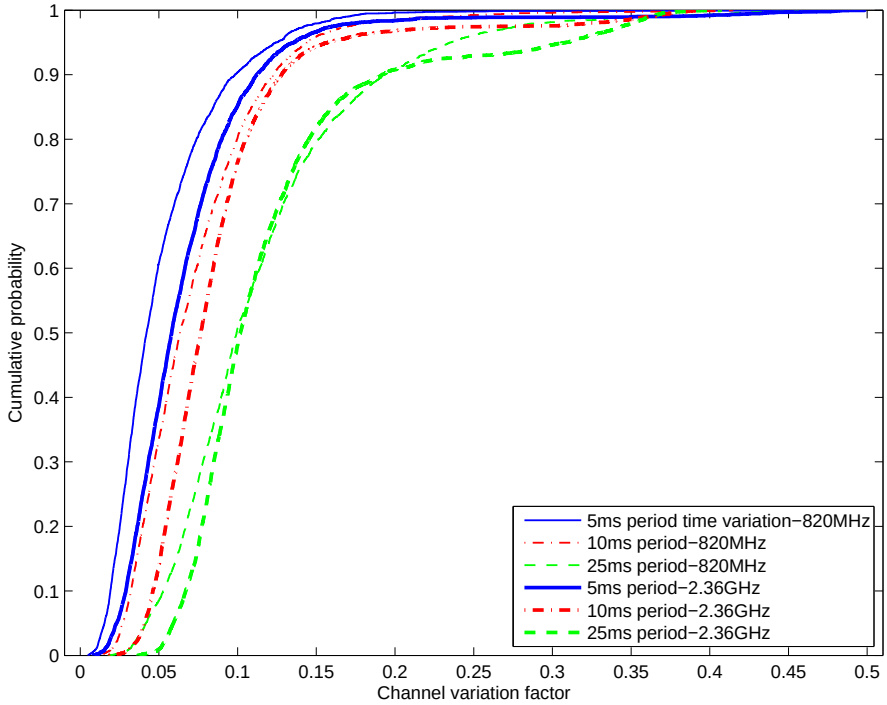

Figure 178: CDF of channel variation factor, back to chest walking, at 820 MHz and 2.36 GHz

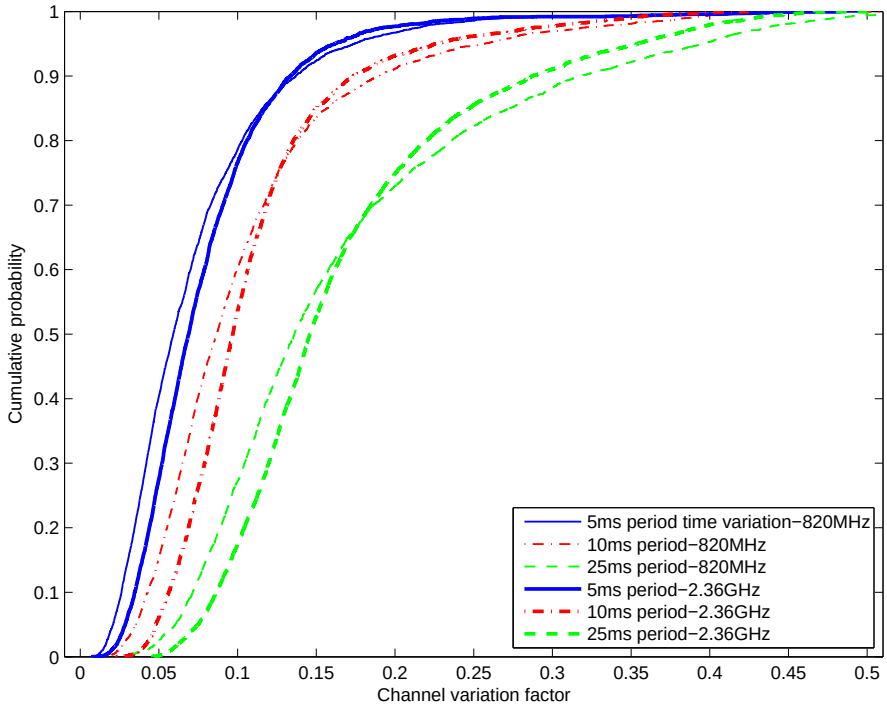

Figure 179: CDF of channel variation factor, back to chest running, at 820 MHz and 2.36 GHz

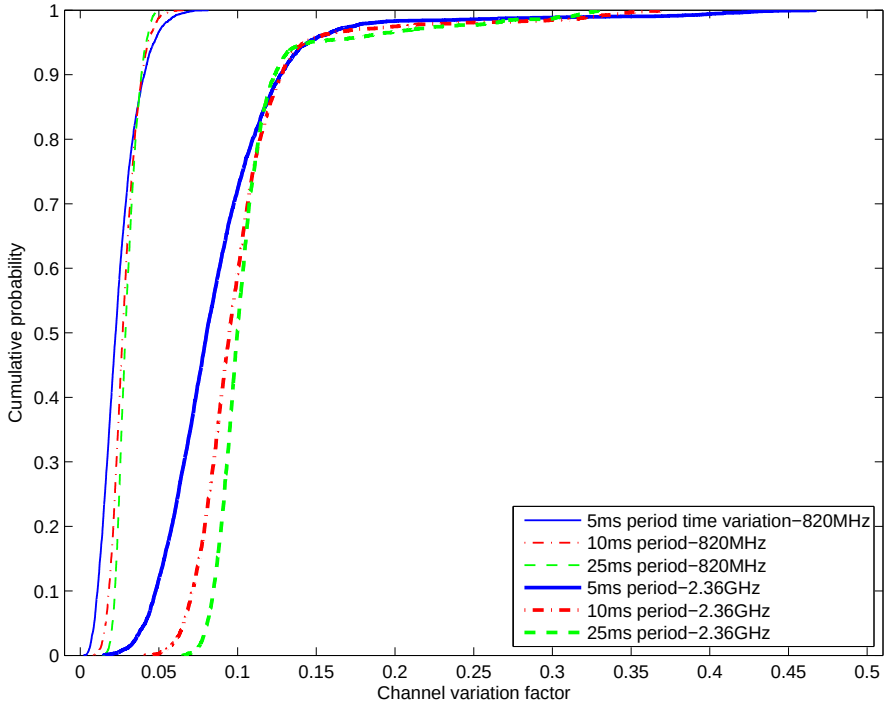

Figure 180: CDF of channel variation factor, back to right hip standing, at 820 MHz and 2.36 GHz

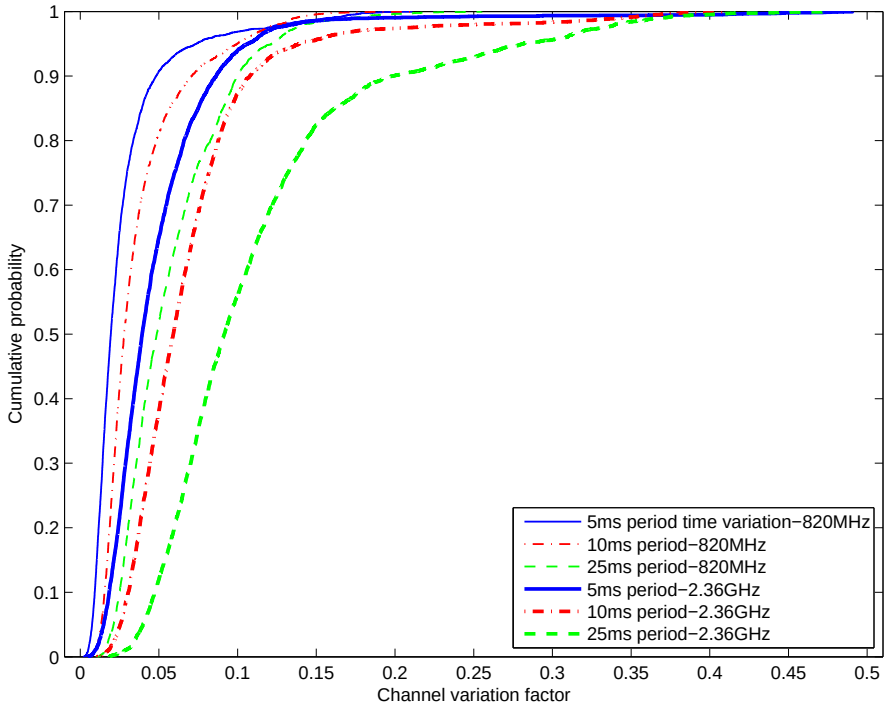

Figure 181: CDF of channel variation factor, back to right hip walking, at 820 MHz and 2.36 GHz

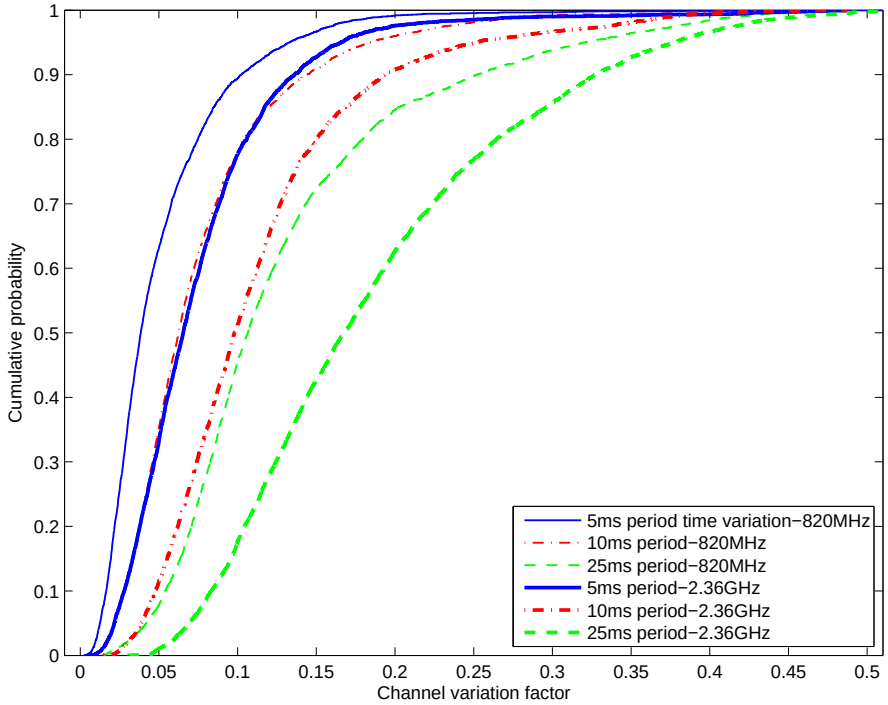

Figure 182: CDF of channel variation factor, back to right hip running, at 820 MHz and 2.36 GHz

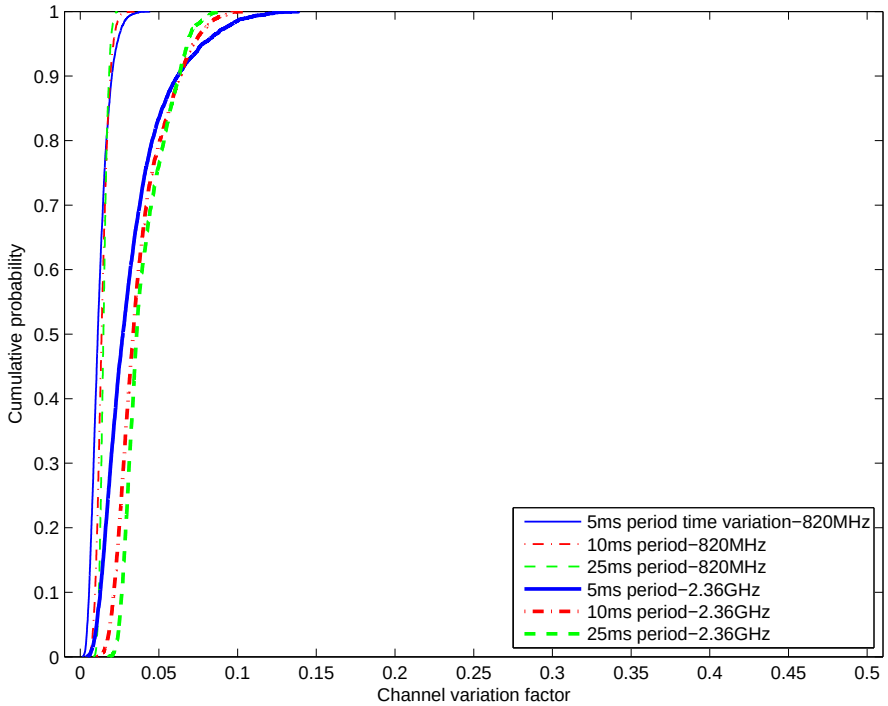

Figure 183: CDF of channel variation factor, chest to right hip standing, at 820 MHz and 2.36 GHz

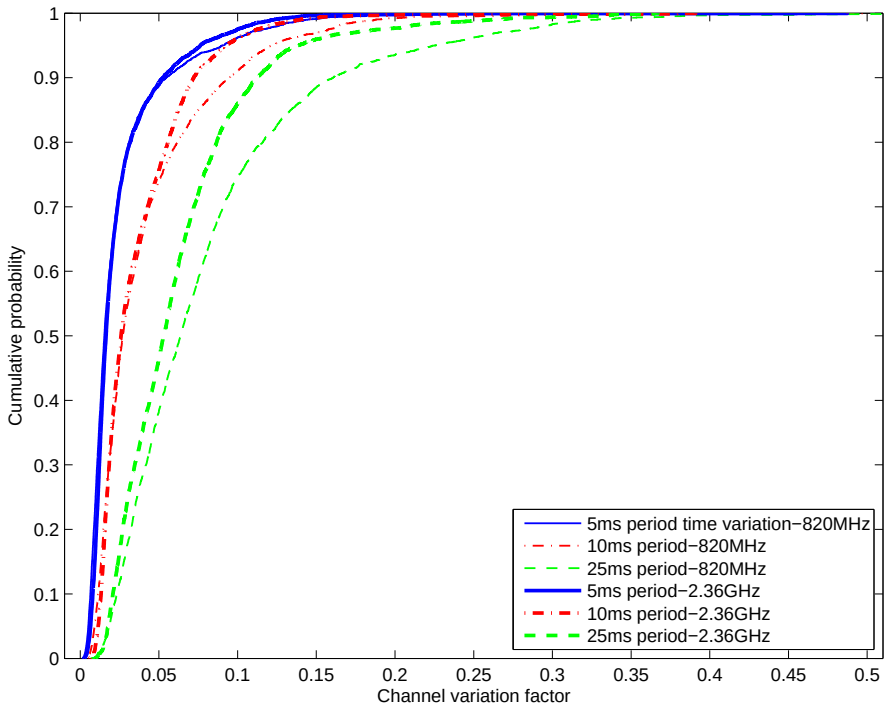

Figure 184: CDF of channel variation factor, chest to right hip walking, at 820 MHz and 2.36 GHz

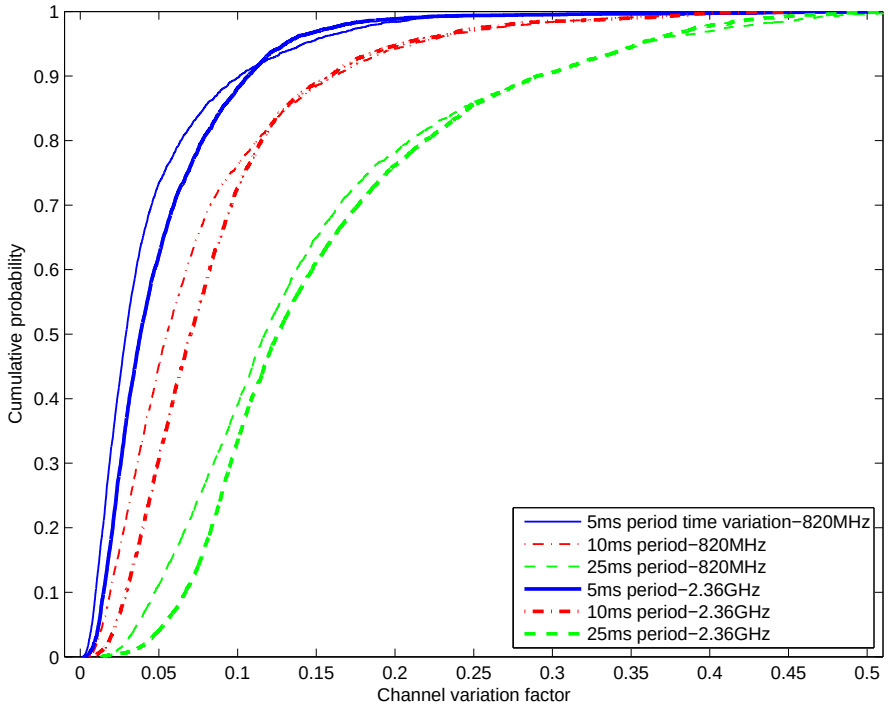

Figure 185: CDF of channel variation factor, chest to right hip running, at 820 MHz and 2.36 GHz

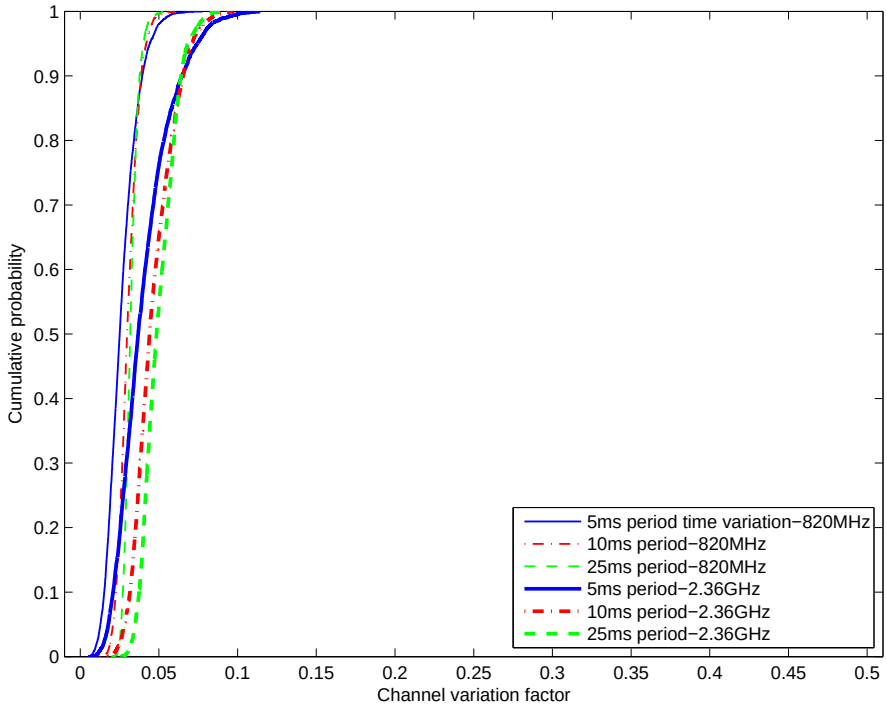

Figure 186: CDF of channel variation factor, left ankle to right hip standing, at 820 MHz and 2.36 GHz

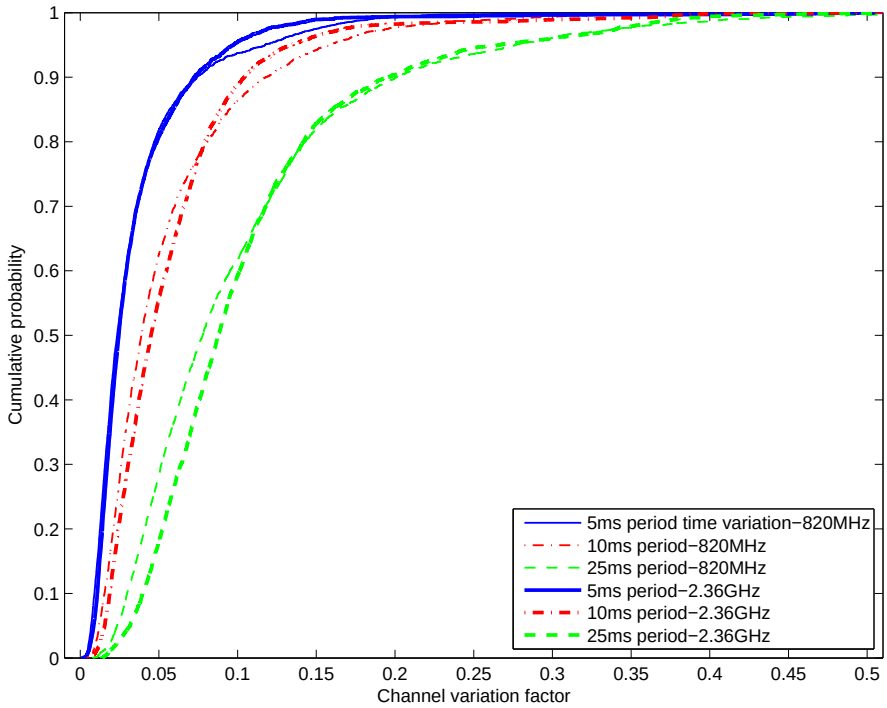

Figure 187: CDF of channel variation factor, left ankle to right hip walking, at 820 MHz and 2.36 GHz

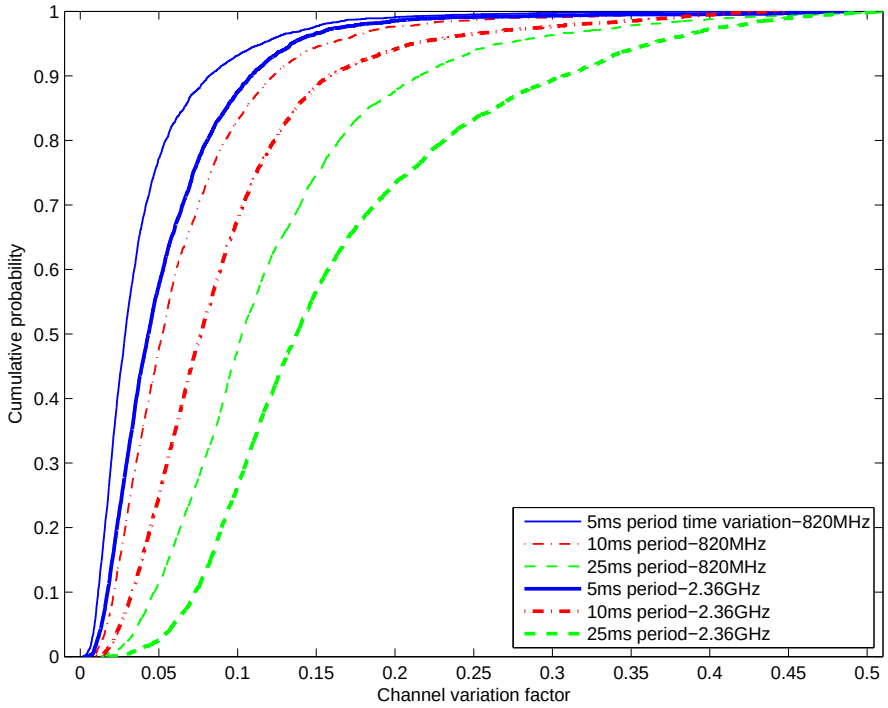

Figure 188: CDF of channel variation factor, left ankle to right hip running, at 820 MHz and 2.36 GHz

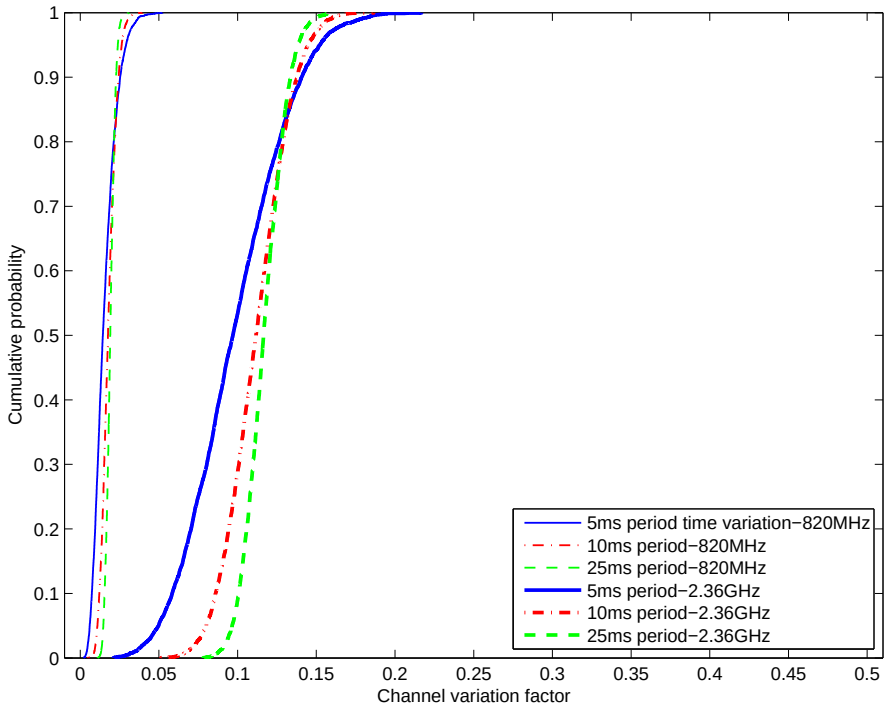

Figure 189: CDF of channel variation factor, left wrist to right hip standing, at 820 MHz and 2.36 GHz

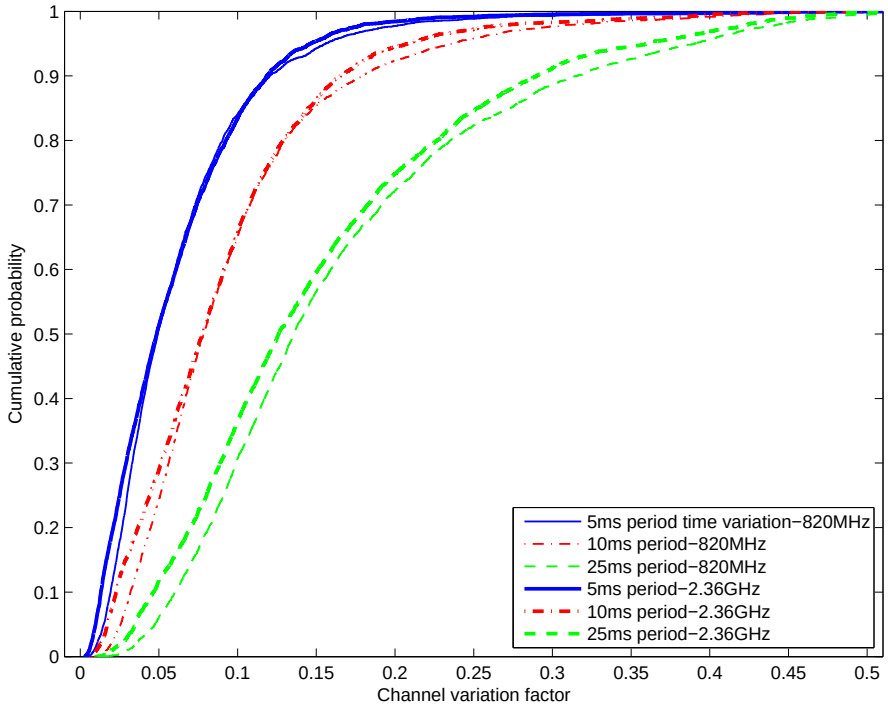

Figure 190: CDF of channel variation factor, left wrist to right hip walking, at 820 MHz and 2.36 GHz

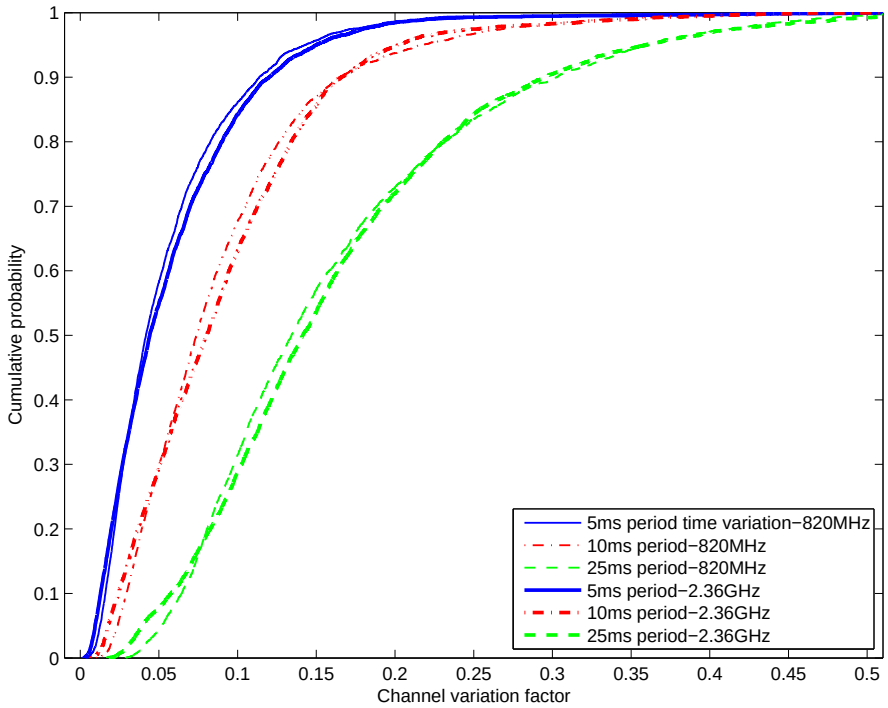

Figure 191: CDF of channel variation factor, left wrist to right hip running, at 820 MHz and 2.36 GHz

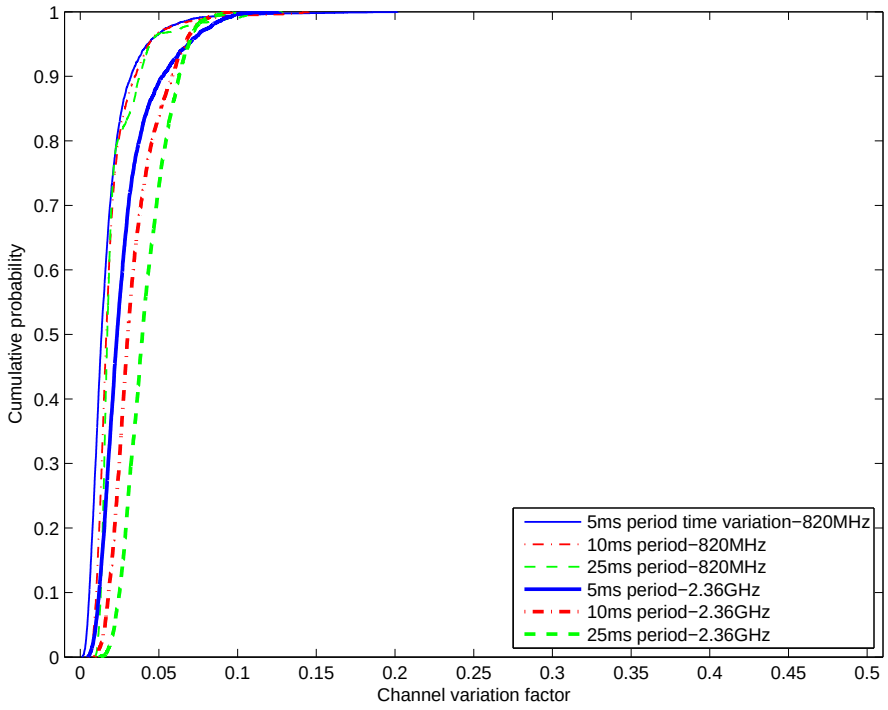

Figure 192: CDF of channel variation factor, right ankle to chest standing, at 820 MHz and 2.36 GHz

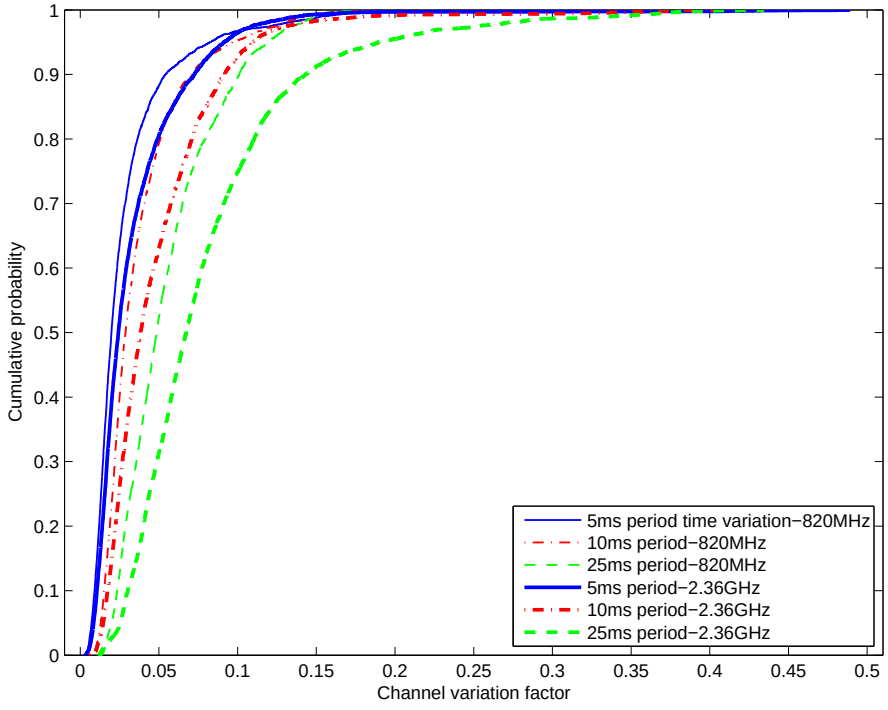

Figure 193: CDF of channel variation factor, right ankle to chest walking, at 820 MHz and 2.36 GHz

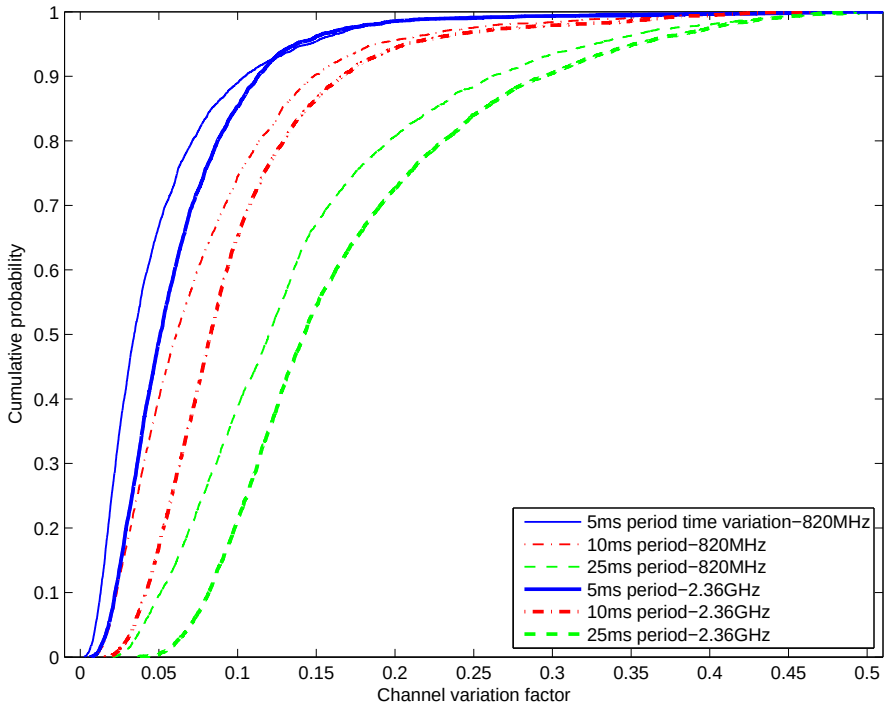

Figure 194: CDF of channel variation factor, right ankle to chest running, at 820 MHz and 2.36 GHz

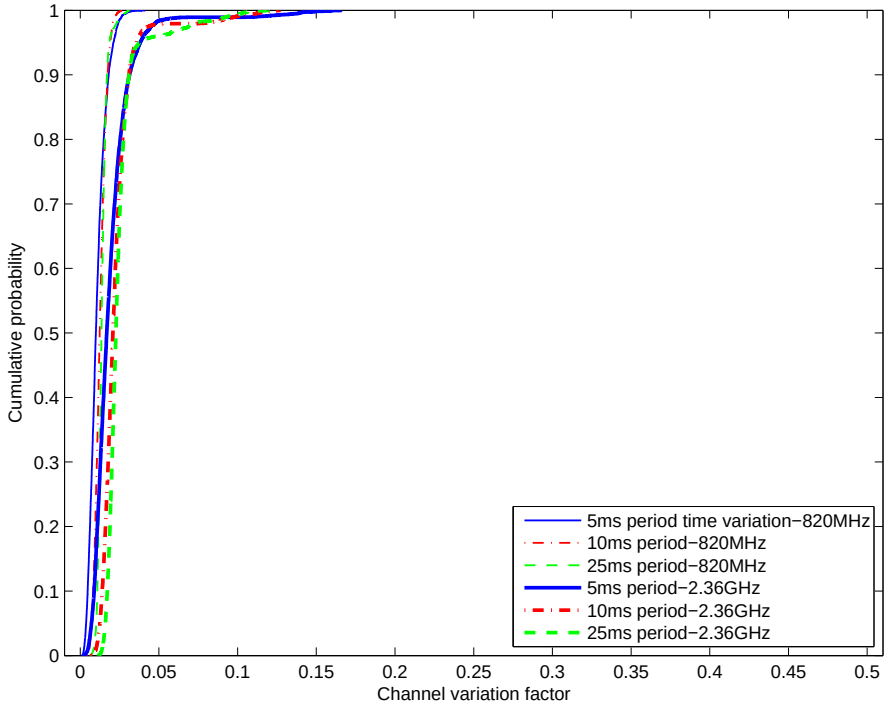

Figure 195: CDF of channel variation factor, right ankle to right hip standing, at 820 MHz and 2.36 GHz

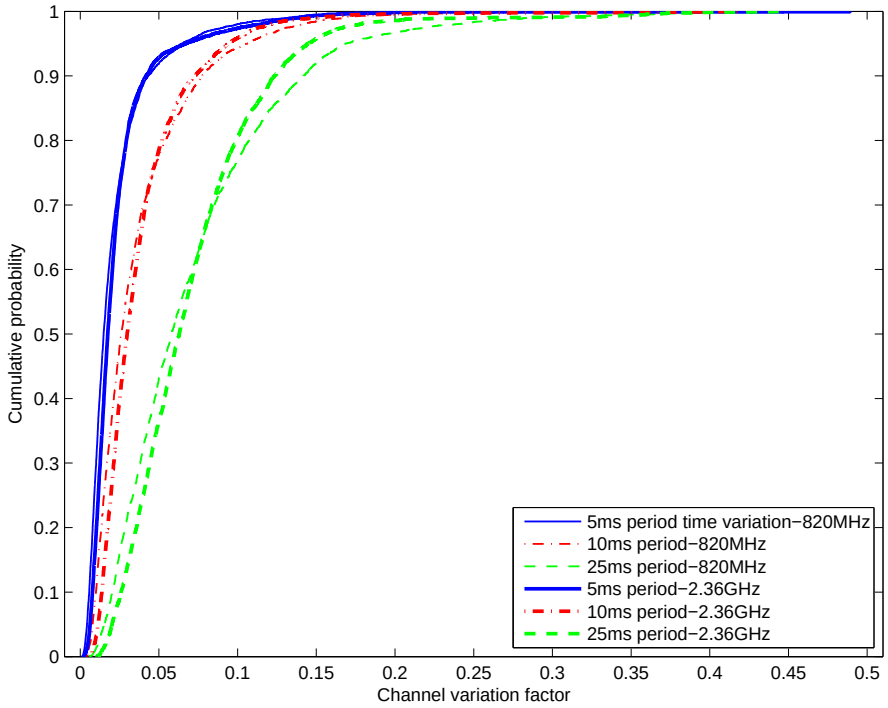

Figure 196: CDF of channel variation factor, right ankle to right hip walking, at 820 MHz and 2.36 GHz

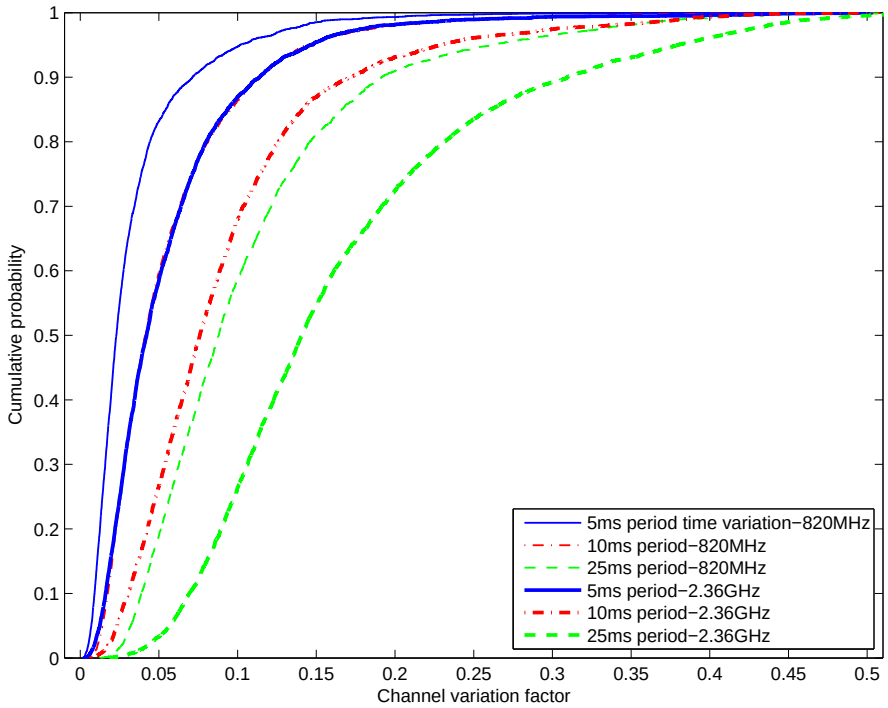

Figure 197: CDF of channel variation factor, right ankle to right hip running, at 820 MHz and 2.36 GHz

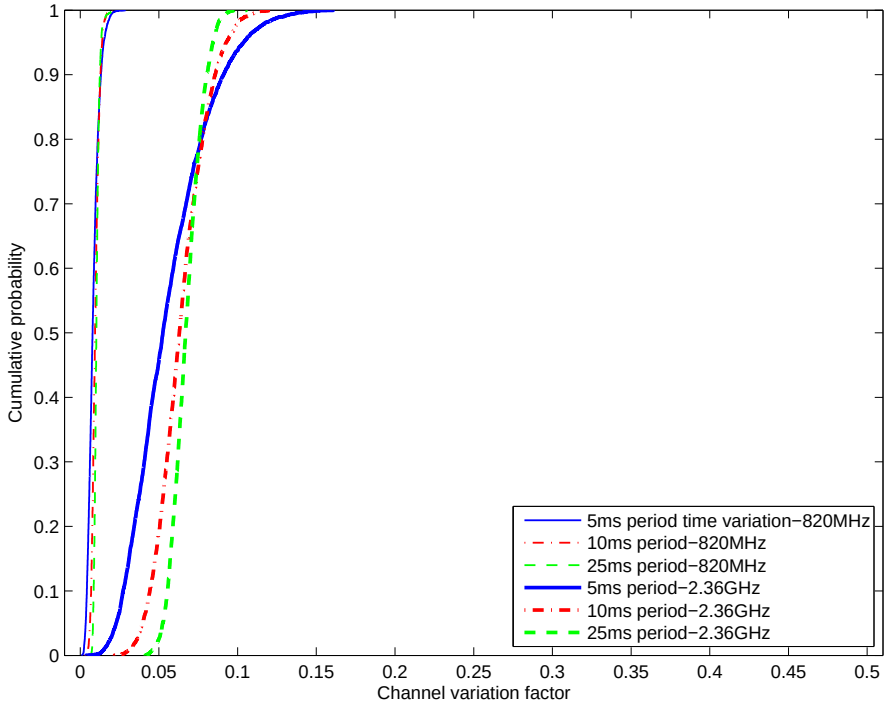

Figure 198: CDF of channel variation factor, right wrist to chest standing, at 820 MHz and 2.36 GHz

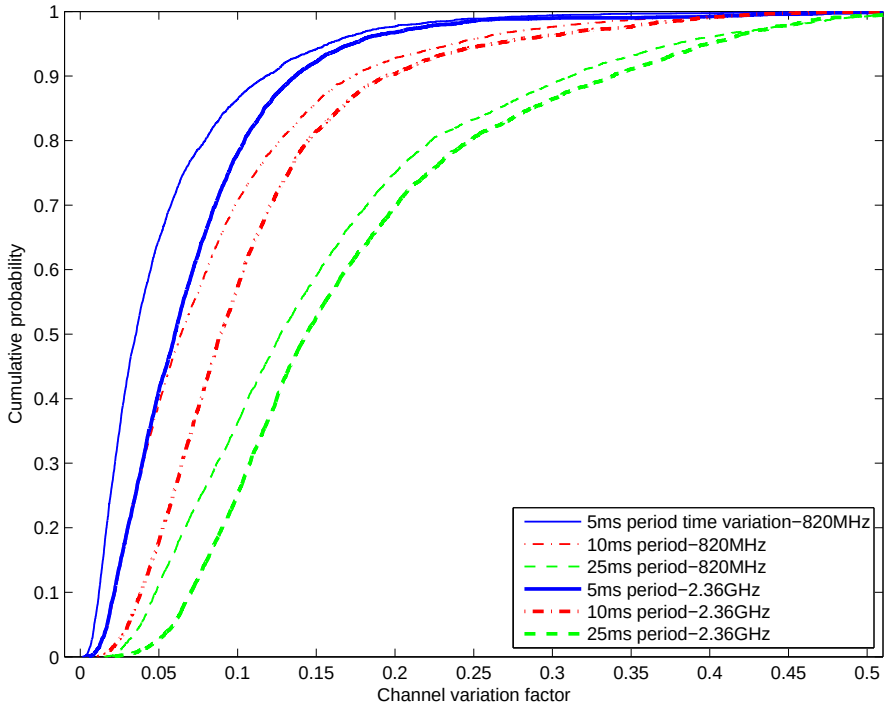

Figure 199: CDF of channel variation factor, right wrist to chest walking, at 820 MHz and 2.36 GHz

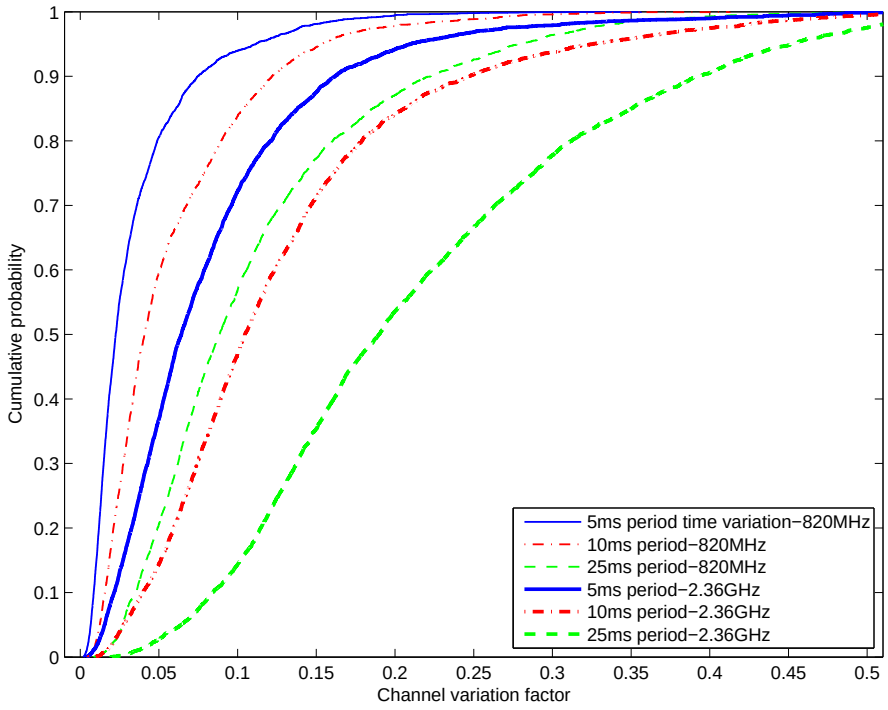

Figure 200: CDF of channel variation factor, right wrist to chest running, at 820 MHz and 2.36 GHz

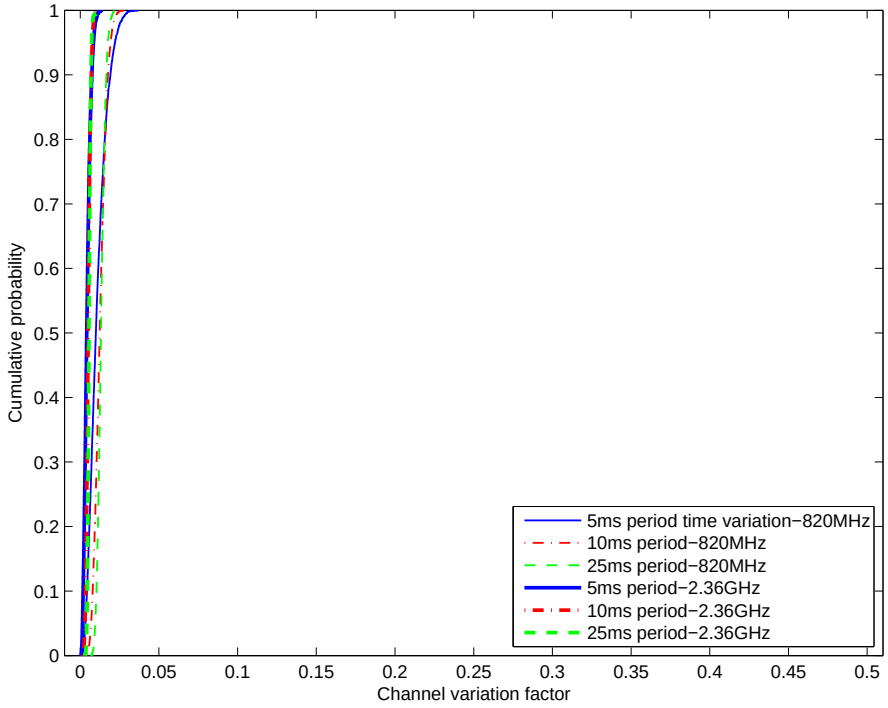

Figure 201: CDF of channel variation factor, right wrist to right hip standing, at 820 MHz and 2.36 GHz

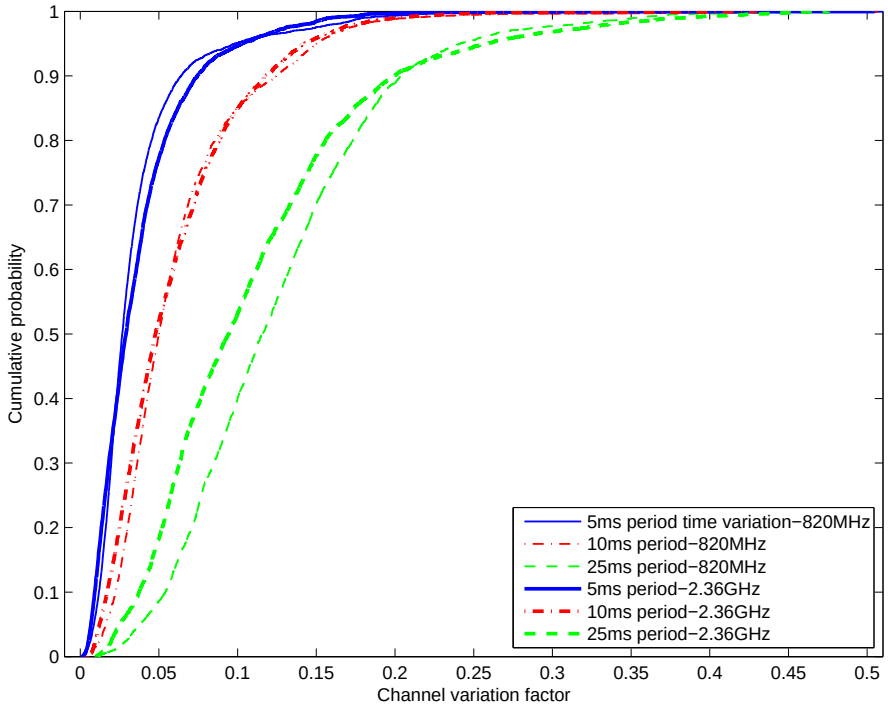

Figure 202: CDF of channel variation factor, right wrist to right hip walking, at 820 MHz and 2.36 GHz

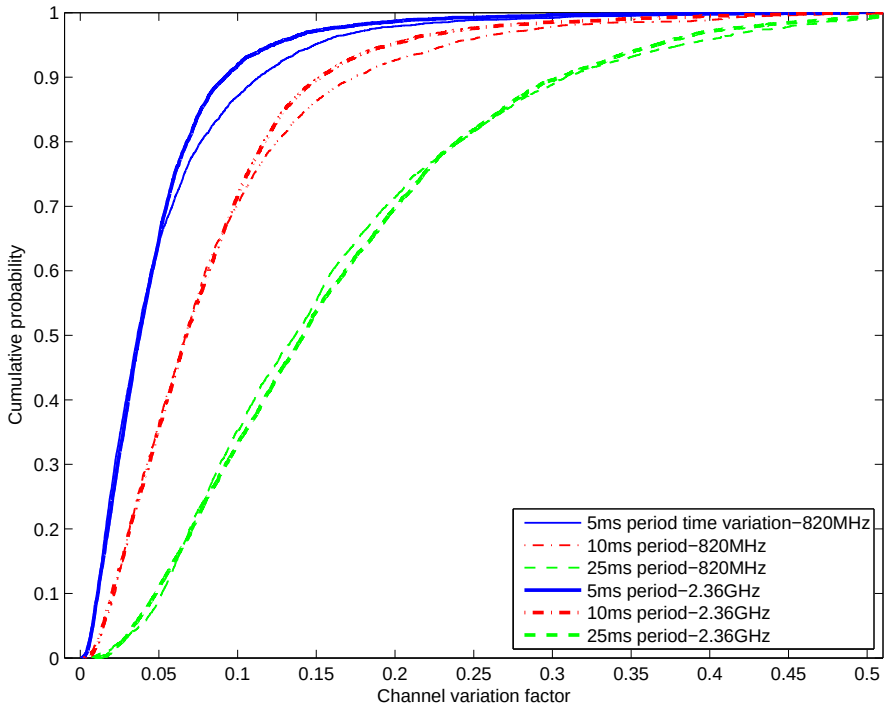

Figure 203: CDF of channel variation factor, right wrist to right hip running, at 820 MHz and 2.36 GHz